

A TELECOM-COMPATIBLE QUANTUM
MEMORY IN THE SOLID-STATE: SINGLE
ERBIUM IONS COUPLED TO SILICON
NANOPHOTONIC CIRCUITS

MOUKTIK RAHA

A DISSERTATION
PRESENTED TO THE FACULTY
OF PRINCETON UNIVERSITY
IN CANDIDACY FOR THE DEGREE
OF DOCTOR OF PHILOSOPHY

RECOMMENDED FOR ACCEPTANCE
BY THE DEPARTMENT OF
ELECTRICAL ENGINEERING
ADVISER: JEFFREY D. THOMPSON

MAY 2021

© Copyright by Mouktik Raha, 2021.

All rights reserved.

Abstract

Single atoms and atom-like defects in solids are promising platforms for realizing single photon sources and long-lived quantum memories, which are essential ingredients for the development of long-distance quantum networks. However, most atomic transitions are in the ultraviolet-NIR regions with wavelengths shorter than $1\text{ }\mu\text{m}$, where propagation losses in optical fibers are prohibitively large. A notable exception is erbium ion, whose optical transition at $1.5\text{ }\mu\text{m}$ is in the “telecom band”, allowing minimal fiber transmission losses. Isolating and addressing individual erbium ions using an optical interface have been elusive so far because of the poor emission rate of erbium due to the electric dipole-forbidden nature of its intra- $4f$ optical transition. We report the observation of fluorescence from single erbium ions for the first time. We achieve this by integrating erbium ions in a low loss, small mode-volume silicon nanophotonic cavity and enhancing their emission rate by over two orders of magnitude.

A crucial component of optically interfaced solid-state defects-based platforms is high-fidelity, projective measurement of the spin state, which is generally accomplished using fluorescence on an optical cycling transition. We demonstrate that the cavity modifies the local electromagnetic environment of an erbium ion (which otherwise lacks strong cycling transitions) and improves its cyclicity by greater than 100-fold, thus enabling high-fidelity single-shot quantum nondemolition readout of the ion’s spin. We also identify dozens of spectrally distinct ions coupled to the same cavity. Combining an optical frequency-domain multiplexing technique and microwave rotations, we individually initialize, manipulate, and perform single-shot spin measurement of six such ions. Our approach is not limited by the spatial separation between individual ions and is readily scalable to tens or hundreds of ions.

Finally, we demonstrate coherent coupling of an erbium electronic spin to a nearby nuclear spin and implement single-qubit and two-qubit gates on them, thus

extending our platform's prowess as a quantum memory by making a long-lived nuclear spin register available for storage and retrieval of information. These results are a significant step towards realizing long-distance quantum networks by utilizing multiplexed quantum repeater protocols and deterministic quantum logic for photons based on a scalable silicon nanophotonics architecture.

Acknowledgements

The work accomplished in this thesis would not have been possible without the unending support provided by a fairly large set of people, and I would like to acknowledge them in this section. While mentioning everyone of you is practically not feasible, I sincerely offer my gratitude to all of you!

First, I would like to thank my adviser, Prof. Jeff Thompson, for being a truly incredible mentor, providing all the guidance, support, and advice in research and beyond. His spirited and unyielding approach towards science is something that I strive to emulate. While tackling a problem, he regularly inspired me to come up with hypotheses, test them, and not to be afraid of switching gears when things are not working out according to expectations. During the early days of building the setup, working alongside him in the lab has also been an enriching experience. All of these have contributed towards my development as an independent researcher, while at the same time, working in the group has been exciting and productive. Jeff, it has been a privilege being your first graduate student, and thank you for putting your trust in me.

I would like to thank Prof. Nathalie de Leon and Prof. Stephen Lyon for serving in my FPO committee. Thank you Nathalie for providing timely advice and invaluable suggestions during various stages of the project. Thank you Steve for your seasoned advice and valuable conversations over the years. I am also grateful to Prof. Alejandro Rodriguez for acting as a reader of this thesis and providing valuable feedback.

In the Thompson lab, I had the pleasure of working with some of the finest researchers, who have shaped my research experience into an enjoyable one and also provided me with support and compassion during demanding times. In the first couple years of graduate school, a significant portion of my work was done in collaboration with Alan Dibos and Chris Phenicie. Alan's diverse knowledge in physics and technical prowess in fabrication have been critical assets when we embarked upon

this journey together of setting up the experiments from scratch. Chris' organized programming practices, dedicated efforts in building robust experimental setup, and good humor have made working on this project over the years considerably easier. I would also like to thank Chris for providing in-depth feedback during various stages of writing this thesis. During the past couple of years, I had the good fortune of collaborating with Songtao Chen. Songtao's immense patience while performing experiments and his strive for excellence are highly contagious; his high caliber in nanofabrication has made many of the later experiments feasible. More recently, it has been a delight to work with and turn the project over to Salim Ourari, Tuna Uysal, Sebastian Horvath, and Lukasz Dusanowski; I know that the project is certainly in good hands. I would also like to acknowledge Slava Dobrovitski for various discussions and theoretical contributions on the electron spin – nuclear spin interactions project. It has been fun sharing the lab space with Jack Wilson, Sam Saskin, Shuo Ma, Alex Burgers, Isaiah Gray, and Adam Turflinger.

The broader community of researchers in our department has also influenced my research experience as they often brought in unique perspectives and I have enjoyed learning newer things from them; whether I got to know you as classmates, colleagues, on departmental social events, or some other way, it has been my pleasure getting to know each one of you. I would like to thank the members of the de Leon lab, Houck lab, and Lyon lab for always extending their help and sharing experimental equipments whenever we reached out to them. Thank you Larry McIntyre and Barry Runner in the SEAS machine shop for assisting me on multiple occasions with machining useful components for my experimental setup. I would also like to sincerely thank Colleen Conrad, Barbara Fruhling, Roelie Abdi, Kate Furda, and other administrative staffs, for supporting me during my program.

I was fortunate enough to get to know Siddhartha and Rajkrishna in Princeton; you guys were the best housemates and friends I could have asked for and you made

my life in Princeton substantially easier. Ayan and Rajanya, I am thankful to you for all the help during both good and bad times. I am also grateful to my loving fiancé Priyanka for being extremely supportive over the years. Finally, I would like to sincerely thank my parents, Malay and Rina, for being with me at every step of the way, encouraging me all the time while being located halfway around the world, and in many aspects, this thesis belongs to them as much as it belongs to me.

To my family.

Contents

Abstract	iii
Acknowledgements	v
List of Tables	xiii
List of Figures	xiv
1 Introduction	1
1.1 Quantum repeater-based quantum networks	1
1.2 Why is Er ³⁺ appealing as a quantum memory?	4
1.3 Thesis outline	6
2 Background: Er³⁺ ion in a cavity	9
2.1 Rare-earth ions in solids	9
2.2 Er ³⁺ :Y ₂ SiO ₅	12
2.3 Purcell effect	16
2.4 Cavity-enhanced cyclicity of optical transitions	24
3 Photonic crystal cavities	27
3.1 A hybrid architecture: PC cavity-on-substrate	27
3.2 PC cavity design	29
3.3 FDTD simulations	33
3.4 Fabrication process	37
3.5 Characterization of PC cavities	39

4 Experimental setup	41
4.1 Measurement configuration	41
4.2 Optical pulse generation setup	43
4.3 Assembly inside Bluefors refrigerator	46
4.4 Achieving fiber-cavity coupling at low temperatures	50
4.5 Tuning the PC cavity resonance	52
4.6 Superconducting magnets	55
5 Isolating and enhancing the emission of single erbium ions	58
5.1 Experimental approach	58
5.2 Spectroscopy of single erbium ions	61
5.3 Extracting atom-cavity coupling parameters and confirming emission from a single ion	63
5.4 Spin-photon coupling	65
5.5 Conclusion and outlook	66
6 Optical quantum nondemolition measurement of a single rare earth ion qubit	69
6.1 Introduction	70
6.2 Experimental approach	71
6.3 Improving the cyclicity of the optical transitions	73
6.4 Single-shot quantum nondemolition measurement	77
6.5 Single Er^{3+} spin dynamics	79
6.6 Conclusion and outlook	81
7 Parallel single-shot measurement and coherent control of solid-state spins below the diffraction limit	82
7.1 Introduction	83
7.2 Experimental approach	84

7.3	Parallel initialization and readout of two ions	86
7.4	Sub-wavelength control over coherent spin rotations using the optical AC Stark shift	88
7.5	Parallel initialization and readout of two ions	90
7.6	Conclusion and outlook	92
8	Coherent interactions between a single rare-earth ion and a nuclear spin in the solid-state	94
8.1	Introduction	95
8.2	Detection and coherent control of a nearby nuclear spin	96
8.3	Implementing nuclear spin gates	99
8.4	Identifying and locating the nuclear spin	99
8.5	Probing the nuclear spin environment	102
8.6	Conclusion and outlook	103
9	Conclusion and outlook	105
9.1	Summary	105
9.2	Towards indistinguishable photons	106
9.3	Extending spin coherence: finding alternate host crystals	108
9.4	Improving device parameters for remote entanglement generation . .	109
9.5	Towards interacting spin ensembles	110
A	Additional data, analyses, and methods for the experiments presented in Chapter 5	112
A.1	Measurement and analysis techniques	112
A.2	Properties of the substrate used in this work	116
A.3	Temperature and magnetic field dependence of the spin-lattice relax- ation time, T_1	118
A.4	Saturation behavior of a single ion	119

A.5 Additional analysis of $g^{(2)}$ data	121
A.6 Bulk Er ³⁺ :YSO lifetime	125
B Additional data, analyses, and methods for the experiments presented in Chapter 6	127
B.1 Experimental details	127
B.2 Theoretical model of cavity-enhanced cyclicity	129
B.3 Calibration of P_{ex}	137
B.4 Estimate of intrinsic cyclicity of Er ³⁺ :YSO transition	138
B.5 Single-shot measurement fidelity	138
B.6 Intrinsic spin relaxation	140
C Additional data, analyses, and methods for the experiments presented in Chapter 7	143
C.1 Experimental configuration	143
C.2 State-selective initialization of spins	145
C.3 Spin coherence	147
C.4 Single qubit gates	149
C.5 Additional measurements on four ions	153
C.6 Generalization to N -ion control	155
Publications and Presentations	158
Bibliography	160

List of Tables

A.1 Lanthanide concentrations from GDMS in a nominally undoped YSO crystal	116
B.1 Parameters for the three ions studied in chapter 6	128

List of Figures

1.1	Principle of operation for a quantum repeater-based quantum network.	3
1.2	Long-distance transmission efficiency in optical fibers at various wavelengths	4
1.3	Entanglement between two multiplexed quantum registers	5
2.1	Center wavelength of Er ³⁺ optical transition across multiple known hosts	12
2.2	Er ³⁺ :YSO level structure	14
2.3	A two-level atom in a cavity	19
2.4	Simplified Er ³⁺ level structure with optical transitions labeled	24
3.1	Sketch of the hybrid Si PC cavity-on-YSO architecture	28
3.2	Design considerations for a Si nanobeam cavity on YSO substrate	31
3.3	PC cavity performance for various structural configurations	34
3.4	FDTD mode profiles and theoretical Purcell factors	36
3.5	Fabrication processes for making Si-on-YSO PC cavities	39
3.6	PC cavity characterization: SEM image and reflection spectrum	40
4.1	Measurement configuration	42
4.2	Optical pulse generation setup	44
4.3	Layout of components inside Bluefors refrigerator	47
4.4	Tapered fiber for fiber-cavity coupling	48

4.5	Adjusting Attocube positions to optimize fiber-cavity coupling during cool-down	51
4.6	Tuning the PC cavity resonance	54
4.7	Cross-sectional view of a superconducting magnet coil	56
5.1	Experimental configuration for enhancing Er ³⁺ emission with a silicon PC cavity	60
5.2	PLE spectrum of single ions in a dilute Er ³⁺ ensemble	62
5.3	Quantifying the Er ³⁺ -cavity coupling and measurement of $g^{(2)}$	64
5.4	Zeeman splitting of a single Er ³⁺ ion spectral line	65
6.1	Experimental approach.	72
6.2	Spin-photon coupling	73
6.3	Measuring the cyclicity of the optical transitions.	74
6.4	Tuning the cyclicity of optical transitions	76
6.5	Quantum nondemolition spin measurement.	78
6.6	Spin dynamics of a single Er ³⁺ ion.	80
7.1	Spectrally addressing multiple ions in a diffraction-limited volume . .	85
7.2	Simultaneous initialization and readout of ions 1 and 2	87
7.3	Coherent optical spin rotation using the AC Stark shift	89
7.4	Ion-selective rotations	90
7.5	Simultaneous initialization and readout of ions 3 – 6	91
8.1	Detection and coherent control of weakly-coupled nuclear spins using an Er ³⁺ electronic spin.	97
8.2	Nuclear spin gates	100
8.3	Locating the nuclear spin	101
8.4	Probing the nuclear spin bath	103

A.1	Experimental configuration for results reported in Chapter 5	113
A.2	Number of ions with a given Purcell factor	117
A.3	Counting peaks in the Er^{3+} spectrum	117
A.4	Temperature dependence of the spin T_1	119
A.5	Saturation spectra and power broadening of a single Er^{3+} ion.	120
A.6	Correlation between $g^{(2)}(0)$ value and SNR of the fluorescence	122
A.7	Power and pulse width dependence of the bunching in $g^{(2)}$	124
A.8	Temperature dependence of bunching in $g^{(2)}$ from a single ion.	125
A.9	Measurement of the bulk $\text{Er}^{3+}:\text{YSO}$ excited state decay rate.	126
B.1	Device details for results reported in Chapter 6	128
B.2	P_{ex} calibration	137
B.3	Extracting the bare ion cyclicity, C_0	139
B.4	Magnetic field amplitude dependence of cyclicity	141
B.5	Additional measurements of $T_{1,\text{dark}}$	142
C.1	Experimental configuration for results reported in Chapter 7	144
C.2	Device details for results reported in Chapter 7	144
C.3	Spin initialization of ions 1 and 2	146
C.4	Spin coherence of ions 1 and 2	148
C.5	Extended spin coherence time of ion 5	148
C.6	Simulation results for the phase shift and change in visibility	151
C.7	Four-ion cyclicity	153
C.8	Measured photon counts per shot for four-ions	154
C.9	Simulated optimal error for simultaneous control of multiple ions	156

Chapter 1

Introduction

1.1 Quantum repeater-based quantum networks

A quantum network lends us the capability to distribute entangled quantum states across large distances [1]. While this was originally motivated with the purpose of implementing quantum cryptography [2] where one can utilize the intrinsic randomness of quantum systems to securely encrypt communications, gradually quantum networks found other applications, ranging from modular quantum computation [3] and experiments involving tests of fundamental physics [4] to distributed quantum sensing [5] and future quantum internet [6].

Directly distributing quantum states across quantum channels such as optical fibers or free-space is primarily hindered by transmission loss and decoherence. A typical telecommunication optical fiber that is optimized for operating around $1.5\text{ }\mu\text{m}$ exhibits a transmission loss of 0.2 dB/km , which translates to a transmission efficiency of $1/e$ over a distance of $\sim 22\text{ km}$. Since the loss scales exponentially, the transmission drops significantly when we start to envision a country- or continent-wide network spanning hundreds or thousands of kilometers, *e.g.*, over a 500 km distance, the transmission efficiency reduces to 10^{-10} . Classical communication gets

around this problem of attenuation by using repeaters to amplify the signal. For a quantum network, a straight-forward application of repeater is not allowed, since it relies on using single photons for communications, which cannot be copied or “amplified” because of the no-cloning theorem [7]. However, a solution to this problem has been proposed in the form a “quantum repeater”, which requires long-lived quantum memories connected by efficient optical interfaces to implement an entanglement-based quantum network [8].

The basic concept of quantum repeater relies on dividing up a long distance (which could be the span of our entire network) into smaller segments, where each segment consists of quantum memories (nodes) connected by optical channels (Figure 1.1a). The first step of the protocol is to generate entangled states within each of these segments. Quantum memories prove to be useful here: instead of the requirement to succeed simultaneously in generating an entangled state at each segment, here we are allowed to perform multiple independent attempts at entanglement generation at each segment, and once we succeed, we store the entangled state in these quantum memories. When entanglement generation succeeds at least once in each segment, we proceed to the second step of the protocol: entanglement swapping between two adjacent memories, which doubles the distance spanned by the entangled state. Entanglement swapping is repeated until the quantum state is distributed across the entire network.

A key ingredient that determines the success probability of the quantum repeater protocol is high entanglement generation rate at each of the aforementioned segments. An entangled state at each segment is often realized by entangling the spin degrees of freedom of a quantum memory and photonic states, followed by performing joint detection of photons (Figure 1.1b). A number of physical platforms have been investigated towards realizing quantum memories, including trapped ions[9], laser-cooled atoms[10], defect centers in diamond (NV^- [11], SiV^- [12]), and quantum dots[13].

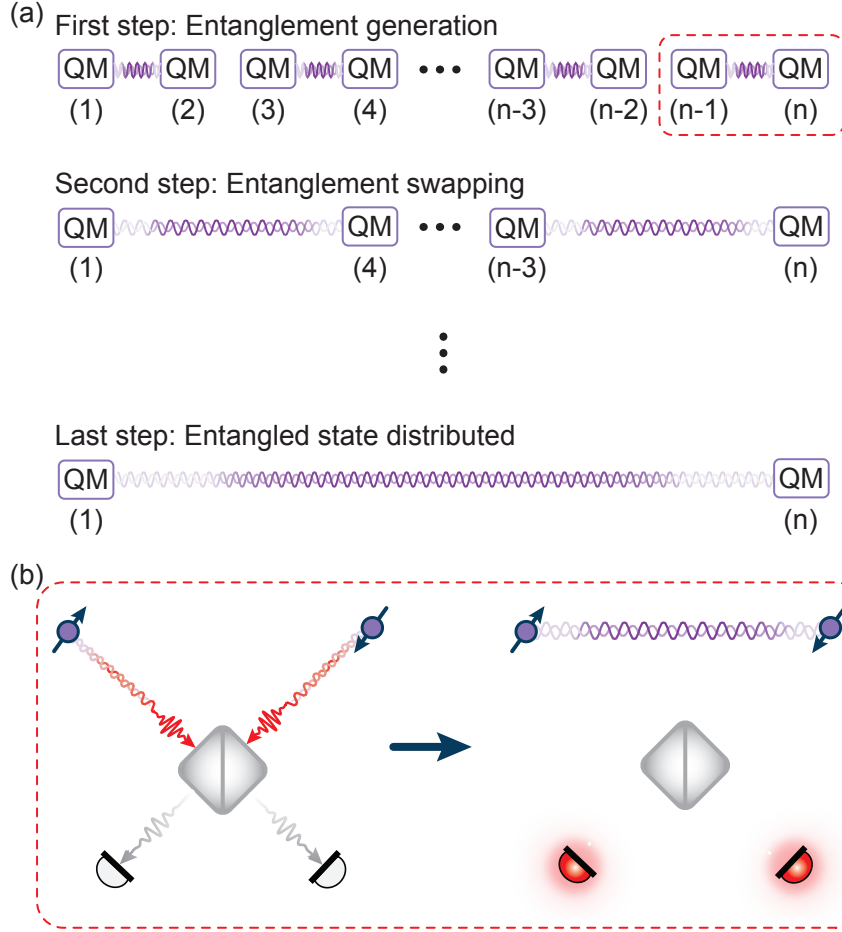


Figure 1.1: Principle of operation for a quantum repeater-based quantum network. (a) Steps outlining the working principle of a quantum repeater. Each quantum node is labeled by index (i). The goal is to distribute entangled states between node (1) and (n), which are likely to be separated by a large physical distance. (b) Typically, entanglement at the shortest segment of the quantum network is generated by entangling the spin and optical degrees of freedom at either quantum memories, followed by joint detection of photons in a way such that the “which-path” information of the photons is erased.

These single atoms or atomic defects in solids have been utilized to demonstrate many of the quantum network tasks, for example, spin-photon entanglement [9, 10, 11, 12, 13], remote entanglement between distant spins [14, 15, 16], unconditional teleportation of quantum states [17], entanglement distillation [18], and deterministic delivery of entangled states over a network [19].

In this thesis, we set out to realize quantum memory in an alternate physical platform: single erbium (Er^{3+})-ions, doped in a solid-state host and integrated within a photonic crystal cavity.

1.2 Why is Er^{3+} appealing as a quantum memory?

Several reasons make Er^{3+} an attractive platform for realizing quantum memories.

First, a primary challenge to distributing quantum states over distances longer than a laboratory scale is that most of the physical systems investigated prior to this work operate with optical transitions in the ultraviolet-to-NIR regions (wavelengths shorter than $1\ \mu\text{m}$) [20], where fiber transmission losses are significantly higher. For example, these losses are approximately $8\ \text{dB}/\text{km}$ for NV^- color centers in diamond (at $637\ \text{nm}$) [16], and $\sim 2\ \text{dB}/\text{km}$ for SiV^0 color centers in diamond [21] or InGaAs quantum dots [13] (both around $980\ \text{nm}$). Er^{3+} is a notable exception since it exhibits an atomic transition in the so-called “telecom band” wavelength of $1.5\ \mu\text{m}$, which has been thoroughly exploited by modern fiber-based telecommunication networks. At this wavelength, propagation losses are about $0.2\ \text{dB}/\text{km}$ [22], which translates to 10^{72} - and 10^{18} -fold improvement in transmissions with respect to that at $637\ \text{nm}$ and

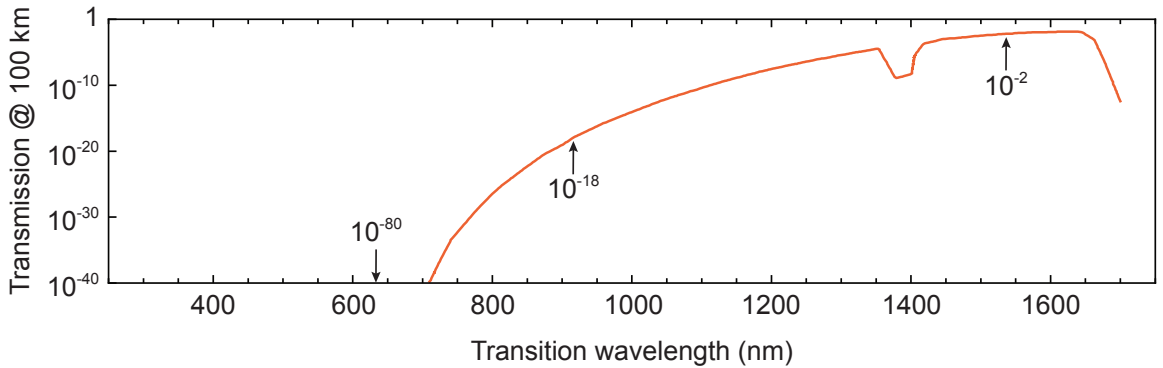


Figure 1.2: **Long-distance transmission efficiency in optical fibers at various wavelengths.** Er^{3+} is one of the few known emitters to exhibit an atomic transition at the telecom “C-band” wavelength of $1.5\ \mu\text{m}$, where transmission losses are minimal.

980 nm, respectively, over a reasonable distance of 100 km (Figure 1.2). However, it should be noted that several efforts toward single-photon wavelength conversion to $1.5 \mu\text{m}$ have been pursued using nonlinear optics [23, 24, 25] as well as using free-space communication (to avoid fiber-optic transmission altogether) [26].

Second, the $1.5 \mu\text{m}$ wavelength is compatible with silicon photonics [27]. This offers us the possibility to leverage the technologically mature silicon nanofabrication capabilities and integrate Er^{3+} ions within high-Q, small mode-volume photonic crystal cavities. A cavity helps in enhancing the photon scattering rate as well as increasing the photon collection efficiency – both contributing to higher spin-photon entanglement generation rate.

Third, the typical energy scale (homogeneous vs. inhomogeneous linewidth) for the optical transitions of Er^{3+} ions allows us to integrate multiple optically-addressable Er^{3+} ions within the mode-volume of the cavity, where individual emitters can be

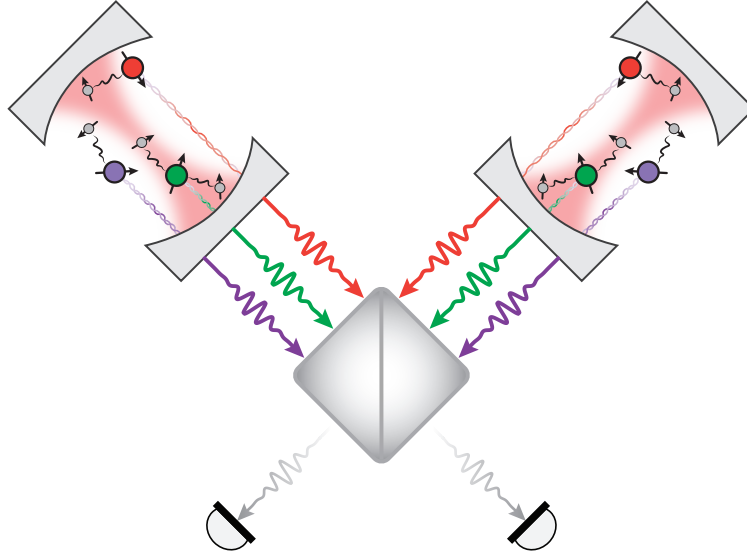


Figure 1.3: Entanglement between two multiplexed quantum registers. Each register consists of Er^{3+} spins (red, green, and purple circles) integrated within a high-Q cavity. Frequency-domain addressing allows us to manipulate and readout these Er^{3+} spins in parallel. Each Er^{3+} spin also coherently interacts with a few nearby nuclear spins (gray circles).

addressed in the frequency domain [28, 29]. Multiplexing over multiple emitters leads to a substantially higher entanglement generation rate. Multiple emitters per node may also contribute to a less-stringent coherence requirement per emitter, as well as, implementing quantum error-correction.

Lastly, Er^{3+} ions are nominally embedded in a solid-state host, where the spin-bath of the Er^{3+} electronic spin might also include coherently interacting nuclear spins. Single-qubit rotations of the nuclear spin and two-qubit gates between electronic and nuclear spins can be developed by directly driving the nuclear spin using radio-frequency (RF) pulses or via microwave-driven dynamical-decoupling pulse sequences on the electronic spin. This allows us the possibility to build a hybrid quantum register of electronic and nuclear spins [30], where the latter typically enjoy longer coherence times thereby making them ideal candidates for auxiliary quantum memories.

The potential to realize all of these features in a single physical platform makes Er^{3+} a unique candidate for quantum memories (Figure 1.3). To that end, in this thesis, I discuss several recent developments from our research group towards realizing such (quantum) memories with Er^{3+} ions and silicon nanophotonic cavities.

1.3 Thesis outline

The rest of this thesis follows the following outline:

Chapter 2 provides a concise overview of the concepts required for understanding the single Er^{3+} ion experiments. This will include a brief discussion of the level structure of Er^{3+} ions in a solid-state host and its spectroscopic properties, followed by the motivation to enclose the ions in a cavity. To that end, we will review the Jaynes-Cummings model for a two-level system inside a (bad)-cavity and extract the Purcell enhancement factor, and finally, conclude the chapter by introducing the concept of cavity-enhanced cyclicity.

Chapter 3 introduces the heterogeneously assembled cavity-on-a-substrate device geometry that will be used in all our experiments. Based on the geometry, we discuss the physical requirements and design principles for generating an optimal photonic crystal cavity that operates at the target wavelength. Performing finite-difference time-domain simulations of the field profiles let us compute the performance metrics of the cavities as well as estimate the Purcell factors across various cross-sections of the device geometry. The chapter concludes with outlining the steps toward fabricating and characterizing these cavities.

Chapter 5 kicks off the single Er³⁺ ion experiments, where we demonstrate the observation of emission from individual erbium dopants for the first time. We identify dozens of spectrally distinct lines that we attribute to be single ions coupled to the same cavity, prove that these are certainly single emitters (from the autocorrelation of emitted photons), and verify that the enhanced emission is indeed due to the presence of the cavity. We conclude the chapter showing coupling of the optical transitions to the Er³⁺ Zeeman spin levels. Results presented in this chapter and the associated supplementary materials (Appendix A) are published in Ref. [31].

Chapter 6 further investigates the modification of the electromagnetic density of states around an emitter in an optical cavity, where we conclude that along-with enhancing the emission rate, a cavity can also induce highly cyclic optical transitions in an emitter that is naturally not cyclic. Leveraging on the cavity-enhanced cyclicity, we realize single-shot quantum nondemolition readout of the ion's spin state. We use this readout to probe the relaxation of the spin as well as its coherent dynamics. Results presented in this chapter and the associated supplementary materials (Appendix B) are published in Ref. [32].

Chapter 7 expands on our ability to spectrally isolate multiple emitters and perform high-fidelity optical manipulations. Combining simultaneous optical frequency-domain addressing and global microwave rotations, we demonstrate

parallel initialization and single-shot spin measurement of six erbium ions coupled to the same cavity. Deep sub-wavelength control over coherent spin rotations is also attained using an optical AC Stark shift. Results presented in this chapter and the associated supplementary materials (Appendix C) are published in Ref. [33]

Chapter 8 reveals coherent interactions between an erbium electronic spin and a nearby nuclear spin, which is realized by driving the electronic spin with dynamical decoupling (microwave) sequences. We combine single-qubit and two-qubit gates to realize SWAP operations between the two spins. The nuclear spin is identified to be consistent with a ^1H spin at a particular location. Furthermore, we utilize the gates developed to probe the bath of the nuclear spin . Results presented in this chapter will appear in Ref. [34].

Chapter 9 summarizes our findings and presents an outlook of future experiments targeted towards quantum science and technologies with single erbium ions and integrated silicon photonics.

Chapter 2

Background: Er³⁺ ion in a cavity

In this chapter, I will provide a theoretical background required for understanding single Er³⁺ ions experiments. This will include discussions on the Er³⁺ electronic level structure, motivation for integrating Er³⁺ ions in a cavity, quantum mechanical treatment of a two-level system in a cavity, and cyclicity-enhancement of Er³⁺ optical transitions in a cavity.

2.1 Rare-earth ions in solids

Erbium (₆₈Er) is a member of the rare-earth group of elements in the periodic table, which is comprised of scandium (₂₁Sc), yttrium (₃₉Y), lanthanum (₅₇La), and the lanthanide group (₅₈Ce through ₇₁Lu). An Er³⁺ ion inherits many of the typical properties of rare earth ions (REIs); therefore, in this section, we will briefly discuss some of these relevant properties of REIs.

2.1.1 “Trapped” ions in solids

Solids-state crystals doped with REIs, in particular, lanthanides have been actively studied for realizing solid-state photonic quantum memories [35, 36]. High-resolution

optical spectroscopy of several REI-doped crystals have reported exceptionally narrow optical transition lines, often accompanied by excellent spin coherence properties at cryogenic temperatures [37]. Notable to mention among them are: optical coherence time $T_2 > 4$ ms measured in $\text{Er}^{3+}:\text{Y}_2\text{SiO}_5$ [38], and spin coherence time exceeding 6 hours shown in $^{151}\text{Eu}^{3+}:\text{Y}_2\text{SiO}_5$ [39]. These coherence results are particularly intriguing because atomic defects or ions in solid-state hosts are primarily susceptible to imperfections in the host lattice, generally giving rise to broad optical and spin transitions. The remarkable coherence properties of REI-doped crystal derives from the fact that the active electrons that contribute to the optical and spin transitions reside in the $4f$ electron shell.

When embedded in a host crystal, the lanthanides are commonly found in a trivalent state such that the electronic configuration takes the following form: $[\text{Xe}]4f^N$ (from $N=1$ in Ce through $N=14$ in Lu). What makes the $4f$ orbitals interesting is that they are located closer to the nucleus than the $5s$ and $5p$ orbitals. These fully-filled $5s$ and $5p$ orbitals effectively form a “Faraday cage” and (partially) shield the $4f$ orbitals from external perturbations [40]. The $4f$ electrons, thus, do not actively participate in chemical bonding with the host lattice, thereby giving rise to an ion trapped-in-a-*crystal* but mimicking the optical and spin properties of an ion trapped-in-*vacuum*.

2.1.2 Level structure of REIs in solids

An in-depth understanding of the optical and spin transition properties requires a thorough knowledge of the energy levels of REIs-in-solids. Extracting the level structure could be daunting task for such complicated multi-electronic species but thanks to decades of excellent experimental and theoretical investigations, we have a fairly good understanding of the same. While an extensive discussion on the level structure of REIs can be found in Ref. [41], detailed analysis can be found in Refs. [42, 43] as well

as references mentioned therein. A brief discussion on the level structure of trivalent REIs-in-solids follows here: we start with the free ion Hamiltonian, which includes terms corresponding to the kinetic and potential energy of $4f$ -electrons as well as pairwise Coulomb repulsion terms between the electrons and spin-orbit coupling terms. The closed-shell [Xe] core is spherically symmetric and thus does not lift the degeneracy of the $4f$ levels. The Coulomb and spin-orbit interaction terms partially lift this degeneracy resulting in states denoted by $^{2S+1}L_J$, which is a standard spectroscopic (Russell–Saunders) notation with S, L , and J indicating the spin, orbital angular, and total angular momentum, respectively. The strong spin-orbit interaction in REIs (comparable in magnitude to the Coulomb interaction) makes J a *good quantum number* here. However, there is a $(2J + 1)$ -fold degeneracy associated with each $^{2S+1}L_J$ state.

Once the (free) ion is embedded in a crystal, the degeneracy is further lifted due to lowering in symmetry brought about due to the ion being positioned in a crystal lattice site. The influence of the crystal lattice on the energy levels is explained by introducing crystal-field terms into the Hamiltonian. Since the lattice interacts weakly with the $4f$ electrons, the crystal-field splitting is quite smaller than the spin-orbit splitting and J remains a relatively good quantum number. A direct evidence of $4f$ orbitals being only weakly perturbed in the presence of crystal fields (arising from the host) can be found in Figure 2.1, where it is shown that the center wavelength of the $[(4f^{11})^4I_{15/2} \leftrightarrow (4f^{11})^4I_{13/2}]$ optical transition in Er^{3+} ion varies only slightly ($\sim 1\text{--}2\%$) while being incorporated in various host materials.

Whether the crystal field will lift all the degeneracies primarily depends on two factors – the crystal site symmetry as well as if the REI has an odd (Kramers) or even (non-Kramers) number of electrons. The Kramers' theorem dictates that for odd electronic systems in the absence of magnetic field, the energy levels are at least doubly-degenerate. A paradigmatic example of this is the level structure of $\text{Er}^{3+}:\text{Y}_2\text{SiO}_5$ (as

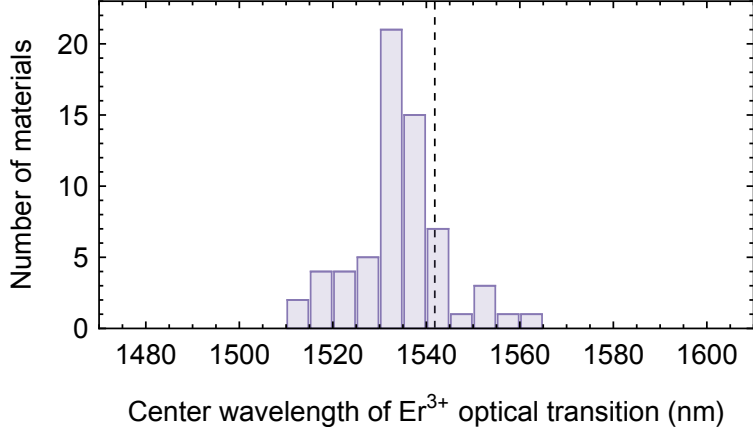


Figure 2.1: **Center wavelength of Er^{3+} $[(4f^{11})^4I_{15/2} \leftrightarrow (4f^{11})^4I_{13/2}]$ optical transition across multiple known hosts.** Histogram compiled from optical spectroscopy data available in the literature for 64 different host materials. Dashed line denotes the estimated transition wavelength for a free Er^{3+} ion.

discussed in Section 2.2): Er^{3+} is an odd-electronic system and inside Y_2SiO_5 , Er^{3+} is located at a low (C_1) symmetry site; this leads to the crystal field interaction breaking up each $^{2S+1}L_J$ multiplet into $J + 1/2$ doubly-degenerate levels. Further lifting of the degeneracies and refinement in the energy levels of REIs-in-solids are introduced by adding terms to the Hamiltonian corresponding to externally applied magnetic (Zeeman) or electric (Stark) fields, applied stress, magnetic hyperfine term (interaction between nuclear and electronic dipole moment), and higher order (quadrupole) interaction terms.

2.2 $\text{Er}^{3+}:\text{Y}_2\text{SiO}_5$

In this section, we will review key spectroscopic properties of Er^{3+} ions doped in a solid-state host, yttrium orthosilicate (Y_2SiO_5 , or YSO). All single Er^{3+} ion experiments reported in this thesis are performed on $\text{Er}^{3+}:\text{YSO}$.

2.2.1 Yttrium Orthosilicate (YSO)

YSO has been extensively investigated over the past few decades, primarily from the standpoint of applications in laser science [44, 45, 46, 47] and quantum optical memory [35, 48]. At cryogenic temperatures, magnetic field fluctuations arising from nuclear magnetic moments of the host nuclear spins often limit the optical and spin coherence properties of dopants. In YSO, the only dominant nuclear spin is ^{89}Y (100% abundance, spin 1/2), which has a small magnetic moment of $-0.137\mu_{\text{N}}$. It also contains ^{29}Si (spin 1/2) and ^{17}O (spin 5/2) with nuclear magnetic moments $-0.555\mu_{\text{N}}$ and $-1.893\mu_{\text{N}}$, respectively, but these have small natural abundance (4.7% and 0.04%) [49]. These led YSO to be often classified as a magnetically “quiet” host. The longest coherence time (to date) in solid-state systems was measured for the hyperfine levels of europium dopants in YSO [39], exceeding 6 hours.

From the crystallographic perspective, YSO is a monoclinic crystal that belongs to the C_{2h}^6 space group, where the Er^{3+} ions substitute for the Y^{3+} ions sitting at two inequivalent crystallographic sites. Both of these sites possess a very low (C_1) symmetry. Since Er^{3+} and Y^{3+} have comparable ionic radii, the Er^{3+} ions fill-up both of these sites roughly equally [50]. Due to different crystal fields around these sites, the two sites are spectroscopically easy to distinguish; all measurements reported in this thesis are performed at Er^{3+} ions situated at “Site 1” in YSO (following the convention in Ref. [50]).

2.2.2 Level structure of $\text{Er}^{3+}:\text{YSO}$

Following up with the discussion on level structure of trivalent REIs in solids in Section 2.1, we can write down the energy levels of $\text{Er}^{3+}:\text{YSO}$ here, as sketched in Figure 2.2. The two lowest spin-orbit manifolds for a free Er^{3+} ion ($[\text{Xe}]4f^{11}$) are $^4I_{15/2}$ and $^4I_{13/2}$ levels, respectively; the 1.5 μm telecom wavelength transition of interest in $\text{Er}^{3+}:\text{YSO}$ correspond to the atomic transition between these two spin-

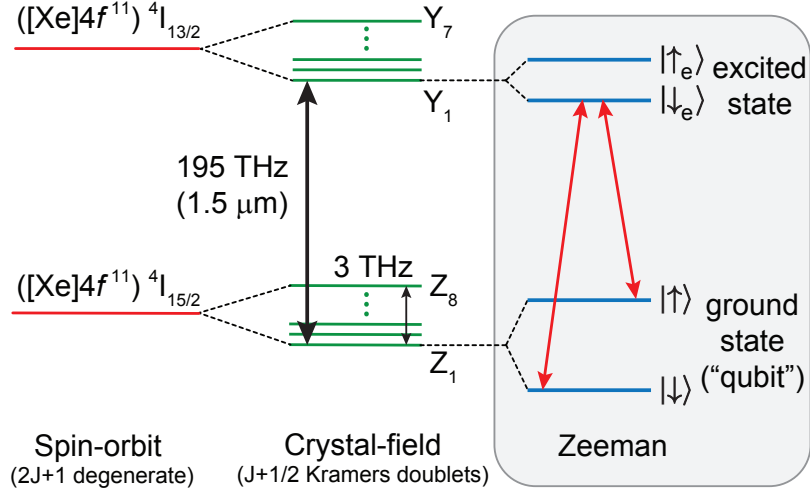


Figure 2.2: $\text{Er}^{3+}:\text{Y}_2\text{SiO}_5$ energy levels. At liquid-helium cryogenic temperature, the relevant level structure is an effective spin-1/2 manifold in both the Z_1 and Y_1 crystal field levels (shaded gray box), which are hereafter denoted by “ground” and “excited” states, respectively. The spin-1/2 ground state forms the “qubit” levels. The ground-to-excited optical transitions (red arrows) are centered around $\sim 1.5 \mu\text{m}$.

orbit levels. When doped in YSO at the C_1 crystal sites, because Er^{3+} is a Kramers’ system, the crystal field splits the $^{2S+1}L_J$ levels into $J+1/2$ doubly-degenerate levels. For example, the $^4I_{15/2}$ and $^4I_{13/2}$ states with 16-fold and 14-fold degeneracies are split up into 8 and 7 Kramers’ doublets, respectively; these crystal field levels are generally labeled as $\{Z_1, Z_2, \dots, Z_8\}$ and $\{Y_1, Y_2, \dots, Y_7\}$. The remaining degeneracies are broken in the presence of an external magnetic field as these doublets further split into single states [50].

2.2.3 Spectroscopic properties of $\text{Er}^{3+}:\text{Y}_2\text{SiO}_5$

Due to lattice imperfections, the crystal field interactions vary from site-to-site. This leads to Er^{3+} ions (and REIs, in general) exhibiting random, static shifts in their optical transitions, thereby giving rise to an inhomogeneous (ensemble) linewidth. Typically, for REIs in solids, this linewidth varies between 0.1 to 10 GHz in crystalline hosts and could be much broader than the homogeneous linewidth of an individual

ion (typically < 1 MHz). We would leverage this property for the case of Er³⁺ ions to optically address multiple individual ions simultaneously in Chapter 7.

At room temperature, the spin-lattice relaxation dominates all spin dynamics in the ground and excited state manifolds (Figure 2.2) of Er^{3+**:YSO}. But when the crystal is cooled to lower than liquid helium temperatures, spin lattice relaxation ceases to be an issue (see Section A.3 for additional discussions). At cryogenic temperatures, the optical transition exhibits high quantum efficiency with no phonon sidebands.

Extensive amount of research work has been performed to study the spectroscopic and coherence properties of bulk-doped Er^{3+**:YSO}. At cryogenic temperature, it has been demonstrated to exhibit long optical coherence time of 4.4 ms and extraordinarily narrow optical lines with near transform-limited homogeneous linewidth of 73 Hz [38]. The optical coherence depends on the external magnetic field strength and orientation, sample temperature, and Er³⁺ concentration [51, 38], while featuring a measured inhomogeneous linewidth of 200 – 500 MHz (depending on the Er³⁺ concentration) [50]. The **g**-tensors for the effective spin-1/2 ground and excited state manifolds were also carefully extracted and they are found to be highly anisotropic [52]. The longest spin lifetime T_1 measured for the ground state is 4.2 s [53], at a temperature of 20 mK and a magnetic field of 0.27 T (an independent study measured a lifetime of 129 ms at 3 K [54]). However, the spin coherence T_2 value (Hahn echo) is extracted to be only $\sim 5.6 \mu\text{s}$ [55], which could be extended upon application of a dynamical decoupling sequence.

Almost all of the features mentioned above suggests Er³⁺ ion as an unique physical platform capable of realizing a quantum memory. However it suffers from one major disadvantage: low photon emission rate. This is because the $1.5 \mu\text{m}$ optical transition corresponds to a $4f \leftrightarrow 4f$ transition, which the parity selection rule demands to be electric-dipole forbidden. Nevertheless, due to crystal field coupling, opposite parity orbitals (*e.g.* 5d states) are mixed with the 4f orbitals, thereby leading to

these optical transitions being *partially* allowed via a *forced* electric dipole transition (additionally, the magnetic dipole moment of the $^4I_{15/2} \leftrightarrow ^4I_{13/2}$ transition in Er³⁺ YSO is comparable to the forced electric dipole moment [45, 56]). This leads to long optical excited state lifetimes in Er^{3+>:YSO} of \sim 10 ms [50], which translates to a very poor photon emission rate of \sim 100 Hz. It is for the same reason emission from other individual REIs (viz., Pr³⁺ and Ce³⁺) has only been realized very recently [57, 58, 59, 60]. Such a low photon emission rate would render the platform unusable as an efficient single photon source and quantum memory.

We propose a direct solution to the poor photon emission rate problem: (Purcell)-enhance the emission rate of single Er³⁺ ions by positioning the Er^{3+>:YSO} crystal in close proximity to a photonic crystal cavity tuned to the transition frequency of the ion. Here, we can leverage the telecom-wavelength compatible optical transition of individual Er³⁺ ions to fabricate low-loss, small mode-volume cavities based on silicon nanophotonics. It should be noted that using Purcell enhancement to modify the emission properties of an atom or atom-like system have been previously explored by numerous research groups.

2.3 Purcell effect

We concluded Section 2.2 with that assertion that enclosing Er³⁺ ions in a cavity will lead to enhancing its emission rate by a phenomenon called the Purcell-effect [61]. In this section, we will review Purcell enhancement for a two-level atomic transition in a single-mode cavity. This is by no-means an exhaustive treatment of the subject, and readers interested in a more rigorous approach of the same may refer to the classic Refs. [62, 63, 64], among other available literature.

2.3.1 Modification of local density of states

Here is an intuitive picture of the phenomenon: consider a two-level atom (ground and excited state) with a transition frequency ω_q . Under the Weisskopf-Wigner approximation, spontaneous emission rate Γ_0 of the atom for decaying from the excited to the ground state is given by Fermi's golden rule [65]:

$$\Gamma_0 = \frac{2\pi}{\hbar^2} |M_{ge}|^2 \rho(\omega), \quad (2.1)$$

where M_{ge} and $\rho(\omega)$ are the electric dipole interaction term and photonic density of states at the atomic transition frequency, respectively. When the atom is in free space (vacuum), it basically decays into a continuum of electromagnetic modes. In this case, $\rho_{vac}(\omega) = \frac{\omega^2 V_0}{\pi^2 c^3}$ and $M_{ge} = \langle \vec{\mu}_{ge} \cdot \vec{E}_{vac} \rangle$, where $\vec{\mu}_{ge}$ is the electric dipole moment of the atomic transition and $E_{vac} = \sqrt{\frac{\hbar\omega}{2\epsilon_0 V_0}}$ is the vacuum electric field. Averaging over all possible random dipole moment orientations with respect to the electric field direction leads to $|M_{ge}|^2 = \frac{1}{3}\mu_{ge}^2 E_{vac}^2 = \frac{\hbar}{3} \frac{\mu_{ge}^2 \omega}{2\epsilon_0 V_0}$, yielding the free-space spontaneous emission rate Γ_{vac} as:

$$\Gamma_{vac} = \frac{\mu_{ge}^2 \omega_q^3}{3\pi\epsilon_0 \hbar c^3} \quad (2.2)$$

In Equation 2.1, noticeably, $\Gamma_0 \propto \rho(\omega)$. Now, let's enclose the atom inside a single-mode cavity. The presence of a cavity with physical dimensions comparable to the wavelength of the atomic transition modifies the density of states dramatically. The density of states accompanying a cavity with resonance centered at ω_c and a full-width half-maximum (FWHM) width of κ is given by [65] (cavity quality factor $Q = \omega_c/\kappa$):

$$\rho_{cav}(\omega) = \frac{1}{\pi} \frac{\kappa/2}{(\omega - \omega_c)^2 + (\kappa/2)^2} \quad (2.3)$$

Here, by ‘single-mode’ it is implied that only one mode of the cavity is near-resonant to the atomic transition frequency while the other modes are far-detuned such that

we can safely ignore them. When the cavity and atomic transition are resonant ($\omega_q = \omega_c$), the density of states computes to $\rho_{\text{cav}} = 2/\pi\kappa = 2Q/\pi\omega_q$. This leads to a cavity-modified spontaneous emission rate Γ_{cav} that is larger than Γ_{vac} by a factor of $\rho_{\text{cav}}(\omega)/\rho_{\text{vac}}(\omega)$. Assuming a perfect alignment of the atomic dipole moment and cavity electric field polarization, the ‘Purcell’ enhancement factor P computes to:

$$P \equiv \frac{\Gamma_{\text{cav}}}{\Gamma_{\text{vac}}} = \frac{3}{4\pi^2} \cdot \frac{Q}{V_{\text{cav}}/\lambda^3}, \quad (2.4)$$

where V_{cav} is the mode-volume of the single-mode optical cavity. It should be noted that the Purcell factor is completely determined by the physical parameters of the cavity since the atomic parameters cancel out. For a large Purcell factor, the atom almost entirely decays into the single-mode of the cavity, thereby increasing the directional emission properties of the atom as well.

2.3.2 Cavity-QED: two-level atom in a cavity

Let us perform a more formal treatment of the subject now using techniques from cavity quantum electrodynamics (QED), adapting an analysis similar to Ref. [66]. Consider a two-level atom $\{|g\rangle, |e\rangle\}$ (with a transition frequency of ω_q) inside a single-mode cavity (with resonance frequency ω_c), being driven by a laser at frequency ω_L , as sketched in Figure 2.3. The rate of coupling between the atom and the cavity is determined by the single photon Rabi frequency, $2g$, given by:

$$g = \frac{\vec{\mu}_{\text{ge}} \cdot \vec{E}_{\text{cav}}}{\hbar} = \frac{\mu_{\text{ge}}}{\hbar} \sqrt{\frac{\hbar\omega}{2\epsilon_0 V_{\text{cav}}}}, \quad (2.5)$$

where $\vec{\mu}_{\text{ge}}$ is the electric dipole moment of the atomic transition, \vec{E}_{cav} is the cavity electric field strength at the atom’s position, and V_{cav} is the mode-volume of the optical cavity, respectively. The final expression for g implicitly assumes that the atomic dipole moment is perfectly aligned with cavity polarization and the cavity field intensity is maximized at the atom’s position. In the rotating-frame of

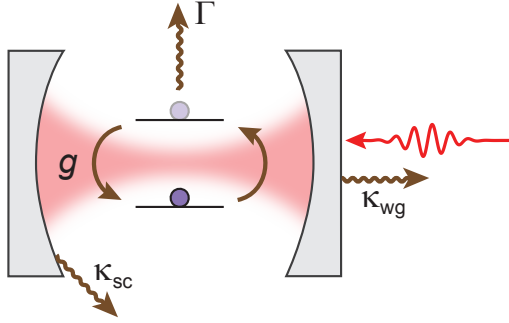


Figure 2.3: **A two-level atom in a cavity.** Dynamics of the atom-cavity system is determined by the single photon Rabi frequency ($2g$), cavity decay rates ($\kappa_{\text{wg}}, \kappa_{\text{sc}}$), and (bare) atomic emission rate Γ .

the laser field, the Jaynes-Cummings Hamiltonian that describes the dynamics of the atom-cavity system is given by (making the rotating-wave approximation; $\hbar = 1$):

$$H_{\text{JC}} = \frac{1}{2}\Delta_q\sigma_z + \Delta_c a^\dagger a + g(a^\dagger\sigma_- + a\sigma_+), \quad (2.6)$$

where $\Delta_q = \omega_q - \omega_L$ and $\Delta_c = \omega_c - \omega_L$ are the detunings of the (bare) atomic and cavity frequency from the incident laser frequency, $a^\dagger(a)$ is the creation (annihilation) operator for a photon in the cavity mode, and σ_\pm, σ_z are the usual Pauli matrices that operate on the atom ($\sigma_+(\sigma_-)$ for atomic state raising (lowering)). Let us introduce the following loss-channels: spontaneous emission rate Γ corresponding to the decay of atom from excited to ground state, and cavity photon decay rate ($\kappa = \kappa_{\text{wg}} + \kappa_{\text{sc}}$) for photon losses through the waveguide (κ_{wg}) and into other loss channels (κ_{sc}) like scattering losses, absorption losses, etc. We will assume that the cavity is single-sided; so light enters the cavity from one-side at rate κ_{wg} .

A typical approach towards investigating the dynamics of such systems is to use the Heisenberg-Langevin formalism, where the loss channels in these “open systems” are introduced via coupling to a continuum of reservoir modes. The Heisenberg-Langevin equations of motion governing the dynamics of the aforementioned system is given by:

$$\dot{a} = -ig\sigma_- - (\kappa/2 + i\Delta_c) a - \sqrt{\kappa_{\text{wg}}} a_{\text{wg,in}} - \sqrt{\kappa_{\text{sc}}} b_{\text{sc}} \quad (2.7)$$

$$\dot{\sigma}_- = ig a \sigma_z - (\Gamma/2 + i\Delta_q) \sigma_- + \sqrt{\Gamma} b_{\text{sp}} \sigma_z \quad (2.8)$$

$$\dot{\sigma}_z = -2ig(a\sigma_+ - a^\dagger\sigma_-) - \Gamma(\sigma_z + 1) - 2\sqrt{\Gamma}(b_{\text{sp}}^\dagger\sigma_- + b_{\text{sp}}\sigma_+) \quad (2.9)$$

where b_{sc} and b_{sp} are operators corresponding to noise channels associated with internal cavity losses and decay of photons via spontaneous emission into other modes (instead of the cavity mode), respectively. The cavity-waveguide coupling is expressed via the operators $a_{\text{wg,in}}$ and $a_{\text{wg,out}}$ denoting the input and output photon field, and they are related to each other by the following input-relation:

$$a_{\text{wg,out}} = -a_{\text{wg,in}} + \sqrt{\kappa_{\text{wg}}} a \quad (2.10)$$

The relative strengths of (g, κ, Γ) determines the atom-cavity dynamics. For all experiments involving Er³⁺ ions in a photonic crystal cavity, we will be operating in the ‘bad cavity’ strong-coupling regime of cavity-QED where the hierarchy of these parameters dictate $g^2/(\kappa\Gamma) \gg 1$ and $\kappa \gg g \gg \Gamma$, such that the cavity decay rate dominates over all other coupling terms. From the physical perspective, this implies that whenever we excite the atom, the rate of transfer of its energy to the cavity mode is faster than it decaying to other modes ($g \gg \Gamma$); but before the atom can reabsorb the photon, the latter decays through the cavity ($\kappa \gg g$). Effectively, every excitation of the atom results in a photon escaping through the cavity. In this limit, we can integrate out cavity modes by performing adiabatic elimination (setting $\dot{a} = 0$) since the cavity mode is over-damped [64], yielding the following expression for the cavity field:

$$a = (-ig\sigma_- - \sqrt{\kappa_{\text{wg}}} a_{\text{wg,in}})/(\kappa/2 + i\Delta_c), \quad (2.11)$$

Notice that in Equation 2.11 and henceforth (following Ref. [64]), we have also ignored b_{sc} and b_{sp} terms since for our operational configuration involving optical frequencies and liquid helium temperatures at high vacuum, the expectation value of b_{sc} and b_{sp} operators over vacuum modes evaluates to zero. Inserting Equation 2.11 back into the Heisenberg-Langevin Equations 2.8 and 2.9, we can extract the equations of motion for the atom dynamics:

$$\dot{\sigma}_- = - \left(\frac{\Gamma}{2} + i\Delta_q + \frac{g^2}{\tilde{\kappa}} \right) \sigma_- - ig \frac{\sqrt{\kappa_{\text{wg}}}}{\tilde{\kappa}} a_{\text{wg,in}} \sigma_z \quad (2.12)$$

$$\dot{\sigma}_z = - \left(\Gamma + \frac{g^2 \kappa}{|\tilde{\kappa}|^2} \right) (\sigma_z + 1) + 2ig \left(\frac{\sqrt{\kappa_{\text{wg}}}}{\tilde{\kappa}} a_{\text{wg,in}} \sigma_+ - \frac{\sqrt{\kappa_{\text{wg}}}}{\tilde{\kappa}^\dagger} a_{\text{wg,in}}^\dagger \sigma_- \right) \quad (2.13)$$

where $\tilde{\kappa} = \kappa/2 + i\Delta_c$. Following Ref. [64], in the bad-cavity limit, we can take the expectation values of the operators in the Heisenberg-Langevin equations and reduce these equations to their semi-classical limit, where the electric field can be treated classically and mean values of the atom and cavity operators are separable. Operating at the cavity resonance ($\Delta_c = 0$), we get:

$$\langle \dot{\sigma}_- \rangle = - \left(\frac{\Gamma}{2} \left(1 + \frac{4g^2}{\kappa \Gamma} \right) + i\Delta_q \right) \langle \sigma_- \rangle - ig \frac{2\sqrt{\kappa_{\text{wg}}}}{\kappa} \langle a_{\text{wg,in}} \rangle \langle \sigma_z \rangle \quad (2.14)$$

$$\langle \dot{\sigma}_z \rangle = -\Gamma \left(1 + \frac{4g^2}{\kappa \Gamma} \right) (\langle \sigma_z \rangle + 1) + 2ig \left(\frac{2\sqrt{\kappa_{\text{wg}}}}{\kappa} \langle a_{\text{wg,in}} \rangle \langle \sigma_+ \rangle - \frac{2\sqrt{\kappa_{\text{wg}}}}{\kappa} \langle a_{\text{wg,in}}^\dagger \rangle \langle \sigma_- \rangle \right) \quad (2.15)$$

Also note that, in Equation 2.11 for the case of a cavity *without* an atom ($g = 0$), the field operator expression reduces to $a = -\sqrt{\kappa_{\text{wg}}} a_{\text{wg,in}}/\tilde{\kappa}$, such that we can compute the mean photon number in the cavity \bar{n} as:

$$\bar{n} = \langle a^\dagger a \rangle = \frac{\kappa_{\text{wg}}}{|\tilde{\kappa}|^2} \langle a_{\text{wg,in}}^\dagger a_{\text{wg,in}} \rangle = \frac{\kappa_{\text{wg}}}{|\tilde{\kappa}|^2} \bar{n}_{\text{in}} \rightarrow 4 \frac{\kappa_{\text{wg}}}{\kappa^2} \bar{n}_{\text{in}} \quad (2.16)$$

where the last expression holds for $\Delta_c = 0$ and $\bar{n}_{\text{in}} = \langle a_{\text{wg,in}}^\dagger a_{\text{wg,in}} \rangle = P_{\text{in}}/\hbar\omega_L$ is the (mean) incident photons per second. Therefore, Equations 2.14 and 2.15 can be re-cast into the following form:

$$\langle \dot{\sigma}_- \rangle = - \left(\frac{\Gamma_{\text{cav}}}{2} + i\Delta_q \right) \langle \sigma_- \rangle - i \frac{\Omega_R}{2} \langle \sigma_z \rangle \quad (2.17)$$

$$\langle \dot{\sigma}_z \rangle = -\Gamma_{\text{cav}}(\langle \sigma_z \rangle + 1) + i\Omega_R (\langle \sigma_+ \rangle - \langle \sigma_- \rangle) \quad (2.18)$$

where $\Gamma_{\text{cav}} = \Gamma(1 + \frac{4g^2}{\kappa\Gamma})$ is the cavity-enhanced spontaneous emission rate of the atom, and $\Omega_R = 2g\sqrt{\bar{n}}$ is the Rabi frequency with \bar{n} being the mean photon number in the cavity. Equations 2.17 and 2.18 are the familiar optical Bloch equations for a two-level system: these semi-classical equations determine the dynamics of the polarization (coherence) and population inversion of the two-level system. Therefore, the dynamics of a two-level system in the bad-cavity limit can be understood simply as a two-level system driven by a field but with a cavity-enhanced spontaneous emission rate (and therefore, a reduced radiative lifetime of the excited state) and a modified optical Rabi frequency.

2.3.3 Purcell factor

Notably, from the expression of Γ_{cav} , the emission rate enhancement factor (Purcell) is seen to be $P = 4g^2/(\kappa\Gamma)$. Inserting the expressions for g and Γ from Equations 2.5 and 2.2, and $\kappa = \omega/Q$, the expression for Purcell factor evaluates to $P = \frac{3}{4\pi^2} \cdot \frac{Q}{(V_{\text{cav}}/\lambda^3)}$, which is identical to the expression we obtained in Equation 2.4 from the ‘density of states modification’ arguments. Again, we note that for a two-level system, the Purcell factor is independent of the atomic transition parameters and directly proportional to the Q/V of the cavity, indicating that the enhancement is pronounced for low-loss, small mode-volume cavities. It is also evident from Equations 2.12 and 2.13 that when the cavity is *not* resonant with the atom, the cavity-enhanced emission rate is given by:

$$\Gamma'_{\text{cav}} = \Gamma \left(1 + \frac{g^2}{\Gamma} \frac{\kappa}{|\tilde{\kappa}|^2} \right) = \Gamma \left(1 + \frac{P}{1 + (2\Delta_{\text{qc}}/\kappa)^2} \right), \quad (2.19)$$

where $\Delta_{\text{qc}} = \omega_{\text{q}} - \omega_{\text{c}}$ is the cavity detuning from the atomic transition. We experimentally illustrate this relationship for the case of an Er^{3+} ion enclosed in a cavity in Chapter 5.

Before we conclude this section, a couple of noteworthy points are mentioned here. First, as mentioned earlier, integrating atoms within cavities may also lead to improving its directional emission properties. An atom in free space does not have any preference in the direction of emission and is equally likely to emit in any random direction. Instead, for an atom in a cavity, the probability of the excited state to decay by emitting a photon into the waveguide is given by: $\frac{\kappa_{\text{wg}}}{\kappa} \cdot \frac{P}{P+1}$, which approaches unity in the limit of $P \gg 1$ and $\frac{\kappa_{\text{wg}}}{\kappa} \rightarrow 1$. However, if we calculate the rate of photons escaping the cavity through the waveguide after emanating from the atom, \bar{n}_{out} (by combining the input-output relation Equation 2.10 and the bad-cavity field expression Equation 2.11 in the absence of an input photons ($a_{\text{wg,in}} = 0$)):

$$\bar{n}_{\text{out}} = \langle a_{\text{wg,out}}^\dagger a_{\text{wg,out}} \rangle = \kappa_{\text{wg}} \langle a^\dagger a \rangle = \frac{\kappa_{\text{wg}}}{|\tilde{\kappa}|^2} g^2 \langle \sigma_+ \sigma_- \rangle \rightarrow \frac{\kappa_{\text{wg}}}{\kappa^2} 4g^2 \langle \sigma_+ \sigma_- \rangle \quad (2.20)$$

(last expression holds for $\Delta_{\text{c}} = 0$), we can see that the $\bar{n}_{\text{out}} \propto \kappa_{\text{wg}}/\kappa^2$. For a cavity with a given κ_{sc} , the expression for \bar{n}_{out} reaches an optimal value when the condition $\kappa_{\text{wg}} = \kappa_{\text{sc}} = \kappa/2$ is satisfied; this is often referred as a ‘critically-coupled’ cavity. Second, in the standard cavity-QED literature, there exists another figure of merit of atom-cavity coupling called the Cooperativity, defined as $\mathcal{C} = 2g^2/(\kappa\Gamma_t)$. Here, Γ_t is the total dephasing rate, and is determined by $\Gamma_t = \Gamma/2 + \Gamma_d$, where Γ_d is the excess dephasing on top of the lifetime-limit that often contributes to broadening of the homogeneous linewidth of the optical transition. Note that, \mathcal{C} reduces to P in the absence of Γ_d . For atoms in vacuum, Γ_d is often negligible or small, whereas in

solid-state defects, Γ_d could be very large (with respect to Γ). I would like to clarify that for most purposes of discussion in this thesis, we are interested in the Purcell factor P which is an improvement over the radiative emission rate Γ only (and *not* over Γ_d) .

2.4 Cavity-enhanced cyclicity of optical transitions

Along with modifying the local density of states around an atom, a cavity can improve other properties of its optical transitions too. For a multi-level atom, highly cyclic optical transitions are critical for performing single-shot spin measurements. High cyclicity is not a ubiquitous property of optical transitions: for several other solid-state defects (NV [67], SiV⁻ [68] centers), it arises from atomic selection rules, while for emitters situated in a low-symmetry environment, it is often absent. Consequently, for emitters without intrinsic cycling transitions, like erbium and other REIs, single-shot readout was not achieved [69]. In this section, first, we define cyclicity of optical transitions for the case of an Er³⁺ ion, followed by sketching a pathway towards enhancing the cyclicity by enclosing the ion in a cavity.

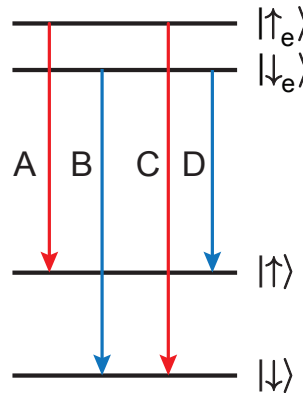


Figure 2.4: Simplified Er³⁺ level structure with optical transitions labeled. Under an external magnetic field, both the spin-1/2 ground and excited doublets split into two levels, giving rise to four optical transitions. Transitions labeled (A,B) are spin-conserving in nature, whereas the remaining two are spin non-conserving.

A simplified level structure of an Er^{3+} ion (doped in YSO) at liquid helium temperature is shown in Figure 2.4. When the Er^{3+} ion is enclosed in a high- Q , small mode-volume photon crystal cavity, the spontaneous emission rate is enhanced and lifetime of the excited states $\{| \downarrow_e \rangle, | \uparrow_e \rangle\}$ are shortened. If an ion initially in the $| \uparrow \rangle$ ground state is excited to the $| \uparrow_e \rangle$ state, it can either decay back down to the $| \uparrow \rangle$ state via optical transition ‘A’ or go to the $| \downarrow \rangle$ state via optical transition ‘C’; these emissions are characterized by Γ_A and Γ_C , respectively (all discussions in this section are applicable for the decay from $| \downarrow_e \rangle$ via transitions ‘B’ and ‘D’ as well). The branching ratio determines the likelihood of the ion decaying back to $| \uparrow \rangle$. The branching ratio for the transition A is given by $R = \Gamma_A / (\Gamma_A + \Gamma_C)$, and therefore, the cyclicity C is defined as: $C = 1/R = 1 + \Gamma_A / \Gamma_C$. In this context, cyclicity is also equivalent to the number of photons emitted while exciting the ion using a single optical transition before the spin state flips.

When the Er^{3+} ion is enclosed in a cavity, the expression for cyclicity is modified to the following: $C = 1 + \Gamma_A^{\text{cav}} / \Gamma_C^{\text{cav}}$. Here, $\Gamma_{A/C}^{\text{cav}} = \Gamma_{A/C}^0 + |g_{||/\perp}|^2 / \kappa$ is the cavity-enhanced spontaneous emission rate, $\Gamma_{A/C}^0$ is the intrinsic spontaneous emission rate such that $\Gamma^0 = \Gamma_A^0 + \Gamma_C^0$ is the total decay rate out of the excited state in the absence of the cavity, and $g_{||/\perp} = \vec{\mu}_{||/\perp} \cdot \vec{E}_{\text{cav}} / \hbar$, where $\vec{\mu}_{||}$ and $\vec{\mu}_{\perp}$ are the dipole moments of optical transitions A and C. We can also define the bare cyclicity of the ion C_0 (in the absence of the cavity) as: $C = 1 + \Gamma_A^0 / \Gamma_C^0$. Therefore, the cavity-modified cyclicity can be expressed as:

$$C = 1 + \frac{\Gamma_A}{\Gamma_C} = 1 + \frac{\Gamma_A^0 + |g_{||}|^2 / \kappa}{\Gamma_C^0 + |g_{\perp}|^2 / \kappa} = 1 + \frac{1 - 1/C_0 + P_{||}}{1/C_0 + P_{\perp}} \quad (2.21)$$

where $P_{||/\perp} = g_{||/\perp}^2 / (\kappa \Gamma^0)$. Note that, as expected, the cyclicity reduces to C_0 in the absence of the cavity. To achieve high cyclicity, we would like $|g_{\perp}| \simeq 0$. This can be realized by choosing the cavity polarization to be orthogonal to $\vec{\mu}_{\perp}$, or (in the case of a fixed cavity polarization) by tuning the magnetic quantization axis. In Chapter 6

of this thesis, we demonstrate that the cyclicity can be controlled by the alignment of the externally applied magnetic field with respect to the local cavity polarization, and in the process, demonstrate greater than two orders of magnitude enhancement of the cyclicity of optical transitions.

Chapter 3

Photonic crystal cavities

In this chapter, I will provide the design principles, finite-difference time-domain (FDTD) simulations of field profiles and Purcell factor estimates, fabrication steps, and characterization of photonic crystal (PC) cavities used in our single erbium ions experiments. All PC design and simulations results in this chapter are discussed from the context of developing silicon-based PC cavities to address single Er^{3+} ions doped in YSO. However, in later work in our group, we have adapted the design to address Er^{3+} ions embedded in other host materials too, viz. MgO , CaWO_4 , TiO_2 , etc. Moreover, the design principles are equally applicable for other physical platforms, as demonstrated in a recent proposal of a heterogeneous assembly of gallium phosphide-based PC cavities-on-diamond to optically address single SiV^0 centers near the surface of diamond [70]. FDTD results presented in Section 3.3.2 are published in Ref. [31].

3.1 A hybrid architecture: PC cavity-on-substrate

In Section 2.3, we noted that enclosing atoms in a cavity can (Purcell) enhance its spontaneous emission rate, and in particular, the Purcell factor is directly proportional to the Q/V ratio of the cavity (Q , Quality factor; V , mode-volume of the cavity mode). Photonic crystals are exceedingly important from this perspective since they

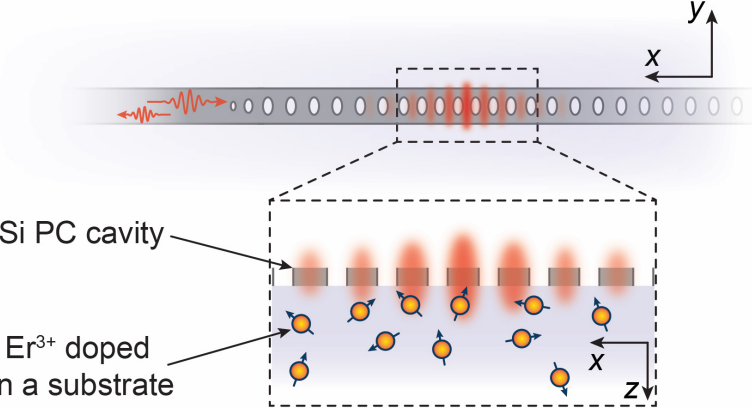


Figure 3.1: **Sketch of the hybrid Si PC cavity-on-YSO architecture.** The Si PC cavity is placed on top of the YSO crystal, which contains Er^{3+} ions as dopants. Electric field guided by the cavity evanescently couples to the erbium ions that are situated near the surface of YSO and underneath the cavity.

can have extremely large Q factors (even as high as 10^7 [71]), while at the same time, providing a wavelength scale confinement of the cavity mode ($V \lesssim \lambda^3$); for certain geometries, even ultra-small mode confinement is also possible ($V \sim 10^{-3}\lambda^3$ [72, 73]).

We would like to leverage the technologically mature silicon nanofabrication capabilities, since PC cavities capable of demonstrating $P > 10^5$ has already been realized [71, 74] (though this P has not been experimentally achieved with emitters). The erbium ions, on the other hand, come as nominally doped in host crystals. One idea would be implant erbium ions in silicon itself. While this is currently being explored [75, 76, 77], getting narrow optical transitions with erbium-implanted silicon turns out to be challenging (due to damage to the crystal from implantation, charge mismatch, mismatch between ionic radii of Si and Er, presence of stray impurities, etc.). An alternate idea is to fabricate devices out of YSO crystal directly but that is very difficult to achieve particularly due to the lack of availability of dry-etching recipes for YSO [78]. To get around these issues, we propose the following: a heterogeneously assembled Si PC cavity-on-substrate architecture, as sketched in Figure 3.1. The main idea is to bring the Si PC cavities as close as possible to erbium ions, which are otherwise trapped in a host crystal underneath the cavity, such that the ions evanes-

cently couple to the cavity mode. This approach has a couple of major advantages: (i) techniques developed for fabricating cavities will be largely unaffected when exploring alternate other host materials for Er^{3+} ions; (ii) we avoid any potential damages that could have arisen from implantation in nanocavities.

3.2 PC cavity design

As previously mentioned, the objective is to construct a PC cavity capable of sustaining a resonant mode that exhibits high Q factor and concentrates the electric field to a small volume while operating at the target frequency, which is the ground-to-excited state optical transition frequency for $\text{Er}^{3+}:\text{YSO}$ (equivalently, target wavelength $\lambda_T = 1.536 \mu\text{m}$; Figure 2.2). Because of its large bandgap with minimal absorption losses at telecom wavelength, silicon has been used to fabricate PC cavities with demonstratively high Q values that are otherwise suspended-in-air [71, 74]. The presence of the YSO substrate underneath introduces design challenges towards achieving high Q because the substrate effectively expands the light cone such that light can couple to the continuum of radiation and leaky modes and leak out of the cavity (Figure 3.2 c). In what follows, we will discuss the design principles to realize quasi-one-dimensional PC cavities capable of supporting resonant modes with quality factors as high as 10^6 . The YSO substrate is included in all simulations, assuming an isotropic refractive index of $n_{\text{YSO}} \sim 1.80$ (its slight birefringence is ignored). All simulations in this section and Section 3.3 are performed using the freely-available software packages MPB [79] and MEEP [80], respectively.

The PC cavity we consider here is formed by a one-dimensional array of elliptical air holes in a silicon waveguide (Figure 3.3a). We start with Si nanobeams with a waveguide thickness $w_z = 250 \text{ nm}$ (silicon-on-insulator wafers with 250 nm thick device layer is an industry standard and easy to procure). The unit cell of the

waveguide is defined by the waveguide width w_y and lattice constant a_{per} with hole diameters in (x, y) -direction denoted by (h_x, h_y) (Figure 3.2a, inset). These unit cell parameters are first optimized to generate a waveguide design where the dielectric-to-air bandgap is maximized, while simultaneously ensuring that the dielectric band-edge is resonant with the target frequency (note that while we have referred it as “bandgap”, the dielectric-to-air gap is not a full bandgap; such a partial bandgap is often denoted by “pseudogap”). Introducing local perturbations in the periodic array of holes creates a defect, thus forming the PC cavity. An adiabatically-introduced defect reduces scattering losses in the cavity. This can be realized by gradually tuning the band-edge frequency such that the target frequency shifts from being resonant with the dielectric band-edge at the center of the defect to being resonant with the mid-gap at the edge of the defect (Figure 3.2d). These can be achieved in several ways, including gradually modifying the hole sizes or lattice constant a_{per} . We choose to implement the latter where a symmetric PC cavity is realized by adiabatically increasing the lattice constant from a_{cav} in the center of the defect to a_{mirr} in the Bragg mirror regions on either sides of the defect (Figure 3.3a) [81, 82].

With the goal of optimizing the bandgap, we set $a_{\text{cav}} = \lambda_T/(2n_{\text{eff}})$, where n_{eff} is the refractive index of the cavity mode, which satisfies $n_{\text{eff}} \in (1.8, 3.5)$ such that it lies between the refractive indices of Si and YSO. Next, we compute the band-structure of the Si nanobeam-on-YSO device for various geometrical parameters; since photons above the light cone are not confined by the cavity, we will only consider modes that are situated below the light cone at $k_x = \pi/a_{\text{cav}}$. To that end, let’s re-define the elliptical holes in terms of two new parameters: $ff = (h_x h_y)/(a_{\text{cav}} w_y)$ and $ar = (h_y/h_x)/(w_y/a_{\text{cav}})$, where ff and ar can be envisioned at the filling-fraction and aspect-ratio of the holes with respect to the unit cell. We will set $ar = 1$ here since it is the size of the hole (ff) that predominantly contributes to the band-structure (additional optimization over ar may also be performed). Figure 3.2a

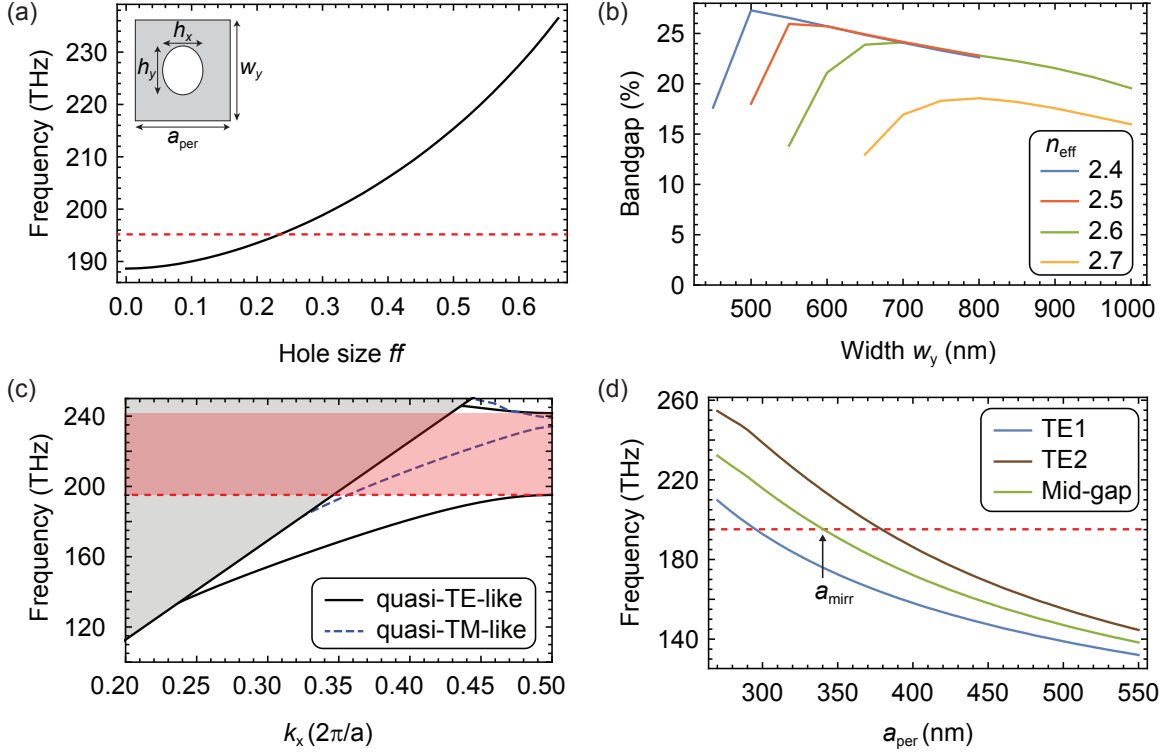


Figure 3.2: Design considerations for a Si nanobeam cavity on YSO substrate **(a)** Band-edge frequency of the fundamental TE band for varying hole sizes [$(w_y, a_{\text{cav}}) = (650, 295)$ nm]. **(b)** Dependence of the fundamental TE bandgap on the waveguide width for varying n_{eff} . All bandgap values are normalized to the target frequency. **(c)** Band-diagram for the Si-on-YSO nanobeam waveguide, defined by the parameters: $(w_z, w_y, h_x, h_y, a_{\text{cav}}) = (250, 650, 143, 315, 295)$ nm, with the lowest two quasi-TE-modes and quasi-TM-like modes given by the solid black lines and dashed blue lines, respectively. The pink-shaded region indicate the quasi-bandgap generated from the symmetry considerations of the quasi-TE modes. Gray region depicts the YSO light cone consisting of continuum of radiation and/or leaky modes. **(d)** Band-edge frequencies of the fundamental TE (dielectric)-band, the next higher-harmonic TE (air)-band, and mid-gap frequency for varying lattice constants while keeping all the other structural parameters unchanged. Red dashed line in all panels correspond to the target frequency, given by c/λ_T .

shows the dependence of the dielectric band-edge frequency with varying ff , where the band-edge gets pushed to higher energies as we insert more of the low-index dielectric (i.e. air) in the waveguide. For a given w_y (with the waveguide a_{per} set to a_{cav}), we extract the ff value that corresponds to the dielectric band-edge being

resonant with the target frequency, and calculate the corresponding dielectric-to-air bandgap. To maximize the bandgap, next, we repeat these steps for a varying number of waveguide widths w_y , and eventually repeating them for different n_{eff} values (Figure 3.2b). With very large n_{eff} values, the modes are pulled down-and-away from the light cone as they move closer to each other thereby reducing the bandgap. For very small n_{eff} , the bandgap will reduce as light gets coupled to leaky modes. We choose to operate with $n_{\text{eff}} = 2.6$, which correspond to a good compromise between near-optimal bandgap and reasonable fabrication parameters (*e.g.* tolerance towards fabrication imperfections, features not too small to possess reproducibility issues, etc.). The optimal design (with $n_{\text{eff}} = 2.6$) has the following structural parameters: $(w_z, w_y, h_x, h_y, a_{\text{cav}}) = (250, 650, 143, 315, 295)$ nm. The band-diagram for the waveguide with these structural parameters is shown in Figure 3.2c, depicting the lowest two quasi-transverse-electric (TE)-like and quasi-transverse-magnetic (TM)-like modes supported by the structure. The quasi-TE band is characterized by the mode for which the electric field has an *odd* symmetry with respect to the $y = 0$ mirror-symmetry plane, whereas the quasi-TM band is characterized by an *even* symmetry for the same. As expected, the target frequency is resonant with the fundamental quasi-TE band-edge frequency, and it exhibits a fundamental TE bandgap of 24% (normalized by the target frequency).

It should be noted that in the absence of the substrate (*i.e.* when the z -axis symmetry is not broken), the electric fields confined in the TE modes exhibited even symmetry around the z -axis and odd symmetry around the y -axis, and vice-versa for the TM modes. In the presence of the substrate where the z -axis symmetry is broken, the y -axis symmetry still persists; therefore, the quasi-TE and quasi-TM modes of our optimal waveguide possess y -odd and y -even symmetry, respectively. However, we can still compute the z -parity (expectation of the z -parity operator, $\langle \hat{z} \rangle$) of these TE/TM modes, and we see that the quasi-TE modes have a $\langle \hat{z} \rangle > 0$, while for the quasi-TM

modes are $\langle \hat{z} \rangle < 0$, indicating that these modes retain many of their features from the suspended-waveguide configuration.

Finally, while attempting to compute the a_{mirr} , we would like to ensure the target frequency is at the middle of the fundamental TE bandgap at the Bragg mirror region. As previously mentioned, in our PC cavity design, we would keep the parameters (w_y, w_y, h_x, h_y) fixed. Thus, we sweep the a_{per} value: increasing a_{per} inserts the higher dielectric medium in the unit cell, thereby dragging the band-edge frequencies down for both the quasi-TE bands to the point that the fundamental band's mid-gap frequency is resonant with the target-frequency (Figure 3.2d). We extract $a_{\text{mirr}} = 340$ nm. Thus, we have all the required structural parameters to generate the cavity, and perform time-domain simulations (or to fabricate it!).

3.3 FDTD simulations

To evaluate the performance of the optimal PC design obtained in Section 3.2, we employ three-dimensional finite-difference time-domain (FDTD) simulations. First, we construct the PC cavity as shown in Figure 3.3a, where we divided the waveguide into two regions: the center of the waveguide is labeled as the ‘cavity’ region while the two Bragg mirror regions located symmetrically around the cavity is labeled as the ‘mirror’ regions. In the cavity region, the lattice constant a_{per} adiabatically increases from a_{cav} at the center of the cavity to a_{mirr} to both ends of the cavity. In the mirror regions, the lattice constant is kept constant at a_{mirr} . Additional holes in the mirror regions are introduced to increase the Bragg mirror reflectivity. The cavity and the mirror regions are characterized by the number of holes: number of ‘cavity holes’ determine the adiabaticity of the defect in the cavity region, while number of ‘mirror pairs’ determine the strength of the Bragg mirror (inserting a mirror pair is equivalent to adding an extra hole on both the mirror regions symmetrically).

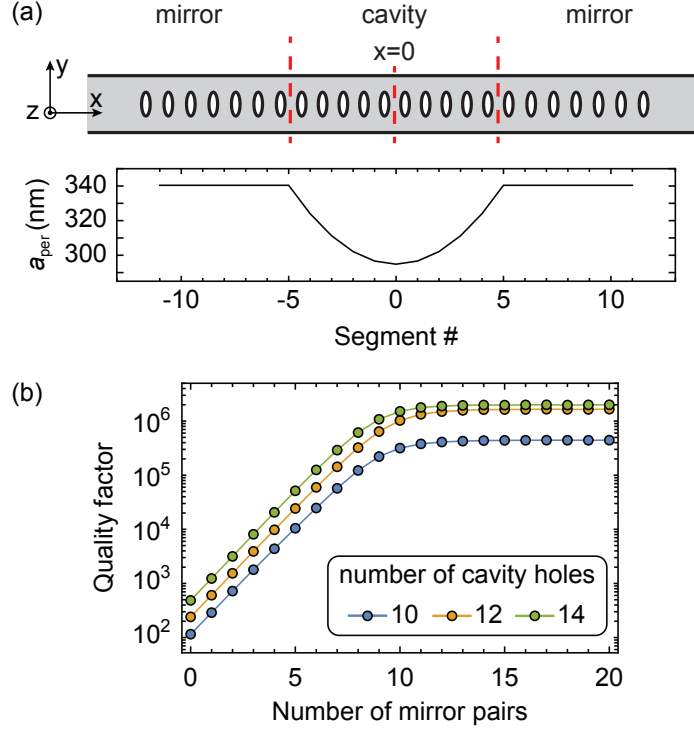


Figure 3.3: **PC cavity performance for various structural configurations.** (a) Schematic of a representative Si-on-YSO nanobeam cavity that is comprised of 24 elliptical-shaped air-holes (10 cavity holes and 7 symmetrically-placed mirror pairs). The nanobeam is symmetric around $x = 0$. The lattice constant in the cavity region follows a parabolic profile, with a lattice constant of a_{cav} at the center and a_{mirr} at either ends of the cavity region. (b) Dependence of the PC cavity Quality factor on the number of mirror pairs for varying number of cavity holes.

3.3.1 Quality factor analysis of the nanobeam cavity

We perform 3D FDTD simulations and evaluate the Q factor of the PC cavity for different cavity configurations (Figure 3.3b). For smaller number of mirror pairs, the Q factor is limited by light escaping the cavity through the Bragg mirror region (this is equivalent to the κ_{wg} loss mechanism discussed in Section 2.3); in this domain, the Q factor increases exponentially for inserting of additional mirror pairs. On the other hand, at a large number of mirror pairs configuration, the Q factor saturates and limited by the radiation loss in the defect/cavity region. One way to increase the Q factor further is tune the adiabaticity of the defect region by increasing the number

of cavity holes. Figure 3.3b shows that with 12 or 14 cavity holes, our Si-on-YSO PC nanobeam cavities can achieve $Q \sim 2 \times 10^6$, which is only a factor of 5 away from the highest demonstrated Q factor of 10^7 in suspended Si PC cavities [71].

3.3.2 Field profile and Purcell factor estimation

Next, we turn towards investigating the field profile of the guided cavity mode, and thereby, estimate the Purcell factor variation across various planes.

The key figure of merit is the electric field amplitude $|\vec{E}|$ in the YSO substrate, where the Er^{3+} ions reside. Figure 3.4c shows the variation of $|\vec{E}|^2$ across a cross-section of the device. The value of $|\vec{E}|^2$ at the Si-YSO interface is roughly 36% of its maximum value in the center of the Si waveguide, indicating that ions at the surface can still be well-coupled to the cavity even though they reside outside of the PC itself. $|\vec{E}|^2$ decreases exponentially into the YSO substrate, falling by half every 45 nm (this depth, in general, depends on the n_{eff} ; the current value is calculated for the optimal cavity design with $n_{\text{eff}} = 2.6$).

The theoretical Purcell factor $P = \Gamma_{\text{cav}}/\Gamma_0 - 1 = 4g(\vec{r})^2/\kappa\Gamma_0$ varies with the position of the ion, depending on the local single-photon Rabi frequency $2g$, given by: $g(\vec{r}) = \frac{\mu_{\text{ge}}}{\hbar} |\vec{E}_{\text{cav}}(\vec{r})|$ (Equation 2.5), where μ_{ge} is the electric dipole moment for the ground-to-excited optical transition in $\text{Er}^{3+}:\text{YSO}$, and $\vec{E}_{\text{cav}}(\vec{r})$ is the electric field of a single photon in the cavity, at position \vec{r} . We determine the electric dipole moment μ_{ge} from the excited state lifetime and previously measured branching ratio ($\beta = 0.21$) of the $\text{Y}_1 \rightarrow \text{Z}_1$ decay [83] using the following expression, including a local field correction [84]:

$$\Gamma_0 = \frac{1}{\beta} \cdot \left(\frac{3n_{\text{YSO}}^2}{2n_{\text{YSO}}^2 + 1} \right)^2 n_{\text{YSO}} \cdot \frac{\mu_{\text{ge}}^2 \omega^3}{3\pi\epsilon_0\hbar c^3} \quad (3.1)$$

where the bare spontaneous emission rate is $\Gamma_0 = 2\pi \times 14$ Hz, and the frequency is $\omega = 2\pi c/\lambda_T = 2\pi \times 195$ THz. This gives $\mu_{\text{ge}} = 2.8 \times 10^{-32}$ C-m, in general

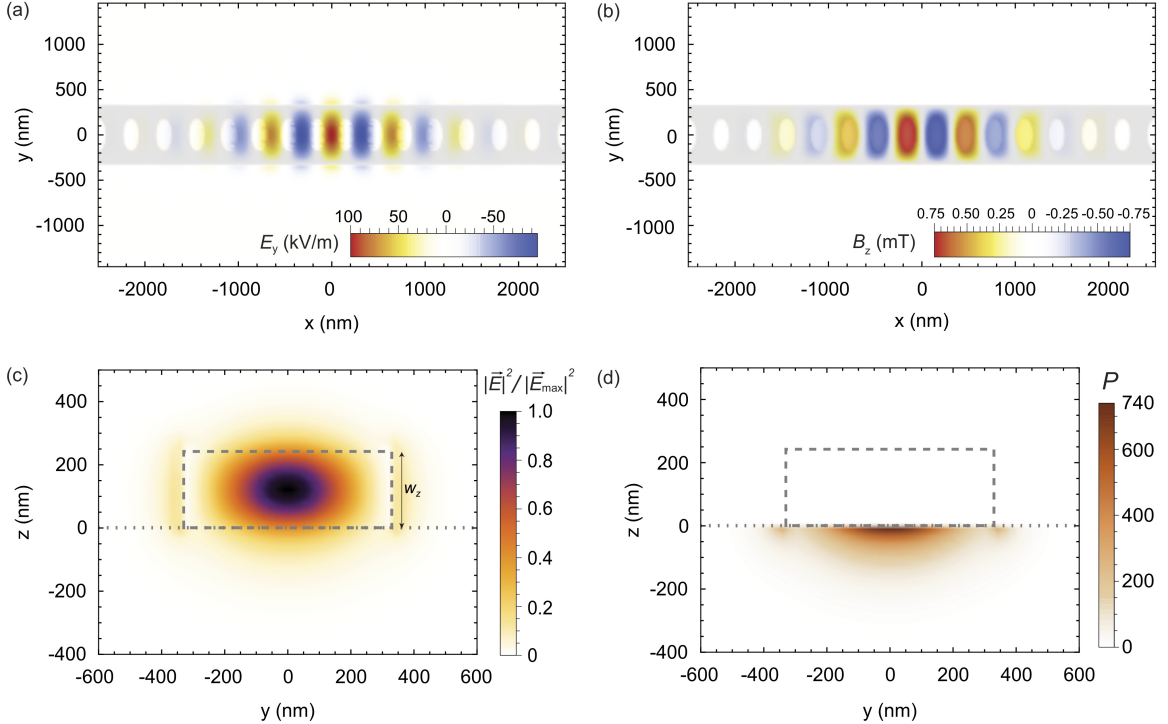


Figure 3.4: FDTD mode profiles and theoretical Purcell factors. (a)-(b) Top-view of the E_y (B_z) component of the electric (magnetic) field in the photonic crystal cavity, in a cut through the middle of the Si layer (at $z = 125$ nm). (c) Electric field $|E|^2$ in the yz -plane (at $x = 0$). The dashed rectangle indicates the Si waveguide; the region below the dashed line is the YSO substrate. $|E|^2$ is scaled with respect to its maximum value at the center of the waveguide, $|E_{\max}|^2$. (d) Variation of Purcell factor as a function of position in the YSO substrate (yz -plane at $x = 0$), assuming purely electric dipole coupling to the cavity.

agreement with the value of 2.07×10^{-32} C-m reported in Ref. [83]. The Purcell factor for different ion locations in the YSO is shown in Figure 3.4d. For a cavity with a Quality factor $Q = 7.3 \times 10^4$ (i.e. a decay rate of $\kappa = 2\pi \times 2.66$ GHz; such a device is used for experiments discussed in Chapter 5), the maximum Purcell value at the Si-YSO interface is 740, corresponding to $g = 2\pi \times 2.62$ MHz. The experimental value of g for any particular ion will likely be lower than this because of sub-optimal positioning and imperfect alignment of the local cavity polarization with the (unknown) dipole moment orientation. The simulated mode-volume for the fundamental mode of the cavity is $0.051 \mu\text{m}^3$, and it is calculated using:

$$V = \frac{\int dV \epsilon(\vec{r}) |E(\vec{r})|^2}{\max(\epsilon(\vec{r}) |E(\vec{r})|^2)}. \quad (3.2)$$

However, we want to emphasize that we do not rely on this estimated mode-volume to compute a Purcell factor and instead use the single-photon electric field directly to compute the Purcell factor, as explained above.

As discussed in the Section 2.1, intra-4*f* electronic transitions are not electric dipole-allowed, as the various 4*f* states all have the same parity. In a host crystal, on a site without inversion symmetry (such as the Y site in YSO), the ligand field may mix 4*f* and 5*d* orbitals to introduce a weak “forced” electric dipole [43]. However, in the particular case of the Er³⁺ $^4I_{15/2} \leftrightarrow ^4I_{13/2}$ transition, the strength of the allowed magnetic dipole transition is comparable to that of the forced electric dipole [45, 56]. While the above calculation of the Purcell factor assumed that the transition is purely electric, we note that the magnetic mode volume of the cavity is also small (Figure 3.4b). Repeating the Purcell factor calculation while assuming a purely magnetic transition results in similar predicted enhancement ($g_{\text{mag}} = 2\pi \times 4.39$ MHz and $P_{\text{mag}} = 2.0 \times 10^3$). Designing structures to selectively enhance the electric or magnetic fields may allow the role of these transitions to be disentangled. Furthermore, interference between electric and magnetic dipole coupling to the cavity may be used to tailor the spin selection rules.

3.4 Fabrication process

Steps outlining the fabrication process for the Si-based PC cavities is mentioned here; discussions in this section are also published in Ref. [31]. The device fabrication consists of three distinct steps: (1) fabrication of Si PCs, (2) preparation of the YSO substrate, and (3) transfer of the PCs to the YSO.

We fabricate suspended Si PCs from silicon-on-insulator (SOI) wafers using electron-beam lithography and plasma etching with SF₆/C₄F₈/O₂ gases in an inductively-coupled reactive ion etcher (SAMCO 800), followed by a hydrofluoric acid undercut (Figure 3.5a). The SOI device layer is 250 nm thick, with a 2 μ m buried oxide.

In one method of sending light into Si waveguides, we use a lensed fiber couple to couple light into the cavity. In order to do so, the waveguides must protrude off the edge of the YSO substrate. The edges of the polished substrate are rounded and poorly defined. Therefore, we cut a sharp edge using a dicing saw, along with a progressively deeper series of relief cuts to give enough clearance for the lensed fiber. In an alternate method of sending light into the cavity, we employ a combination of an angle-polished fiber and a grating coupler to guide and couple light into the PC cavity; details of this coupling mechanism is discussed in Ref. [85].

After the undercut, we transfer the suspended Si devices onto the YSO substrate using a stamping procedure adapted from the stacking of 2D van der Waals materials [86], as shown in Figure 3.5b. The process is carried out in a wafer bonder (Tresky T-3000-FC3), which controls the pressure, heating and alignment. In the waveguide design, we engineer pinch points which allow the suspended waveguides to be deterministically broken free from the SOI with the application of pressure using a PDMS stamp. The PCs can then be pulled off the SOI wafer using a polypropylene carbonate (PPC) film on the stamp that is heated to 60°C to promote adhesion. Then, the stamp is positioned so a column of PCs is aligned with the YSO edge, and pressed down onto the YSO. The stamp and YSO are heated to 130°C, which melts the PPC layer to release the PCs and PPC from the PDMS stamp. Finally, we dissolve the PPC in chloroform, which leaves the PCs in place on the YSO substrate (Figure 3.5c). We align the PCs on the substrate such that the principal electric field polarization (E_y in Figure 3.4a) is parallel to one of the optical axes of YSO crystal

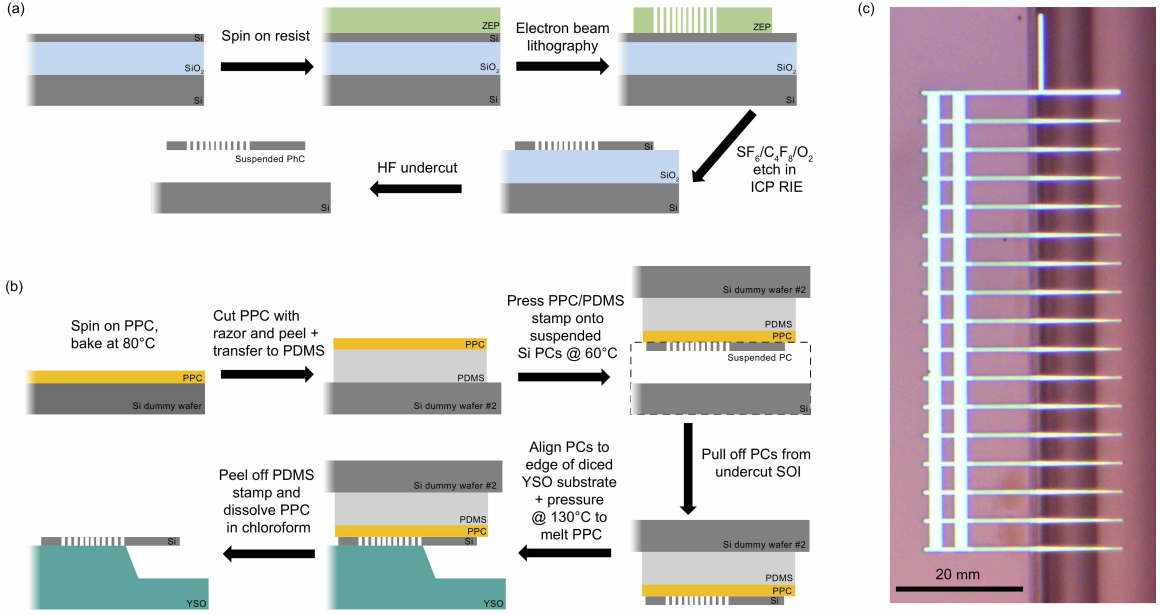


Figure 3.5: Fabrication processes for making Si-on-YSO PC cavities. (a) Side view diagram of the process flow for fabricating suspended Si photonic crystal cavities from an SOI wafer. (b) The process flow for transfer of these Si photonic crystal cavities onto the diced edge of an erbium-doped YSO crystal. (c) Top-down optical image of an array of PCs stamped along the edge of the YSO substrate. The orientation of the photonic crystal cavities is the same as in panel (b). The vertical beam at the top of the image is used for alignment.

(the D_2 axis); previous spectroscopy has shown that site 1 Er³⁺:YSO ions have a larger absorption cross section for light with this polarization [50].

3.5 Characterization of PC cavities

A brief characterization of typical PC cavities fabricated for our experiments is discussed in this section. In Figure 3.6a, we include the scanning electron micrograph of a representative PC cavity (before it was transferred onto YSO). The device consists of 10 cavity holes and 6 mirror pairs symmetrically placed around the cavity. Notice that there are a few extra holes included in the device for the following reason: since we work with single-sided PC cavities, we insert 10 additional mirror holes on

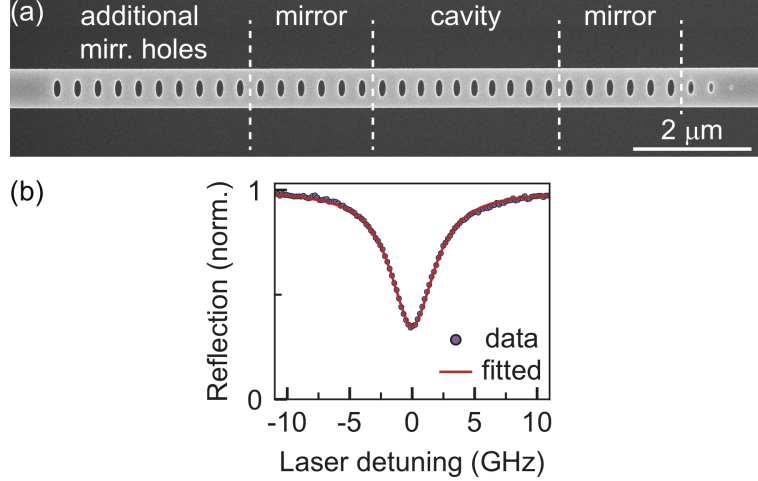


Figure 3.6: PC cavity characterization: SEM image and reflection spectrum.
(a) Scanning electron microscope (SEM) image of a representative silicon PC cavity.
(b) Reflection spectrum of a cavity used in some of our experiments, with a measured quality factor $Q = 4.6 \times 10^4$.

one side of the device such that the corresponding Bragg mirror is almost perfectly reflective (i.e. $\kappa_{wg,L} \sim 0$). On the other (insertion) side of the device, we insert 3 extra holes whose sizes are adiabatically reduced to enable efficient adiabatic mode-transfer from the Si waveguide to the device.

The reflection spectrum of a single-sided PC cavity is shown in Figure 3.6b. Fitting a Lorentzian function to the spectrum extracts a cavity (full width at half maximum) linewidth of $\kappa = 2\pi \times 4.24$ GHz, and therefore, $Q = \omega/\kappa = 4.6 \times 10^4$. The cavity losses are determined from the ratio of the on- and off-resonance reflection level R_0 , which depends on the ratio of the internal (κ_{sc}) and waveguide (κ_{wg}) loss channels from the cavity as $R_0 = (1 - 2\eta_{cav})^2$, where $\eta_{cav} = \kappa_{wg}/(\kappa_{wg} + \kappa_{sc})$. While this measurement cannot distinguish which of the two κ terms is greater, a separate phase-sensitive measurement of the cavity reflection [87] using a fast modulator and photodiode together with a vector network analyzer determined that $\kappa_{wg} < \kappa_{sc}$. For the device in Figure 3.6b, we compute $\eta_{cav} = 20.4\%$, and hence, $(\kappa_{wg}, \kappa_{sc}) = (0.86, 3.38)$ GHz, indicating that the cavity quality factor is primarily limited by internal losses.

Chapter 4

Experimental setup

In this chapter, I will provide an overview of the experimental setup used in our single Er^{3+} ion experiments. In the previous chapter, we already discussed the design and fabrication techniques of our heterogeneously-assembled devices consisting of photonic crystal (PC) cavities transferred onto a solid-state crystal (YSO), where the latter contains Er^{3+} ions embedded as defects. Here, I will lay down the steps toward integrating these devices in our experimental setup, focusing primarily on the measurement configuration and details of key components required for detection and control of individual ions. Since mid-2016 when we started building our setup, it went through several major and minor upgrades; I will primarily restrict my discussion to the most up-to-date configuration of the setup. All results presented in this thesis are realized using the exact or some variation/subset of the current setup configuration.

4.1 Measurement configuration

The experimental and measurement configuration for addressing single ions can be boiled down to a few key elements, as sketched in Figure 4.1. An externally-stabilized tunable laser generates the light, which is sent through an EOM and a couple of AOMs to generate the optical pulses; further description on laser-linewidth and optical pulse

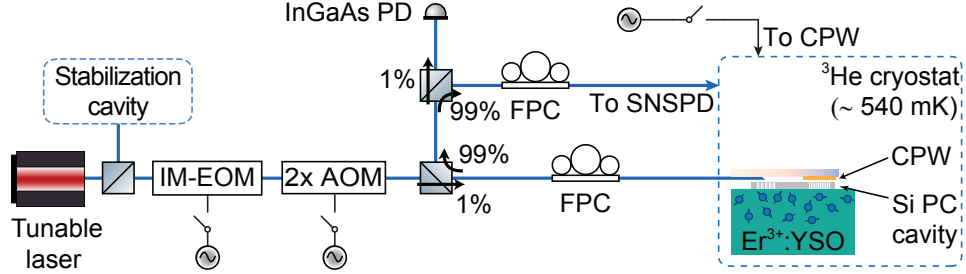


Figure 4.1: **Measurement configuration.** Schematic diagram of the experimental setup. See Section 4.1 for explanations of abbreviations.

generation follows in Section 4.2. A fiber polarization controller (FPC) matches the laser polarization to the PC cavity. Light enters into the ^3He cryostat via optical fibers and couples to PC cavities; Section 4.3 details the device assembly and layout of the key components inside the cryostat.

Light returning from the single-sided PC cavity is redirected to a fiber-coupled superconducting nanowire single-photon detector (SNSPD). For most experiments reported in this thesis (Chapters 5, 6, 7), the SNSPD (Quantum Opus) used is lodged inside a separate cryostat (at ~ 2.3 K) and nominally operated at a detection efficiency $\eta_{\text{det}} \sim 65\% - 70\%$ with ~ 10 Hz dark-count rate. In the most updated version of the setup as well as for results in Chapter 8, the SNSPD (PhotonSpot) used is lodged inside the same cryostat as the PC cavity/YSO device; although the latter detector was expected to operate at $\eta_{\text{det}} \sim 90\%$ with equivalent dark-count rate, due to technical reasons we could only operate at $\eta_{\text{det}} \sim 50\%$ with < 1 Hz dark-count rate. The current bias of the SNSPDs are supplied by an SRS SG345 function generator through a $100 \text{ k}\Omega$ resistor, which allows the bias to be switched off during an excitation pulse, preventing the detector from latching; the function generator let us turn the bias on/off quickly on a timescale of $\sim 1 - 2 \mu\text{s}$. An additional polarization controller adjusts the polarization incident on the SNSPD to maximize the detection efficiency. The total photon collection efficiency, which is the probability for a photon in the

cavity to result in a click on the detector, is extracted to be $\sim 25\%$ (see Appendix A.1.3 for a discussion on how this is estimated).

Photons arrival times at the detector are “tagged” using a single-photon counter (Swabian TimeTagger 20). A tiny fraction of the reflected light is sent to an InGaAs photodiode (New Focus 2011) for monitoring the PC cavity reflection while tuning the cavity resonance. Microwave pulses are generated using a signal generator modulated by an IQ mixer driven by an arbitrary waveform generator and amplified to 21 W before entering the cryostat. The circuit for generating microwave pulses is sketched in Figure C.1c. A low duty cycle is used to avoid heating the sample. The microwave pulses are eventually delivered to the ions via a coplanar waveguide (CPW). This is fabricated by patterning a thin gold film (thickness $1 \mu\text{m}$) onto the top surface of a quartz carrier, situating it about $125 \mu\text{m}$ away from the PC cavity [85]. All digital waveforms (TTL pulses) controlling the experiments are generated from a NI PXI-6542 digital waveform generator.

4.2 Optical pulse generation setup

In this section, we will discuss the optical pulse generation setup with the goal of achieving frequency-stabilized light combined with fast-switching of the laser frequency (Figure 4.2). This would enable us to perform the experiments in Chapter 7, where we achieved high-fidelity optical control and detection of multiple ions coupled to the same cavity (other experiments reported in this thesis either used the identical optical setup or some reduced version of the same).

We start with a reference laser (NKT Koheras BASIK E15), which has a center wavelength of 1536.48 nm and can be thermally tuned by ± 0.5 nm around the center; this center wavelength corresponds to optical transition of Site 1 Er^{3+} ions in bulk $\text{Er}^{3+}:\text{YSO}$ [51]. Fine stabilization and linewidth narrowing of the reference laser

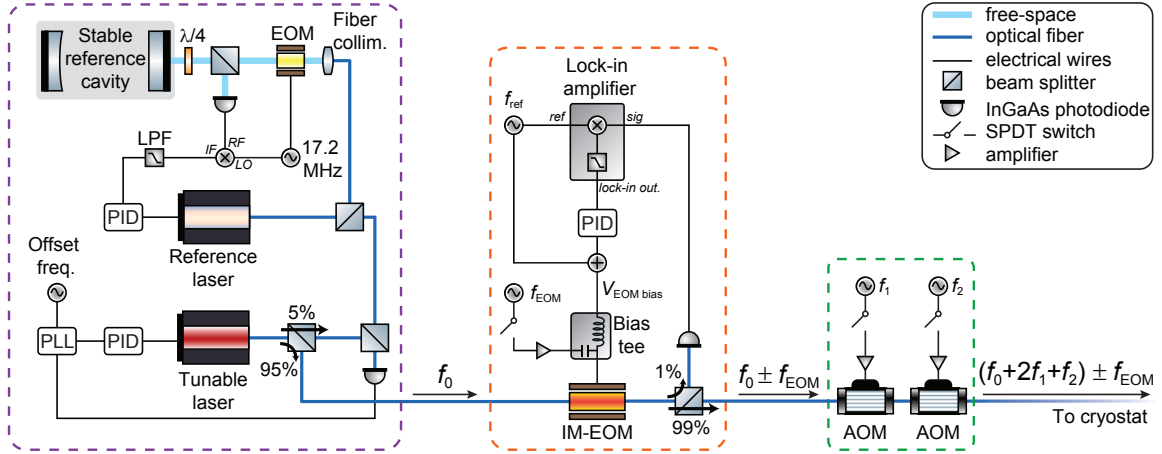


Figure 4.2: **Optical pulse generation setup.** Schematic diagram of the setup for generating optical pulses. The purple-dashed box sketches the setup for frequency-stabilization of the tunable CW laser. The orange-dashed box includes the setup for the DC-bias stabilization of the IM-EOM. See Section 4.2 for further discussion.

are achieved using a stable reference cavity (Stable Laser Systems) housed in an ultrahigh vacuum chamber via the Pound-Drever-Hall technique [88]. The stabilized reference laser linewidth is considerably less than 30 kHz. The laser frequency is often monitored using a wavemeter.

Optical excitation pulses for the experiments are generated using a tunable laser (Toptica CTL1500). The Toptica laser is offset-frequency locked to the reference laser. A small-fraction of light originating from the Toptica laser is interfered with light from the frequency-stabilized reference laser, and measured on a photodiode (Ortel 2860F-C16). The beat-note frequency is stabilized to a known offset frequency via a Phase-Locked-Loop (PLL, Analog Devices ADF4159). The offset frequency is generated from a Novatech 409B DDS signal generator. The beat-note signal is measured to have a FWHM linewidth of 24 kHz. This indicates that the stabilized Toptica laser output has a linewidth that is considerably less than 100 kHz (estimated from the convolution of the stabilized reference laser signal and beat-note signal). The entire laser linewidth stabilization setup is housed inside a homemade vibration-isolation box whose walls are made of layered stacks of plywood, corrugated cardboard filled

with sand, and foam. The stabilized laser light, which exits the vibration-isolation box and gets directed to the IM-EOM and AOMs, is a pure tone (frequency f_0) without any locking sidebands. Tuning the offset frequency changes f_0 .

To enable fast switching of the laser frequency, we address the ions using RF sidebands (at frequencies $f_0 \pm f_{\text{EOM}}$) generated by a intensity modulating electro-optic modulator (IM-EOM, Lucent X-2623Y). f_{EOM} is generated using a fast-switching RF generator (Holzworth HSM6001B), which is capable of switching the sideband frequency on the $\sim 100 \mu\text{s}$ timescale over a $\sim 6 \text{ GHz}$ bandwidth. The RF signal at frequency f_{EOM} is modulated by a SPDT switch (Mini-Circuits ZASWA-2-50DR+) driven by a arbitrary waveform generator (Rigol DG4162) and amplified (Mini-circuits ZHL-4240W+) before being delivered to the EOM. Low RF power at f_{EOM} will ensure higher-order sidebands ($\pm 2f_{\text{EOM}}, \pm 3f_{\text{EOM}}$, etc.) generated from the IM-EOM are suppressed.

The DC bias voltage for the IM-EOM is chosen to suppress the carrier transmission (at f_0). We attain a 20 dB extinction ratio for the IM-EOM pulse On vs. Off cases. However, the DC bias point often drifts slowly over time. This reduces the extinction ratio of the IM-EOM pulses as well as increases the inadvertent risk of exciting other ions using the carrier frequency light. To counteract this, we stabilize the DC bias via active feedback control. We dither the DC bias using a small reference signal $V_{\text{ref}} = (0.1 \text{ V}) \sin(2\pi f_{\text{ref}} t + \phi_{\text{ref}})$, where $f_{\text{ref}} = 10 \text{ kHz}$ (the IM-EOM DC switching voltage $V_\pi = 3.1 \text{ V}$). The transmission response of the IM-EOM is measured in a InGaAs photodiode (Thorlabs PDA10CS2). The derivative of the IM-EOM transmission signal has a zero-crossing at the optimal DC bias voltage; therefore, we can perform active feedback upon it. The signal derivative is extracted by mixing the transmission signal with the reference signal in a lock-in amplifier. The lock-in output, which now is the error signal, is fed into a PID controller to extract the desired DC bias voltage $V_{\text{EOM bias}}$. The $V_{\text{EOM bias}}$ signal and RF pulses (originating

from the Holzworth RF synthesizer) are combined using a Bias-Tee (Mini-circuits ZFBT-6GW+) before being delivered to the IM-EOM. Thus, light exiting the IM-EOM are optical pulses at frequencies $f_0 \pm f_{\text{EOM}}$, with the DC bias stabilized such that the carrier frequency at f_0 is suppressed by 20 dB.

Light out of the IM-EOM is additionally modulated using two acousto-optic modulators (AOMs, Isomet 1205C-1 and 1250C-868) in series. The two AOMs cumulatively provide a 142 dB optical power extinction ratio (one double-pass, one single-pass). The AOMs are driven by a Novatech 409B DDS signal generator (at fixed frequencies f_1 and f_2), with the RF pulses generated using SPDT switches modulated by digital (TTL) pulses and amplified to the optimal power by Mini-circuits ZHL-1-2W-S+ amplifiers. Finally, light exiting the AOM setup has the frequency components $f' \pm f_{\text{EOM}}$ (with $f' = f_0 + 2f_1 + f_2$); this enters into the cryostat. For usual operations involving addressing single Er^{3+} ions, we choose f' and f_{EOM} such that $f' - f_{\text{EOM}}$ is far-detuned from any other ions while $f' + f_{\text{EOM}}$ is resonant with the ion(s) of interest or vice-versa, where fast switching of the optical frequency is attained by tuning the f_{EOM} .

4.3 Assembly inside Bluefors refrigerator

In this section, I will discuss about the experimental setup inside the cryostat (Bluefors LD250HE). Figure 4.3 includes a detailed sketch of the key components relevant for single ion experiments.

Light originating from the optical pulse generation setup (Figure 4.2) enters into the cryostat via optical fibers. The fiber is introduced from ambient to high-vacuum configurations by feeding it through a custom-made Teflon ferrule (with a drilled-in center hole of diameter slightly larger than the fiber diameter) that replaces a

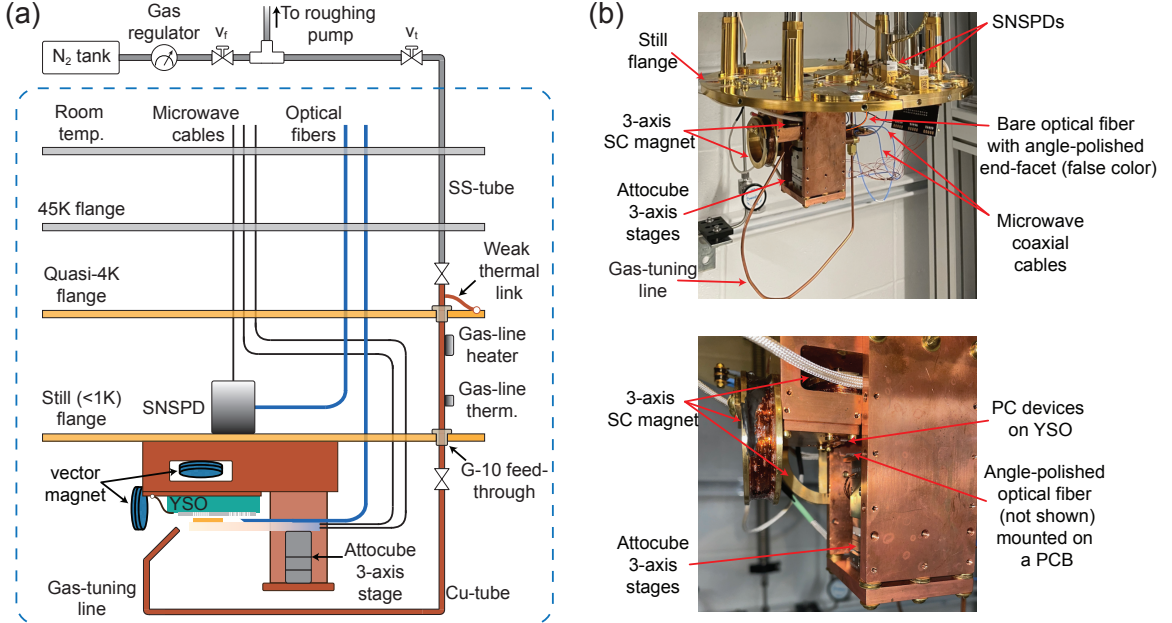


Figure 4.3: **Layout of components inside Bluefors refrigerator.** See Section 4.3 for detailed discussion on the components.

standard Swagelok® connector [89]. A small amount of fiber is spooled and clamped on the still flange before being redirected to deliver light to the PC cavity.

There is a large size mismatch between the fundamental mode confined in a PC cavity and that guided by an optical fiber, which leads to an inefficient coupling of light between them. Broadly, three different approaches have been undertaken in our lab in the past few years to couple light from the optical fiber to the PC cavity. In the first approach, we utilized conical-shaped tapered optical fiber to adiabatically transfer light from the fiber to the PC cavity, adapting a technique developed in Ref. [90], where the tapered fibers were fabricated using a homebuilt fully-automated fiber-pulling rig that utilizes a heat-and-pull process to fabricate conical-shaped tapered fiber tips from commercially available SM fiber (Figure 4.4). Average one-way fiber-cavity coupling efficiencies of $\sim 75\%$ were achieved in ambient conditions. However, when installed in a cryostat, the fiber-cavity coupling suffered from the mechanical vibrations of the cryostat: the tapered fiber would frequently detach itself from the PC

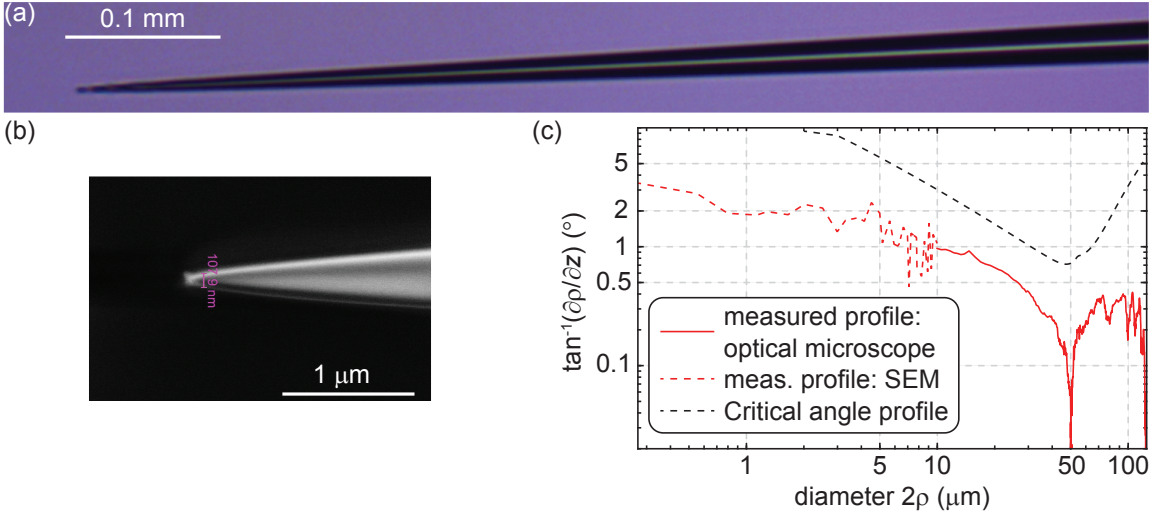


Figure 4.4: Tapered fiber for fiber-cavity coupling. (a) Optical and (b) SEM images of a typical conical tapered optical fiber. (c) Extracted local fiber angle profile as a function of the local fiber diameter. Adiabatic mode-transfer requires the fiber angle profile lies to be below the critical angle profile. See Ref. [90] for a detailed discussion on the technique.

waveguide (satisfying the adiabaticity criterion led to the total tapered fiber length being 16–18 mm long). Eventually, this approach was relinquished.

In the next approach to coupling light from fiber to PC cavity, we used an AR-coated lensed optical fiber (OZ Optics, TSMJ-X-1550-9/125-0.25-7-2-12-2-AR) with 2 μm focal spot size to send light into/out of the PC cavity [91]. This approach requires that the PC cavity is stamped on the edge of the host substrate, with the end-facet suspended in the air. The end-facet of the PC cavity has a width and height of 220 nm and 250 nm, respectively, where the width of the waveguide is adiabatically tapered from the PC cavity width of 650 nm over a length of 14 μm . This approach of fiber-cavity coupling yielded 40 – 60% fiber-waveguide coupling efficiency and has been utilized for all results in Chapters 5 and 6 (except Figure 6.6c,d). In the latest (current) approach based on Ref. [85], an angle-polished fiber is used to deliver the light into a grating coupler, which eventually directs the light into the PC cavity. This approach also allows an ease of integration of a coplanar waveguide (CPW) along the

polished fiber: the CPW, which is made of gold films and situated about $125\ \mu\text{m}$ away from the PC cavity, is useful for delivering microwave to the Er^{3+} spins. The hybrid optical-microwave probe has been utilized for all results in Chapter 7 and 8 (as well as Figure 6.6c,d) and generally yields $35 - 40\%$ fiber-waveguide coupling efficiency.

The YSO crystal (on which the PC cavities were transferred) is installed on a custom-made OFHC copper sample-mount in an inverted-geometry fashion as sketched in Figure 4.3a. A clamp constructed out of thin phosphor-bronze sheet presses on the crystal thereby preventing it from falling down and ensuring good thermal contact between the crystal and the sample-mount, which in turn is firmly attached to the Still flange that reaches a base temperature of $\sim 540\ \text{mK}$. Additionally, a thin layer of Apiezon N grease is applied between the YSO crystal and the sample mount for improved thermal contact. The hybrid optical-microwave probe is mounted on top of a 3-axis translation stage (Attocube ANPx312 for x, y -axes with 6 mm translation range and ANPz102 for z -axis with 5 mm translation range). These stages allow fine movement of the optical probe thereby letting us attain the optimal fiber-waveguide coupling. Notably, the cryostat does not have any visible/free-space optical access; see Section 4.4 for details on achieving fiber-cavity coupling at low temperatures.

Light returning from the cavity is redirected to a SNSPD (PhotonSpot) that is also installed in the refrigerator on the Still flange. Electronic signals to/from the SNSPD as well as CPW are carried through microwave coaxial cables. Total (one-way) loss of microwave power between the SMA connector at the top of the refrigerator to input-port of the CPW is 2.3 dB (and similar loss along the return line). The output/return line of the CPW is eventually terminated with a 30 dB attenuator and a $50\ \Omega$ terminator (outside the fridge).

The PC cavity resonance is tuned by depositing N_2 gas on the cavity; see Section 4.5 for detailed discussion on gas tuning. Additionally, a home-built 3-axis

vector superconducting (SC) magnet is also integrated with the sample-mount assembly for manipulating the highly anisotropic ground and excited state Zeeman splittings of Er^{3+} spin; see Section 4.6 for additional details on these SC magnets.

4.4 Achieving fiber-cavity coupling at low temperatures

For coupling light from the optical fiber to the PC cavity, the fiber (which is mounted on top of the Attocube stack) needs to be physically maneuvered to a location in the physical proximity of the PC cavity. The exact position of the fiber that yields optimal coupling depends on the approach (lensed fiber or angle-polished fiber) that is used to couple light into the cavity. At room temperature while the vacuum cans of the cryostat are taken down, an optical microscope is temporarily installed in setup to perform coarse alignment of the lensed/angle-polished fiber with the cavity. Fine alignment is performed by measuring the cavity reflection signal on an InGaAs photodiode (Thorlabs PDA10CS2) and maximizing the signal; it is beneficial to detune the laser a bit from the cavity resonance center in order to measure the reflected power. Note that at this stage one needs to adjust the polarization of the input light to match it up with the cavity polarization. Since the cryostat does not have a visible/optical port access, once we initiate cool-down we cannot perform the coarse alignment any more and we have to rely on the fine alignment capabilities only.

If we do not correct the Attocube positions during the cool-down of the cryostat, due to differential contraction of various metals and alloys involved in the setup and arranged in a particular geometry, the fiber-cavity coupling would slowly drift away from the optimal coupling configuration to the point that no cavity reflection signal would be visible. To counteract this, while cooling down the cryostat, we repeatedly perform fine alignment at regular intervals to optimize the fiber-cavity coupling: this

lets us update the Attocube positions while maintaining optimal coupling all the way from room-to-base temperature. It is critical that the Attocube capacitances are updated during every attempt of fine alignment because the capacitances also decrease as the Attocube cools. The input light polarization also needs to be adjusted roughly once every 3 hours.

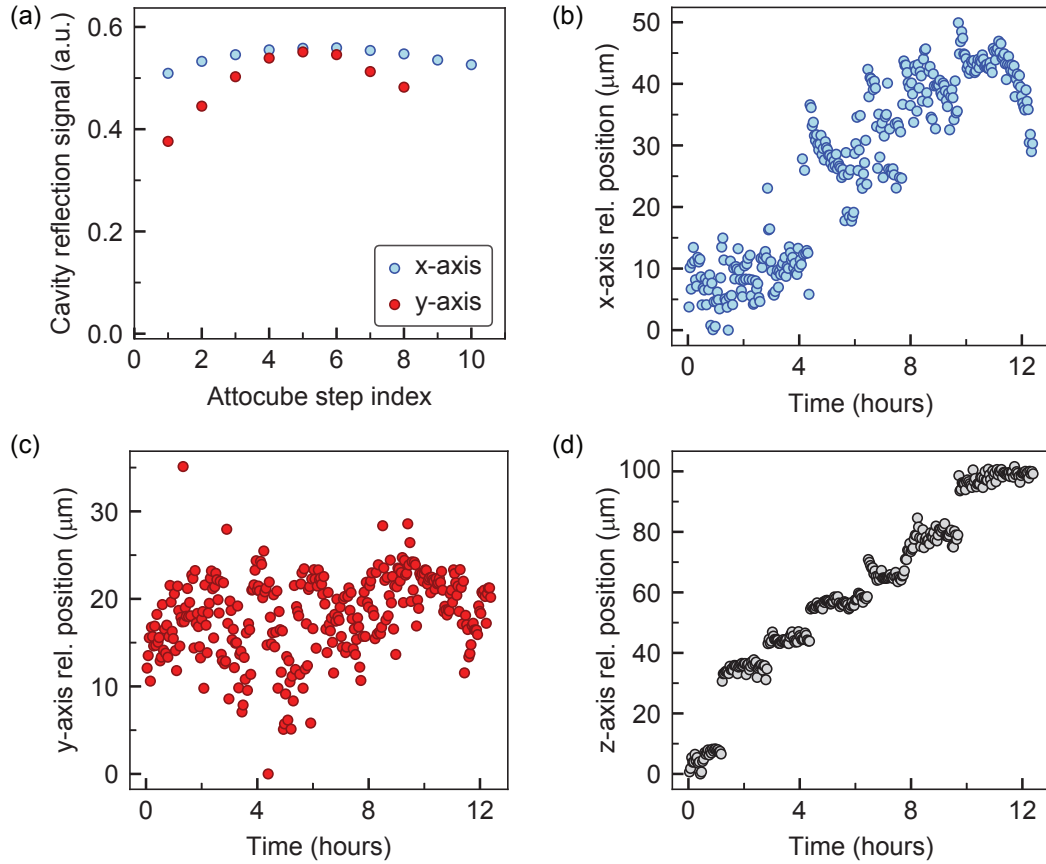


Figure 4.5: Adjusting Attocube positions to optimize fiber-cavity coupling during cool-down. (a) Variation of cavity reflection signal during one attempt of fine alignment while cooling down the cryostat. (b,c,d) Relative Attocube positions (with respect to an arbitrary offset) to maintain optimal fiber-cavity coupling during a typical cool-down. It should be noted that while the x and y -axes positions for optimal coupling are extracted in an automated fashion by executing a feedback script every ~ 1.5 mins, the z -axis positions are manually optimized every ~ 2 -hours. The x, y, z -axes denoted here are oriented identical to that in Figure 3.1. See Section 4.4 for further discussion.

Figure 4.5 discuss results for a typical cool-down using angle-polished fiber to couple light into the PC cavity. During each attempt of fine alignment of the Attocube position (along a particular axis), we take discrete steps of the Attocube and record the cavity reflection signal. When the signal crosses the maximum, we retrace back to the optimal position and record the Attocube position. Repeating the fine alignment across multiple axes yields the optimal Attocube positions. For the particular case of coupling angle-polished fiber to a PC cavity, it is beneficial to deliberately back-out the Attocube a bit in the z -axis direction to a sub-optimal position while cooling-down (to avoid the possibility of the fiber crashing onto the grating coupler), note down the reflection signal at room temperature and perform z -axis fine alignment throughout the cool-down while attempting to maintain the same reflection signal. On the other hand, if light was coupled from a lensed-fiber to the PC cavity, automated feedback along all three axes needs to be performed.

4.5 Tuning the PC cavity resonance

Due to nanofabrication uncertainties, the fabricated PC cavity is often detuned from the target wavelength by a fair amount. Moreover, even if the cavity is coarsely at the target wavelength, individual Er^{3+} ions are spectrally situated over a few GHz wide inhomogeneous distribution (Figure 5.2). Since the linewidth of a high- Q cavity is also of the order of a few GHz (*e.g.* $\kappa \sim 2$ GHz for $Q = 10^6$), it is critical to attain the capability of fine-tuning the cavity into resonance with individual ions of interest. When operating at low temperature, tuning the PC cavity resonance *in situ* is achieved by condensing N_2 gas on the top surface of the PC cavity [92, 93]. Clean, dry N_2 gas is applied through a nozzle to form a thin layer of ice, which can decrease the cavity resonance frequency by up to 6 – 8 nm (0.8 – 1 THz). In this method, by deterministically adding N_2 gas, the cavity resonance can tuned but only towards

lower frequencies; however, the process is reversible as one can desorb *all* the ice by heating the sample/Still flange to \sim 30 K using a platform heater installed on the quasi-4K flange. A fairly controlled amount of desorption can also be attained by shining intense laser light (\sim 100 μ W of 1536 nm light resonant with the cavity).

A sketch of the gas-tuning rig is provided in Figure 4.3a while images of the gas-tuning line (nozzle) is shown in Figure 4.3b. In practice, first we would like to put a small amount of clean, dry N₂ gas into the reservoir section, which is the region between the fill-valve (v_f) and the tuning-value (v_t) and constituted by a couple feet of stainless-steel tubing, followed by slowly letting the gas into the cryostat. The line feeding the fill-valve (Swagelok® SS-4BK) is purged at the beginning; the reservoir section is cleaned by repeated application of pump and purge while keeping the tuning-valve (Swagelok® SS-4BK) closed. Eventually, we settle down with a \sim 1 mbar, clean N₂ gas in the reservoir; we are now ready to introduce gas into the gas-tuning line.

The gas-tuning line is composed to two sections: a stainless steel tubing section and a copper tubing section, with both tubing having an OD 1/4" and an ID 0.18". The SS region originates from outside the cryostat (right after the tuning-valve) and runs all the way to somewhere between 45 K and quasi-4K flange while being firmly clamped to the 45 K flange. The copper tubing at one end is connected to the SS tubing while the other end runs all the way to the bottom of the cryostat and finally turns around to form a nozzle that is directed carefully to the PC cavity. Note that the copper tubing does *not* make a direct (metallic) connection to the quasi-4K and Still flanges; instead, the tubing goes through these flanges via thermally insulating (G-10) feedthroughs. The copper tubing is thermally anchored weakly to the quasi-4K stage via weak thermal links (constructed out of thin copper wires soldered onto the copper tubing as well as on the quasi-4K flange). A small cartridge heater (Lakeshore HTR-50), along-with a thermometer, is installed on copper tubing to locally heat up the gas-tuning line. The weak thermal links ensure that when the cryostat is cold,

the gas-tuning line is cooled down to a temperature close to 4 K, while heating the gas-tuning line to \sim 30 K can be achieved without using too much of heater power since it is only weakly clamped to the quasi-4K flange.

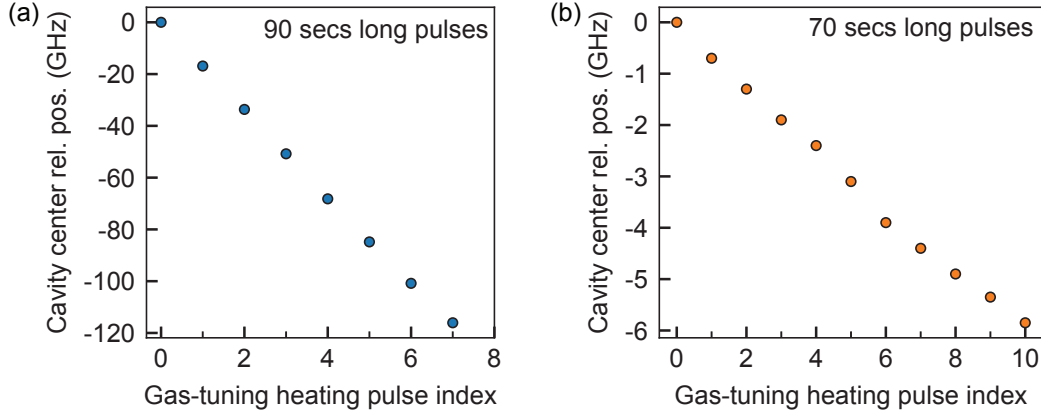


Figure 4.6: **Tuning the PC cavity resonance.** Panel (a) and (b) shows the cavity resonance frequency (with respect to an arbitrary offset) after iterative application of gas-tuning heating pulses where the pulses were switched on for 90 seconds and 70 seconds, respectively. The gas-tuning line, starting from its base temperature of \sim 5 K, reaches a peak temperature of 45.7 K and 43.0 K, respectively, after application of each heating pulse. The PC cavity used in these experiments has linewidths of $\kappa = 4.5$ GHz and $\kappa = 2.9$ GHz, respectively. In both cases, 140 mA current is passed through the heater, thus generating \sim 1 W of power.

All gas-tuning operations of the cavity resonance is performed when the pulse-tube of the cryostat is operational while the ^3He -circulation is disabled (therefore, Still flange is at \sim 4 K). When the tuning-valve v_t is switched on for a few seconds, N_2 gas enters into the gas-tuning line and gets frozen along the way. For tuning the PC cavity resonance we do the following: when the cartridge heater is switched on, the gas-tuning temperature goes up; when the local temperature in the gas-tuning exceeds \sim 30 K, the pre-solidified N_2 turns becomes gaseous again and shoots out of the nozzle, and thus, immediately solidifies upon contact with a cold-surface of the cavity (which is still at \sim 4 K). Switching the heater on for a finite amount of time condenses a finite amount of N_2 ice. Setting a fixed value of current passing through the heater (140 mA current generates \sim 1 W heating power) and varying

the pulse-width of the heating pulses thus gives us the capability to deposit varying amount of N₂ ice on the PC cavity, thereby attaining deterministic cavity resonance tuning capabilities. Figure 4.6 shows the results of tuning the cavity resonance upon repeated application of heating pulses. While fine-tuning of the cavity resonance at the few hundreds of MHz level is attained using shorter heating pulses, coarse-tuning at the order of hundreds of picometers is also achieved using longer heating pulses.

4.6 Superconducting magnets

Magnetic fields essential for the single ion experiments are generated using home-built superconducting (SC) magnets, whose locations are sketched in Figure 4.3a and they are shown in Figure 4.3b. The SC magnets are built by winding SC wire (Supercon Inc., SC-54S43-0.152 mm, 0.152 mm bare diam., 0.178 mm diam. with formvar insulation) on a custom-made bronze cylindrical bobbin designed for clamping onto the sample stage. SC wires originating from the magnets are soldered on to the high current leads provided by Bluefors; these high current leads originate from the quasi-4K stage of the cryostat and run all the way to outside of the cryostat. The magnets are driven by stable, high-current sources (KEPCO BOP) capable of generating up to ± 20 A current; an evaluation board (Analog Devices EVAL-AD5791) generates the control voltage that determines the magnitude of the current delivered by the current source. A diode quench protection circuit is also installed for each magnet. Each magnet is individually trained to sustain high currents; at least one of the SC magnet has been trained to circulate the full range of current (± 20 A) generated by the current supply. To stabilize the current flowing through the coils, we perform an automated (software-based) feedback on the control voltage of the current source: we siphon off a tiny amount of current circulating through the coil and measure it using a multimeter; deviation of the multimeter reading from the estimated current is used

as an error-signal to implement a PID feedback on the control voltage. The current through the coils is stabilized at a level better than 10^{-5} .

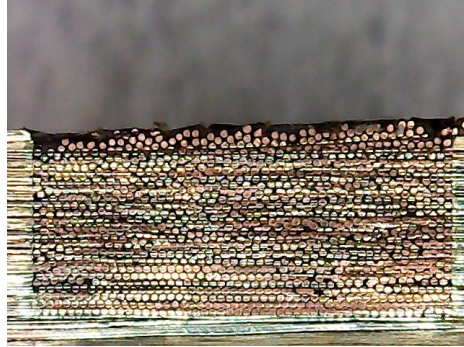


Figure 4.7: Cross-sectional view of a superconducting magnet coil. Note that for major part of the cross-section, the wires are tightly stacked in a hexagonal packing arrangement. This particular image if from a dummy bobbin chopped into half using a band saw and the wires constituting the coil are made of inexpensive copper (34 AWG) of equivalent outer diameter to that of the aforementioned SC wires.

A cross-sectional view of a typical bronze bobbin depicting the stacked layer of wires in a magnet can be found in Figure 4.7. Steps for making a home-built SC magnet is discussed here. First, we need to design the bronze bobbin around which the SC wires will be wound. The sample mount design dictates the closest a coil can be with respect to the device (PC cavity-YSO). Each magnet coil is designed such that the coil generates an axial magnetic field at the device. For the simple case of a single circular loop of radius R , the axial magnetic field generated per unit current goes $\propto R^2/(z^2 + R^2)^{3/2}$; for a device situated at a distance z away from the loop, this is optimized for $R = \sqrt{2}z$. Extending this to the complicated case of a finite-sized coil with stacked layers of loops, we numerically optimize the inner radius of the bobbin as well as the number of wires along the length and breadth of the bobbin cross-section (considering the finite diameter of the SC wires), finally yielding the bobbin design parameters capable of accommodating a SC magnet that generates optimal axial magnetic field per unit current.

Winding the SC wires on the bobbin is accomplished using an winding machine (New Computer CNC Automatic Coil Winder, for 0.03 – 1.2 mm wire). While winding the SC wires, we will wind one row at a time, starting from the bottom layer first (Figure 4.7). Before winding the first layer of SC wires, cover the side-walls and inner wall of the bobbin with a thin layer of PTFE tape: while wrapping the SC wire under high tension around the bronze bobbin, it is quite easy to scratch off some of the formvar insulation around the SC wire, which would leave the SC wire exposed to the bronze bobbin thus creating an electrical short circuit; the PTFE layer reduces friction between the insulation and the bronze inner walls. Once a row of SC wires is winded, we apply a coating of epoxy (Stycast 1266) using a paint-brush. This is followed by winding the second row of SC wires as well as applying another coating of epoxy on top of the second row. This is repeated until the desired number of rows in the bobbin’s cross-section is reached. During the entire winding process, it is critical to ensure that no electrical short circuit is formed between the magnet wire and the bobbin: this can be checked intermittently by measuring the resistance between one of the open ends of the magnet wire and the body of the bobbin. Once the winding is done, put the magnet (bobbin + SC wires) in a bell jar and initiate degassing to ensure that all the trapped air bubbles have escaped (may take 15 – 20 mins). Finally, bake the magnet at an elevated temperature for curing the epoxy.

Chapter 5

Isolating and enhancing the emission of single erbium ions

In this chapter, we discuss the experiments leading to the observation of emission of single photons from a single Er^{3+} ion (in a solid-state host) for the first time. As mentioned in preceding chapters, this is enabled by integrating Er^{3+} ions with silicon nanophotonic structures, which results in an enhancement of the photon emission rate by a factor of more than 650. Dozens of distinct ions can be addressed in a single device, and the splitting of the lines in a magnetic field confirms that the optical transitions are coupled to the electronic spin of the Er^{3+} ions. Results presented in this chapter are published in Ref. [31].

5.1 Experimental approach

Like other rare earth ions, Er^{3+} features coherent spin and optical transitions even in solid-state hosts, as the active $4f$ electrons are situated close to the nucleus and therefore only weakly coupled to phonons in the host crystal (Section 2.2.2). Observations of single rare earth ions have been hampered by the electric dipole-forbidden nature of intra- $4f$ optical transitions, which results in long excited state lifetimes

and correspondingly low photon emission rates (Section 2.1). Consequently, optical emission from single rare earth ions (Pr^{3+} and Ce^{3+}) has only recently been observed [57, 58, 59, 60], although single Er^{3+} ions in silicon have also been detected using a charge-sensing approach [75].

The key idea of our experimental approach is to enhance the emission rate of single Er^{3+} ions by positioning an Er-doped crystal in close proximity to a silicon photonic crystal (PC) cavity tuned to the transition frequency of the ion (Figure 5.1) [83, 94]. The enhancement resulting from the cavity, denoted by the Purcell factor P , is maximized for small mode-volume, low-loss cavities (Section 2.3). Recently, other resonator geometries have been used to enhance the decay rate of rare earth ion ensembles by a factor of 20 [95, 94]. Silicon PCs capable of achieving $P > 10^5$ have been demonstrated [71, 74], which would result in photon emission rates from single Er^{3+} ions of more than 10 MHz, despite the low initial rate of $2\pi \times 14$ Hz [50]. Importantly, this is possible because the Er^{3+} 1.5 μm transition is radiatively efficient despite its small transition moment, enabling large enhancement of the total emission rate by modifying the electromagnetic environment.

Our devices consist of one-dimensional silicon PCs on an Er-doped yttrium orthosilicate (Y_2SiO_5 , or YSO) substrate. We fabricate the silicon PhCs from a silicon-on-insulator wafer using electron beam lithography and reactive ion etching, then transfer them onto YSO using a stamping technique (Section 3.4). YSO is chosen as a host because it is available in high-quality, transparent single crystals, and Er substitutes easily for Y (Section 2.2.1). Our YSO crystals contain trace quantities of Er^{3+} with an independently measured concentration of 0.2 ppm (Appendix A.2). Ions near the YSO surface couple to the cavity through the evanescent electric field, whose magnitude $|E|$ at the Si-YSO interface is 60% of its maximal value in the center of the Si layer (Section 3.3.2). The substrate is mounted on a cold finger inside a closed-cycle cryostat ($T \approx 4$ K). A lensed fiber couples light to and from the

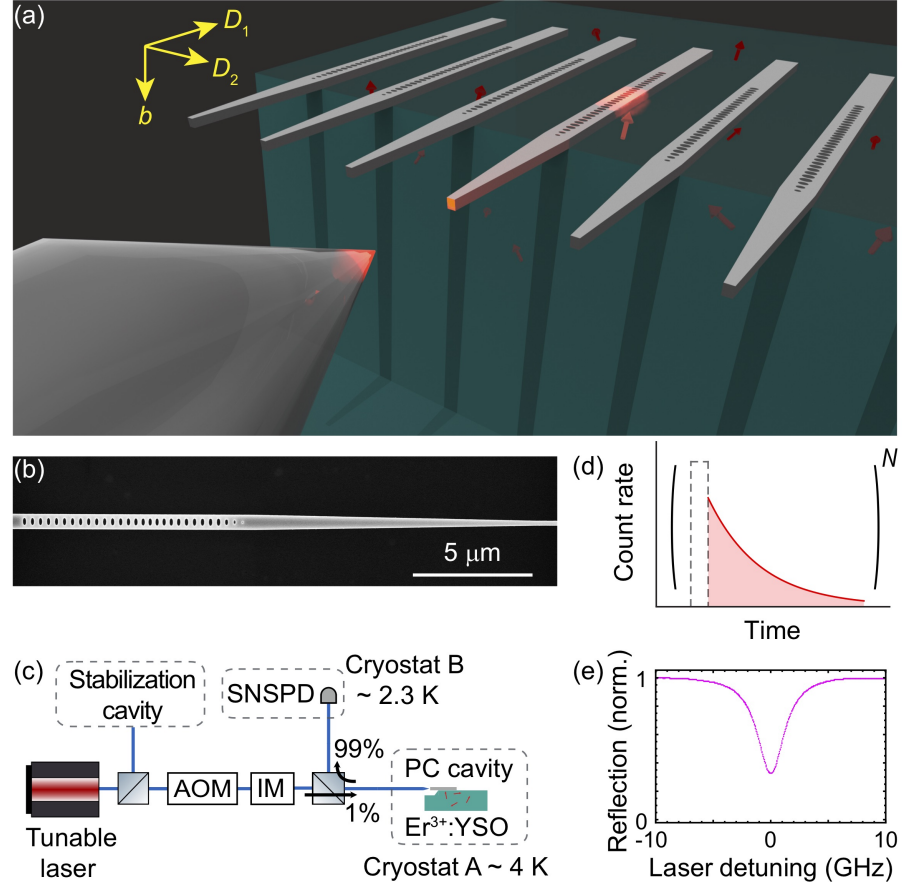


Figure 5.1: Experimental configuration for enhancing Er^{3+} emission with a silicon photonic crystal. (a) Schematic illustration of the fabricated devices. Silicon waveguides patterned with photonic crystal cavities evanescently couple to Er^{3+} ion impurities in a YSO crystal. The suspended, tapered ends of the Si waveguides protrude off the edge of the YSO crystal, allowing coupling to a lensed fiber. The axes (D_1 , D_2 , b) denote the orientation of the YSO crystal [52]. (b) Scanning electron microscope image of a photonic crystal cavity and tapered waveguide prior to transfer onto the YSO substrate. (c) Schematic layout of the experiment. The Si-YSO device is situated in a cryostat ($T \approx 4 \text{ K}$). A stabilized laser in combination with a double-pass acousto-optic modulator (AOM) and electro-optic intensity modulator (IM) produces short pulses of light with an on/off ratio of 90 dB. A superconducting nanowire single photon detector (SNSPD) inside a second cryostat detects the return light from the cavity. (d) The PLE measurement sequence consists of a $10 \mu\text{s}$ excitation pulse, followed by a fluorescence collection window. (e) Reflection spectrum of the cavity used in these experiments, with quality factor $Q = 7.3 \times 10^4$, limited by internal losses.

single-sided cavity with around 50% one-way efficiency, and a fiber-coupled superconducting nanowire single photon detector (SNSPD) located in a second cryostat detects light leaving the cavity (Figure 5.1c). We tune the frequency of the cavity resonance *in situ* by condensing gas on the surface of the device. Additional details about the fabrication and measurement techniques are discussed in Section 3.4 and Appendix A.1.

5.2 Spectroscopy of single erbium ions

We search for ions coupled to the cavity using photoluminescence excitation spectroscopy (PLE), with the pulse sequence shown in Figure 5.1d. We record a spectrum by scanning the laser frequency and cavity resonance together through a spectral region near the Er³⁺:YSO (site 1) bulk absorption resonance at 1536.48 nm. The resulting spectrum features a series of sharp peaks (Figure 5.2a), which we interpret as the optical transitions of individual Er³⁺ ions. The width of the individual peaks is approximately 5 MHz (Figure 5.2b). The height of a single peak above the background saturates at high excitation powers to about 0.02 detected photons following each excitation pulse (Figure 5.2b inset). Given the combined detection and collection efficiency of light in the cavity (0.04), the observed count rate is consistent with a single ion with nearly perfect emission into the cavity and an incoherent excitation probability of 0.5. The inhomogeneous distribution of the individual ions' transitions results from local variations in the crystal environment caused by strain and proximity to other defects. This distribution is slightly shifted and broadened compared to the absorption spectrum of a reference bulk Er³⁺:YSO crystal (Figure 5.2a); this difference could originate from strain caused by sample mounting or proximity to the surface. However, the inhomogeneous width is substantially smaller than in glass hosts such as silica fibers, which is typically of order 10 THz [43].

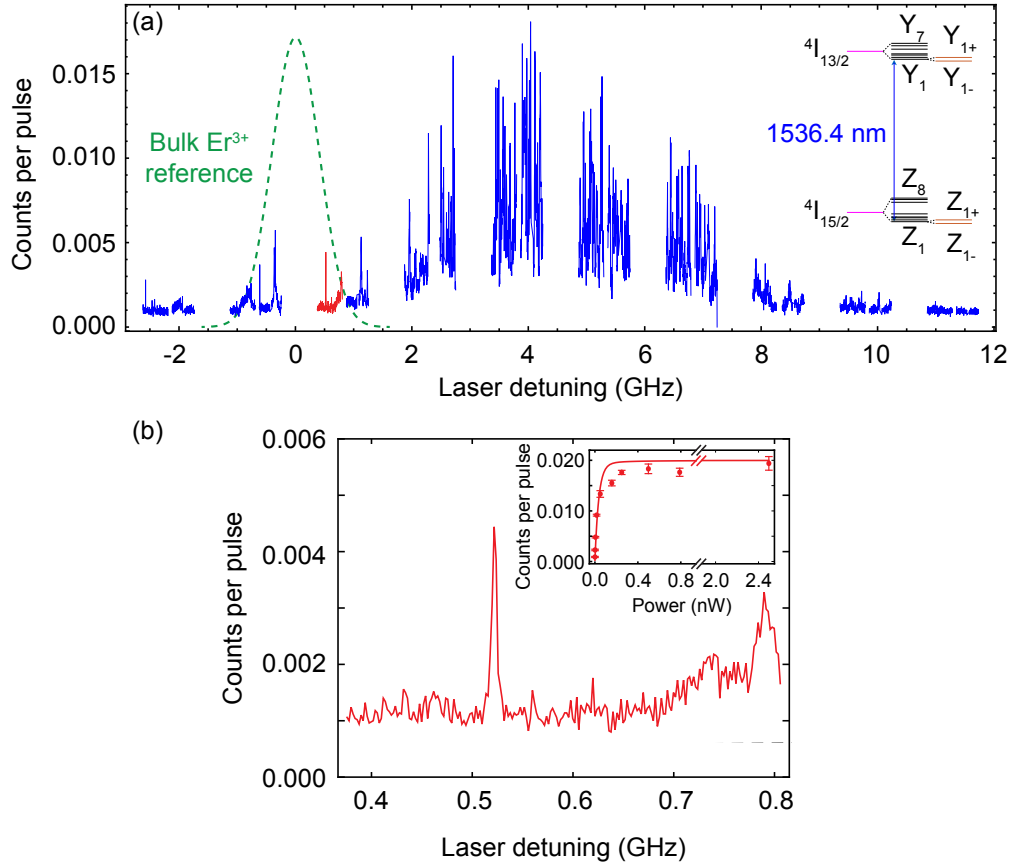


Figure 5.2: **Photoluminescence excitation (PLE) spectrum of single ions in a dilute Er^{3+} ensemble.** (a) PLE spectrum, measured by scanning the laser frequency and cavity resonance (with linewidth $\kappa = 2\pi \times 3.85$ GHz) together through a spectral region near the bulk Er^{3+} :YSO absorption resonance at 1536.48 nm (determined from a second crystal, and indicated schematically by the green dashed line). The vertical axis indicates the average number of photons detected in an 82 μs integration window following each excitation pulse (as in Figure 5.1d). The spectrum shows individually resolvable peaks, which we interpret as the optical transitions of single Er^{3+} ions. The interruptions in the scan result from spectral regions that are inaccessible with our laser stabilization technique. Inset: Energy levels of Er^{3+} in YSO (Section 2.2.2). The cavity is resonant with the Z_1 - Y_1 transition at 1536.46 nm (YSO site 1). (b) Expanded view of the red portion of (a), showing an isolated line with a width of 5 MHz (full-width at half-maximum, FWHM) on a nearly dark-count-limited background (gray dashed line), characteristic of the tails of the inhomogeneous distribution. Inset: The background-subtracted height of this isolated peak saturates with increasing excitation power. The solid line is a model based on independently measured parameters (Appendix A.4).

5.3 Extracting atom-cavity coupling parameters and confirming emission from a single ion

To quantify the strength of the atom-cavity coupling, we focus on a single peak in the inhomogeneous distribution and extract the excited-state lifetime from the time constant of the fluorescence decay (Figure 5.3a). The measured value, $17.0 \pm 0.1 \mu\text{s}$, is 669 ± 4 times shorter than the bulk lifetime of $1/\Gamma_0 = 11.4 \text{ ms}$ for $\text{Er}^{3+}:\text{YSO}$. To confirm that the increased decay rate results from resonant enhancement by the cavity, we tune the cavity away from the atomic transition (by an amount Δ_c) while keeping the laser frequency fixed at the atomic transition. We observe that the decay rate is described by $\Gamma = \frac{P\Gamma_0}{1 + (2\Delta_c/\kappa)^2} + \Gamma_\infty$ (see Equation 2.19), where $P = 658 \pm 5$ is the Purcell factor describing the cavity contribution to the enhancement, $\Gamma_\infty = (3 \pm 5)\Gamma_0$ is the asymptotic decay rate, and κ is the cavity decay rate (Figure 5.3b). Using the relationship $P = 4g^2/(\kappa\Gamma_0)$, we determine the complete cavity-QED parameters $(g, \kappa, \Gamma_0) = 2\pi \times (2.48 \text{ MHz}, 2.66 \text{ GHz}, 14 \text{ Hz})$ for this ion (here, $2g$ is the single-photon Rabi frequency; see Equation 2.5). The hierarchy $\kappa \gg g \gg \Gamma$ places this system in the bad-cavity or weak-coupling regime. The value of g is roughly consistent with our theoretical prediction of $2\pi \times 2.62 \text{ MHz}$ for an ion at the Si-YSO interface (Section 3.3.2); interestingly, the predicted g is similar for either electric or magnetic dipole coupling to the cavity, since the electric and magnetic dipole transition strengths are comparable in $\text{Er}^{3+}:\text{YSO}$ [43]. The discrepancy between predicted and measured values can be attributed to the position of the ion or a misalignment between the atomic dipole moment and the local cavity polarization.

To confirm that the sharp spectral peaks result from the transitions of individual Er^{3+} ions, we measure the second-order autocorrelation function, $g^{(2)}$, of the fluorescence (Figure 5.3c). The value of $g^{(2)}(0) = 0.055 \pm 0.007$ indicates that the majority of the detected photons originate from a single emitter. It is consistent with an estimate

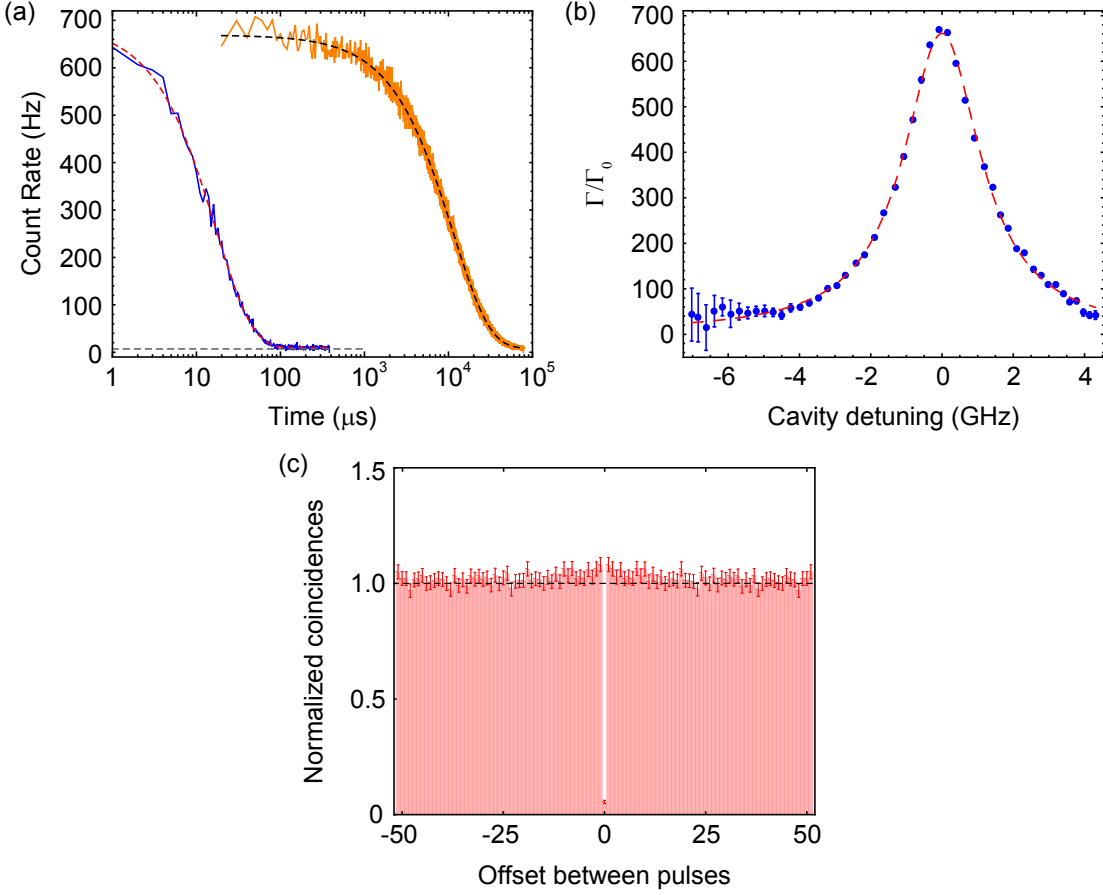


Figure 5.3: **Quantifying the Er^{3+} -cavity coupling and measurement of $g^{(2)}$.** (a) Time-resolved fluorescence from a single cavity-coupled Er^{3+} ion (blue) following an excitation pulse, which decays to the detector dark count rate (gray dashed line). The fluorescence from a bulk ensemble without cavity enhancement is shown for comparison (orange; measured in a second crystal, and on an arbitrary vertical scale). (b) Fixing the laser frequency to the atomic transition and sweeping the cavity resonance reveals that the decay rate enhancement Γ/Γ_0 varies with the atom-cavity detuning. A Lorentzian fit to the data (red dashed curve) yields a width of 2.62 ± 0.04 GHz (in agreement with the cavity linewidth), and a maximum decay rate enhancement of $P = 658 \pm 5$. (c) Second-order autocorrelation function ($g^{(2)}$) of the fluorescence from a single ion. We bin all photons detected after a single excitation pulse into a single time bin, so the horizontal axis shows the autocorrelation offset in units of the pulse repetition period (100 μ s). The data is symmetric around zero offset since a single detector is used to record the fluorescence and compute a true autocorrelation; however, both positive and negative offsets are plotted for clarity.

of accidental coincidences from dark counts (Appendix A.5.1). The autocorrelation also shows bunching ($g^{(2)} > 1$) that decays on the order of 1 ms, which we believe results, at least in part, from spectral diffusion (Appendix A.5.2).

5.4 Spin-photon coupling

Lastly, we apply a magnetic field using a permanent magnet and observe that a single-ion peak splits into two lines (Figure 5.4). The magnetic field is oriented along an axis at an angle of 45 degrees to the YSO D₁ axis, in the D₁-D₂ plane (Figure 5.1a). The measured splitting is consistent with the difference of the ground and excited state g -factors ($\Delta g = 1.55$) for this orientation of the magnetic field [52]. The doublet nature of the ground and excited states (Figure 5.2a, inset) should give rise to four distinct

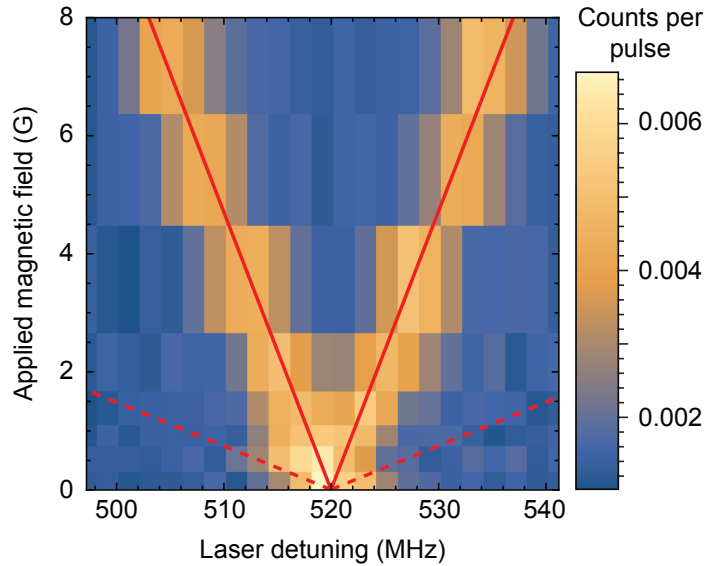


Figure 5.4: **Zeeman splitting of a single Er³⁺ ion spectral line.** A magnetic field splits a single spectral line into two transitions. The field is oriented approximately 45 degrees between the D₁ and D₂ axes in the D₁-D₂ plane. The predicted transition frequencies are shown with red lines, including an offset field of around 1 G. Since the g -factors are highly anisotropic, the slope of the predicted splitting is not linear when the applied field is smaller in magnitude than the offset field, which has a different orientation.

transitions. The reason we observe just the two spin-conserving transition lines here is likely due to the high cyclicity of these optical transitions enabled by the cavity, compounded with insufficient optical excitation power available during these experiments to drive the spin non-conserving transitions. Detailed discussion on cyclicity of Er^{3+} optical transitions in an optical cavity will be taken up in Chapter 6, wherein we observe all four transition lines emanating from a single ion. These measurements show that the optical transitions are coupled to the spin, which is crucial for future spin-photon entanglement.

5.5 Conclusion and outlook

For experiments discussed in this chapter, we note that we have not been able to observe any dynamics of the ground state spin, such as optical spin polarization. This is presumably because of rapid spin-lattice relaxation in the ground or excited states [96], such that spin-lattice relaxation time (T_1) is short compared to the optical excited state lifetime. Prior measurements of the T_1 for $\text{Er}^{3+}:\text{YSO}$ reveal a steep temperature dependence around 4 K, with $T_1 = 1.5 \text{ ms}$ at 4 K, but only $7.5 \mu\text{s}$ at 6 K [97]. Therefore, a slightly elevated sample temperature resulting from poor heatsinking in the cryostat could result in a significantly reduced T_1 . Further discussion on ground state spin T_1 will be taken up in Appendix A.3, as well as, in Chapter 6 and Appendix B.6.

The experiments described above demonstrate that nanophotonic structures can be used to enhance and efficiently collect the photon emission from Er^{3+} ions, enabling the observation of fluorescence from single Er^{3+} ions for the first time. These results suggest several avenues for further investigation. First, operating at temperatures below 1 K should increase T_1 to more than 10^3 seconds (Appendix A.3), to allow the exploration of spin-photon entanglement and coherent atom-photon interactions. While the longest spin coherence time T_2 (Hahn) observed for the ground state in Er^{3+}

:YSO is $5.6 \mu\text{s}$ [55] (believed to be limited by the ^{89}Y nuclear spin bath), longer spin coherence times may be achieved using fast dynamical decoupling, or by implanting Er^{3+} ions into a host crystal without nuclear spins, such as silicon [76]. Second, implanting a small number of ions into an otherwise erbium-free substrate will allow the number of ions coupled to the cavity to be controlled, and eliminate background fluorescence from distant, weakly-coupled ions. This may require changing to a host without yttrium, since the rare earth elements are difficult to chemically separate from each other; several candidates are already known [43]. Finally, increasing the cavity quality factor to ten million [71] will increase the Purcell factor and lifetime-limited linewidth 140-fold; further improvement may be possible using smaller mode-volume cavity designs [74]. This will bring the Purcell-enhanced lifetime-limited linewidth close to the observed single-ion linewidth of 5 MHz, which is 10^3 times broader than the current lifetime-limited linewidth $2\pi \times 9 \text{ kHz}$. The observed linewidth is presumably broadened by dephasing or fast spectral diffusion. Significantly lower spectral diffusion resulting in homogeneous linewidths of 74 Hz has been observed in bulk photon echo spectroscopy of Er^{3+} :YSO at lower temperatures and in higher magnetic fields [38]. While the broadening mechanisms involved at low fields, as in the present work, are not well understood, future single-ion measurements will help to disentangle the contributions of phonons, ion-ion interactions, and coupling to the nuclear spin bath.

This work opens the door to realizing long-distance quantum networks based on a scalable and mature silicon nanophotonics platform. The ability to simultaneously couple the cavity to many spectrally resolvable atoms is promising for multiplexed repeater schemes, as envisioned with multimode ensemble quantum memories using rare earth ion ensembles [98]. Indistinguishable photons from ions with different transition frequencies may be generated by frequency-shifting photons during transit or using quantum eraser techniques with fast photon detection, both possible because

the total inhomogeneous linewidth is less than typical electronic bandwidths. Additionally, spectral addressing of ions that are spatially nearby (the average ion-ion separation is 80 nm in the present device) is a promising starting point for exploiting their electric or magnetic dipolar interactions for quantum logic [99] or quantum simulations of strongly interacting spin systems.

Chapter 6

Optical quantum nondemolition measurement of a single rare earth ion qubit

In this chapter, we demonstrate single-shot spin readout of a single rare earth ion qubit, Er^{3+} . In previous work with laser-cooled atoms and ions, and solid-state defects, spin readout is accomplished using fluorescence on an optical cycling transition; however, Er^{3+} and other rare earth ions generally lack strong cycling transitions (see Section 2.4 for a definition of cyclicity in the present context). We demonstrate that modifying the electromagnetic environment around the ion can increase the strength and cyclicity of the optical transition by several orders of magnitude, enabling single-shot quantum nondemolition readout of the ion’s spin with 94.6% fidelity. We use this readout to probe coherent dynamics and relaxation of the spin. Results presented in this chapter are published in Ref. [32].

6.1 Introduction

Atomic and atom-like defects in the solid state provide an optical interface to individual electronic and nuclear spin qubits [100], and are used for a variety of quantum technologies. As sensors, they can probe temperature and magnetic and electric fields with nanoscale spatial resolution [101, 102, 103]. In quantum networks, spin-photon entanglement [11, 13, 104] has enabled deterministic entanglement of remote spins [16]. Defect spins have also been used to demonstrate key components of quantum information processors, including quantum error correction [105] and 10-qubit quantum registers with multi-qubit gates [30].

These works primarily leverage the well-studied nitrogen vacancy (NV) center in diamond. However, a much broader range of defects exists that may be advantageous for particular applications. For example, the SiV⁻ [106] and SiV⁰ [21] color centers in diamond are promising for quantum networks because of their low spectral diffusion, while color centers in silicon carbide [107] may be easier to integrate with nanoscale devices. Rare earth ions are another family of defects that can offer long spin coherence [39] and narrow, stable optical transitions (in the telecom band for the case of Er³⁺) [38], and may be doped into a variety of host crystals. Several recent works have begun to probe individual rare earth ions [57, 58, 59, 60, 31, 75, 108], using an optical cavity to overcome their low intrinsic photon emission rates [31, 108].

A key capability for atomic defects is high-fidelity spin readout using the optical transition [100]. Single-shot optical spin measurements have been achieved in quantum dots [109] and in the NV [67] and SiV⁻ [68] color centers in diamond by leveraging highly cyclic optical transitions that arise from atomic selection rules. However, cyclic optical transitions are not a universal feature of atomic defects, and are often absent in low-symmetry defects and in the presence of strain [110] or spin-orbit coupling without careful alignment of the magnetic field [68, 109].

Single-shot readout has not been achieved in atomic defects without intrinsic cycling transitions, such as rare earth ions [69].

In this work, we demonstrate that tailoring the electromagnetic density of states around an atom with an optical cavity can induce highly cyclic optical transitions in an emitter that is not naturally cyclic. Using a single Er^{3+} ion in YSO coupled to a silicon nanophotonic cavity (Figure 6.1a), we demonstrate a greater than 100-fold enhancement of the cyclicity: under conditions where the branching ratio of the bare ion results in a spin flip after scattering fewer than 10 photons, a cavity-coupled ion can scatter over 1200. This is sufficient to realize single-shot spin readout with a fidelity of 94.6%, and to enable continuous, quantum nondemolition measurement of quantum jumps between the ground state spin sublevels. The improvement in the cyclicity arises from selective Purcell enhancement of the spin-conserving optical decay pathway (Figure 6.1b), determined primarily by the alignment of the cavity polarization and the spin quantization axis defined by a magnetic field. A small additional enhancement arises from detuning of the spin-non-conserving transitions from the optical cavity, an effect that was recently used to enhance the cyclicity of a quantum dot in a nanophotonic cavity [111]. This generic technique opens the door to exploiting a much broader range of atomic defects for quantum technology applications, and is a particular advance for individually addressed rare earth ions.

6.2 Experimental approach

Our experimental approach, following Chapter 5 (Ref. [31]), is based on a YSO crystal doped with a low concentration (< 1 ppm) of Er^{3+} ions placed in close proximity to an optical cavity in a silicon photonic crystal waveguide (Figure 6.1a). Assembled devices are placed inside a ${}^3\text{He}$ cryostat at 0.54 K with a 3-axis vector magnet. Light is coupled to the cavities using a lensed optical fiber on a 3-axis translation stage. The

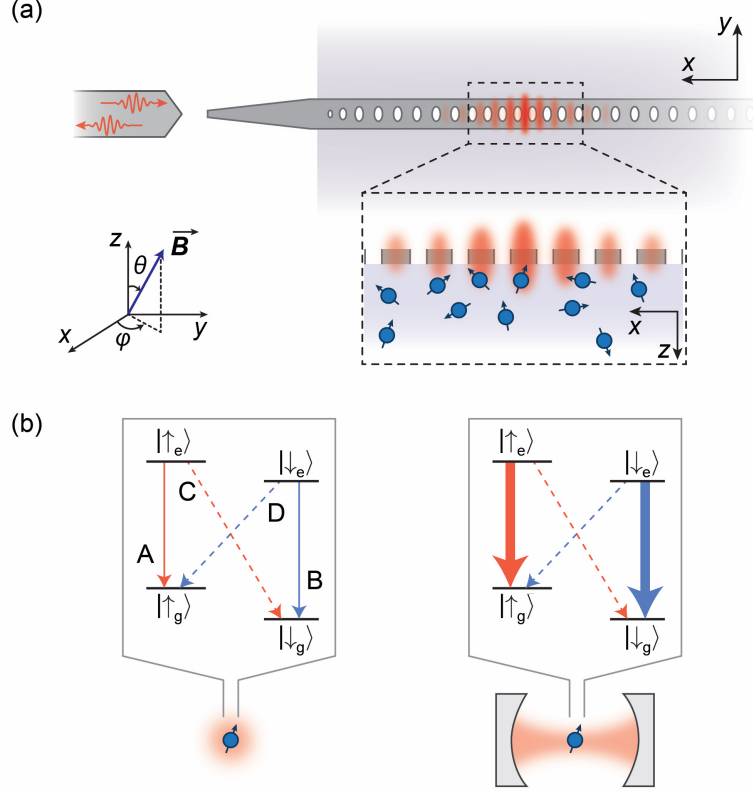


Figure 6.1: Experimental approach. ((a)) The experimental device is a silicon photonic crystal cavity on top of an Er^{3+} -doped YSO crystal. Light in the cavity evanescently couples to the Er^{3+} ions. (inset) Definition of magnetic field angle (φ, θ); (x, y, z) refer to the (D_1, D_2, b) optical axes of the YSO crystal. (b) Without a cavity, the spin-conserving transitions A,B and spin-non-conserving transitions C,D are comparable in strength. The cavity selectively enhances A,B, resulting in highly cyclic optical transitions.

high quality factor (6×10^4) and small mode volume of the cavity, together with the high radiative efficiency of the Er^{3+} optical transition, enable Purcell enhancement of the Er^{3+} emission rate by a factor of $P = 700$ (Figure 6.3a). There are several hundred ions within the mode volume of the cavity, but their optical transitions are inhomogeneously broadened over a several GHz span, such that stable, single ion lines can be clearly isolated (Figure 6.2a) [31].

The ground and excited states of the $1.536 \mu\text{m}$ optical transition in $\text{Er}^{3+}:\text{YSO}$ are effective spin-1/2 manifolds, which emerge as the lowest energy states of the 16-

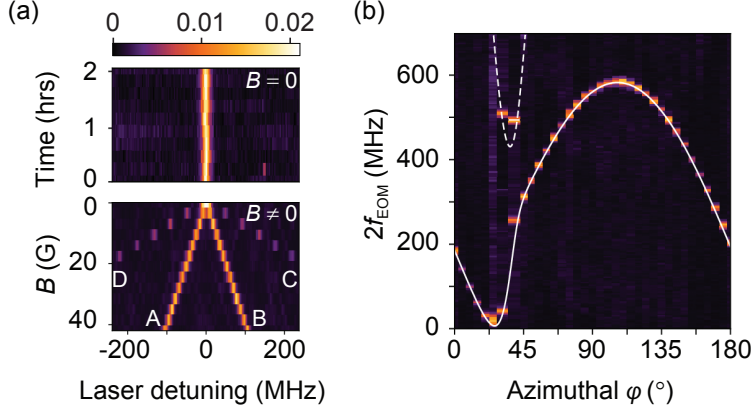


Figure 6.2: **Spin-photon coupling.** (a) In the absence of a magnetic field, the four transitions are degenerate and give rise to a single, stable optical transition with a full width at half maximum of 6 MHz (centered at $\lambda = 1536.48$ nm). A magnetic field lifts the degeneracy. The color bar denotes the fluorescence intensity (arbitrary units). (b) The Zeeman splitting is strongly anisotropic, measured here by applying a 112 G magnetic field at various angles φ ($\theta = 90^\circ$) while driving the ion with a phase-modulated laser containing frequencies $f_0 \pm f_{\text{EOM}}$, where f_0 is the transition frequency when $B = 0$. The solid (dashed) line shows the predicted splitting between the A-B (C-D) transitions [52].

(14-)fold degenerate ${}^4\text{I}_{15/2}$ ground (${}^4\text{I}_{13/2}$ excited) free-ion multiplets in the crystal field potential, respectively. In the absence of a magnetic field, the ground and excited states are two-fold degenerate, as required by Kramers' theorem [112]. This degeneracy is lifted in a small magnetic field, revealing four distinct optical transitions (Figures 6.1b and 6.2a). Transitions A and B conserve the spin, while C and D flip the spin.

6.3 Improving the cyclicity of the optical transitions

To probe the selection rules of the optical transition, we excite the spin-conserving A and B lines alternately (Figure 6.3a). The average fluorescence following the A and B pulses is the same, since the transitions are symmetrically detuned from the

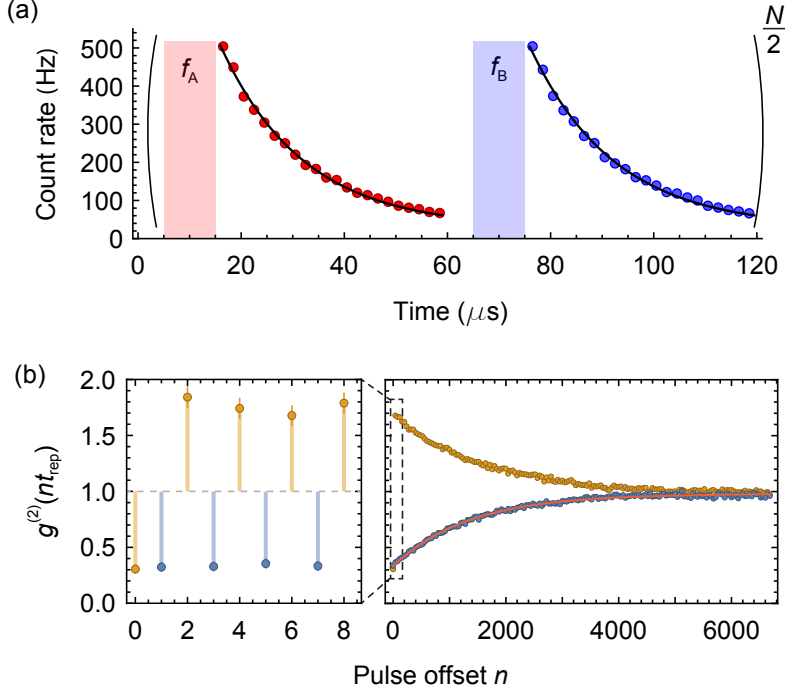


Figure 6.3: Measuring the cyclicity of the optical transitions. (a) The measurement sequence consists of alternating pulses on the A and B transitions ($10 \mu\text{s}$) followed by a fluorescence collection window ($45 \mu\text{s}$), repeating every $t_{\text{rep}} = 60 \mu\text{s}$. The fluorescence lifetime is $16.2 \pm 0.2 \mu\text{s}$, shortened from its free-space value of 11.4 ms by $P = 703 \pm 6$ in this device. (b) The intensity autocorrelation $g^{(2)}$ is computed from the integrated fluorescence after each pulse. Odd values of n (blue points) probe the correlation between pulses driving different transitions and are anti-bunched as a result of the spin staying in the same state over many excitation cycles. $g^{(2)}$ decays as e^{-n/n_0} because of optical pumping, giving the cyclicity $C \approx n_0/2$. In this measurement, $C = 660 \pm 66$. $g^{(2)}(0) = 0.3$ is consistent with the signal-to-background ratio of 10. In all plots, error bars denote estimated $\pm 1\sigma$ statistical uncertainty.

cavity and the spin is on average unpolarized from continuous optical pumping by the excitation light. However, the intensity autocorrelation function, $g^{(2)}(nt_{\text{rep}})$ (where n is the offset in the number of pulses) is anti-bunched for odd-numbered pulse offsets (*i.e.*, A-B correlations) and bunched for even offsets (*i.e.*, A-A or B-B correlations), revealing that only one of the transitions A or B is bright at any given time, depending on the instantaneous spin state (Figure 6.3b). Note that the fluorescence after each pulse is integrated before computing the autocorrelation, so $g^{(2)}(nt_{\text{rep}})$ is only defined

for discrete times. Eventually, the spin relaxes and $g^{(2)}$ decays exponentially to 1 after an average of n_0 pulses. Under the assumption (to be verified later) that the observed spin relaxation arises primarily from optical pumping between the spin sublevels, we extract the optical transition cyclicity $C = n_0 P_{\text{ex}}$, where $P_{\text{ex}} \approx 1/2$ is the probability to excite the ion in each pulse. This value of P_{ex} is assured by using an intense excitation pulse to saturate the ion, and is verified using the independently measured collection efficiency (Appendix B.3).

We repeat this measurement with different orientations of the magnetic field, and find that the cyclicity varies by nearly three orders of magnitude (Figure 6.4a,b), with a maximum value of 1260 ± 126 . This results from the changing orientation of the atomic transition dipole moment with respect to the cavity polarization, with the maximum cyclicity occurring when the spin-conserving transitions A, B are aligned to the cavity and the spin-flip transitions C, D are orthogonal to it. It can be captured by a simple model where the decay rates on each transition are proportional to the projection of an associated dipole moment \mathbf{d} onto the cavity polarization $\boldsymbol{\epsilon}$ at the position of the ion (Appendix B.2). For the spin conserving transition, $\Gamma_{AB} \propto |\langle \uparrow_e | \boldsymbol{\epsilon} \cdot \mathbf{d}_{||} | \uparrow_g \rangle|^2$, while Γ_{CD} is defined analogously with $\mathbf{d}_{||}$ replaced by \mathbf{d}_{\perp} . When the magnetic field is rotated, the spin sublevels mix such that $|\uparrow(\varphi', \theta')\rangle = \alpha |\uparrow(\varphi, \theta)\rangle + \beta |\downarrow(\varphi, \theta)\rangle$, with the coefficients α, β completely specified by the anisotropic \mathbf{g} tensor describing the Zeeman shifts (Figure 6.2b) [52]. Together with the time-reversal symmetry properties of the Kramers' doublets, this allows the complete angular dependence of $C = \Gamma_{AB}/\Gamma_{CD} + 1$ to be described by only two parameters: $\boldsymbol{\epsilon} \cdot \mathbf{d}_{||}$ and $\boldsymbol{\epsilon} \cdot \mathbf{d}_{\perp}$ at a single (arbitrary) reference orientation . In this model, the role of the cavity is to restrict the decay to a particular polarization, such that the decay rates are determined by a single matrix element $|\boldsymbol{\epsilon} \cdot \mathbf{d}|^2$; in free space, there is no preferred $\boldsymbol{\epsilon}$.

Since the dipole matrix elements for $\text{Er}^{3+}:\text{YSO}$ and the cavity field polarization at the position of the atom are not known, we treat $\boldsymbol{\epsilon} \cdot \mathbf{d}_{||}$ and $\boldsymbol{\epsilon} \cdot \mathbf{d}_{\perp}$ as fit parameters. A

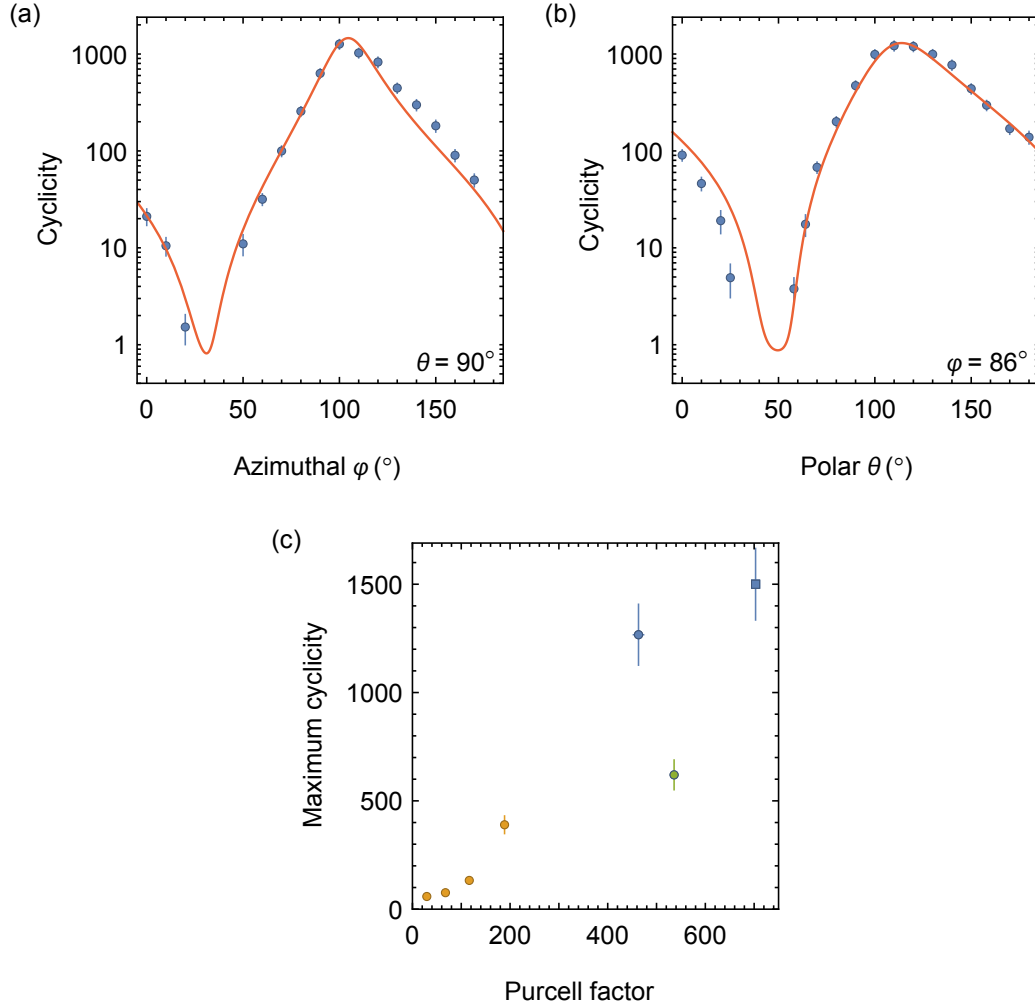


Figure 6.4: **Tuning the cyclicity of optical transitions.** (a, b) The cyclicity varies dramatically with the angle of the external magnetic field, but is described by a model (red line) based on the independently measured \mathbf{g} tensors (see text). (c) The cyclicity decreases rapidly with the Purcell factor, demonstrated here by measurements on several ions (shown in different colors) with the detuning varied to change P .

fit to this model displays excellent agreement with the data, and allows the complete angle dependence of the cyclicity to be extracted from a small number of measurements. While this discussion centers on electric dipole coupling, the Er^{3+} transition we study has comparable electric and magnetic dipole matrix elements [56], and the predicted magnetic Purcell factor for our structures is similar [31], depending on the precise position of the ion. We show in the Supplementary Information that the

electric and magnetic contributions have the same angular dependence and may be summed into a single term (Appendix B.2). We also demonstrate that the detuning of the C, D transitions from the cavity makes an additional, small contribution to the cyclicity at the highest magnetic fields used (Appendix B.6).

To quantify the extent to which the cyclicity is enhanced by the cavity, we study a second ion with lower Purcell factor and then lower it further by detuning the cavity. The cyclicity is observed to decrease roughly linearly with P (Figure 6.4c). Based on the dependence of the cyclicity on the cavity detuning for this ion, we estimate that the cyclicity C_0 of the ion alone is less than 10 (limited by the bare ion branching ratio, which may be affected by decays through intermediate crystal field levels and phonon-assisted excitation to higher excited states; see Appendix B.4), such that the enhancement by the cavity is greater than 100. We note that C_0 has not been directly measured for $\text{Er}^{3+}:\text{YSO}$.

6.4 Single-shot quantum nondemolition measurement

Next, we focus on using the cavity-enhanced cyclicity to measure the spin state. Figure 6.5a shows a time trace of photons recorded in a single run of the experiment, with telegraph-like switching between $|\downarrow_g\rangle$ (where transition B is bright) and $|\uparrow_g\rangle$ (where transition A is bright) clearly visible. A continuous estimation of the spin state occupation using a Bayesian estimator applied to the full measurement record [113] shows clearly resolved quantum jumps between these states, demonstrating the quantum nondemolition nature of the measurement. The quantum jumps are driven by optical pumping from the measurement process itself, because of the finite cyclicity.

To demonstrate single-shot measurement of the spin, we use a maximum likelihood (ML) algorithm to estimate the state at time t using photon counts from times $t' > t$.

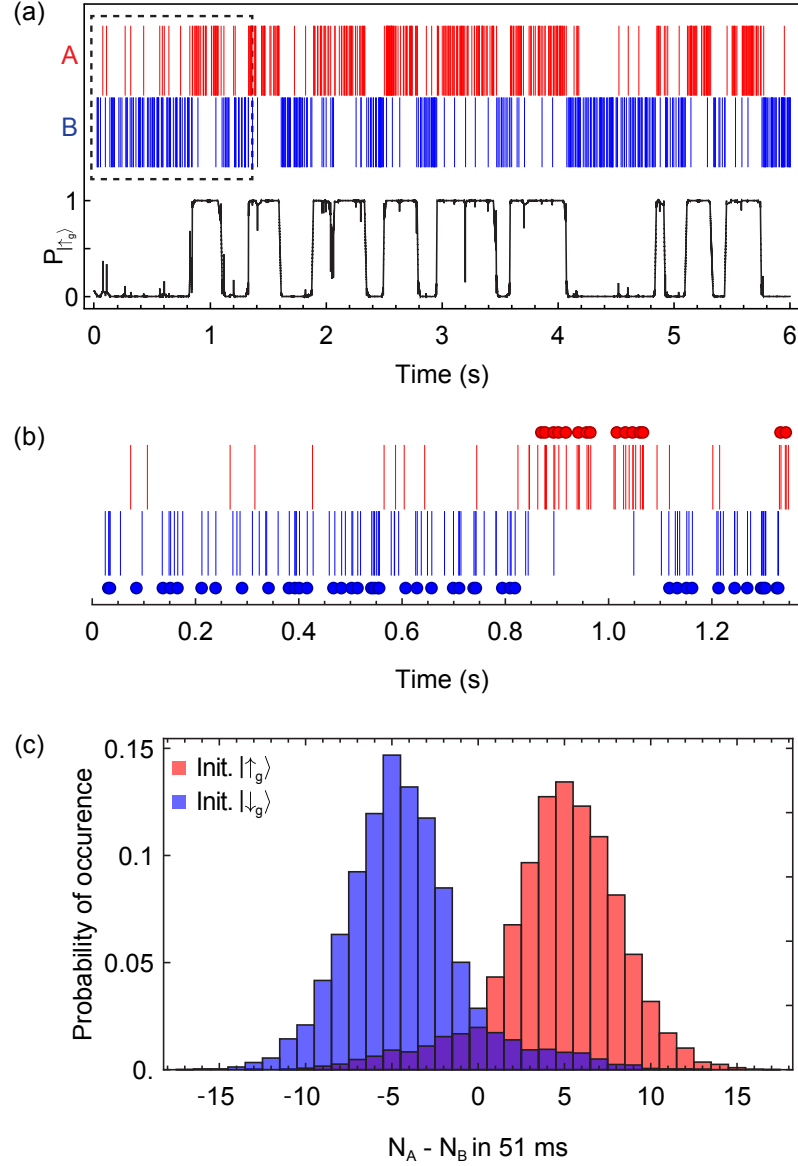


Figure 6.5: **Quantum nondemolition spin measurement.** (a) Photons detected during a single run of the experiment using the sequence in Figure 6.3a. The black curve shows the probability to be in $|\uparrow_g\rangle$ inferred from a Bayesian analysis, revealing quantum jumps between the spin states induced by optical pumping. (b) An adaptive maximum likelihood (ML) algorithm is used to perform successive single-shot spin measurements, with the result of each, independent measurement indicated by a circle [data from dashed box in (a)]. (c) Histogram of photon counts for a fixed integration window of 51 ms following initialization using a ML measurement. The horizontal axis is the difference between the number of A and B photons detected in the measurement window.

The measurement duration is adaptive: each measurement terminates when a set fidelity threshold or time limit is reached, and a new, independent measurement is begun [114]. The outcome of each measurement is shown by the circles in Figure 6.5b. The average measurement fidelity estimated by the ML algorithm is 94.6%, and 91% of consecutive measurements have the same outcome. The average time to complete a measurement is 20 ms, which corresponds to the average time to detect two photons. The optimum fixed measurement window is 51 sms, resulting in a slower measurement with a lower average fidelity of 91.1% (Figure 6.5c).

6.5 Single Er^{3+} spin dynamics

Lastly, we apply these spin measurement techniques to investigate the ground state spin dynamics. We infer the intrinsic spin relaxation rate $T_{1,\text{dark}}$ by reducing the optical excitation rate $1/t_{\text{rep}}$ until the total spin lifetime $T_1 = 1/(T_{1,\text{dark}}^{-1} + T_{1,\text{op}}^{-1})$, measured via $g^{(2)}$, saturates (Figure 6.6a). $T_{1,\text{op}} = Ct_{\text{rep}}/P_{\text{ex}}$ is the optical pumping time. $T_{1,\text{dark}}$ increases with increasing magnetic field strength, in a manner that starkly diverges from the expected B^{-4} behavior of spin-lattice relaxation (Figure 6.6b)[112]. One possible explanation is flip-flop interactions with nearby Er^{3+} ions [115], which is consistent with the fact that $T_{1,\text{dark}}$ varies sharply with the magnetic field angle and is different by a factor of 20 between three ions studied (Appendix B.6). In this device, the average separation between magnetically equivalent Er^{3+} ions is estimated to be 70 nm, such that the dipole-dipole interaction strength is around 1 kHz; the flip-flop rate is likely much slower because of spectral diffusion from nearby ^{89}Y nuclear spins.

In Figure 6.6c, we use single-shot spin measurements to directly measure $T_{1,\text{dark}} = 45 \pm 4$ s in a different ion. This is the longest electronic spin T_1 measured for Er^{3+} , to the best of our knowledge [53]. In Figure 6.6d, we demonstrate high-visibility Rabi

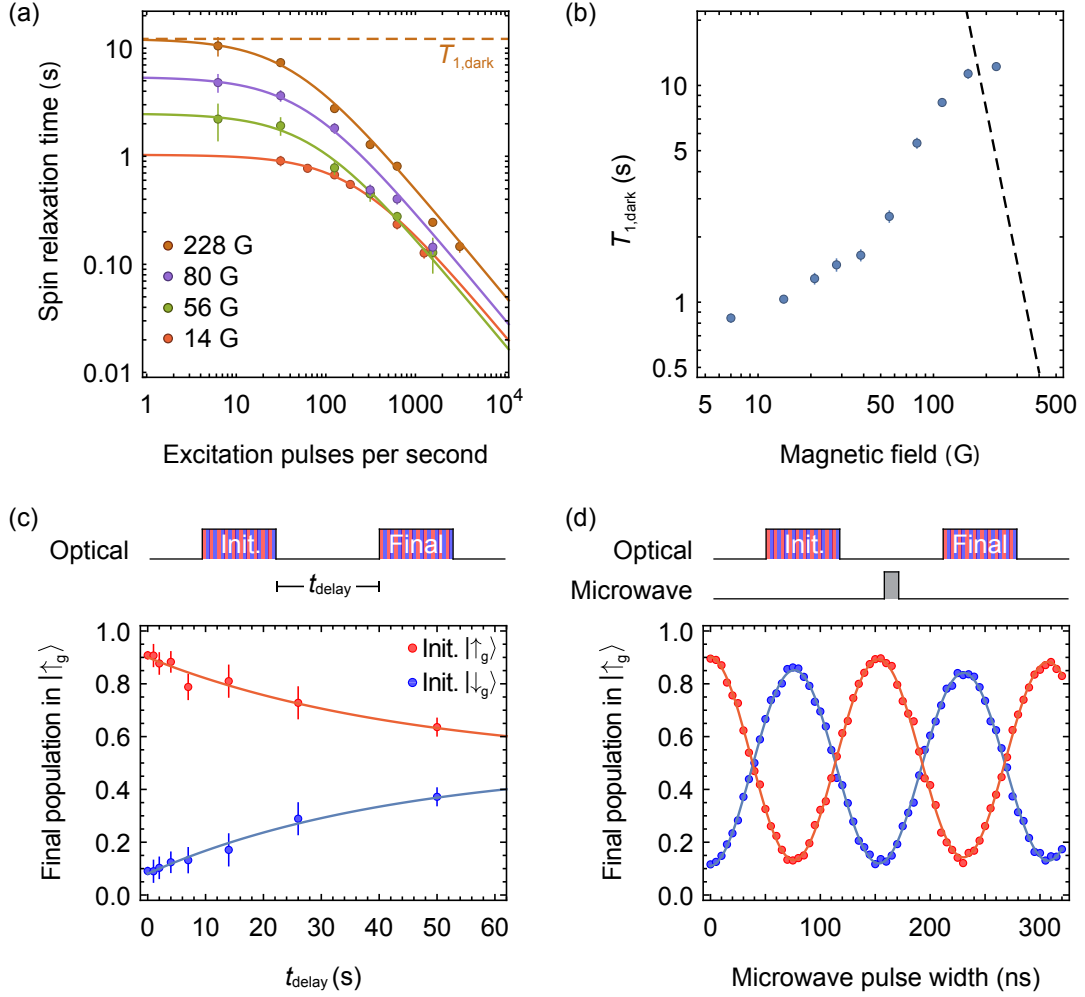


Figure 6.6: **Spin dynamics of a single Er^{3+} ion.** (a) Spin relaxation times measured at varying repetition rates of the pulse sequence for several magnetic field amplitudes $[(\varphi, \theta) = (100, 90)^\circ]$. At low excitation rates, the spin relaxation time becomes independent of the optical excitation rate, revealing an intrinsic relaxation time $T_{1,\text{dark}}$. (b) $T_{1,\text{dark}}$ varies strongly with the amplitude of the magnetic field. The dashed line indicates the expected spin-lattice relaxation rate (Appendix B.6) [97]. (c) Using a single-shot projective measurement to initialize the spin, we can directly measure $T_{1,\text{dark}}$. This experiment is performed on a different ion (ion 3) at 112 G, where $T_{1,\text{dark}} = 45 \pm 4$ s is roughly five times longer than in the ion used in panels (a,b). (d) Rabi oscillations can be observed between the two states using a microwave pulse of variable length ($f_{\text{MW}} = 1.76$ GHz for $B = 112$ G). In panels (c,d), the contrast is consistent with a measurement fidelity of $\sim 95\%$ for this ion, which enters twice through the initial and final measurements.

oscillations between the ground state spin sublevels, driven by a microwave magnetic field applied through a coplanar waveguide. We measure $T_2^* = 125 \pm 5$ ns (in a Ramsey experiment), and $T_2 = 3.3 \pm 0.2$ μ s (Hahn echo), consistent with previous measurements of electron spin coherence in solid-state hosts with abundant nuclear spins [60, 116]. Longer coherence times to enable storage of quantum states and the observation of coherent dynamics between interacting Er³⁺ ions may be achieved using dynamical decoupling (Figure C.5). Ultimately, it will be beneficial to use alternative host crystals with lower nuclear spin content; Er³⁺ incorporation has been demonstrated in several candidates including CaWO₄, Si and TiO₂ [117].

6.6 Conclusion and outlook

Our results demonstrate that the optical properties of atomic systems are malleable through control of their local environment. Using a photonic nanostructure, we have achieved more than two orders of magnitude improvement in the emission rate and cyclicity of a single Er³⁺ ion, and demonstrated single-shot readout of its spin. Realistic improvements in the quality factor of the optical cavity and photon collection efficiency η will enable another 20-fold enhancement in emission rate and spin readout with $F > 0.99$ in 50 μ s ($Q = 10^6$ and $\eta = 0.2$; see Appendix B.5). These results represent a significant step towards realizing quantum networks based on single Er³⁺ ions. This measurement approach may also be extended to address many closely-spaced Er³⁺ spins in the same device by exploiting small differences in their optical transition frequencies, providing a foundation for studying strongly interacting spin systems. Finally, this technique will enable a much broader class of atomic defects to be explored for quantum technologies.

Chapter 7

Parallel single-shot measurement and coherent control of solid-state spins below the diffraction limit

The realization of larger-scale quantum systems with solid-state defects will require high-fidelity control over multiple defects with nanoscale separations, with strong spin-spin interactions for multi-qubit logic operations and the creation of entangled states. In this chapter, we demonstrate an optical frequency-domain multiplexing technique, allowing high-fidelity initialization and single-shot spin measurement of six rare earth (Er^{3+}) ions, within the sub-wavelength volume of a single, silicon photonic crystal cavity. We also demonstrate sub-wavelength control over coherent spin rotations using an optical AC Stark shift. Our approach may be scaled to large numbers of ions with arbitrarily small separation, and is a step towards realizing strongly interacting atomic defect ensembles with applications to quantum information processing and fundamental studies of many-body dynamics. Results presented in this chapter are published in Ref. [33].

7.1 Introduction

A central appeal of solid-state atomic defects for quantum technology is the possibility to realize strong dipolar interactions between closely spaced spins [118]. This coupling enables multi-qubit logic operations (to realize, for example, error correction [105, 119] or deterministic teleportation over a quantum network [17]) as well as fundamental studies of many-body quantum phenomena [120]. Typically, these interactions are appreciable for defect separations less than several tens of nanometers. However, for optically-addressed spins, it is an open challenge to achieve simultaneous, high-fidelity initialization, control, and readout of spins separated by less than the diffraction limit of the addressing light, typically several hundred nanometers. Several techniques have been demonstrated to simultaneously address pairs of closely spaced NV centers, such as super-resolution microscopy [121], and variations in the Larmor frequency arising from different defect orientations [122, 123] or magnetic field gradients [124]; however, these approaches have not been extended to high-fidelity operations such as single-shot spin readout, or to larger numbers of defects. Alternatively, an array of nuclear spins surrounding a single atomic defect can be distinguished by their positions in the gradient of the hyperfine coupling [125, 126, 127]; while this approach has been used to generate entanglement between as many as 10 spins [30], it suffers from the bottleneck that all operations are performed through a single, central electron spin.

Rare earth ions (REIs) in solid-state hosts are a promising platform for many applications because of their demonstrated long coherence times (for example, exceeding 6 hours for Eu^{3+} [39]) as well as operation in the telecom band and compatibility with silicon photonics (in the case of Er^{3+} [31]). Furthermore, their unique spectral characteristics enable frequency-domain addressing of many defects within the same spatial volume. REIs experience random, static shifts of their optical transition frequencies that give rise to an inhomogeneous (ensemble) linewidth Γ_{inh} (typically 1-10 GHz in crystalline hosts) that is much broader than the homogeneous

linewidth of an individual ion Γ_h (typically < 1 MHz). In a given sample volume, this allows a large number of distinct subsets of ions to be separately addressed, of order $N_{ad} \approx \Gamma_{inh}/\Gamma_h > 10^3$. This approach can be applied to any solid-state emitter, in principle, but the uniquely small magnitude of Γ_{inh} and Γ_h in REIs allows the entire inhomogeneous distribution to be addressed with electro-optic sidebands on a single laser. Using spectral hole burning, this effect has been exploited in rare earth ensembles to realize multimode atomic memories for quantum networks [28, 29]. Quantum gate architectures based on ensemble spectral-hole qubits have also been proposed [128, 129, 130, 131] and demonstrated [132, 133, 99].

7.2 Experimental approach

Frequency-domain addressing can also be used to address individual REIs within a diffraction-limited volume, if the total number of ions N is less than N_{ad} . While detecting individual REIs is challenging due to their low photon emission rates, this problem can be overcome using Purcell enhancement in nanophotonic optical cavities [31, 108], as exemplified by recent demonstrations of single-shot spin readout of single REIs [32, 134]. We combine frequency-domain addressing and high fidelity optical control to realize initialization and single-shot spin readout of six Er^{3+} spins with sub-micron separations, coupled to a single photonic crystal cavity.

Our experimental approach consists of an Er^{3+} -doped Y_2SiO_5 (YSO) crystal coupled to a silicon photonic crystal cavity (Figure 7.1a). Among rare earth ions, Er^{3+} is attractive for its telecom-wavelength optical transition and potential application to quantum networks. The cavity enhances the emission rate of the ions [31], and modifies the selection rules to make the optical transitions highly cyclic, enabling single-shot spin readout [32]. The zero-field photoluminescence excitation (PLE) spectrum (Figure 7.1b) shows several hundred ions within the $0.05 \mu\text{m}^3$ mode volume

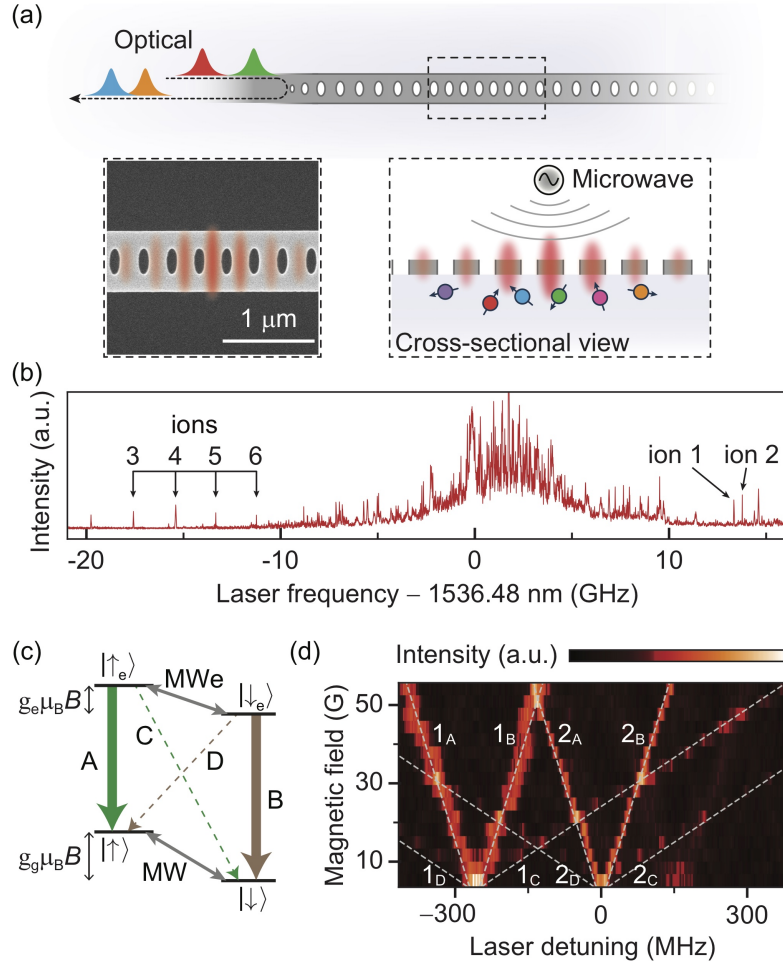


Figure 7.1: Spectrally addressing multiple ions in a diffraction-limited volume. (a) Schematic drawing of the device, showing multiple ions with different transition frequencies (colors) coupled to the cavity. (inset) Scanning electron microscope image of a representative cavity, showing the extent of the optical mode. (b) PLE spectrum of Er^{3+} ions in a single device with magnetic field $B = 0$. Arrows indicate the six ions used in this work. (c) Level structure of $\text{Er}^{3+}:\text{YSO}$ in a magnetic field, with optical (A-D) and microwave (MW, MWe) transitions indicated. g_g (g_e) denotes the ground (excited) state magnetic g -factor. (d) PLE spectrum of ion 1 and ion 2 in the presence of a magnetic field (oriented along the D_2 axis of the YSO crystal). ($1_A, 1_B$) and ($2_A, 2_B$) correspond to the spin-conserving optical transitions (A,B) of the two ions, respectively. Zero detuning in this panel and subsequent figures refers to the ion 2 resonance when $B = 0$.

of the optical cavity, with an inhomogeneous linewidth of several GHz. We first focus on a pair of ions located in the blue tail of the inhomogeneous distribution, labeled

ion 1 and ion 2, which couple to the cavity with Purcell factors of 330 and 200, respectively, when resonant with the cavity. Because the ions are addressed through a single-mode cavity, the optical signal provides no spatial information about the ions: they are, by definition, within a single, diffraction-limited volume. Instead, the ions are addressed in the frequency domain, relying on a separation between their transitions of approximately 250 MHz, which is considerably larger than their linewidths (24 and 10 MHz) but smaller than the cavity linewidth of 4.2 GHz. In a magnetic field, each ion’s optical transition splits into four lines that can be used to interface with its spin (Figure 7.1,cd).

7.3 Parallel initialization and readout of two ions

First, we demonstrate simultaneous initialization and single-shot spin measurement of ion 1 and ion 2. The measurement relies on cavity-enhanced cyclicity of the optical transitions, which is controlled by the alignment of the magnetic field to the local cavity polarization [32]. A magnetic field orientation of $[(\theta, \varphi) = (90, 150)^\circ]$ allows high cyclicity for both ions (Figure 7.2a), indicating similar cavity polarization at their respective positions. We initialize the spins by optical pumping, driving the excited state spin transition with microwaves to mix the spin levels (Figure 7.2,bc) [134, 135]. Then, we perform a simultaneous single-shot spin measurement by alternately exciting the spin-conserving optical transitions (A,B) on each ion. For both initialization and measurement, the laser frequency is rapidly switched between transitions using a sideband from a fiber-coupled electro-optic modulator. We infer an initialization fidelity of $\geq 95\%$, 97% (Appendix C.2) and an average readout fidelity of 76%, 88% (Figure 7.2d) for ion 1 and ion 2, respectively. The ions’ spins can be coherently manipulated using microwave pulses that address both ions equally (Figure 7.2e), since the disorder in the Larmor frequency is much smaller than that of the optical

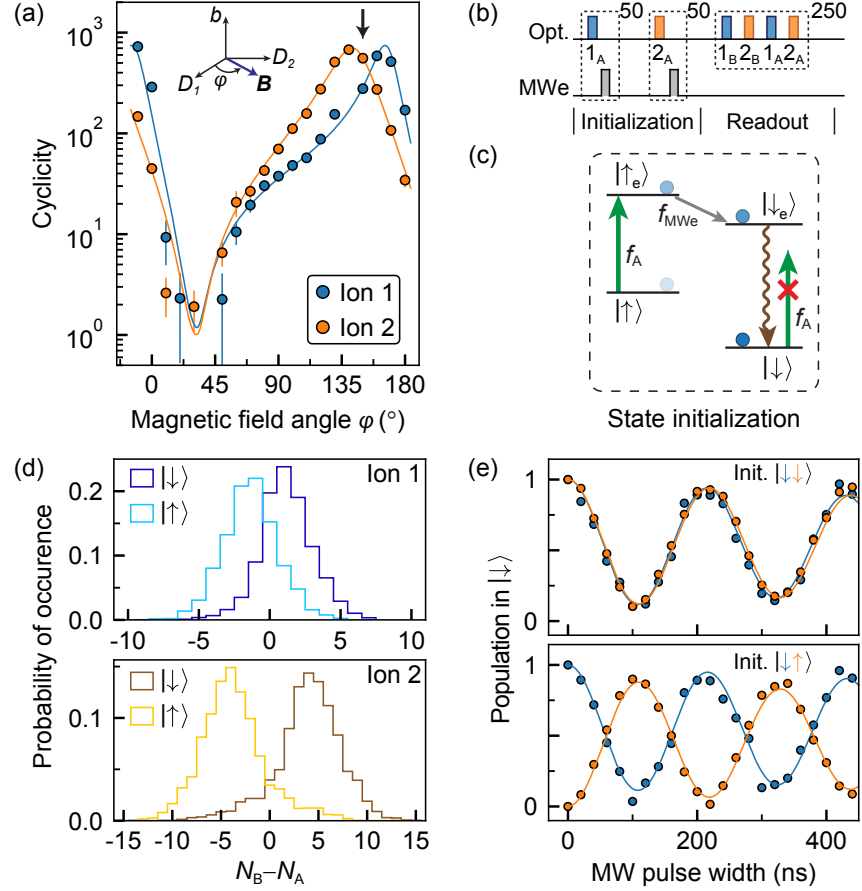


Figure 7.2: **Simultaneous initialization and readout of ions 1 and 2.** (a) Cyclicity of the optical transitions (defined as $1 + \Gamma_{A,B}/\Gamma_{C,D}$, where Γ_i is the Purcell-enhanced decay rate on transition i) as a function of magnetic field angle (see inset). The solid lines are fits to a theoretical model from Ref. [32] and the black arrow indicates the orientation used in subsequent experiments ($\varphi = 150^\circ$). (b) Pulse scheme used for spin initialization (in this case, to $|\downarrow\rangle$) and readout. Superscripts represent the number of repetitions of the pulses. All optical and microwave pulses are π pulses. (c) Diagram of the initialization sequence. A dark state emerges in $|\downarrow\rangle$ from the combination of optical excitation of the spin-conserving A transition and microwave driving of the excited-state spin. Exciting B instead will initialize the spin to $|\uparrow\rangle$. (d) Photon histograms showing simultaneous single-shot readout for both ions. The ions are probed alternately on their A and B transitions, and $N_B - N_A$ denotes the difference in detected counts. $N_B > N_A$ indicates that the spin state is $|\downarrow\rangle$. (e) Simultaneous Rabi oscillations are observed while driving the ground state spin of both ions with a microwave pulse after initialization into the indicated states. The vertical axes is corrected for initialization and readout fidelity.

transition. Details about the spin lifetime and coherence times can be found in Appendix 7.

7.4 Sub-wavelength control over coherent spin rotations using the optical AC Stark shift

Next, we turn to demonstrating individually addressed spin manipulations. To achieve this, we utilize the AC Stark shift from a detuned optical pulse to induce a net phase shift ϕ between $|\uparrow\rangle$ and $|\downarrow\rangle$ [136]. The optical pulses are inserted into an XY8 sequence that mitigates low-frequency magnetic field noise during the phase accumulation time. For each ion, the accumulated phase shift is $\phi = T\Omega^2 (\Delta_B^{-1} - \Delta_A^{-1}) / 4$, where T is the pulse duration, Ω is the optical Rabi frequency and Δ_A , Δ_B are the detunings of the laser from the spin-conserving transitions A, B (Figure 7.3a, inset). For a given laser frequency and intensity, the detuning and Rabi frequency are different for each ion, enabling local control of the phase shift. To control N ions, $N - 1$ laser frequencies are needed, since microwave rotations provide an additional control axis (Appendix C.6). Here, with $N = 2$, we can control both ions independently using a single laser frequency. In addition to the phase shift, there is also a loss of coherence from photon scattering and fluctuations in the optical transition frequency (*e.g.*, from spectral diffusion), which happens at a rate $\Gamma' \propto \Gamma\Omega^2 (\Delta_A^{-2} + \Delta_B^{-2})$, where Γ is the effective transition linewidth (Appendix C.4.2).

We measure the optically induced phase shift and decoherence using Ramsey spectroscopy, where the decoherence manifests as a change in visibility (Figure 7.3a). To select the optimum operational point, we characterize the phase shift and decoherence as a function of laser frequency (Figure 7.3b). The results are in good agreement with a theoretical model. The ratio of phase shift to decoherence is optimized for large detunings, and we predict a 2.55% loss of visibility per radian of differential phase

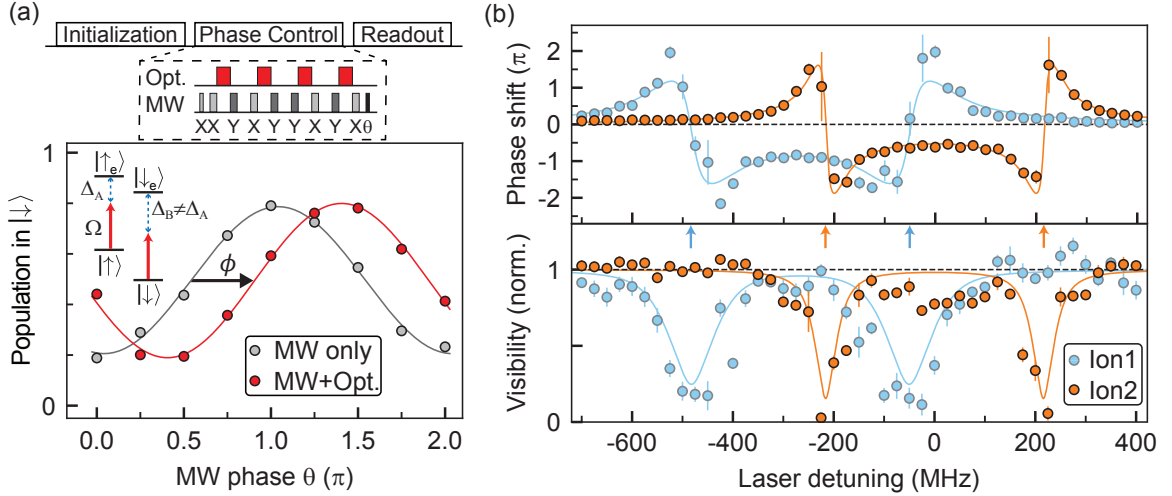


Figure 7.3: Coherent optical spin rotation using the AC Stark shift.

(a)(upper) Optical phase shifts are generated using a sequence of detuned optical pulses interleaved with a microwave-driven XY8 decoupling sequence. **(lower)** The phase shift is detected by varying the phase of the final microwave $\pi/2$ pulse before measuring the spin population. The phase shift (ϕ) and visibility are extracted from a sinusoidal fit. **(b)** Frequency dependence of the phase shift and change in visibility for each ion after a $2 \mu\text{s}$ optical pulse. The solid lines are numerical simulations including spectral diffusion. The arrows indicate the frequencies of the A,B transitions for each ion.

shift $\Delta\phi = \phi_2 - \phi_1$ at 350 MHz detuning. In this regime, the experimental loss of visibility over a $\pi/2$ phase shift is below our measurement resolution.

In combination with a global microwave rotation $R_z(-\phi_1)$, the differential phase $\Delta\phi$ gives rise to a net rotation on ion 2 alone: $R_z^{(2)}(\Delta\phi) = \mathbb{I} \otimes R_z(\Delta\phi)$ (Figure 7.4a). Similarly, a global microwave rotation $R_z(-\phi_2)$ generates a rotation on ion 1 alone. Here, $R_{\hat{n}}(\alpha)$ denotes a rotation by an angle α about axis \hat{n} . Universal control of a single qubit requires arbitrary angle rotations around two orthogonal axes. However, global microwave rotations can transform ion-selective optical z rotations into rotations around an arbitrary axis (Appendix C.4.3). As an example, we demonstrate rotations about the x axis, $R_x^{(i)}(\Delta\phi)$, where $i = 1, 2$ denotes the target ion (Figure 7.4,ab), realizing more than 2π rotation as the optical pulse duration is varied.

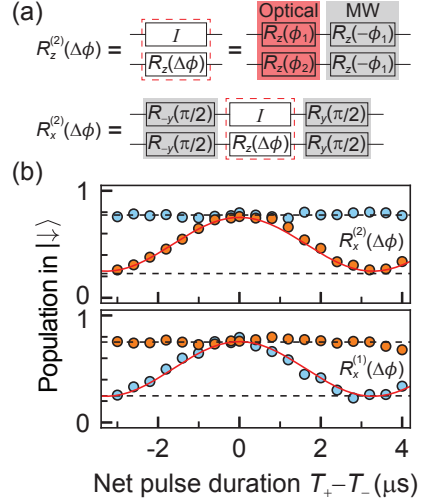


Figure 7.4: **Ion-selective rotations.** (a) Circuit diagram for implementing $R_{z,x}^{(i)}(\Delta\phi)$ rotations. (b) Ion-selective Rabi oscillations $R_x^{(i)}(\Delta\phi)$. Positive (negative) phase shifts are generated by placing optical pulses after the odd (even) numbered π pulses in the XY8 sequence, with total duration T_+ (T_-) (the laser detuning is 275 MHz with respect to Figure 7.3b). The dashed lines show the loss of contrast from dephasing measured in the absence of any optical pulses – excess dephasing from the optical pulses is not observable.

7.5 Parallel initialization and readout of two ions

Lastly, we extend our approach to demonstrate simultaneous spin initialization and readout with four additional ions, labeled ion 3 through ion 6 (Figure 7.1b). To access them, we shift the cavity resonance to -14.8 GHz (with respect to Figure 7.1b), resulting in Purcell factors of 130, 260, 360, and 50. After choosing a magnetic field orientation that allows high cyclicity for all ions (Appendix C.5), we perform single-shot readout measurements. Because of the larger spread of these ions' frequencies (6.4 GHz) with respect to the cavity linewidth, it is advantageous to perform the readout using only one of the A or B transitions for each ion, whichever has larger Purcell enhancement (Figure 7.5a). The average readout fidelities for each ion are 80%, 74%, 87%, and 71%, respectively (Figure 7.5b). The mean readout fidelity of the four-ion set is 78%, which is slightly lower than the two-ion set of 82%, because

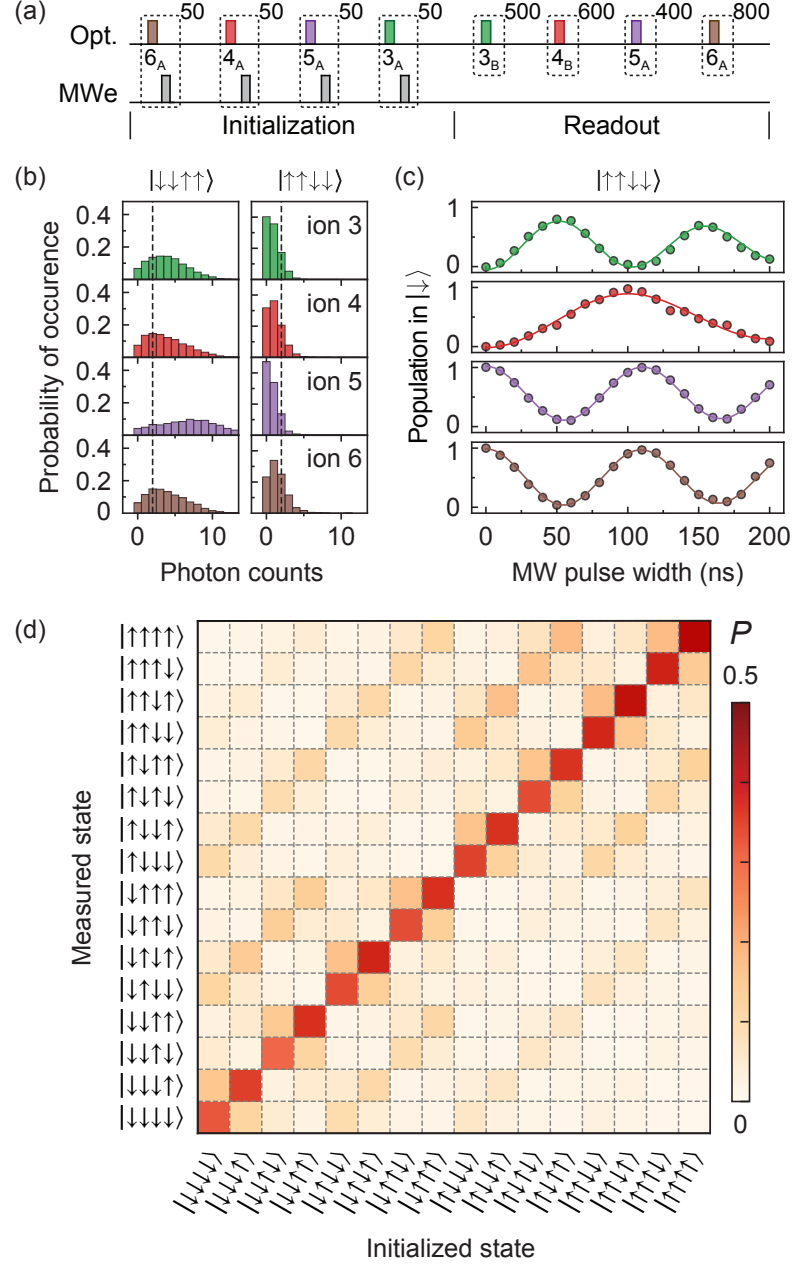


Figure 7.5: Simultaneous initialization and readout of ions 3 – 6. (a) Pulse sequence for initialization and readout. (b) Histograms of detected photon counts for different initial states. The dashed lines indicate the threshold used for state discrimination. The spin state giving rise to higher counts depends on which transition is used for readout, which differs between ions. (c) Simultaneous microwave Rabi oscillations of all ions after being initialized to $|\uparrow\uparrow\downarrow\downarrow\rangle$. (d) Single-shot readout results for all 16 four-ion initial states. The average probability to obtain the correct state for all four ions is $\bar{P} = 0.37$.

of the low Purcell factor of ion 6. Although the ions are measured sequentially, the total measurement duration (300 ms) is much shorter than the ground state spin T_1 (typically > 10 s; Appendix C.3), such that the measurements are effectively simultaneous.

In Figure 7.5c, we show simultaneous microwave-driven Rabi oscillations on all four ions after initializing into $|\uparrow\uparrow\downarrow\downarrow\rangle$. Because ion 4 is situated in a rotated crystallographic site from the other ions, it has a different coupling to the microwave waveguide and correspondingly different Rabi frequency. In this measurement, the static field B lies in the $D_1 - D_2$ plane such that all ions have the same Larmor frequency, but we note that rotating B out of this plane would make the ion 4 Larmor frequency different, enabling spectral addressing of its microwave transition. In Figure 7.5d, we show the initialization and single-shot measurement outcomes for all 16 four-spin states.

7.6 Conclusion and outlook

We have demonstrated simultaneous frequency-domain addressing of multiple Er^{3+} spins within a diffraction-limited volume, realizing a complete set of operations: initialization, coherent control, and single-shot spin measurement. This is a step towards two applications. First, combined with realistic improvements in optical and spin coherence enabling indistinguishable single-photon emission and long-term quantum memories (using host crystals with higher site symmetry [134] and lower nuclear spin content [117]), this work may lead to frequency-multiplexed quantum repeaters with significantly faster entanglement generation rates. Second, this approach enables probing and manipulating single defects within dense, strongly interacting ensembles. The creation of these ensembles is within reach using ion implantation: $N \approx 20$ ions implanted into a $(30 \text{ nm})^3$ volume would have a typical

separation of 11 nm, corresponding to a magnetic dipolar interaction strength of 1 MHz (given the large magnetic moment in Er³⁺), faster than the decoherence rate of the ground state spin with dynamical decoupling (Figure C.5).

Chapter 8

Coherent interactions between a single rare-earth ion and a nuclear spin in the solid-state

Among optically interfaced solid-state defects, single Er^{3+} ions in the solid are particularly attractive for their emission in the telecom band and compatibility with silicon photonics. In this chapter, we observe coherent interactions between an Er^{3+} electronic spin and a nearby nuclear spin, where the latter is situated in the spin bath surrounding the electronic spin. We isolate the interaction by using microwave-driven, dynamical decoupling pulses on the electronic spin. This lets us construct single-qubit and two-qubit gates, which we utilize to study the coherent dynamics of the nuclear spin and identify its location with respect to the electron spin. Furthermore, we utilize the gates developed above to probe the nuclear spin bath. These results provide a pathway towards combining a long-lived quantum register to a telecom-compatible quantum memory for future quantum repeater-based quantum network applications. Results presented in this chapter are part of an ongoing investigation and will appear in Ref. [34].

8.1 Introduction

Solid-state spins with optical addressability are emerging candidates for realizing quantum technologies. They offer the potential of scaling to large numbers [137] while featuring efficient optical access for easy manipulation and distribution of quantum states [100]. Typically, optical transitions arise from atomic transitions between electronic spin levels. However, preserving quantum information in electronic spins is often challenging as they are prone to loss of coherence due to magnetic noise originating from background spins. Nuclear spins, on the other hand, by virtue of their much smaller gyromagnetic ratio than electronic spins, are less susceptible to fluctuating magnetic fields. Moreover, these spins are less perturbed by optical excitations delivered to the system. Consequently, nuclear spins are posed as ideal candidates for long-lived quantum memories. The lack of optical access is a major hindrance however. An effective work-around is to envision a hybrid register of electronic spins coupled to a few nuclear spins where the electronic spin provides the optical access while the coherent interaction helps with storage and retrieval of quantum information. This approach has been thoroughly exploited with NV⁻ centers in diamond, where weak (or strong) interactions between NV electronic spin and distant (or nearby) nuclear spins have been utilized to realize long-lived quantum registers [138, 139], distribute entangled states across a quantum network [17, 18, 19], perform quantum error-correction tasks [105, 119, 140], and build a multi-qubit quantum register [30].

Rare-earth ions (REIs)-in-solids are an emerging platform for quantum technologies as they offer demonstratively long coherence times (6 hours for Eu³⁺ [39]) and telecom-compatible optical transitions (for Er³⁺), of whom the latter is particularly interesting as it offers compatibility with silicon photonics and a potential to directly achieve long-distance quantum networks without any optical frequency conversion. Detection, control, and readout of individual Er³⁺ spins are performed by integrating

these ions in a silicon photonic crystal (PC) cavity to overcome their poor photon emission rate [31, 32]. REIs are often available as dopants in yttrium-based host materials (YSO, YVO, YAG, YLiF₄, and Y₂O₃) that generally feature ensemble of nuclear spins in the bath. However, individual nuclear spins (⁸⁹Y, ²⁹Si) were detected only recently using Ce³⁺:YSO [141], but coherent rotations of the nuclear spins have not been demonstrated yet.

In this work, we demonstrate coherent coupling of an Er³⁺ electronic spin ($S = 1/2$) to a nearby nuclear spin. We realize this by using microwave-driven, dynamical decoupling (DD) sequences on the electronic spin. We use similar DD sequences to implement single-qubit and two-qubit gates that let us probe the coherent dynamics of the nuclear spin. Based on hyperfine parameters at a few different magnetic field configuration, we identify the nuclear spin to be consistent with a ¹H spin at a particular location. These results lend additional capabilities to our platform by associating a long-lived quantum register to Er³⁺ spins, which in the current host substrate, suffer from poor spin coherence properties (spin $T_2^* = 125$ ns; Section 6.5 and Section C.3).

8.2 Detection and coherent control of a nearby nuclear spin

Our experimental platform consists of Er³⁺ ions embedded in a Y₂SiO₅ (YSO) host matrix and situated in a bath of nuclear spins (Figure 8.1a). Single Er³⁺ electronic spins are addressed by a combination of optical and microwave excitations to perform state initialization, control, and single-shot readout (Figure 8.1c)[32, 33]. We probe the electronic spin-bath by performing microwave-driven dynamical decoupling sequences (XY- $N := (\tau - \pi - \tau)^N$) on the Er³⁺ spin while varying the inter-pulse separation 2τ . On top of the extended population decay ($T_{2,\text{XY16}} = 16.1 \pm 0.2 \mu\text{s}$), we observe a sharp resonance at $2\tau_0 = 0.875 \mu\text{s}$ (Figure 8.1d). At the resonance,

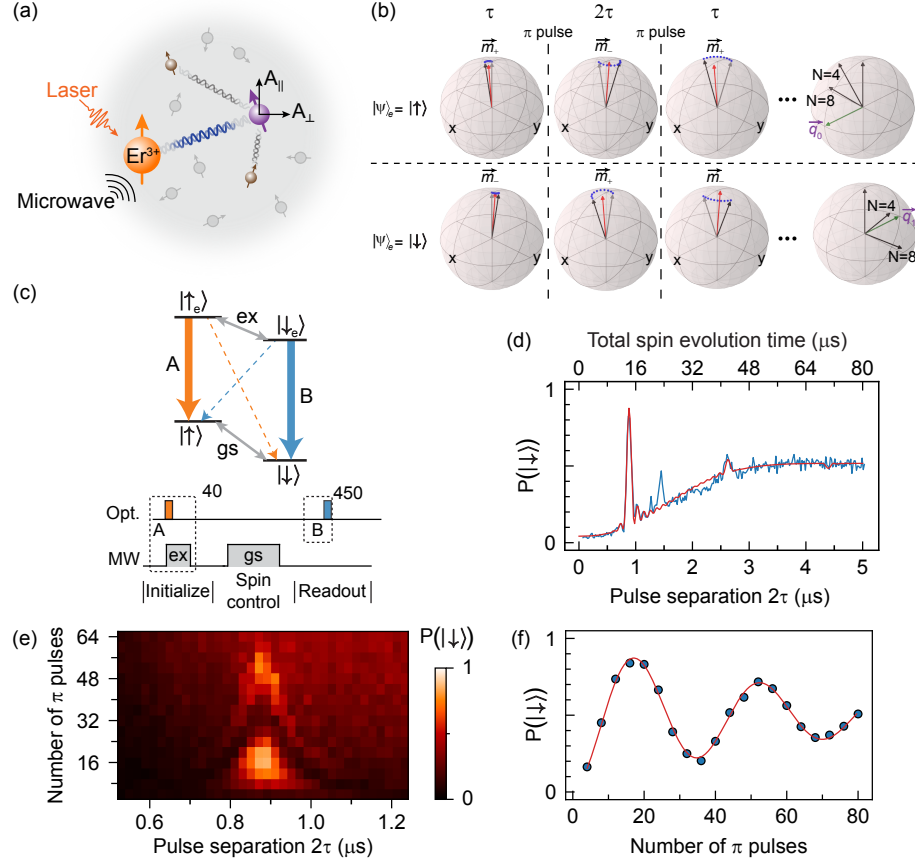


Figure 8.1: Detection and coherent control of weakly-coupled nuclear spins using an Er^{3+} electronic spin. (a) Measurement scheme. A single Er^{3+} spin, which is initialized, controlled, and readout via a combination of optical and microwave excitations, probes a nearby nuclear spin, which additionally may also weakly couple to other (“dark”) spins in its spin bath. (b) Conditional evolution of a nuclear spin based on the Er^{3+} electronic spin state for one unit ($\tau - \pi - 2\tau - \pi - \tau$) of our decoupling sequence. Repeating this unit leads to a conditional x -rotation of the nuclear spin. (c) (top) Er^{3+} level structure; (bottom) Pulse scheme for initialization and single-shot readout of Er^{3+} spin state. (d) Evolution of an Er^{3+} spin under an XY-16 sequence as the separation between consecutive π -pulses (2τ) is varied. (e) The Er^{3+} spin population is plotted as a function of 2τ and number of π -pulses (N) in the XY- N sequence near the resonance centered at $2\tau_0 = 0.875 \mu\text{s}$. The “chevron” interference pattern originates from coherent interaction between the Er^{3+} spin and a nuclear spin (f) Coherent controlled rotation of the nuclear spin as a function of N at the 2τ resonance position. All experiments were performed at the magnetic field configuration $(B, \theta, \phi) = (130 \text{ G}, 95^\circ, 110^\circ)$.

varying the number of π pulses N in the XY- N sequence yields coherent oscillations of the Er³⁺ spin population (Figure 8.1f). We attribute these features to a coherent interaction between the Er³⁺ electronic spin and a nuclear spin.

To understand this phenomenon, we consider the interaction between an $S = 1/2$ electronic spin and a $I = 1/2$ nuclear spin in the rotating frame of the electronic spin under the secular approximation ($\hbar = 1$): $H = 2S_z(A_{||}I_z + A_{\perp}I_x) + \omega_L I_z$, where \mathbf{S} (\mathbf{I}) is the electron (nucleus) spin operator, $A_{||}$ and A_{\perp} are parallel and perpendicular hyperfine coupling parameters, and ω_L is the (bare) Larmor frequency of the nuclear spin. Rearranging terms in the Hamiltonian, it is evident that the nuclear spin precession is conditional on the Er³⁺ electronic spin state, governed by: $H = |\uparrow_g\rangle\langle\uparrow_g|\omega_+ \mathbf{I} \cdot \mathbf{m}_+ + |\downarrow_g\rangle\langle\downarrow_g|\omega_- \mathbf{I} \cdot \mathbf{m}_-$, where $\omega_{\pm} = \sqrt{(\omega_L \pm A_{||})^2 + A_{\perp}^2}$ and $\mathbf{m}_{\pm} = (\pm A_{\perp}, 0, \pm A_{||} + \omega_L)/\omega_{\pm}$ are the effective Larmor frequency and rotation axes of the nuclear spin, respectively.

In the strong magnetic field regime ($\omega_L \gg \sqrt{A_{||}^2 + A_{\perp}^2}$), ω_{\pm} and \mathbf{m}_{\pm} constitute only small deviations from free precession parameters, but the interaction can be harnessed using an XY sequence at the resonant condition $2\tau_0 = \pi/\omega_0$, where $\omega_0 = (\omega_+ + \omega_-)/2 \sim \omega_L$ such that $2\tau_0$ scales inversely with the magnetic field strength. When the rotation axis (\mathbf{m}_{\pm}) of the nuclear spin is resonantly toggled in an XY sequence (Figure 8.1b), the perpendicular hyperfine term A_{\perp} leads to an effective rotation of the nuclear spin around the $\pm x$ -axis conditional on the initial electronic state (Figure 8.1b). Thus, the total conditional evolution of the nuclear spin under an XY sequence can be written as: $U_{\text{XY-}N} = |\uparrow_g\rangle\langle\uparrow_g| R_x(N\alpha) + |\downarrow_g\rangle\langle\downarrow_g| R_x(-N\alpha)$, where $\alpha \sim 2A_{\perp}/\omega_L$ is the magnitude of rotation generated per π pulse (Figure 8.1f). Based on the extracted hyperfine parameters ($|A_{||}|, A_{\perp}, \omega_L$) = (19.4, 50.5, 567.4) kHz, which confirms the strong field regime, we conclude that XY-8 and XY-16 sequences approximately implement a conditional- $R_x(\pm\pi/2)$ and an unconditional- $R_x(\pi)$ gate on the nuclear spin, respectively.

8.3 Implementing nuclear spin gates

We use these gates to probe the coherence of the nuclear spin. Combined with single qubit rotations on the electronic spin, the conditional- $R_x(\pm\pi/2)$ gate is adapted to a C_nNOT_e gate, where the nuclear spin acts as a control for the electronic state. The control is along the x -axis, which is roughly perpendicular to the precession axes (\mathbf{m}_\pm), enabling us to probe the coherence of the nuclear spin via a Ramsey measurement. Inserting a π -pulse on the electron decouples the electronic spin, revealing an oscillation at a frequency of ω_0 (Figure 8.2a). $T_{2,\text{Hahn}}$ is extracted by inserting an unconditional- $R_x(\pi)$ gate on the nuclear spin during the Ramsey sequence, which is further extended upon repeated application of the $R_x(\pi)$ in a CPMG sequence (Figure 8.2b).

A SWAP gate can be implemented by combining conditional- $R_x(\pm\pi/2)$ rotations with single qubit rotations of the electronic spin and z -rotations of the nuclear spin (realized via its free precession) as shown in the circuit diagram in Figure 8.2c. We demonstrate SWAP operations by storing information in the nuclear spin and retrieving it (Figure 8.2c). The fidelity of a SWAP operation is 87%, which is limited by the interaction of the nuclear spin with other (“dark”) spins in the bath. In particular, the nuclear spin state survives Er^{3+} spin initialization and readout, which involve optical excitations to and spontaneous decay from the Er^{3+} excited state (lifetime $\sim 70 \mu\text{s}$). Although we haven’t directly measured it, we estimate the nuclear spin $T_1 > 2 \text{ s}$ from these measurement.

8.4 Identifying and locating the nuclear spin

The hyperfine parameters ($A_{||}$, A_\perp , ω_L) depend on the external magnetic field, the gyromagnetic ratio of the nuclear spin, and its relative position with respect to the electronic spin. In order to elucidate the origin of the nuclear spin, we perform a series

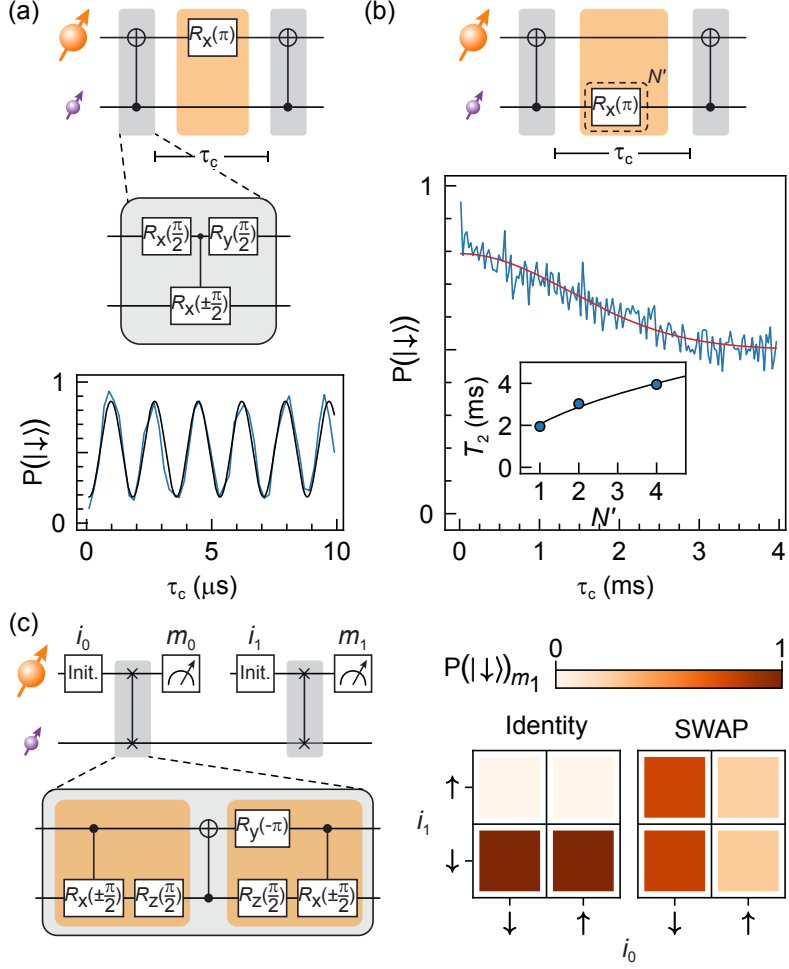


Figure 8.2: **Nuclear spin gates.** (a) Ramsey spectroscopy of the nuclear spin is performed by changing the delay τ_c between two $C_n NOT_e$ gates. Applying a π pulse on the electron at the halfway-point leads to an oscillation at $\omega_0 = (\omega_+ + \omega_-)/2$ (b) Applying a single $R_x(\pi)$ rotation between two $C_n NOT_e$ gates yields a $T_{2,\text{Hahn}} = 1.9 \pm 0.1$ ms for the nuclear spin, which can be extended to $T_{2,\text{CPMG}} = 3.9 \pm 0.2$ ms with repeated application of $R_x(\pi)$ (inset). (c) Demonstration of SWAP gate operations between the electronic and nuclear spin using the indicated circuit, where measurement at the m_1 register is plotted for various initialization sequences. The SWAP gate enters twice (storage and retrieval) with respect to an Identity gate. Extracted SWAP gate fidelity based on m_1 measurements is 87%.

of experiments at different magnetic field orientations. Based on the extracted ω_L , we infer a gyromagnetic ratio = 42.64 ± 0.39 kHz/G, which is consistent with ^1H nuclear spin (42.58 kHz/G). Independent Fourier-transform infrared spectroscopy (FTIR) of other YSO crystals (not used in this work) at cryogenic temperatures indicated the

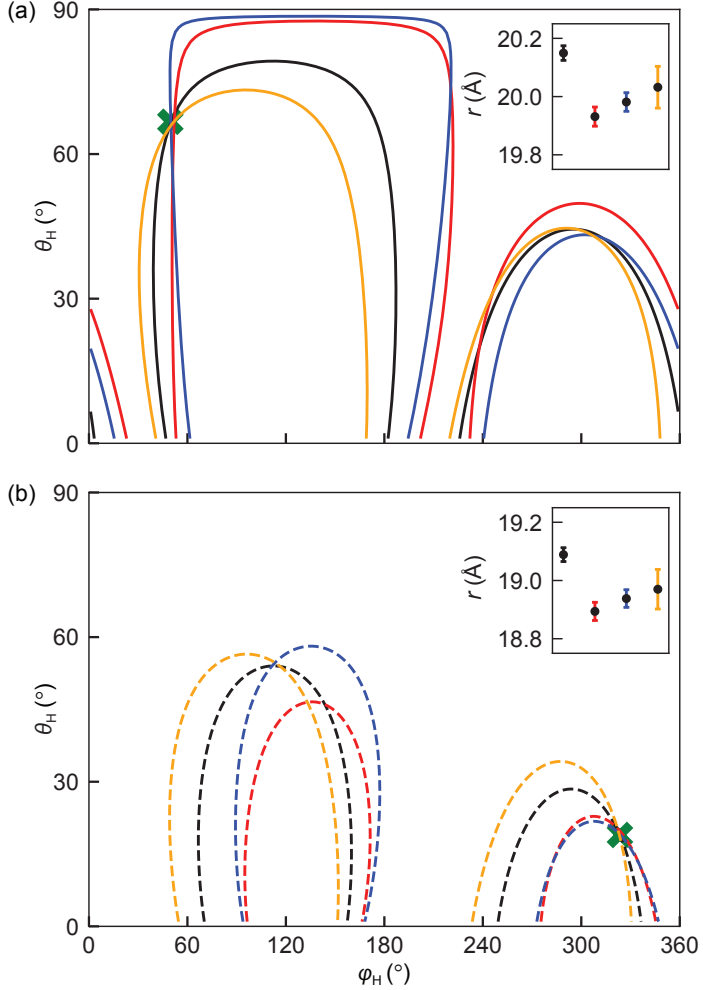


Figure 8.3: **Locating the nuclear spin.** $A_{||}/A_{\perp}$ contour plots, where each contour line (black, red, blue, orange) corresponds to nuclear spin positions (θ_H, ϕ_H) that satisfy measurements at magnetic field orientations $(\theta, \phi) = (95, 110), (95, 140), (85, 140), (100, 90)$ respectively. The intersection of the contour lines, marked by a green cross, represents a solution. Inset: Calculated distances for each orientation at the indicated solution along with error bars obtained from a Monte-Carlo simulation of measurement uncertainty. **(a)** Asserting $A_{||} > 0$ leads to a solution at $(r, \theta_H, \phi_H) = (20.0 \text{ \AA}, 66.7^\circ, 49.6^\circ)$. **(b)** Asserting $A_{||} < 0$ leads to a solution at $(r, \theta_H, \phi_H) = (19.0 \text{ \AA}, 19.0^\circ, 323.6^\circ)$.

presence of OH molecules as impurities, thus offering one possible reasoning behind the presence of ^1H within the YSO crystal; however, we have not performed similar FTIR measurements of our current YSO sample yet and we are currently exploring this avenue. To pinpoint the nuclear spin position based on extracted $(|A_{||}|, A_{\perp})$, we

first consider the ratio $A_{||}/A_{\perp}$ to determine the angular location (θ_H, ϕ_H) . For each field orientation, the extracted ratio is satisfied on a 1D manifold in the (θ_H, ϕ_H) plane so that the intersection of the manifolds reveals the angular location. At this angular location, the magnitude $\sqrt{A_{||}^2 + A_{\perp}^2}$ measured at each orientation yields the relative distance, r (Figure 8.3).

8.5 Probing the nuclear spin environment

Finally, we probe the nuclear spin environment using the Ramsey sequence as in Figure 8.2a with precession time extending up to 1 ms (Figure 8.4a). Fourier transform of the signal isolates four oscillation frequencies centered around ω_0 (Figure 8.4b). This might be consistent with the picture that the nuclear spin is coupled to two additional “dark” spins, d_1 and d_2 , with coupling strengths of 2 and 7 kHz, respectively. Telegraph signals that capture the nuclear spin state for repeated Ramsey experiments at two different precession times $(\tau_{c,1}, \tau_{c,2})$ clearly depict quantum jumps (Figure 8.4c). These jumps may be attributed to originate from the d_1 spin toggling between discrete states. These precession times are chosen in the following manner: at $\tau_c \approx (\tau_{c,1} + \tau_{c,2})/2$, the nuclear spin accumulates a relative π -phase conditional on the d_1 spin state, while $(\tau_{c,2} - \tau_{c,1}) = \pi/\omega_0$ ensures maximal population contrast. This manifests in the anti-correlated nature of quantum jumps at these two precession times (Figure 8.4d). We perform readout on d_1 spin (Figure 8.4c,d), and extract an average readout fidelity of 98% for d_1 . Compiling a histogram of the jump-duration lets us extract a spin lifetime of 5.19 ± 0.55 mins for d_1 spin.

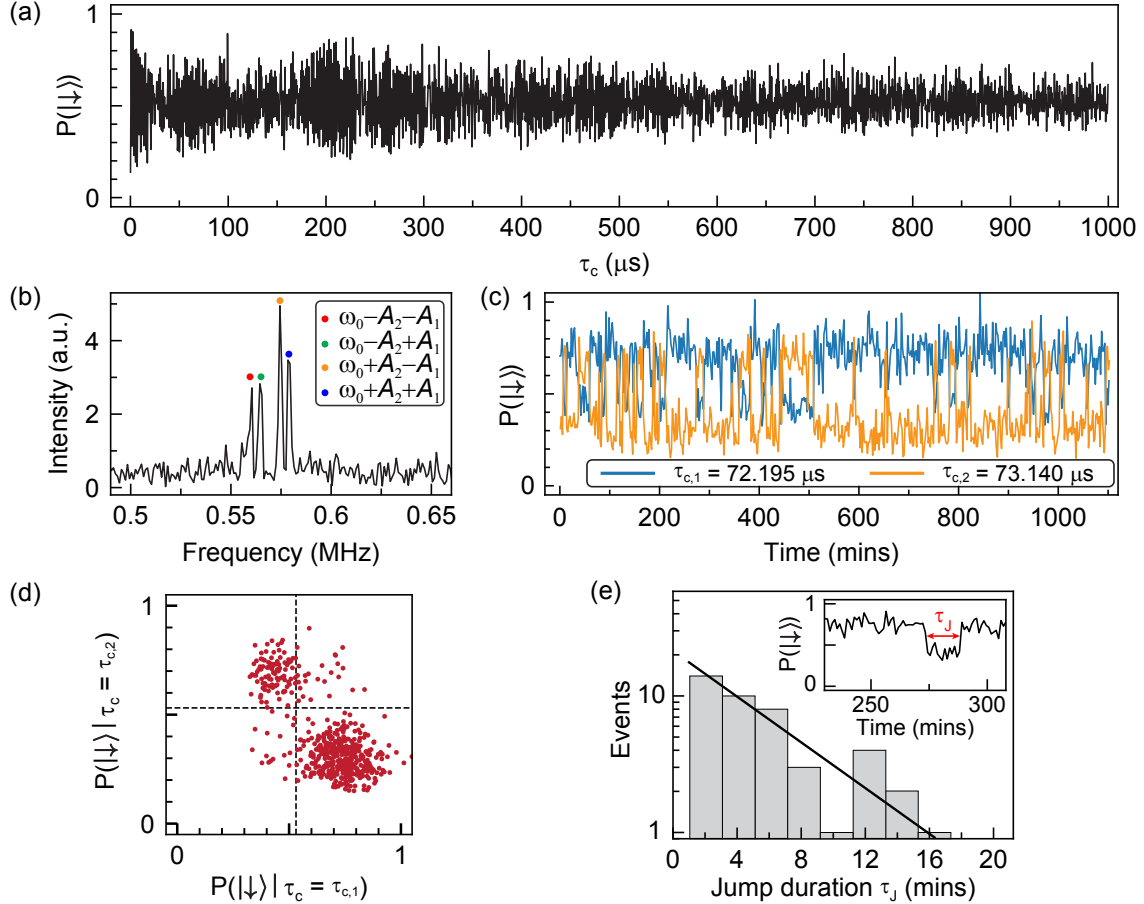


Figure 8.4: Probing the nuclear spin bath. (a) Ramsey spectroscopy of the nuclear spin bath (equivalent to Figure 8.2a). (b) Fourier transform of the data shown in (a) reveals four distinct peaks [$(\omega_0, A_1, A_2) = (569.7, 2, 7)$ kHz]. We identify (A_1, A_2) to likely originate from coupling to two dark spins (d_1, d_2). (c) Repetitive Ramsey experiments at two different τ_c reveal quantum jumps between two states of d_1 . (d) Distribution of the measured populations in (c) are unequally weighted bimodal and anti-correlated at the two τ_c . (e) Duration of the quantum jumps shown in (c) is consistent with a spin state lifetime of 5.19 ± 0.55 mins (black line is the fitted exponential decay). Inset: A representative jump event from (c).

8.6 Conclusion and outlook

In this work, we demonstrated coherent interaction between a rare-earth electronic spin and a nuclear spin, where single-qubit and two-qubit gates were implemented using dynamical decoupling sequences. If more than one nuclear spin is coherently coupled to the electronic spin, a pathway towards driving all the nuclear spins may

involve interleaving the DD sequences with phase-controlled radio-frequency (RF) pulses to drive the nuclear spins directly [30]. Finally, in previous works involving NV⁻ centers in diamond, a primary bottleneck of these multi-qubit registers is that all optical operations are enabled via a single, electronic spin. Presence of multiple optically-addressable emitters per node brings forth multiple advantages, viz. enables higher entanglement generation rate, allows less stringent coherence requirements per emitter, facilitates quantum error correction, etc. Recently, with Er³⁺:YSO we have utilized a frequency-domain multiplexing technique to demonstrate parallel initialization, control, and readout of multiple Er³⁺ spins coupled to the same cavity[33]. Combining this earlier work with results from the current work, we can ultimately envision a hybrid quantum register that is comprised of multiple, telecom-compatible, optically interfaced solid-state spins with single particle control at each node, where each spin is individually coupled to one (or few) long-lived nuclear spin register(s) (Figure 1.3).

Chapter 9

Conclusion and outlook

9.1 Summary

In this thesis, we worked towards developing single photon sources and quantum memories using single erbium ions (doped in a solid-state crystal) and integrated silicon nanophotonics. To that end, here is a summary of the key results:

- Observed fluorescence from single erbium ions via Purcell-enhancing the emission rate by over two orders of magnitude. Showed coupling between the spin states of an ion and its optical transitions.
- Leveraging cavity-enhanced cyclicity of optical transitions, performed optical QND measurements of an ion's spin state. Utilized the single-shot readout technique to probe the coherent dynamics and relaxation of the spin. Coherent control of the spin is realized using microwave pulses.
- Combined simultaneous frequency-domain addressing and global microwave control to demonstrate parallel initialization, manipulation, and single-shot readout of multiple ions coupled to the same cavity. Deep sub-wavelength independent control of spins is achieved by using an optical AC Stark shift.

- Realized coherent coupling between an erbium electronic spin and a nearby nuclear spin, followed by implementing single-qubit and two-qubit gates. Probed the nuclear spin environment and detected additional features in the spin bath.

9.2 Towards indistinguishable photons

Building up on the results from above, ultimately, we would like to realize some useful quantum technologies with this platform. As discussed in Section 1.1, the success of a quantum repeater-based quantum network relies on generating spin-photon entanglement at remote nodes and performing joint-detection of photons using a Hong-Ou-Mandel (HOM)-type measurement [142]. Instead of interfering two photons originating from two different ions (nodes), a simpler version of the experiment to demonstrate spin-photon entanglement and estimate the entanglement generation rate would involve the following: excite the same ion with two consecutive optical pulses (separated by a time-delay larger than the optical excited state lifetime, $T_1 = 1/\Gamma$), route the emitted photons through an unbalanced Mach-Zehnder interferometer, followed by HOM-type measurement [143]. The length of the long-arm of the interferometer is adjusted such that the time taken by a photon to travel the extra length in this arm is equal to the time-delay between the ‘early’ and the ‘late’ photon. Coincidence occurs when the ‘early’ photon travels through the long arm of the interferometer, while the ‘late’ photon travels through the short-arm.

The probability of coincidence is given by the indistinguishability parameter, $I = T_2^*/(2T_1)$ [143], where T_2^* is the optical coherence time and is related to the total dephasing rate of the optical transition, Γ_t as $T_2^* = 1/\Gamma_t$. Recall (from Section 2.3.3) that the total dephasing rate of the optical transitions $\Gamma_t = \Gamma/2 + \Gamma_d$, where Γ_d is the pure dephasing rate; therefore, $I = \frac{\Gamma}{2\Gamma_t} = \frac{1}{1 + 2\Gamma_d/\Gamma}$. In the absence of additional

spectral diffusion, the linewidth ($2\pi \times \Delta\nu$ Hz) of the optical transition is given by: $\Delta\nu = 2\Gamma_t/(2\pi) = 1/(\pi T_2^*)$, such that, $I = \frac{\Gamma}{2\pi \Delta\nu}$. For the best ion we measured (“ion 1” in Chapter 6), the Purcell-enhanced radiative linewidth $\Gamma = 2\pi \times 9.8$ kHz, whereas the linewidth was more than two orders of magnitude larger ($2\pi \times 6$ MHz); therefore the indistinguishability computes to $I = 1.6 \times 10^{-3} \ll 1$.

Pathway towards increasing the indistinguishability involve achieving higher Purcell factor to decrease the excited state lifetime as well as increasing optical coherence time. A silicon PC cavity with a $Q > 10^7$ [71] could bring about 150-fold improvement in the Purcell factor for the ion mentioned above; ultra-low mode-volume cavities [72, 73, 74] may also provide further emission rate enhancement. While we are currently exploring what limits the optical T_2^* , it is believed to be due to fluctuating electric fields in the host crystal. The effect of the field noise is particularly exacerbated here for the case of Er³⁺:YSO since Er³⁺ sits at a lattice site with no symmetry while the energy levels comprising the optical transition exhibit a permanent electric dipole moment, thereby making the transition first-order sensitive to fluctuating fields. But this problem could be side-stepped by finding a *favorable* host crystal for Er³⁺ ion (see Section 9.3). In a recent work from our group [117], we have observed inhomogeneous optical linewidths (460 MHz; comparable to bulk-doped crystals containing Er³⁺) in erbium-implanted TiO₂. It is believed that the narrow optical lines therein are likely a consequence of the incorporation of Er³⁺ at a non-polar crystallographic site with an inversion (D_{2h}) symmetry: the latter doesn’t allow the 4f and 5d levels to mix, thus preventing a forced electric dipole transition, while the non-polar feature yields zero permanent electric dipole moment of the levels, rendering the optical transition first-order insensitive to field noise. It remains to be seen whether these narrow inhomogeneous linewidths in alternate hosts actually translate to prolonged optical coherence in single Er³⁺ ions.

9.3 Extending spin coherence: finding alternate host crystals

For applications involving Er^{3+} ions as a quantum memory, we would like to store the information in the qubit levels of the ion while we attempt remote entanglement generation. This requires long spin coherence times; or in other words, the spin dephasing rate needs to slower the entanglement generation rate, which is largely limited by the optical excited state lifetime. However, the ground state spin coherence of Er^{3+} ions in YSO (spin $T_2^* = 125$ ns; Section 6.5 and Section C.3) is too short for any meaningful applications and limited by weak interactions with a bath of host nuclear spins (consisting of ^{89}Y and ^{29}Si with 100% and $\sim 5\%$ natural abundance, respectively; Section 2.2.1).

We concluded Section 9.2 with the understanding that the optical coherence of Er^{3+} ions in YSO is also limited by specific properties of the host matrix. It is important to realize that these sub-optimal spin and optical coherence times are problems originating from the inferior host crystal properties and has little to do with the emitter i.e. Er^{3+} itself. Thus, this can be mitigated by finding a more suitable host. Moreover, this is another front where our hybrid device architecture of cavity-on-host substrate pays off (Section 3.1): we can swap through various host crystals with making only small changes to the cavity fabrication steps while the optical addressing capabilities remain largely unaffected.

Along-with the requirement that it should exhibit a wide band-gap and accommodate Er^{3+} at a non-polar crystallographic site for good optical properties (Section 9.2), the other requirements for good spin properties in an alternate host is as follows. Studies of REIs in YSO and other host materials have shown that magnetic noise originating from the abundant non-zero nuclear spin isotopes present in the host crystal limits the coherence properties of the electronic spins; therefore, arguably we

are interested in materials that accommodate stable zero-spin nuclear isotopes only. However, having a few non-zero nuclear spins isotopes nearby could be beneficial as they can operate as a long-lived quantum register; something that has been thoroughly exploited in experiments with NV⁻ centers in diamond and we just started to venture along that path too (Chapter 8). We would also like the host substrate to be free of trace amounts of other lanthanides or paramagnetic impurities (Table A.1) as they can also dephase the Er³⁺ spin. And finally, we would like to control the amount of Er³⁺ ions in the host as well.

Ion implantation, combined with high-temperature annealing, turns out to be an efficient approach to the problem of embedding erbium ions in various crystals, as one can control the ion concentration and position in this method [106, 144] while retaining many of the bulk-doped properties. After our initial success with TiO₂ [117], several erbium-implanted oxides, sulphides, tungstates, titanates, etc. are currently being explored.

9.4 Improving device parameters for remote entanglement generation

Eventually, we would like to generate entanglement between two remote spins. A typical entanglement generation protocol might involve something like Barrett-Kok's proposal [145], combined with fast photon detection to erase the frequency difference between the photons originating from two nodes (quantum eraser techniques; see Ref. [146]). If we assume unity efficiency in generating indistinguishable photons from two remote ions, the success probability of Barrett-Kok's protocol in generating an entangled state is given by $P_{eo} = \frac{1}{2}\tilde{\eta}^2$, with $P_{eo} = 1/2$ being the theoretical upper limit [145]. Here, $\tilde{\eta}$ is the probability that a photon emitted by an ion eventually gets detected and is determined by $\tilde{\eta} = \eta_{\text{Er}} \eta_{\text{cav}} \eta_{\text{fib/wg}} \eta_{\text{fib}} \eta_{\text{det}}$, where these parame-

ters are discussed in Section A.1.3. Using the typical values for our current devices: $(\eta_{\text{Er}}, \eta_{\text{cav}}, \eta_{\text{fib/wg}}, \eta_{\text{fib}}, \eta_{\text{det}}) \simeq (1, 0.2, 0.4, 0.8, 0.7)$, we get $\tilde{\eta} \simeq 0.045$; this is primarily limited by the cavity losses (η_{cav}) and fiber-waveguide coupling efficiency ($\eta_{\text{fib/wg}}$). The estimated $\tilde{\eta}$ yields an entanglement generation success probability of $P_{\text{eo}} \simeq 1 \times 10^{-3}$. For ions whose optical transitions are moderately Purcell-enhanced ($P = 500$), we can employ optical excitation rates of 10 kHz. Therefore, the final entanglement generation rate is 10 Hz. Future cavity fabrication efforts are targeted towards increasing Q, η_{cav} and $\eta_{\text{fib/wg}}$, while independent efforts are underway to increase η_{fib} and η_{det} . The final entangled state fidelity will be limited by the qubit spin coherence times, detector dark counts, and sub-optimal mode-matching between the photons originating from the two ions.

9.5 Towards interacting spin ensembles

The typical Er^{3+} ion concentration in the YSO crystals used in our experiments above is around 0.2 – 0.3 ppm (Section A.2). This translates to a few hundred ions situated in the mode-volume of the cavity (Section A.2.1). Consequently, the center of the inhomogeneous distribution is densely crowded with overlapping spectral lines from multiple ions and isolated lines are only observed in the tail of the distribution (Figure 7.1). We would like to reduce the number of ions (ideally, to one or a few ions per cavity). But that would lead to an increased averaged separation between two ions: in our current samples, the average ion-ion spacing is around 70-80 nm, such that magnetic dipolar interaction strength is ~ 1 kHz. From the materials perspective, attaining lower ion concentration is challenging too since these YSO samples are nominally undoped (Er^{3+} exists as contaminants in yttrium-based crystals).

Ion implantation in newer (Er^{3+} free) host materials could be a very powerful technique in this regard. This technique has been used for deterministic placement

of single color centers in diamond [147, 148, 106, 21], and recently with REIs (Ce^{3+} and Pr^{3+}) in YAG [149, 150, 144]. We can utilize implantation masks to create small regions of host with localized high concentration of Er^{3+} ions. Controlling this would lead to a sparsely-populated inhomogeneous distribution while the physical separation between ions is reduced: assembling 10-20 ions into volumes of order $(30 \text{ nm})^3$ such that the average separations are below 15 nm can be realized. These ions would exhibit magnetic dipolar interaction strengths $\sim 1 \text{ MHz}$ (based on an effective g -factor $g \approx 15$ in $\text{Er}^{3+}:\text{YSO}$); such a system could be classified as “strongly interacting ensembles”. This would open up the door towards application of multi-qubit quantum logic operation (entanglement swapping, quantum error correction, deterministic teleportation) as well as studies of fundamental many-body quantum phenomena, where we could implement our aforementioned techniques of single-particle control (Chapter 7) to initialize, manipulate, and perform single-shot readout of multiple Er^{3+} spins.

Appendix A

Additional data, analyses, and methods for the experiments presented in Chapter 5

A.1 Measurement and analysis techniques

A.1.1 Experimental configuration

In this section, we present a more detailed description of our measurement configuration (Figure A.1). The laser (Toptica CTL1500) frequency is coarsely stabilized by probing the absorption of a bulk Er:YSO crystal (50 ppm Er concentration) housed in the same cryostat as the PC. Fine stabilization and linewidth narrowing are achieved using a stable reference cavity (Stable Laser Systems) housed in an ultrahigh vacuum chamber. To be able to tune the laser frequency while stabilizing to the reference cavity, we lock a sideband of the laser to the cavity. To achieve this, a small portion of the laser output passes through a phase modulating fiber EOM (PM) to add frequency sidebands at $\omega_{\text{laser}} \pm \omega_{\text{sb}}$. The sideband at $\omega_{\text{laser}} - \omega_{\text{sb}}$ is locked to the external cavity via the Pound-Drever-Hall technique, using sidebands applied by a second, free-space EOM, at 17.2 MHz. After locking, the sideband frequency is fixed to the cavity ($\omega_{\text{laser}} - \omega_{\text{sb}} = \omega_{\text{cav}}$), but the laser frequency itself can be tuned over a

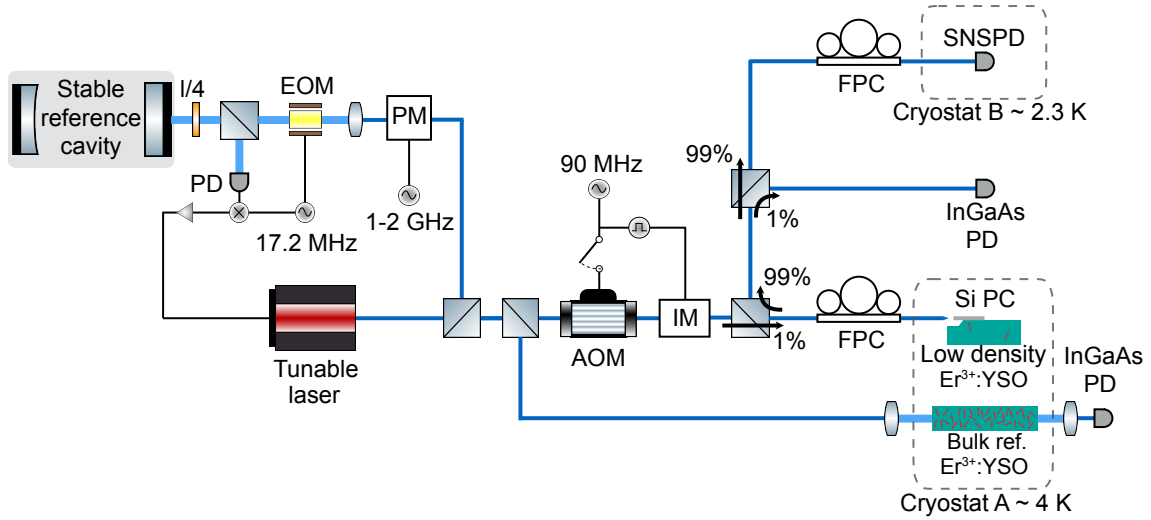


Figure A.1: Experimental configuration for results reported in Chapter 5.
A more detailed version of the experimental configuration presented in Figure 5.1c.
Abbreviations are explained in Section A.1.1.

large range by changing ω_{sb} . The stabilized laser linewidth is considerably less than 30 kHz. The light directed to the experiment is a pure tone without any locking sidebands.

Laser pulses to excite the ions are produced using a double-pass acousto-optic modulator and intensity modulating electro-optic modulator in series (AOM and IM, respectively). This pair of modulators gives an on/off ratio of 90 dB. A fiber polarization controller (FPC) matches the laser polarization to the PC cavity. An AR-coated lensed optical fiber (OZ Optics, TSMJ-X-1550-9/125-0.25-7-2-12-2-AR) with 2 μm focal spot size is used to couple photons to/from the PC cavity. The light returning from the cavity is detected by a superconducting nanowire single photon detector (SNSPD, Quantum Opus) in a separate cryostat. The current bias of the SNSPD is supplied by an SRS SG345 function generator through a 100 $\text{k}\Omega$ resistor, which allows the bias to be switched off during an excitation pulse, preventing the detector from latching. An additional polarization controller adjusts the polarization incident on the SNSPD to maximize the detection efficiency. A small fraction of the reflected

light is sent to an InGaAs photodiode, which is used to measure the cavity reflection spectrum while tuning the cavity resonance.

A.1.2 Tuning the cavity resonance

The resonance of a PC is tuned in the cryostat by manipulating a thin layer of N₂ ice on the cavity [92, 93]. Clean, dry N₂ is applied through a nozzle to form an ice layer, which can decrease the cavity resonance frequency by up to 1 THz. To increase the resonance frequency, we desorb the ice using either laser light ($\sim 100 \mu\text{W}$ of 1536 nm light resonant with the cavity), or by heating the cryostat cold finger with a resistive heater. These techniques allow us to fix the resonance frequency with a precision better than 100 MHz. Condensation of background gas in the cryostat causes a persistent redshift at a rate of $\sim 1 \text{ GHz/hr}$.

A.1.3 Photon collection efficiency

The collection efficiency η of light from the PC can be determined from several independent measurements. The contributions are inefficiencies in the cavity (η_{cav}), at the fiber-waveguide interface ($\eta_{\text{fib/wg}}$), in the optical fiber network between the cryostat and the SNSPD (η_{fib}), and the finite detection efficiency of the SNSPD (η_{det}). The product of these, η , represents the probability for a photon in the cavity to result in a click on the detector.

The fiber-waveguide interface losses are determined by measuring the power reflection coefficient of the PC away from the cavity resonance, and taking the square root to convert round-trip losses into one-way losses. Light is coupled into the device using a lensed fiber, as mentioned in Section A.1.1. The simulated coupling efficiency (using the mode overlap) is $\sim 80\%$ for this particular lensed fiber geometry and an end facet size of 215 nm \times 250 nm. The observed coupling of $\sim 50\%$ likely results

from a combination of imperfect waveguide facet size, a waveguide taper that is too short to be perfectly adiabatic, and scatter at the edge of the YSO.

The cavity losses are estimated from the reflection spectrum, as discussed in Section 3.5. The figure of merit here is $\eta_{\text{cav}} = \kappa_{\text{wg}} / (\kappa_{\text{wg}} + \kappa_{\text{sc}})$, where κ_{sc} and κ_{wg} are internal and waveguide loss channels from the cavity, respectively. For the cavity used in this work, $\kappa_{\text{wg}} < \kappa_{\text{sc}}$. The detector efficiency is measured using a calibrated power meter and neutral density filters, and the fiber network transmission is directly measured. For measurements on ion “A” (Section A.1.4), we find the product of these efficiencies ($\eta_{\text{cav}} = 0.16$, $\eta_{\text{fib/wg}} = 0.46$, $\eta_{\text{fib}} = 0.8$, $\eta_{\text{det}} = 0.67$) to give $\eta = 0.04$, as mentioned in Chapter 5 text and Section A.4.

The actual collection efficiency of light from an Er ion is determined by the product of η and the probability for an ion in the excited state to decay by emitting a photon into the cavity. Given the total decay rate $\Gamma = P\Gamma_0 + \Gamma_\infty$, where the first term represents the cavity decay and the second term the free-space decay (see text in Chapter 5), the probability to decay into the cavity is given by $\eta_{\text{Er}} = P/(P + \Gamma_\infty/\Gamma_0)$. For the parameters presented here ($P > 100$, $\Gamma_\infty/\Gamma_0 \approx 1$), $\eta_{\text{Er}} \approx 1$.

A.1.4 Ions measured

The measurements in Figures 5.2b and 5.4 of Chapter 5 were performed using a single ion (“A”), at 520 MHz to avoid overlapping transitions with nearby ions in higher magnetic fields. Ion A was also used for the measurements in Figure A.5. The PC cavity coupled to ion A had a quality factor of $Q = 5.0 \times 10^4$ and $\eta_{\text{cav}} = 0.16$, and the maximum Purcell enhancement for this ion was $P \sim 130$. The measurements demonstrated in Figure 5.3 were performed with a single ion (“B”) coupled to a different PC cavity ($Q = 7.3 \times 10^4$, $\eta_{\text{cav}} = 0.23$). Ion B was also used in Figure A.7 and A.8.

A.2 Properties of the substrate used in this work

The YSO crystal used in this work was grown, cut and polished by Scientific Materials (boule #07-0552). The RMS roughness of the surface is less than 0.5 nm (as measured by AFM), with occasional long scratches of 1-2 nm depth. The crystal has dimensions of $10 \times 10 \times 3$ mm, with the crystallographic orientation shown in Figure 5.1a. It was not intentionally doped with erbium during growth, but trace quantities are present. Glow discharge mass spectrometry (GDMS) was used to estimate the concentration of Er (and other lanthanides), with the results summarized in Table A.1. A secondary ion mass spectroscopy (SIMS) analysis was also conducted, and yielded upper bounds for the lanthanide concentrations that were roughly 1-2 orders of magnitude higher than the GDMS values.

Element	La	Ce	Pr	Nd	Sm	Eu	Gd	Tb	Dy	Ho	Er	Tm	Yb
Conc. (ppm)	0.4	0.09	0.4	0.1	0.9	0.4	0.1	0.09	0.09	0.2	0.2	0.09	0.1

Table A.1: **Lanthanide concentrations from GDMS in a nominally undoped YSO crystal.** Measured concentrations of several lanthanide elements from GDMS analysis of a YSO crystal from the same boule as the sample used in the experiments. The quoted concentrations are relative to the concentration of yttrium. Values in italics indicate an upper bound, all other (non-italicized) values are estimated to have 30% relative error.

A.2.1 Number of ions coupled to the cavity

The number of Er^{3+} ions that should be coupled to the cavity depends on the ion density in the substrate (Table A.1) as well as the size and shape of the cavity mode (Figure 3.4). Using these simulation results, we can estimate the average number of ions that should experience a certain magnitude of Purcell enhancement, as shown in Figure A.2).

We can estimate the number of ions that are coupled to the cavity used in Figure A.3a by fitting the distribution using a sum of Lorentzian lineshapes, each constrained to have the same homogeneous linewidth and an amplitude 3σ above dark

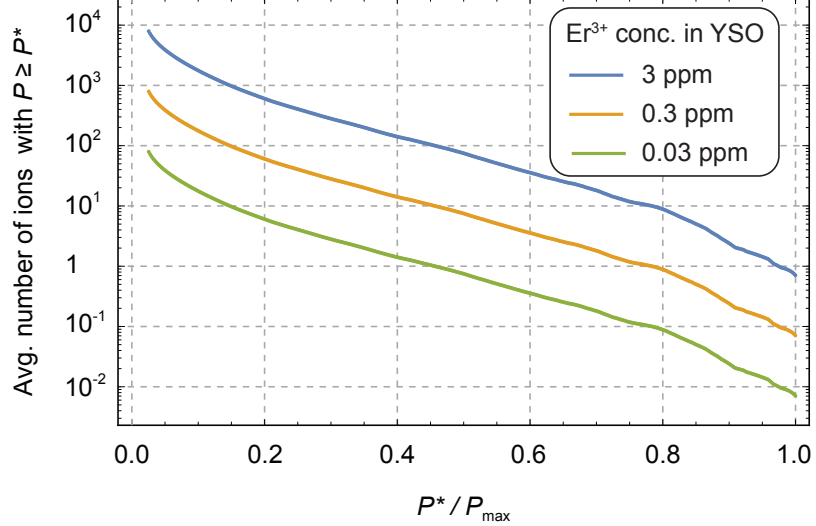


Figure A.2: **Number of ions with a given Purcell factor.** Average number of ions with a Purcell factor $P \geq P^*$. P^* is normalized to the maximum Purcell factor at the Si-YSO interface. In this figure, only ions at crystallographic site 1 are considered, since only these ions couple to the cavity resonance at 1536.4 nm.

counts. The fitted Lorentzians overlap significantly near the center of the inhomogeneous distribution, so the counting results are only a rough estimate. The resulting spectral density of peaks is approximately Gaussian with a standard deviation of ($\sigma = 2.9$ GHz). Integrating this fit yields a total of approximately 500 peaks. Most of the peaks correspond to ions with Purcell factors $P > 0.1 P_{\max}$ given that the data was collected with a fluorescence integration window of 82 μ s (much shorter than the

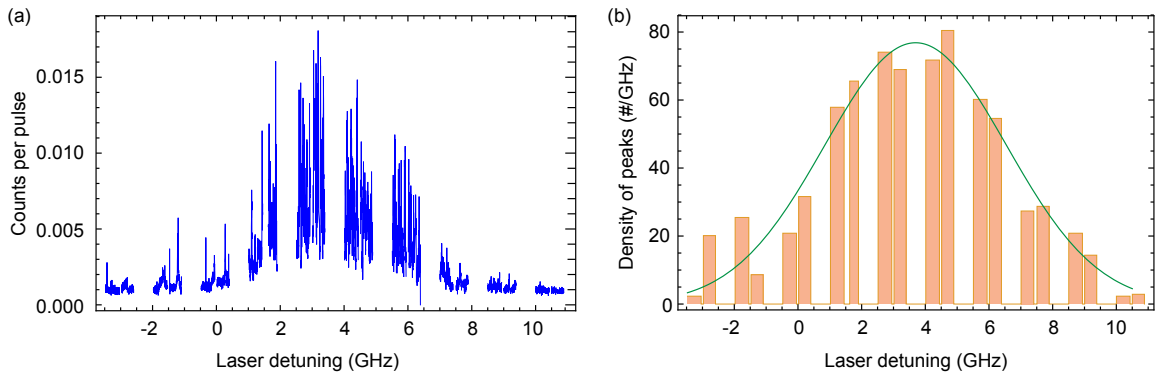


Figure A.3: **Counting peaks in the Er^{3+} spectrum.** (a) PLE data from Figure 5.2a. (b) A plot of the density of Lorentzian peaks that could be fit to the data.

bulk lifetime of 11.4 ms). Given the measured concentration of 0.2 ppm, this estimate is in general agreement with the predicted value of a few hundred coupled ions from Figure A.2.

A.3 Temperature and magnetic field dependence of the spin-lattice relaxation time, T_1

The longest spin relaxation time measured for the Z_1 ground state in $\text{Er}^{3+}:\text{YSO}$ is 4.2 s [53], at a temperature of 20 mK and a magnetic field of 0.27 T. However, modeling the field- and temperature-dependence of the specific spin-lattice relaxation mechanisms involved leads to a prediction that dramatically longer relaxation times, exceeding 10^3 seconds, should be achievable at higher temperatures (≈ 1 K) but lower magnetic fields. Figure A.4 shows the expected behavior at several magnetic fields, together with several measurements from the literature.

The relaxation time T_1 of the ground state spin is limited by phonon-mediated processes. At cryogenic temperatures, direct, Raman and Orbach processes contribute to the total rate [112], with the functional form:

$$T_1^{-1} = A_d \left(\frac{g\mu_B B}{h} \right)^5 \coth \left(\frac{g\mu_B B}{2kT} \right) + A_r T^9 + A_o e^{-\Delta/(kT)} \quad (\text{A.1})$$

Here, $g\mu_B B$ is energy difference between the two Z_1 spin sublevels in the magnetic field B , k is Boltzmann's constant, and h is Planck's constant. The coefficients describing the direct, Raman, and Orbach processes have previously been measured for $\text{Er}^{3+}:\text{YSO}$ [97, 50] using bulk, X-band ESR to be $(A_d, A_r, A_o) = (5.0 \times 10^{-5} \text{s}^{-1} \text{GHz}^{-5}, 1.3 \times 10^{-3} \text{s}^{-1} \text{K}^{-9}, 2.5 \times 10^{10} \text{s}^{-1})$, with an Orbach intermediate state energy of $\Delta = 6.4 \text{meV}$.

The temperature dependence of the Raman and Orbach processes is very steep, restricting T_1 to values less than 10 ms for $T > 3$ K. In large magnetic fields, where $g\mu_B B/h$ is more than a few GHz, the direct process sets in around 2–3 K, preventing

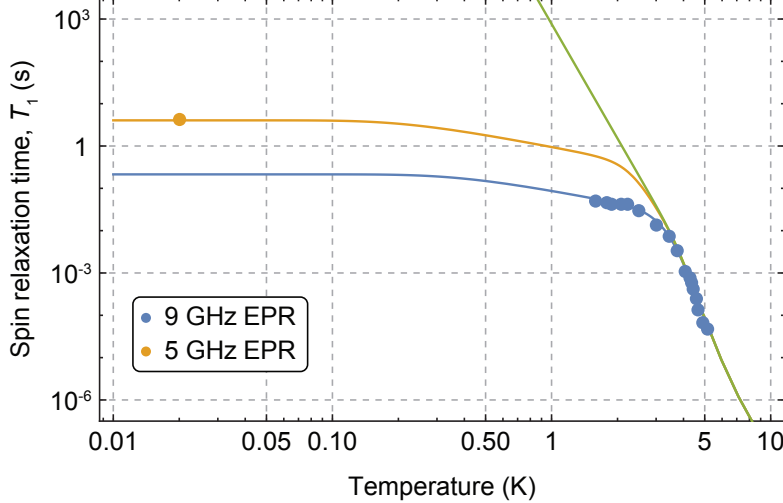


Figure A.4: **Temperature dependence of the spin T_1 .** The blue points are data from Ref. [97] (X-band EPR, $g\mu_B B/h \approx 9$ GHz, site 1), while the yellow point is from Ref. [53] ($g\mu_B B/h \approx 5$ GHz). The blue line represents the model from Ref. [97] (Eq. A.1), while the yellow line shows the same model with $g\mu_B B/h$ changed from 9 GHz to 5 GHz. The green line shows the same model with $g\mu_B B/h = 0.1$ GHz, illustrating the potential for extremely long spin-lattice relaxation times in the presence of small magnetic fields.

dramatic improvements at lower temperatures. However, the direct process is highly suppressed in low magnetic fields, as B^4 , which should allow $T_1 > 10^3$ s, if $g\mu_B B/h < 100$ MHz. To the best of our knowledge, this regime has not been experimentally explored, as most studies of spin-lattice relaxation in $\text{Er}^{3+}:\text{YSO}$ are performed with electron paramagnetic resonance (EPR), which relies on large magnetic fields for spin polarization. What other limits arise in this regime (for example, from coupling to nuclear spins or other paramagnetic impurities) is unclear.

A.4 Saturation behavior of a single ion

We have repeated the single-ion PLE spectroscopy (Figure 2) over a wide range of input powers to probe the saturation of the photon emission rate. At all powers, the spectrum qualitatively resembles a Gaussian peak on a flat background (Figure A.5a).

While the background level increases linearly with input power, the height of the peak corresponding to a single ion transition saturates near 0.02 detected photons per excitation pulse (Figure A.5b). After accounting for the independently measured detection efficiency of 0.04 (Section A.1.3), this number is consistent with 0.5 emitted photons per excitation pulse, as expected for saturated excitation in the presence of dephasing. The linear background likely originates from a large number of weakly coupled ions, which do not saturate and have a flat distribution in frequency. To understand the saturation behavior of the ion, we model it as a two-level system and numerically solve the optical Bloch equations. The model parameters are all

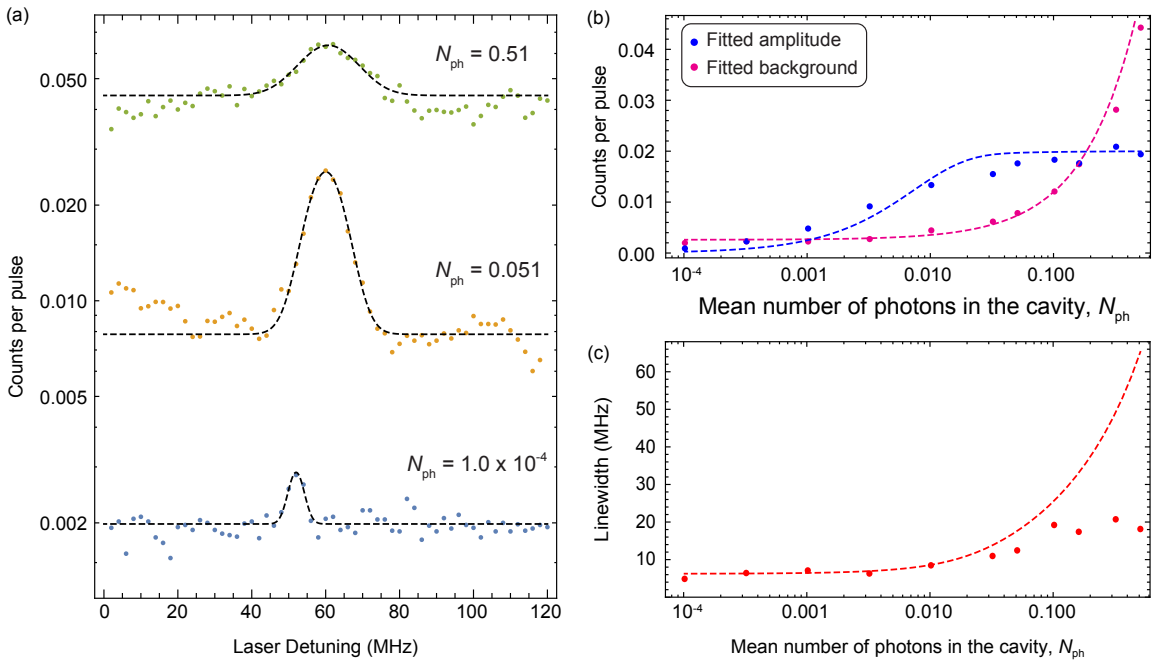


Figure A.5: Saturation spectra and power broadening of a single Er^{3+} ion. (a) PLE spectra recorded at several pump powers. The excitation power is indicated in units of the mean intracavity photon number N_{ph} . Each spectrum is fit to a Gaussian with a flat offset (black dashed line). (b) Peak heights (blue) and offsets (magenta) determined from the Gaussian fits, for various excitation powers. The offsets increase linearly with power (dashed line), while the amplitudes are well-described by a numerical model (see Section A.4). (c) The linewidths (FWHM) from the Gaussian fits, for various excitation powers. The dashed line is from the same model as (b).

independently measured. The Rabi frequency is $\Omega = 2g\sqrt{N_{\text{ph}}}$, where $g = 2\pi \times 1.3$ MHz is the single-photon Rabi frequency determined from the Purcell factor (130 for this ion), and N_{ph} is the mean photon number in the cavity for a given input power P_{in} , and it is given by: $N_{\text{ph}} = 4\frac{\kappa_{\text{wg}}}{\kappa^2}\frac{P_{\text{in}}}{\hbar\omega}$ (see Equation 2.16). The excited state decay rate is $\Gamma = 2\pi \times 1.8$ kHz. We also incorporate an additional excited-state dephasing rate $2\Gamma_d = 2\pi \times 6.2$ MHz, chosen to match the observed linewidths at low power (Figure A.5c). The duration of the excitation pulse is 10 μs . The results of this model are in good agreement with the observed power-dependence of the fluorescence amplitude, as shown in Figure A.5b. The linewidth agrees qualitatively, but not quantitatively, with the experimental observations.

A.5 Additional analysis of $g^{(2)}$ data

A.5.1 Dependence of $g^{(2)}(0)$ on the signal-to-noise ratio

As demonstrated in Figure A.5b, although emission from a single ion (i.e. “signal”) saturates at higher incident powers of the excitation pulse, emission from the weakly coupled ions continues to increase. Thus our ability to isolate a single emitter is strongly dependent on the signal-to-noise ratio (SNR), where both dark counts and emission from these weakly coupled ions contribute to the “noise”. This limits the minimum value of $g^{(2)}(0)$ because of accidental coincidences from background light and dark counts. This limit can be computed by representing the photons detected in a given bin i (n_i) as the sum of two contributions: photons from a single atom (n_i^{ion}), and uncorrelated background (n_i^{bg}). Then:

$$g^{(2)}(0) = \frac{\langle n_i^2 \rangle}{\langle n_i \rangle^2} = \frac{\langle (n_i^{\text{ion}})^2 \rangle + \langle (n_i^{\text{bg}})^2 \rangle + 2\langle n_i^{\text{ion}} \rangle \langle n_i^{\text{bg}} \rangle}{\langle n_i^{\text{ion}} + n_i^{\text{bg}} \rangle^2} = \frac{2A+1}{(A+1)^2} \quad (\text{A.2})$$

where $A \equiv \text{SNR} = \langle n_i^{\text{ion}} \rangle / \langle n_i^{\text{bg}} \rangle$. We measured $g^{(2)}$ for several different ions exhibiting different SNRs. As shown in Figure A.6, the experimentally measured $g^{(2)}(0)$ value

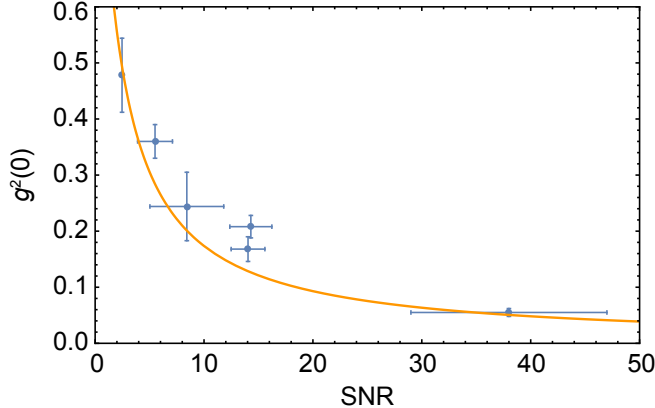


Figure A.6: **Correlation between the value of $g^{(2)}(0)$ and the signal-to-noise ratio (SNR) of the fluorescence from a single ion.** Blue points correspond to $g^{(2)}(0)$ values experimentally measured for different ions. The yellow curve is a theoretical estimate of $g^{(2)}(0)$ based on Equation A.2.

each ion is strongly correlated to the SNR for that ion, and it is in good agreement with Equation A.2. The SNR for an ion is estimated by performing a narrow-range frequency scan in the neighborhood of the spectral line of that ion under identical excitation conditions as the $g^{(2)}$ measurement.

A.5.2 Bunching feature of $g^{(2)}$

At times greater than 0, $g^{(2)}$ exhibits bunching. As shown in Figure A.7, the bunching feature varies with the excitation power and duration, and is generally well-described by a bi-exponential decay. Bunching in single emitters has been attributed to transient occupation of a dark state (either a metastable shelving level [151], spin level [152], or charge state), optical nutation or spectral diffusion [153]. The Er^{3+} level structure does not have any shelving levels in the $^4I_{13/2}$ and $^4I_{15/2}$ manifolds: other than the Y_1 state, the lifetime of the other crystal field levels are extremely short because of phonon relaxation. We rule out shelving in another spin state because the rapid temperature dependence of the spin-lattice relaxation time (Figure A.4) is not mirrored in the temperature dependence of the bunching time constant (Figure A.8).

Together, these also suggest that optical nutation is not the origin, since this coherent phenomenon occurs on shorter timescales than spontaneous relaxation, while the observed bunching timescales are quite long compared to the excited state decay rates and expected Zeeman-level lifetimes. Charge state or ionization dynamics seem unlikely because the mean count rate does not change with power over a wide range (Figure 5.2b inset), the amplitude of the bunching decreases with increasing excitation power (Figure A.7), and because rare earth ions do not generally exhibit charge instability.

Ruling out these other mechanisms leaves spectral diffusion as the most likely candidate. There are several possible noise sources, including magnetic fields from nearby ^{89}Y nuclei and other rare earth ions, as well as electric field noise from the static dipole moment of other excited Er^{3+} ions [50]. To check whether the observed dependence on excitation power and pulse duration results from a change in the noise *magnitude* or a change in the *sensitivity* to noise (*e.g.* from changing the spectral selectivity of the laser excitation), we have performed a control experiment alternating strong and weak pulses (data not shown). We find that the strong pulses change the bunching observed after the weak pulses, suggesting that the noise itself changes and is therefore driven in part by the laser excitation. Further experiments will help elucidate the specific mechanisms involved.

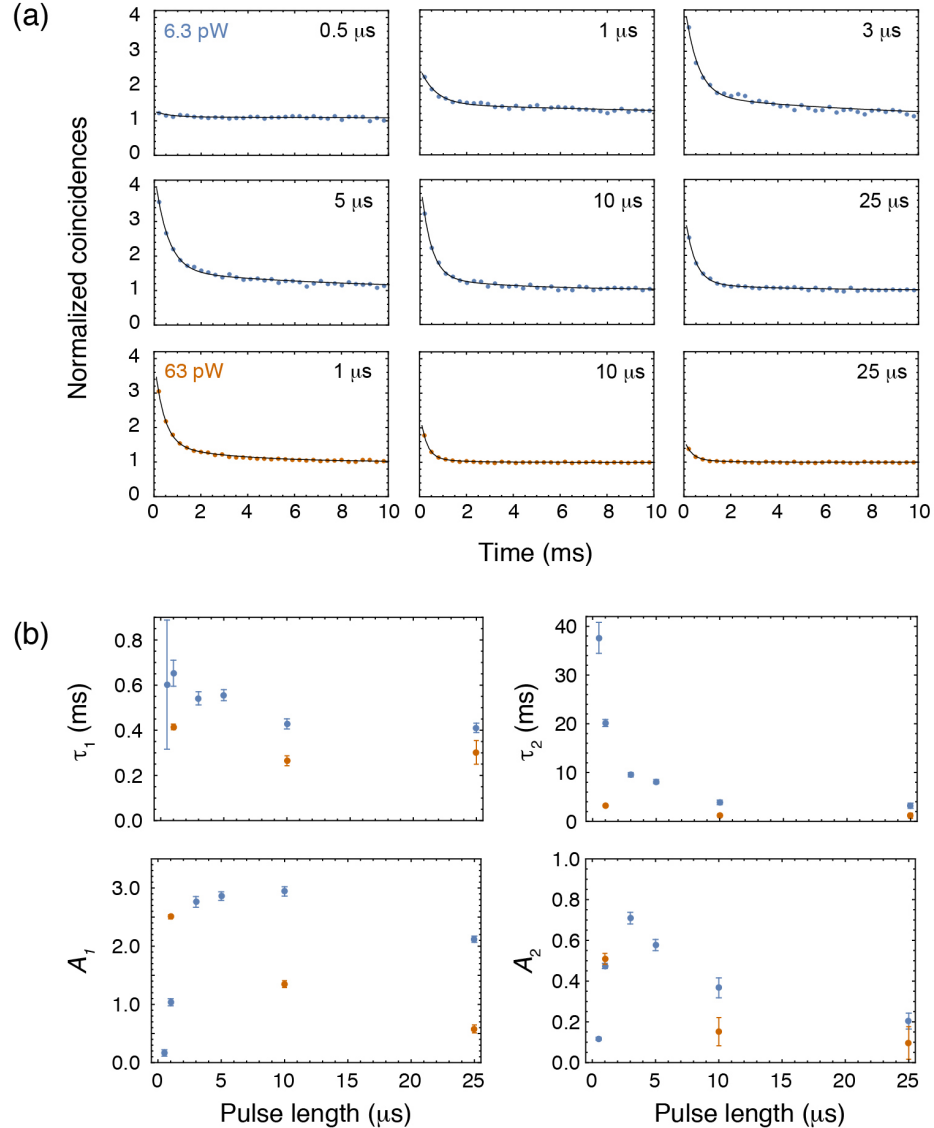


Figure A.7: **Power and pulse width dependence of the bunching in $g^{(2)}$.** (a) Bunching behavior under different resonant excitation conditions (two laser powers, 6.3 pW (blue) and 63 pW (orange), and a variety of pulse durations). The data is best described by a bi-exponential decay (neglecting the bunching at $t = 0$): $g^{(2)}(t) = A_1 e^{-t/\tau_1} + A_2 e^{-t/\tau_2} + 1$ (fits shown in black curves). (b) Decay time constants and amplitudes extracted from the biexponential fit to the $g^{(2)}$ data in (a). Note that the fluorescence obtained with the two shortest pulse widths at 6.3 pW excitation power is very close to background count rates. Since $g^{(2)} \rightarrow 1$ as the signal-to-background ratio approaches 0, we believe that the decrease in bunching amplitudes for these points is an artifact of the background.

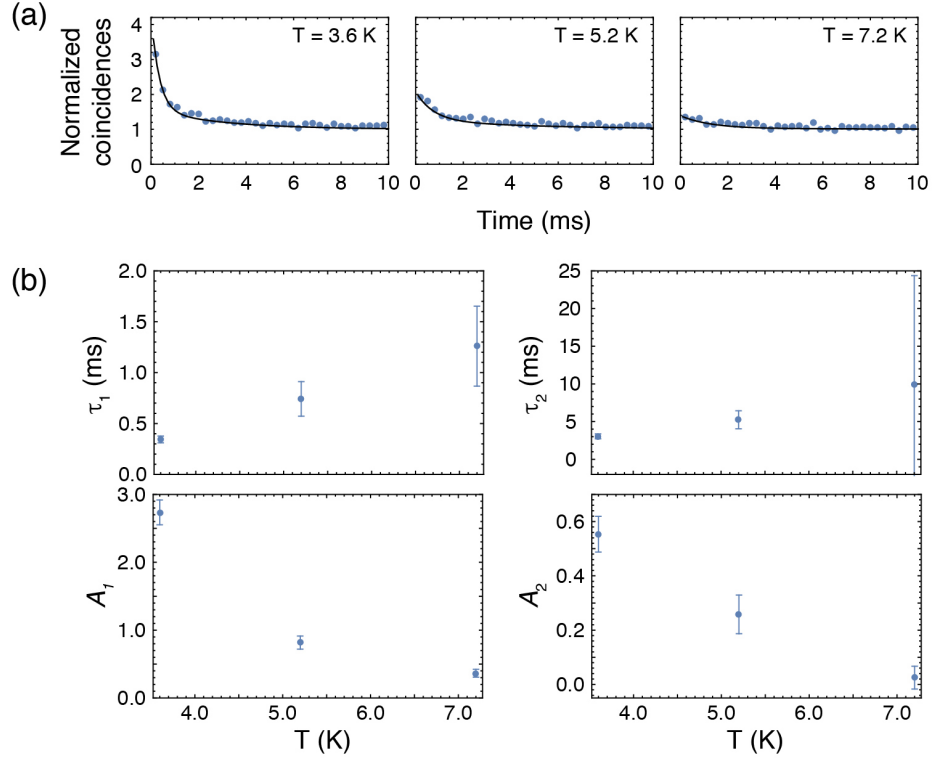


Figure A.8: **Temperature dependence of bunching in $g^{(2)}$ from a single ion.** (a) Similar to Figure A.7, we have fitted a biexponential function $g^{(2)}(t) = A_1 e^{-t/\tau_1} + A_2 e^{-t/\tau_2} + 1$ to the data at the indicated temperatures. For comparison to Figure A.7, the CW power in this experiment is 3 pW with 10 μ s pulse width. (b) Decay time constants and amplitudes extracted from the biexponential fits.

A.6 Bulk Er³⁺:YSO lifetime

In Figure A.9 we show a measurement of the bulk Er³⁺:YSO excited state decay rate. Previous work has shown that the fluorescence lifetime can increase as a result of radiation trapping in dense samples [45, 154]. In Figure A.9a, we find that the measured lifetime is largest at the detuning where the optical depth is highest, and decreases as the laser is detuned. The increase in the excited state lifetime at zero detuning may be associated with radiation trapping in the crystal, as the optical depth of the crystal is approximately 1 at this frequency. However, the decrease at large detunings beyond 1 GHz cannot plausibly be attributed to radiation trapping, because the optical depth decreases much more rapidly than the lifetime (using the

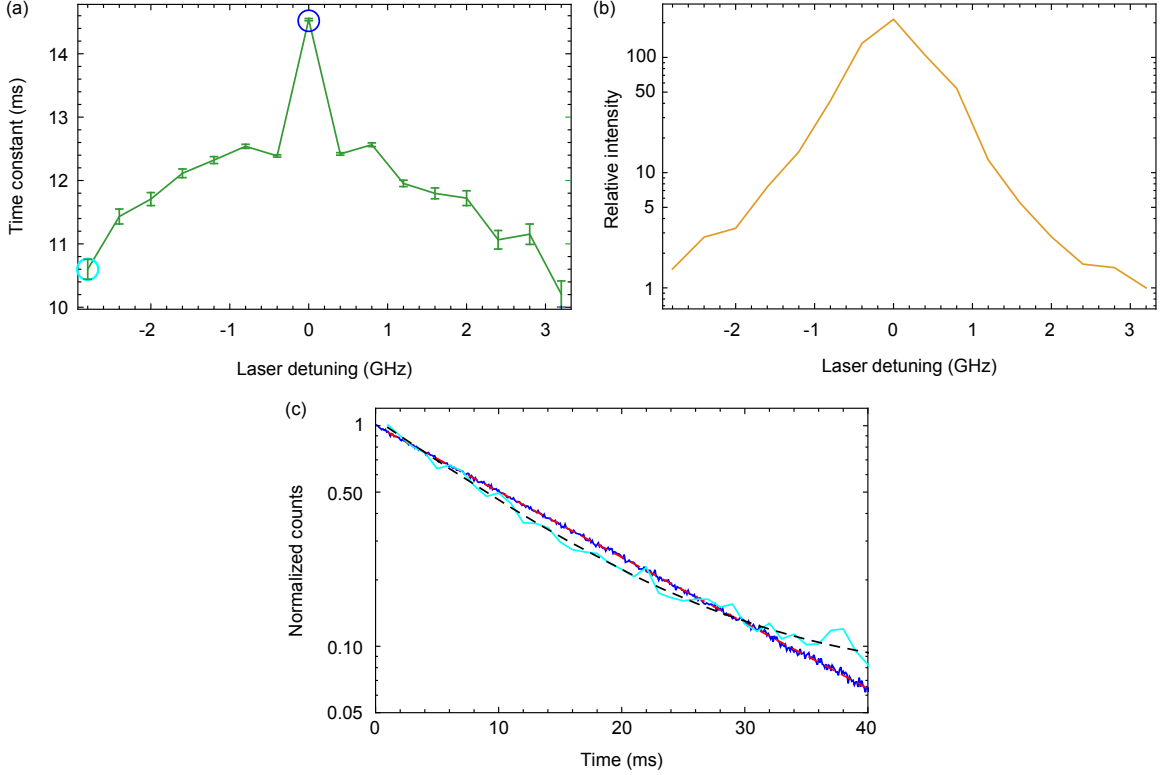


Figure A.9: Measurement of the bulk Er^{3+} :YSO excited state decay rate. (a) Fluorescence lifetime of the ${}^4I_{13/2} Y_1$ state (site 1) in a 50 ppm Er^{3+} :YSO crystal, as a function of the detuning of the excitation laser from the center of the inhomogeneous distribution. (b) The associated fluorescence intensity for each of the detunings plotted in panel (a). (c) Example time traces for detunings of -2.8 GHz (cyan) and 0 GHz (blue).

fluorescence amplitude in Figure A.9b as a proxy for optical depth). Instead, this may result from strain or other effects that alter the crystal field levels and shift the transition away from the center of the inhomogeneous distribution. To avoid these complications, we rely on the previously reported literature value of $\tau_0 = 11.4$ ms to compute Γ_0 , which was measured at the center of the inhomogeneous distribution in a lower density sample in Ref. [50].

Appendix B

Additional data, analyses, and methods for the experiments presented in Chapter 6

B.1 Experimental details

The devices and substrates used in this work are identical to those in Chapter 5, and are described in detail there (Figure B.1). The key difference in the present work (with respect to Chapter 5) is that the measurements take place in a ^3He cryostat with a base temperature of approximately $T = 540$ mK. At $T = 4$ K, spin dynamics are unobservable, presumably because of rapid spin-lattice relaxation in the ground or excited states [96]. For most experiments, light is coupled into the devices using a lensed fiber. The measurement of Rabi oscillations in Figure 6.6d uses a slightly different device geometry that incorporates a microwave coplanar waveguide approximately 125 μm from the photonic crystal, and it is described in Ref. [85]. Microwave pulses are generated using a signal generator (SRS SG386) modulated by an IQ mixer driven by an arbitrary waveform generator (Agilent 33622) and amplified to 21 W (MiniCircuits ZHL-30W-252+) before entering the cryostat. A low duty cycle is used to avoid heating the sample. The optical pulses are derived from a laser

Ion index	Purcell factor	Maximum cyclicity (C_{\max})	Cavity Q factor	Cavity losses (η_{cav})	Total collection efficiency (η)	ML readout fidelity
ion 1 (Fig. 6.5)	703 ± 6	1500 ± 150	6.6×10^4	0.063	0.028	0.946
ion 1 (Fig. 6.4)	463 ± 10	1260 ± 126	4.3×10^4	0.045	0.020	-
ion 2	189 ± 5	390 ± 39	7.3×10^4	0.088	0.037	0.83
ion 3	536 ± 5	620 ± 62	4.8×10^4	0.159	0.038	0.968

Table B.1: **Parameters for the 3 ions studied in this work.** Cavity losses $\eta_{\text{cav}} = \kappa_{\text{wg}} / (\kappa_{\text{wg}} + \kappa_{\text{sc}})$, where κ_{wg} and κ_{sc} are waveguide and internal loss channels from the cavity, respectively, such that $\kappa_{\text{wg}} + \kappa_{\text{sc}} = \kappa$ is the cavity linewidth. η includes η_{cav} as well as the measured fiber-waveguide coupling efficiency (typ. 40-60%), other measured component losses and the detector quantum efficiency (67%).

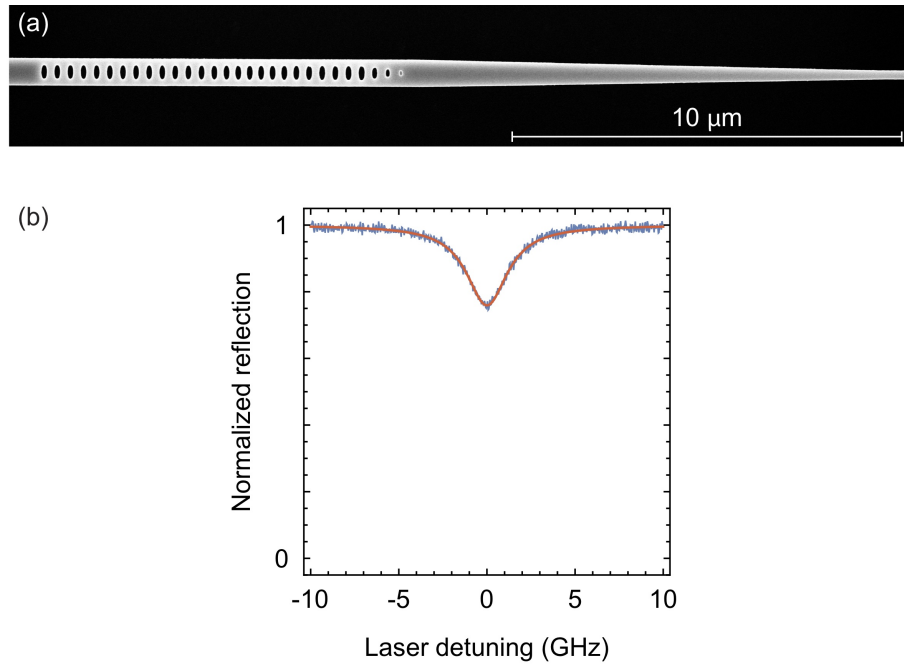


Figure B.1: **Device details for results reported in Chapter 6.** (a) Scanning electron microscope image of a representative silicon photonic crystal cavity. The cavity supports a single, non-degenerate high- Q resonance.(b) Reflection spectrum of ion 1 cavity (first row in Table B.1), demonstrating a linewidth $\kappa = 2.85$ GHz.

stabilized to a ULE reference cavity, and shaped with a sequence of acousto-optic modulators and an electro-optic intensity modulator.

All data in this work comes from measurements on 3 different ions (Table B.1). Figures 6.2, 6.3, 6.4ab, 6.5, B.2, B.5b and part of Figure 6.4c are based on “ion 1”, while Figures 6.6ab, B.3, B.4 and part of Figure 6.4c, are based on “ion 2”. Figure

[6.6cd](#) and part of Figure [6.4c](#) are based on “ion 3”. Figure [B.5a](#) contains data from all the above three ions. Ions 1 and 2 are coupled to different photonic crystals on the same YSO substrate, while ion 3 is in a different YSO crystal. Out of the many ions coupled to each cavity, these particular ions were selected for careful study because they are strongly coupled to the cavity (large Purcell factor) and spectrally well-separated from other ions. Importantly, no additional selection was made on the basis of cyclicity or spin readout fidelity. The transition from ion 1 to ion 2 was necessitated by the accidental destruction of the photonic crystal coupled to ion 1 (which was also damaged, lowering Q , after the measurements in Figure [6.3a](#) and [6.5](#) but before those in Figure [6.4a,b](#), while the transition to ion 3 was motivated by a new device geometry allowing for microwave driving of the spins.

The Er concentration in the YSO substrates used here is estimated to be several hundred ppb. [31], such that the average separation between ions is around 80 nm.

B.2 Theoretical model of cavity-enhanced cyclicity

In this section, we develop a theoretical model describing the cyclicity of the optical transitions measured in Figures [6.3](#) and [6.4](#) of Chapter [6](#). Calculating the cavity coupling strength for all four possible transitions A-D is not currently possible because the relevant transition dipole moments of $\text{Er}^{3+}:\text{YSO}$ have not been measured, and the precise position of the ion in the cavity is not known. As an alternate approach, we demonstrate that these four rates and their dependence on the magnetic field angle can be reduced to only two fit parameters that physically correspond to the decay rates of the AB and CD transitions into the cavity at a single magnetic field orientation. The agreement of this model with the data validates our interpretation of the underlying physics, and is also practically useful for predicting conditions where the cyclicity is maximized from a small number of measurements.

B.2.1 Atom-cavity Hamiltonian

The $\text{Er}^{3+} \ ^4I_{13/2} \rightarrow \ ^4I_{15/2}$ transition in YSO has roughly equal contributions from electric (ED) and magnetic (MD) dipole transition amplitudes [56]. The Hamiltonian describing this mixed coupling to a field is [155]:

$$H = -\mathbf{d} \cdot \mathbf{E} - \boldsymbol{\mu} \cdot \mathbf{B} \quad (\text{B.1})$$

Here, \mathbf{d} is the electric dipole operator and $\boldsymbol{\mu}$ is the magnetic dipole operator. Typically, expressions for multipolar coupling include electric quadrupole (E2) terms at the same order as MD contributions. However, for Er^{3+} , it has been calculated that the vacuum E2 emission rate is approximately 7 orders of magnitude smaller than the MD rate [56], justifying its exclusion in the present analysis.

We quantize the electric and magnetic fields in the cavity as:

$$\mathbf{E} = \mathbf{E}(\mathbf{r})ae^{-i\omega t} + \mathbf{E}^*(\mathbf{r})a^\dagger e^{i\omega t} \quad (\text{B.2})$$

$$\mathbf{B} = i[\mathbf{B}(\mathbf{r})ae^{-i\omega t} - \mathbf{B}^*(\mathbf{r})a^\dagger e^{i\omega t}] \quad (\text{B.3})$$

The i appearing in the expression for \mathbf{B} reflects the fact that the magnetic field oscillates out of phase with the electric field in a standing wave cavity. For nanophotonic cavities, the TE/TM polarization mode splitting is high enough that we only consider a single polarization mode.

We then introduce four transition dipole operators σ_i , corresponding to the four transitions A-D. Each operator couples to electric and magnetic fields via the dipole moments \mathbf{d}_i and $\boldsymbol{\mu}_i$, respectively. The complete atom-photon interaction Hamiltonian is ($\hbar = 1$):

$$H = -\sum_{i=1}^4 \left[\left(\mathbf{d}_i \sigma_i + \mathbf{d}_i^* \sigma_i^\dagger \right) \cdot \left(\mathbf{E}(\mathbf{r}_0)ae^{-i\omega t} + \mathbf{E}^*(\mathbf{r}_0)a^\dagger e^{i\omega t} \right) \right. \\ \left. - i \left(\boldsymbol{\mu}_i \sigma_i + \boldsymbol{\mu}_i^* \sigma_i^\dagger \right) \cdot \left(\mathbf{B}(\mathbf{r}_0)ae^{-i\omega t} - \mathbf{B}^*(\mathbf{r}_0)a^\dagger e^{-i\omega t} \right) \right] \quad (\text{B.4})$$

Making the rotating wave approximation and taking the cavity to be resonant with the atomic transition (neglecting Zeeman splittings), we arrive at:

$$H = - \sum_{i=1}^4 (\mathbf{d}_i \cdot \mathbf{E}^*(\mathbf{r}_0) \sigma_i a^\dagger - i \boldsymbol{\mu}_i \cdot \mathbf{B}^*(\mathbf{r}_0) \sigma_i a^\dagger) + h.c. \quad (\text{B.5})$$

In the limit $\kappa \gg (\mathbf{d} \cdot \mathbf{E}, \boldsymbol{\mu} \cdot \mathbf{B})$, the atom-cavity dynamics are simply Purcell-enhanced spontaneous emission into the cavity (the *bad-cavity* limit of cavity-QED). The decay rate on the transition i into the cavity is given by:

$$\Gamma_i = \frac{|\mathbf{d}_i \cdot \mathbf{E}^*(\mathbf{r}_0) - i \boldsymbol{\mu}_i \cdot \mathbf{B}^*(\mathbf{r}_0)|^2}{\kappa}, \quad (\text{B.6})$$

where κ is the cavity linewidth. In previous work, we have shown that the contributions from electric and magnetic coupling to the cavity could be of similar magnitude [31], depending on the position of the ion within in the cavity standing wave.

B.2.2 Reducing parameters using Kramers' theorem

Er^{3+} has an odd number of electrons, so in the absence of a magnetic field, its eigenstates are all even-fold degenerate according to Kramers' theorem. In a low-symmetry environment like the Y site in YSO (C_1 point group), the degeneracy is minimal and all eigenstates are doublets [112]. The application of a magnetic field lifts the degeneracy of the doublets, resulting in the non-degenerate states $\{\downarrow_g, \uparrow_g, \downarrow_e, \uparrow_e\}$ shown in Figure 6.1b.

The states emerging from the same doublet are time-reversal conjugates of each other: $\hat{\Theta} |\uparrow_j\rangle = |\downarrow_j\rangle$ and $\hat{\Theta} |\downarrow_j\rangle = -|\uparrow_j\rangle$, where $\hat{\Theta}$ is the antiunitary time-reversal operator. This has implications for the matrix elements of the electric and magnetic dipole operators, which are even and odd under time reversal ($\Theta^{-1} A \hat{\Theta} = \pm A$), respectively [112]. In particular:

$$\mathbf{d}_1 = \langle \downarrow_e | \mathbf{d} | \downarrow_g \rangle = \langle \hat{\Theta} \uparrow_e | \mathbf{d} | \hat{\Theta} \uparrow_g \rangle = \langle \uparrow_e | \hat{\Theta}^{-1} \mathbf{d} \hat{\Theta} | \uparrow_g \rangle^* = \langle \uparrow_e | \mathbf{d} | \uparrow_g \rangle^* = \mathbf{d}_4^* \quad (\text{B.7})$$

$$\mathbf{d}_2 = \langle \downarrow_e | \mathbf{d} | \uparrow_g \rangle = -\langle \hat{\Theta} \uparrow_e | \mathbf{d} | \hat{\Theta} \downarrow_g \rangle = -\langle \uparrow_e | \hat{\Theta}^{-1} \mathbf{d} \hat{\Theta} | \downarrow_g \rangle^* = -\mathbf{d}_3^* \quad (\text{B.8})$$

$$\boldsymbol{\mu}_1 = -\boldsymbol{\mu}_4^* \quad (\text{B.9})$$

$$\boldsymbol{\mu}_2 = \boldsymbol{\mu}_3^* \quad (\text{B.10})$$

We can now revisit the atom-photon coupling Hamiltonian, Equation (B.5). Writing the atomic operators σ_i in the basis $\{\downarrow_g, \uparrow_g, \downarrow_e, \uparrow_e\}$:

$$H = - \begin{pmatrix} 0 & 0 & \mathbf{d}_1 & \mathbf{d}_3 \\ 0 & 0 & \mathbf{d}_2 & \mathbf{d}_4 \\ 0 & 0 & 0 & 0 \\ 0 & 0 & 0 & 0 \end{pmatrix} \cdot \mathbf{E}^*(\mathbf{r}_0) a^\dagger + i \begin{pmatrix} 0 & 0 & \boldsymbol{\mu}_1 & \boldsymbol{\mu}_3 \\ 0 & 0 & \boldsymbol{\mu}_2 & \boldsymbol{\mu}_4 \\ 0 & 0 & 0 & 0 \\ 0 & 0 & 0 & 0 \end{pmatrix} \cdot \mathbf{B}^*(\mathbf{r}_0) a^\dagger \quad (\text{B.11})$$

$$+ h.c. \quad (\text{B.12})$$

$$= - \begin{pmatrix} 0 & 0 & \mathbf{d}_{||} & \mathbf{d}_\perp \\ 0 & 0 & -\mathbf{d}_\perp^* & \mathbf{d}_{||}^* \\ 0 & 0 & 0 & 0 \\ 0 & 0 & 0 & 0 \end{pmatrix} \cdot \mathbf{E}^*(\mathbf{r}_0) a^\dagger + i \begin{pmatrix} 0 & 0 & \boldsymbol{\mu}_{||} & \boldsymbol{\mu}_\perp \\ 0 & 0 & \boldsymbol{\mu}_\perp^* & -\boldsymbol{\mu}_{||}^* \\ 0 & 0 & 0 & 0 \\ 0 & 0 & 0 & 0 \end{pmatrix} \cdot \mathbf{B}^*(\mathbf{r}_0) a^\dagger \quad (\text{B.13})$$

$$+ h.c. \quad (\text{B.14})$$

$$= - \begin{pmatrix} 0 & 0 & g_{||}^e - ig_{||}^m & g_\perp^e - ig_\perp^m \\ 0 & 0 & -g_\perp^{e*} - ig_\perp^{m*} & g_{||}^{e*} + ig_{||}^{m*} \\ 0 & 0 & 0 & 0 \\ 0 & 0 & 0 & 0 \end{pmatrix} a^\dagger + h.c. \quad (\text{B.15})$$

$$= - \begin{pmatrix} 0 & 0 & g_{||} & g_{\perp} \\ 0 & 0 & -g_{\perp}^* & g_{||}^* \\ 0 & 0 & 0 & 0 \\ 0 & 0 & 0 & 0 \end{pmatrix} a^\dagger + h.c. \quad (\text{B.16})$$

In going from the first to the second line, we have made use of Equations (B.7) - (B.10). In going from the second to the third line, we have taken the cavity fields to be real-valued, which is an excellent approximation as they are highly linearly polarized.

The final expression, Equation (B.16), has the same form for the electric and magnetic dipole moments despite the difference in their transformation properties in Equations (B.7) - (B.10). Mathematically, this arises from the factor of i in front of the magnetic field term in Equation (B.5). Physically, this means that interference of the electric and magnetic dipole decay channels into the cavity does not introduce any chirality (*i.e.*, preference for decays from $|\uparrow_e\rangle$ relative to $|\downarrow_e\rangle$) into the atom-cavity system, which is intuitive for a standing-wave optical cavity.

B.2.3 Angle dependence of the cyclicity

We now turn to computing the cyclicity and its dependence on the orientation of the external magnetic field defining the spin quantization axis. The branching ratio between spin-non-conserving and spin-conserving decays through the cavity is $R = \Gamma_{\perp}/(\Gamma_{||} + \Gamma_{\perp}) = |g_{\perp}|^2/(|g_{||}|^2 + |g_{\perp}|^2)$, and the cyclicity is $C = 1/R$. The spin eigenstates are given by the effective spin Hamiltonian:

$$H_Z = \mu_B \mathbf{B} \cdot \mathbf{g} \cdot \mathbf{S}, \quad (\text{B.17})$$

where \mathbf{B} is the applied magnetic field, $\mathbf{S} = \{\sigma_x, \sigma_y, \sigma_z\}$ is a vector of Pauli matrices, μ_B is the Bohr magneton and \mathbf{g} is a symmetric, real 3x3 matrix. For Er³⁺:YSO,

\mathbf{g} is highly anisotropic in both the ground and excited electronic states, with principal components (14.65, 1.80, 0.56) for the ground state and (12.97, 0.85, 0.25) for the excited state [52]. Note that the orientation of the eigenvectors of \mathbf{g} is different from the crystal axes and also slightly different between the ground and excited states. A consequence of the anisotropy of \mathbf{g} is that the spin eigenvectors are not generally parallel to the applied magnetic field.

The eigenvectors at one magnetic field orientation (φ', θ') can be expressed in terms of those at another orientation as: $|\uparrow_g(\varphi', \theta')\rangle = \alpha |\uparrow_g(\varphi, \theta)\rangle + \beta |\downarrow_g(\varphi, \theta)\rangle$. Denoting the matrix of atom-cavity coupling matrix elements in Equation (??) as $M(\varphi, \theta)$, we can transform it to another basis according to:

$$g_{||}(\varphi', \theta') = \langle \downarrow_g(\varphi', \theta') | M(\varphi, \theta) | \downarrow_e(\varphi', \theta') \rangle \quad (\text{B.18})$$

$$g_{\perp}(\varphi', \theta') = \langle \downarrow_g(\varphi', \theta') | M(\varphi, \theta) | \uparrow_e(\varphi', \theta') \rangle \quad (\text{B.19})$$

and evaluate the cyclicity as before.

We note that a similar model was applied to the orientation dependence of the *absorption* of linearly polarized light by Nd³⁺:YVO₄ in Ref. [135]. The applicability of this model to *emission* in our work stems from the restriction of the emission to a single polarization by the high Purcell factor coupling to a single-mode, non-degenerate cavity.

This model is used to fit the data in Figure 6.4 of chapter 6. The model is fit using $M(100^\circ, 90^\circ)$ as the fit parameters, and the result is $g_{||} = e^{-i1.15}$, $g_{\perp} = 0.024 \times e^{-i1.476}$. Since the cyclicity only depends on the ratio of these quantities, we constrain $|g_{||}| = 1$.

B.2.4 Correction for free-space decay

As the Purcell factor is finite, free-space emission can influence the cyclicity when it is very large. We incorporate this by adding free space decays to the branching ratio expression, such that the cyclicity becomes C_0 when the cavity coupling vanishes:

$$C = \frac{\Gamma_{CD} + \Gamma_{AB}}{\Gamma_{CD}} = 1 + \frac{\Gamma_{AB}^0 + |g_{||}|^2/\kappa}{\Gamma_{CD}^0 + |g_{\perp}|^2/\kappa} = 1 + \frac{1 - 1/C_0 + P_{||}}{1/C_0 + P_{\perp}} \quad (\text{B.20})$$

In this expression, Γ_i^0 denotes the decay rate on transition i in the absence of a cavity, $C_0 = 1 + \Gamma_{AB}^0/\Gamma_{CD}^0$ is the cyclicity in the absence of a cavity, and $P_{||/\perp} = g_{||/\perp}^2/(\kappa\Gamma^0)$, where Γ^0 is the total decay rate out of the excited state in the absence of the cavity.

For the ions studied here with P of order several hundred, the inclusion of this correction does not meaningfully improve the fit. We believe this occurs because the fit function can artificially increase g_{\perp} by a small amount at the orientation of maximum cyclicity to account for the free space decay without significantly impacting the cyclicity at other angles. However, measuring the same ion with different Purcell factors (realized by changing the cavity detuning) makes the free-space decay evident and allows C_0 to be estimated (Section B.4).

B.2.5 Highest achievable cyclicity

For an atom with Purcell factor P and bare cyclicity C_0 , the highest possible cyclicity is $C = PC_0$, achieved when $g_{\perp} = 0$. This can always be realized by choosing the cavity polarization to be perpendicular to \mathbf{d}_{\perp} , for some spin quantization axis (although in the special case that $\mathbf{d}_{||} \parallel \mathbf{d}_{\perp}$, P will also vanish). In contrast, if the cavity polarization is fixed, it may be possible to tune the quantization axis angle to achieve $g_{\perp} = 0$. We consider three cases:

1. If the \mathbf{g} tensors in the ground and excited state are isotropic (or equal), it is always possible to choose an orientation of \mathbf{B} where $g_{\perp} = 0$. This can be proved from the normality of the matrix m formed by the upper-right 2x2 block of M .
2. If the \mathbf{g} tensors for the ground and excited states are not simultaneously diagonalizable (having different axes), then it is not possible to achieve $g_{\perp} = 0$ in

general. This is proved by the specific counterexample of Er³⁺:YSO, where we observe (in a numeric model) that g_{\perp} can be made small but never quite zero for certain values of M .

3. If the \mathbf{g} tensors for the ground and excited states are parallel but have different (non-zero) magnetic moments, it appears (numerically) to always be possible to make $g_{\perp} = 0$. We have not proven this mathematically.

Er³⁺:YSO falls into the second case because of the C_1 site symmetry of the Er site. However, the principal axes of the ground and excited state \mathbf{g} tensors are only rotated by about 15° from each other [52], which may explain the success in achieving high cyclicity anyway. Many other host crystals for REIs and other defects have higher site symmetry, which forces the alignment of the \mathbf{g} tensor axes to the crystal, and are therefore covered by the third case. Therefore, we expect that this technique is fairly general.

B.2.6 Correction of cyclicity estimate at small n_0 values

In Figure 6.3b and thereafter, the intensity autocorrelation $g^{(2)}$ has been fitted to an exponential function and the decay constant n_0 is utilized to extract $C = P_{\text{ex}}n_0$. This expression for C is only valid when $n_0 \gg 1$ because of the discrete time steps in the measurement. We estimate the value of C more accurately by using the following expression:

$$C = \frac{P_{\text{ex}}}{(1 - e^{-1/n_0})}, \quad (\text{B.21})$$

which reduces to the previous expression for C at large n_0 values.

B.2.7 Extracting n_0 from $g^{(2)}$ at low optical pumping rates

The spin relaxation time is extracted from fits to $g^{(2)}$ measurements as described in Figure 6.3b. When these time constants are longer than 1 s, the even- and odd-offset

$g^{(2)}$ time constants begin to differ. We believe this results from spectral diffusion of the optical transitions. Under the assumption that this is uncorrelated with the spin dynamics and acts identically on the A and B transitions, we find that the spin time constant can be isolated by fitting an exponential to the *difference* of the even- and odd-offset traces.

B.3 Calibration of P_{ex}

For the measurements in Figure 6.4 of chapter 6, we use saturating optical pulses to ensure $P_{\text{ex}} \approx 0.5$ regardless of the magnetic field orientation. The approximate value of P_{ex} is confirmed by counting the emitted photons and comparing to the independently measured collection and detection efficiency (Figure B.2). We note that the finite duration of the excitation pulse may allow for $P_{\text{ex}} > 0.5$ if a photon is emitted during the pulse and the ion is re-excited, and have observed increased values

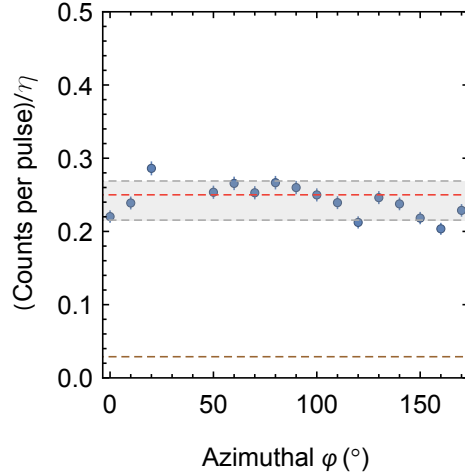


Figure B.2: P_{ex} calibration. Average number of collected photons following each excitation pulse during the measurement in Figure 6.4a. The photon numbers are scaled by the independently measured collection and detection efficiency $\eta = 0.020$. Since the spin is on average unpolarized and only resonant with the laser half of the time, $P_{\text{ex}} = 1/2$ (as defined here) corresponds to 1/4 photon per pulse. In all plots, error bars denote estimated $\pm 1\sigma$ statistical uncertainty.

of C at certain angles when using optical π pulses instead. In that sense, the values of C that we quote should be interpreted as lower bounds.

B.4 Estimate of intrinsic cyclicity of Er³⁺:YSO transition

A central claim of our work is that the cyclicity of the ion is enhanced by the optical cavity. Since the cyclicity C_0 of the spin transitions in Er³⁺:YSO without a cavity has not been previously measured, there is no direct basis for comparison. In ensemble experiments, C_0 has been estimated to be around 10 using measurements of the optical pumping rate and a number of simplifying assumptions [54]. We have attempted to measure C_0 using a single ion by detuning the cavity as much as possible, which increases the fraction of decays into free space and yields a weighted average of the cavity-enhanced C and C_0 (Equation B.20).

In Figure B.3c, we show several measurements of the same ion with increasing cavity detuning to decrease the total Purcell factor. The maximum cyclicity is strongly reduced: at the highest detuning, we observe a cyclicity of 53 ± 5 , which sets an upper bound on C_0 . In Supplementary Figure B.3d, we plot the cyclicity vs. detuning together with a theoretical model for several values of C_0 . From this model, we conclude that C_0 is less than 10, and likely closer to 2. Direct measurements at higher detunings are not possible because the count rate falls dramatically.

B.5 Single-shot measurement fidelity

Two factors contribute to the ML fidelity: the statistical error set by the signal-to-background ratio during the collection period (SNR), and the probability to decay

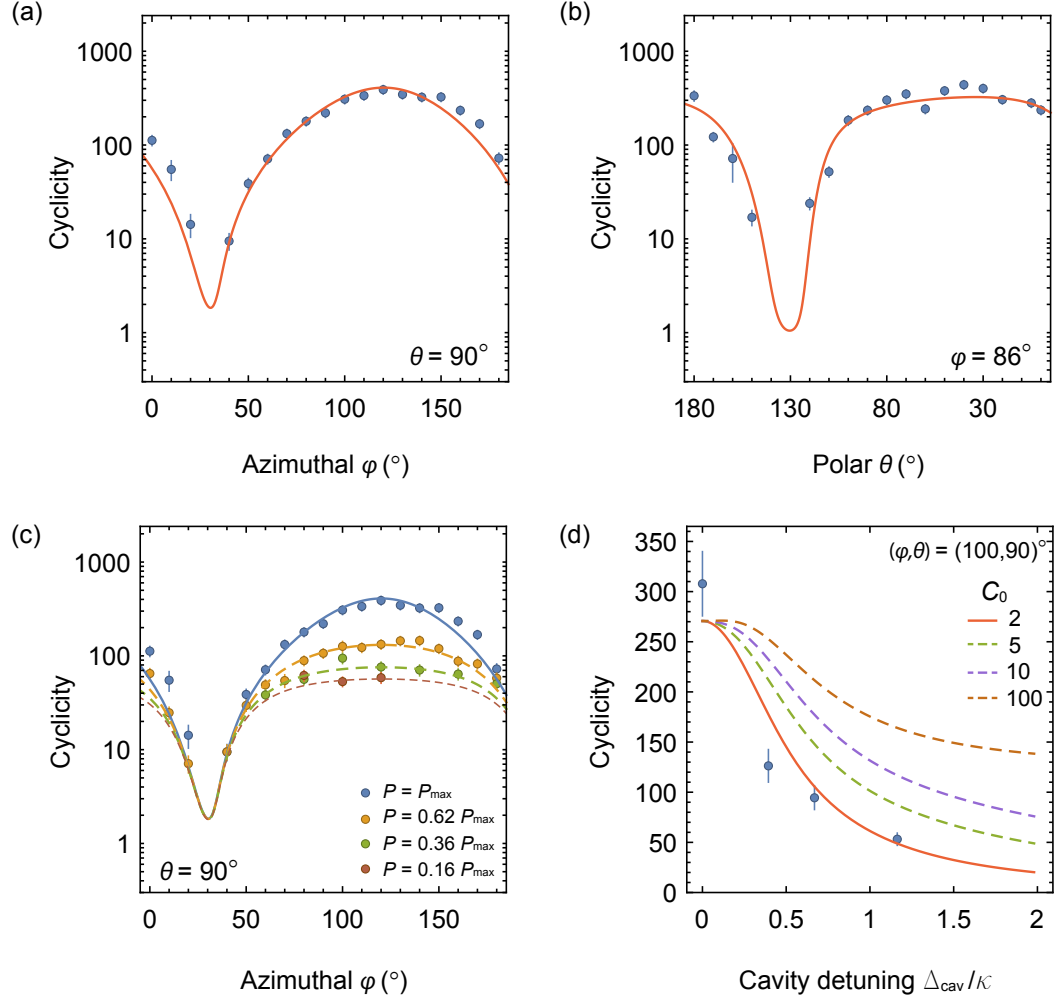


Figure B.3: **Extracting the bare ion cyclicity, C_0 .** (a,b) Cyclicity measurements on ion 2 (situated in a different cavity) show a similar orientation dependence to ion 1. Each of the two crystallographically inequivalent Y sites in YSO has two possible orientations related by a C_2 rotation about the b axis. Ion 2 is in the opposite site from ion 1, so we have inverted the θ axis to make the apparent dependence the same. (c) Measurement of cyclicity for the same ion 2 at several different Purcell factors, achieved by detuning the cavity from the atomic transition by an amount Δ_{cav} . The data is fit to Equation B.20. Here, $B = 112$ G and $\theta = 90^\circ$. (d) Cyclicity at $(\varphi, \theta) = (100, 90)^\circ$ vs. cavity detuning. The model is Equation B.20, where $P_{||}$ and P_{\perp} acquire a detuning dependence $P(\Delta_i) = \frac{P_{\max}}{1+(2\Delta_i/\kappa)^2}$ based on the known Zeeman splittings of the four transitions. Since the decay rates out of the two excited states are no longer equal when the cavity is detuned (*i.e.*, $\Gamma_A \neq \Gamma_B$), Equation B.20 is averaged over the two excited states. A fit yields $C_0 = 2 \pm 3$.

to the wrong state before enough photons are collected, $m/(\eta C)$, where m is the number of photons needed to reach the target fidelity F_T . m is related to the SNR as $F_T = SNR^m/(SNR^m + 1)$. In our experiment, SNR is typically high enough (14 for ion 1, limited by a timing error, and around 20 for ions 2 and 3, limited by dark counts) that by the time a single photon is detected, the error from the finite cyclicity is larger than the statistical error. In this regime, a nearly-optimal strategy is to infer that the spin state is $|\uparrow_g\rangle$ whenever an “A” photon is detected, and $|\downarrow_g\rangle$ whenever an “B” photon is detected. The average measurement fidelity is $1 - 1/(\eta C)$, and the average measurement duration is $t_{\text{meas}} = 1/(P_{\text{ex}}\eta C)$.

Based on this model, we can project how improved devices might lead to improved measurements. Assuming the same demonstrated cyclicity (1500), fiber-waveguide coupling and photon detection efficiency, but improving the cavity to realize $Q_{\text{int}} = 10^6$ with critical coupling ($\kappa_{\text{wg}} = \kappa_{\text{sc}}$) and using optical π pulses to increase P_{ex} to 1, it should be possible to realize an average measurement fidelity of 0.996 in average time of 50 μs . This assumes that SNR remains dark-count limited as the Purcell factor is increased.

B.6 Intrinsic spin relaxation

The spin relaxation rates in Figure 6.6a are fit to a model of the form $T_1^{-1} = T_{1,\text{dark}}^{-1} + P_{\text{ex}}/(t_{\text{rep}}C)$, where the repetition rate t_{rep} is varied to change the optical pumping strength. The intrinsic relaxation rate $T_{1,\text{dark}}$ varies strongly with the magnetic field amplitude, and the cyclicity C also has a weak dependence. The latter is explained by the larger Zeeman shift of the spin-non-conserving transitions CD (~ 13.1 MHz/Gauss) compared to the AB transitions (~ 2.5 MHz/Gauss) shifting the former out of resonance with the cavity more quickly Figure B.4). From this data, we can also affirm that the selective Purcell enhancement of the spin-conserving trans-

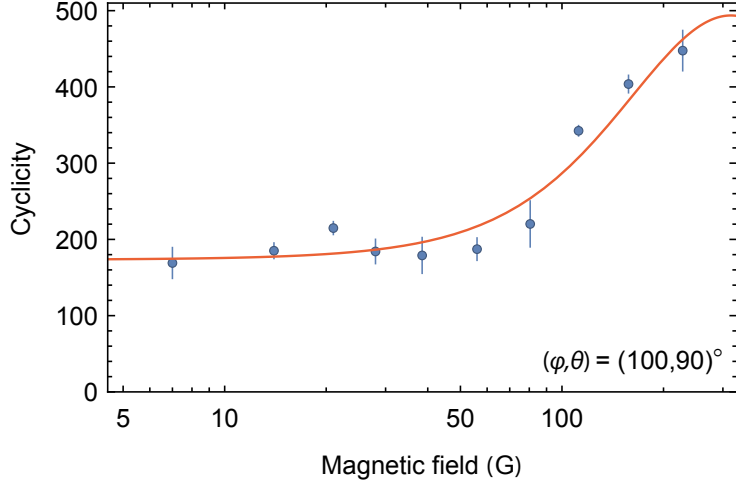


Figure B.4: **Magnetic field amplitude dependence of cyclicity.** Based on the data for Ion 2 in Figure 6.6ab of chapter 6, we extract the cyclicity of the optical transitions at a fixed magnetic field orientation for varying field amplitudes. The data is fit to the model in Equation B.20, incorporating the detuning-dependence of the Purcell enhancement as described in the caption to Figure B.3. C_0 fits here to 5 ± 1 .

sition does not primarily arise from detuning the CD transitions, as in Ref. [111], although this effect does provide an additional factor of 2-3 at the highest magnetic fields.

The magnetic field dependence of $T_{1,\text{dark}}$ disagrees markedly with predictions based on the measured coefficients for the Raman, Orbach and direct processes for Er³⁺:YSO [97]. At $T = 0.5$ K, these are dominated by the direct process, which should have a magnetic field dependence $T_1 \propto B^{-4}$, which arises from the combination of the frequency-dependence of the phonon density of states and the magnetic field-dependence of the spin-phonon coupling [112]. The measured values display a $B^{1/2}$ dependence at low fields, transitioning to a more rapid increase around $B = 50$ Gauss before saturating at 200 Gauss. We note that the point where $T_{1,\text{dark}}$ saturates is roughly consistent with the onset of the direct process, and that the disagreement could be attributed to anisotropy in the direct process rate. Anomalous magnetic field dependence in the low-field relaxation of rare earth ions has been previously

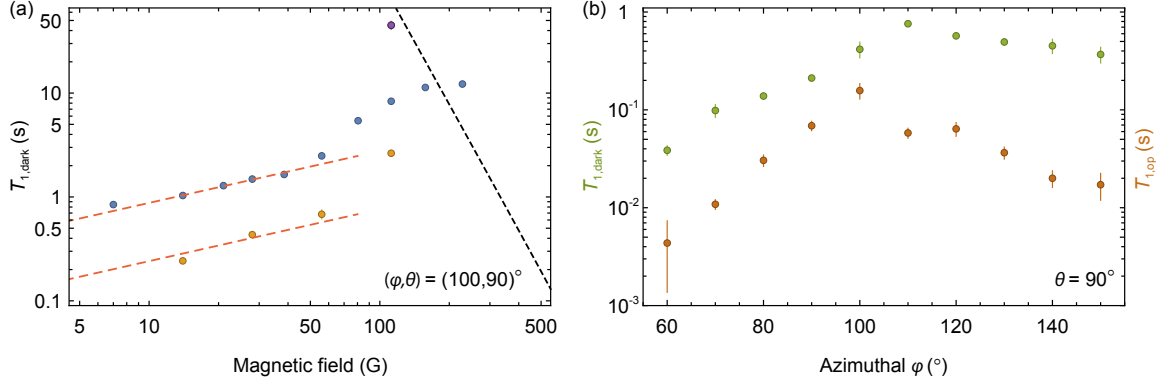


Figure B.5: Additional measurements of $T_{1,\text{dark}}$. (a) Intrinsic spin relaxation time ($T_{1,\text{dark}}$) of ion 1 (yellow) measured under the same conditions as ion 2 (blue points, reproduced from Figure 6.6b). $T_{1,\text{dark}}$ for ion 3 (purple point, reproduced from Figure 6.6c), measured for a field oriented along $(\varphi, \theta) = (130, 90)^\circ$, is also included here. The empirical $B^{1/2}$ scaling observed at low fields is indicated by the red, dashed line. The relaxation rate for ion 1 follows a similar trend to ion 2 but is 4 times faster. The black, dashed line is the model from Ref. [97]. (b) $T_{1,\text{dark}}$ (green points) measured at a few field orientations ($B = 28$ G) reveal the anisotropic nature of $T_{1,\text{dark}}$. The angle dependence qualitatively agrees with flip-flop limited $\text{Er}^{3+}:\text{YSO}$ lifetimes measured in Ref. [115]. The brown points denote the optical pumping time constants under these conditions, showing that the cyclicity measurements are generally not limited by $T_{1,\text{dark}}$.

observed in electron paramagnetic resonance [156] without a definitive explanation. Concentration-dependent spin relaxation has been observed in spectral hole burning experiments [115] and attributed to flip-flop interactions between nearby Er ions. This is a likely explanation for our observations, which is bolstered by the difference in $T_{1,\text{dark}}$ for different ions [which may arise from the stochastic arrangement of ions in this low-density sample ($[\text{Er}] \approx 300$ ppb)] and a strong anisotropy in $T_{1,\text{dark}}$ (Figure B.5).

Appendix C

Additional data, analyses, and methods for the experiments presented in Chapter 7

C.1 Experimental configuration

This section lays out a detailed description of our experimental setup (Figure C.1(a)). A tunable laser (Toptica CTL1500), stabilized to a reference cavity (Stable Laser Systems), provides a single tone optical signal f_{laser} . Optical pulses are generated using an intensity modulating electro-optic modulator (IM-EOM, Lucent X-2623Y) and two acousto-optic modulators (AOMs, Isomet 1205C-1 and 1250C-868) in series. The two AOMs cumulatively provide a 142 dB optical power extinction ratio (one double-pass, one single-pass). The light enters a ^3He cryostat (BlueFors LD250HE) in a single-mode optical fiber and is coupled to the PC cavity (Figure C.2) using a grating coupler [85] with 40% one-way efficiency. The fiber end, mounted on top of a three-axis nanopositioner (Attocube), is angle-polished to guide and couple light into the grating coupler [85]. Returning photons are separated using a 90:10 beamsplitter and detected in a superconducting nanowire single photon detector (SNSPD, Quantum Opus) in a separate, 2.2 K cryostat.

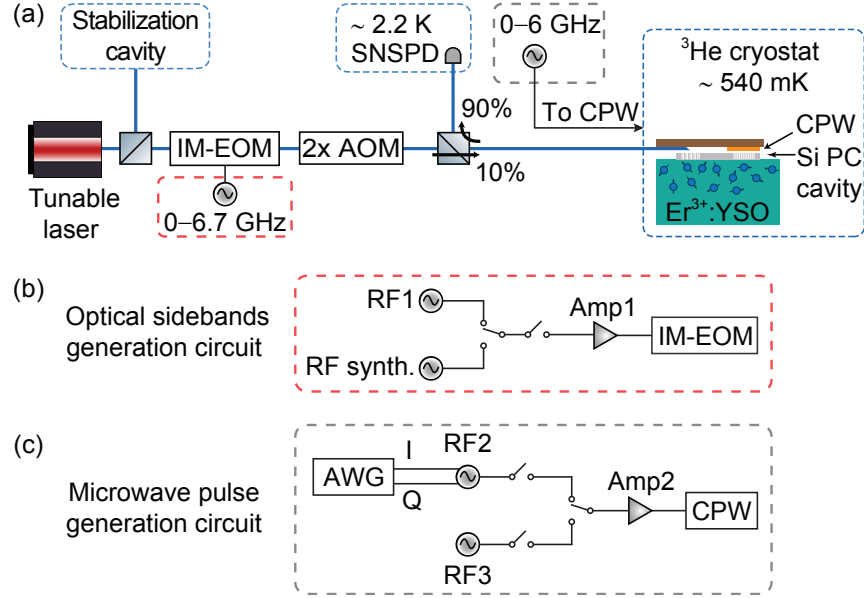


Figure C.1: **Experimental configuration for results reported in Chapter 7.**
(a) Sketch of the experimental setup. **(b,c)** Optical sidebands and microwave (MW) pulse generation circuit diagrams. See Section C.1 for abbreviations. *Additional component details:* Amp1, Mini-Circuits ZHL-4240W+; Amp2, Mini-Circuits ZHL-30W-252+; SPDT switches, Mini-Circuits ZASWA2-50DR-FA+.

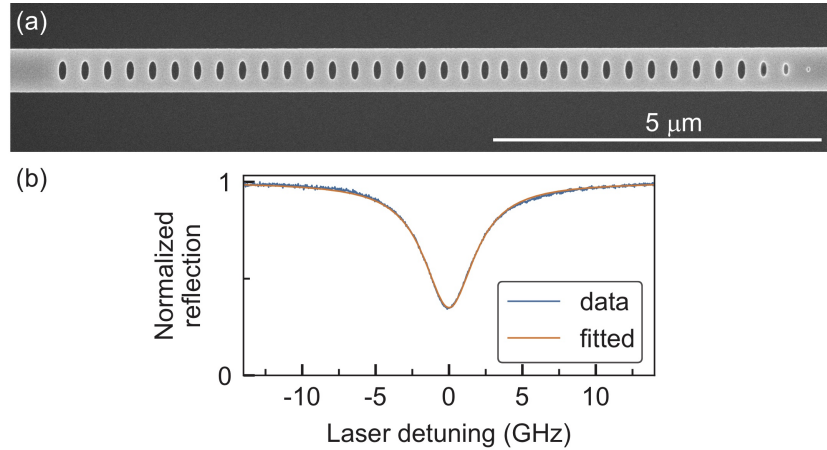


Figure C.2: **Device details for results reported in Chapter 7.** **(a)** Scanning electron microscope image of a representative silicon photonic crystal cavity. **(b)** Reflection spectrum of the cavity used in this work with a measured quality factor $Q = 4.6 \times 10^4$.

To enable fast switching of the laser frequency, we address the ions using RF sidebands generated by the IM-EOM (Figure C.1b), with a DC bias chosen to suppress

the carrier transmission. The initialization and readout sequences require switching the sideband frequency on the $\sim 100 \mu\text{s}$ timescale, which is accomplished with a fast-switching RF generator (RF synth., Holzworth HSM6001B), while the optical phase shift pulse is generated by a separate synthesizer (RF1, SRS SG386). The spin transitions are driven with microwave magnetic fields generated by a coplanar waveguide attached to the end of the optical fiber. The ground and excited state spin transitions are driven by separate synthesizers (RF2 and RF3, respectively; SRS SG386) with signals being amplified to 21 W before entering the cryostat (Figure C.1c). An arbitrary waveform generator (AWG, Agilent 33622) drives an IQ mixer that modulates the signal from RF2 to generate MW pulses with different phases for the ground state.

C.2 State-selective initialization of spins

In this section, we provide a detailed characterization of the state-selective initialization protocol. A sketch of the protocol for initializing the spins is shown in Figure C.3b,c. The initialization fidelity is significantly better than the readout fidelity, such that we cannot directly probe the initialization error. To get a better estimate of the initialization fidelity, we look at the photon number distributions during the measurement while implementing the pulse sequence in Figure C.3a. In an ideal case of perfect initialization to $|\uparrow\rangle$, a histogram of detected photon counts while exciting the ion using transition B exhibits a dark count-limited Poisson distribution. Imperfect initialization leads to the presence of an additional Poisson distribution with a higher mean photon count due to residual population in $|\downarrow\rangle$. Representative histograms of B photons while ion 1 and ion 2 are initialized to $|\uparrow\rangle$ are shown in Figure C.3d,e. The data is fitted to a bimodal Poisson distribution of the form $A_d \exp(-\mu_d) \mu_d^x / x! + A_b \exp(-\mu_b) \mu_b^x / x!$, where μ_b, μ_d are the mean photon counts while exciting each ion on the A,B transitions (when the ions are initialized to $|\uparrow\rangle$),

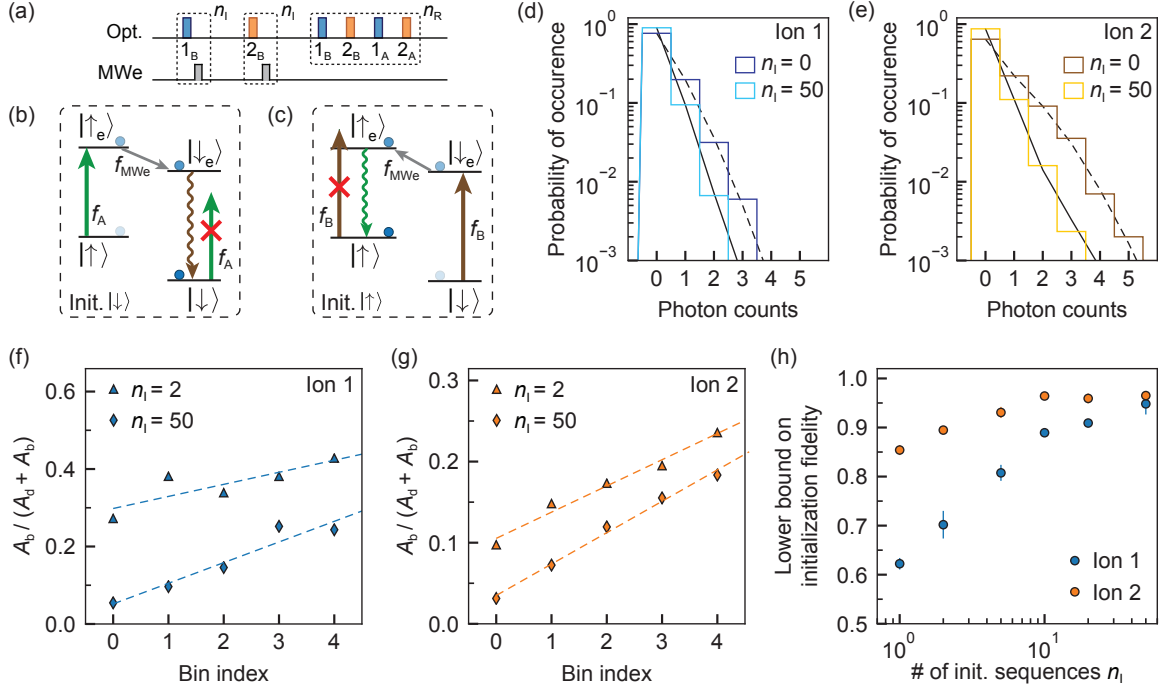


Figure C.3: Spin initialization of ions 1 and 2. (a) Pulse scheme used for spin initialization (here, to $|\uparrow\rangle$) and readout. (b,c) Schematics depicting a combination of resonant optical and MW driving the excited state to initialize an Er^{3+} ion to $|\downarrow\rangle$ and $|\uparrow\rangle$. (d,e) Histograms of B photon counts when ion 1 and ion 2 are initialized to $|\uparrow\rangle$ for different n_i . Black lines (solid and dashed) are fits to a bimodal Poisson distribution (see Section C.2). Photons acquired during the first 50 readout pulses for each ion are considered here. (f,g) Fitted amplitudes of the bimodal distribution. Each bin consists of 50 consecutive readout pulses. Fitting the data to a linear function reveals y -intercept as an upper bound on the initialization *infidelity*. (h) Initialization fidelity for the two ions using varying number of initialization sequences n_i .

and A_b, A_d are the fitted amplitudes of corresponding distributions. If μ_b is big enough that the histogram is bimodal, A_b can be fitted with high precision.

However, finite cyclicity of the spin-conserving transitions A,B introduces a small probability ($\propto n_R$, for $n_R \ll$ cyclicity) to flip the electron spin during the readout process. To that end, while the readout sequence involves $n_R = 250$ pulses, we compute photon count histograms considering each group of 50 consecutive readout pulses (denoted as a “bin”) at a time, and fit the histograms to the aforemen-

tioned bimodal Poisson distribution. We conservatively interpret $A_b/(A_b + A_d)$ to be the probability that the spin was in the wrong state at the *beginning* of the bin. As expected, the extracted probability value increases linearly with the bin index (Figure C.3f,g). By fitting a linear function to the data, we interpret the *y*-intercept to be an upper bound on the initialization *infidelity*. We show the result of this fidelity analysis for varying number of repetitions of the initialization sequence, n_I , in Figure C.3h, revealing initialization fidelity for ion 1 and ion 2 to be at least 95% and 97% respectively, using $n_I = 50$. The lower bound is limited by the finite probability of optically pumping the ion inside the first bin, and we believe that the saturated initialization fidelity should be nearly perfect, limited only by off-resonant driving of the wrong transition. The slower rate of saturation and inferior initialization fidelity of ion 1 can be attributed to its larger spectral diffusion, leading to less efficient optical excitation probability per pulse.

C.3 Spin coherence

We measure the ground state spin T_1 value by initializing ions to the $|\downarrow\rangle$ state and performing spin readout at varying delay times (t_{delay}); a single exponential fit to the data gives T_1 of 19.9 ± 4.1 seconds and 23.3 ± 1.3 seconds for ion 1 and ion 2, respectively (Figure C.4a). Ramsey measurements reveal T_2^* of 88 ± 9 ns and 94 ± 6 ns, respectively, extracted from fitting a single exponential to the data (Figure C.4b). For the optical phase control, we embed optical pulses within an XY8 sequence. The coherence decay during an XY8 sequence of total length t is well-described by a Gaussian $\exp[-(t/T_2)^2]$ with $T_{2,\text{XY8}}$ of 16.5 ± 0.5 μs and 15.3 ± 0.3 μs (Figure C.4c).

We note that a spin coherence time of 110 ± 7 μs can be achieved using a CPMG dynamical decoupling sequence with 128 MW π pulses (Figure C.5). Other spin coherence characteristics of ion 5 were reported in Chapter 6 (in that chapter, it

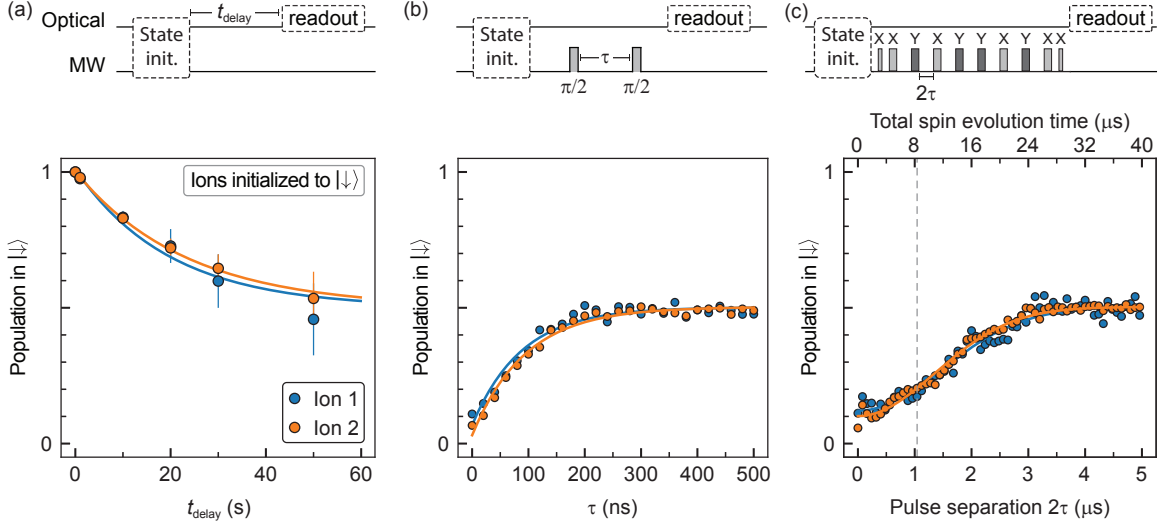


Figure C.4: **Spin coherence of ions 1 and 2.** (a) Measurement of T_1 . (b) Measurement of T_2^* . (c) Measurement of coherence during XY8 sequence. The dashed line denotes the pulse separation ($2\tau = 1042$ ns) used for all experiments in Figures 7.3 and 7.4. All measurements were performed with the magnetic field configuration $(B, \theta, \phi) = (112 \text{ G}, 90^\circ, 150^\circ)$.

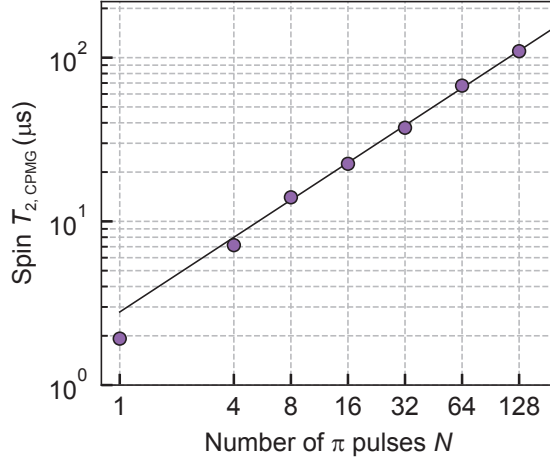


Figure C.5: **Extended spin coherence time of ion 5.** Measurement of spin $T_{2,\text{CPMG}}$ for ion 5 using a CPMG dynamical decoupling sequence with increasing number of MW π pulses at $(B, \theta, \phi) = (112 \text{ G}, 90^\circ, 130^\circ)$. The solid line is a fit to the power function $A \cdot N^k$, with fitted $A = 2.80 \pm 0.20 \mu\text{s}$ and $k = 0.76 \pm 0.02$.

was referred as “ion 3”), with values of $T_1 = 45 \pm 4$ seconds, $T_2^* = 125 \pm 5$ ns, $T_{2,\text{Hahn echo}} = 3.3 \pm 0.2 \mu\text{s}$ reported for experiments performed at slightly different magnetic field configurations.

C.4 Single qubit gates

C.4.1 Theory of ion-selective phase-shifts and loss of visibility

We apply detuned optical pulses to accumulate phase shift using AC Stark effect. Consider the atom as a two-level system $\{|g\rangle, |e\rangle\}$ with a transition splitting of $\hbar\omega_0$, driven by a laser at frequency ω . Under the dipole approximation, the effective non-Hermitian Hamiltonian in the rotating frame of the laser field (making the rotating-wave approximation) is given by:

$$H = \frac{\hbar\Omega}{2}(|g\rangle\langle e| + |e\rangle\langle g|) - \hbar(\Delta + i\Gamma/2)|e\rangle\langle e|, \quad (\text{C.1})$$

where Ω is the Rabi frequency, $\Delta = \omega - \omega_0$ is the detuning of the optical drive from the transition frequency, and Γ is the spontaneous emission rate. The perturbed ground state and its corresponding energy shift are:

$$|\psi\rangle = |g\rangle + \frac{\sqrt{(\Delta + i\Gamma/2)^2 + \Omega^2} - (\Delta + i\Gamma/2)}{\Omega}|e\rangle \approx |g\rangle + \frac{\Omega}{2(\Delta + i\Gamma/2)}|e\rangle \quad (\text{C.2})$$

$$\Delta E = \text{Re} \left\{ \frac{\hbar}{2} \left[\sqrt{(\Delta + i\Gamma/2)^2 + \Omega^2} - (\Delta + i\Gamma/2) \right] \right\} \approx \hbar \frac{\Omega^2}{4} \frac{\Delta}{\Delta^2 + \Gamma^2/4} \quad (\text{C.3})$$

for $\Omega \ll \sqrt{\Delta^2 + \Gamma^2/4}$. For a given laser frequency, the two spin-conserving transitions A,B of an Er^{3+} ion experience dissimilar detunings, denoted by Δ_A, Δ_B . However, Ω must be the same for the two transitions since the spin states originating from the same doublet are related to each other via time-reversal symmetry [32]. Treating these transitions as two independent two-level systems, the net phase shift imprinted between $|\downarrow\rangle$ and $|\uparrow\rangle$ resulting from the detuned optical pulse is:

$$\phi = T \frac{\Omega^2}{4} \left(\frac{\Delta_B}{\Delta_B^2 + \Gamma^2/4} - \frac{\Delta_A}{\Delta_A^2 + \Gamma^2/4} \right), \quad (\text{C.4})$$

where T is the optical pulse width. On the other hand, due to mixing of $|e\rangle$ in the perturbed ground state (Equation C.2), there is a possibility of spontaneous emission from the excited state, which reduces the visibility (\mathcal{V}) of the fringes in the phase

shift measurements. This can be calculated perturbatively from the excited state population $\Omega^2/(4\Delta^2 + \Gamma^2)$ for each transition as:

$$\Delta\mathcal{V} = 1 - \exp \left[-T\Gamma \frac{\Omega^2}{4} \frac{1}{2} \left(\frac{1}{\Delta_A^2 + \Gamma^2/4} + \frac{1}{\Delta_B^2 + \Gamma^2/4} \right) \right]. \quad (\text{C.5})$$

For far-detuned optical drive pulses ($\Delta_A, \Delta_B \gg \Gamma$), Equations C.4 and C.5 reduces to the following forms:

$$\phi = T \frac{\Omega^2}{4} \left(\frac{1}{\Delta_B} - \frac{1}{\Delta_A} \right), \quad \Delta\mathcal{V} = 1 - \exp \left[-T\Gamma \frac{\Omega^2}{4} \frac{1}{2} \left(\frac{1}{\Delta_A^2} + \frac{1}{\Delta_B^2} \right) \right]. \quad (\text{C.6})$$

C.4.2 Linewidth broadening

In our experiments, the observed linewidth is more than two orders of magnitude broader than the spontaneous emission rate, presumably because of spectral diffusion. While the calculation above estimates the loss of coherence from radiative decay of the excited state, the spin can also dephase from fluctuations in the optical transition frequency that cause uncertainty in the AC Stark shift. From numerical simulations of the master equation (Figure C.6), we find that the functional form of the loss of coherence (Equation C.5) is identical for the following cases: pure radiative decay, pure dephasing, or slow diffusion of the transition with a Lorentzian probability distribution. If multiple processes are present, the functional form is unchanged and their (Lorentzian) linewidths sum. Conversely, slow diffusion with a Gaussian probability distribution gives rise to a different line shape. In the experiment, we do not probe the loss or lineshape with sufficient precision to distinguish these cases.

C.4.3 Simultaneous arbitrary rotations on two qubits

Universal control of a single qubit requires arbitrary rotations around two orthogonal axes. MW control alone imparts arbitrary but identical rotations on all spin qubits

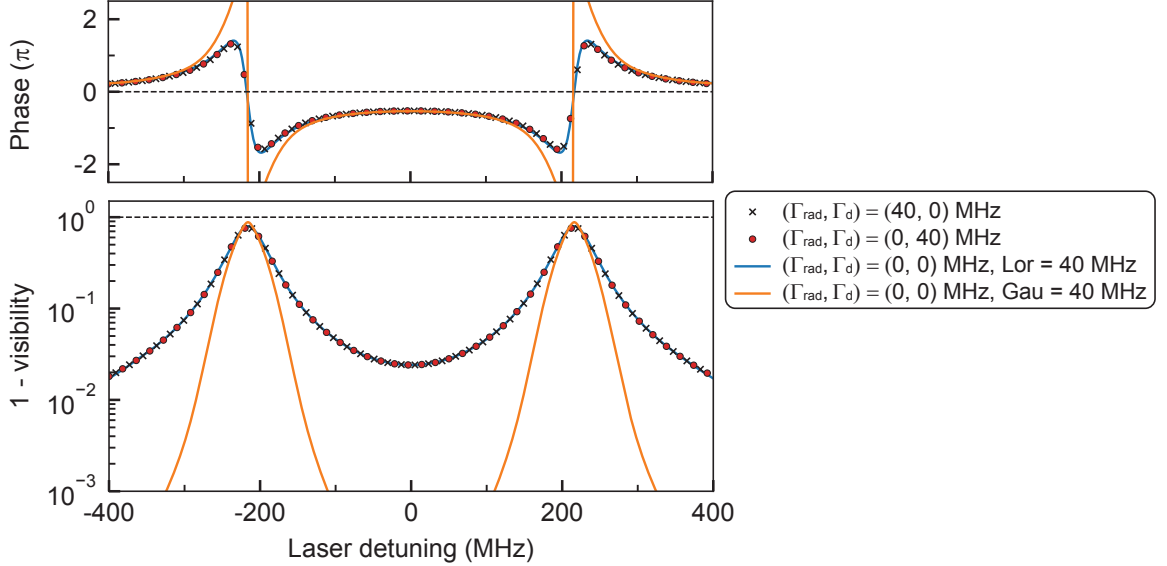


Figure C.6: Simulation results for the phase shift and change in visibility. Numerical simulation of the master equation with line broadening from different sources. To consider the slow spectral diffusion effect, we average the results over different spectral profiles including Gaussian (“Gau.”) and Lorentzian (“Lor.”). Γ_{rad} and Γ_d represent broadening due to radiative relaxation and dephasing, respectively. The linewidths listed for Gaussian and Lorentzian profiles are FWHM.

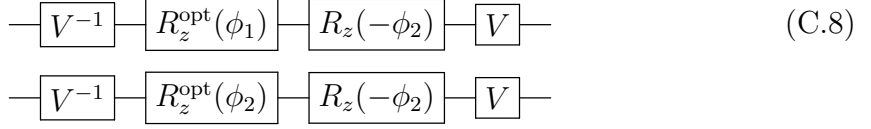
since it addresses the spins *globally*. In this section, we theoretically show that arbitrary rotations on multiple spins can be achieved by combining MW rotations and ion-selective optical z rotations.

We start with the simple case of two qubits. Arbitrary unitary operations on two qubits of the form $U \otimes U'$ can be decomposed into two consecutive operations $U \otimes \mathbb{I}$ and $\mathbb{I} \otimes U'$. First, let's implement the operation $U \otimes \mathbb{I}$. Consider the following quantum circuit:

$$\begin{array}{c} \boxed{V^{-1}} \quad \boxed{R_z^{\text{opt}}(\phi_1)} \quad \boxed{V} \\ \hline \end{array} \quad \begin{array}{c} \boxed{V^{-1}} \quad \boxed{R_z^{\text{opt}}(\phi_2)} \quad \boxed{V} \\ \hline \end{array} \quad (\text{C.7})$$

where $R_z^{\text{opt}}(\phi_j)$ is the ion-selective optical z rotation and V is a global unitary rotation using MW pulses. To implement identity operation on qubit 2, we can insert a global z rotation $R_z(-\phi_2)$, which can be accomplished by shifting the phase of MW pulses

in V relative to V^{-1} :



Since the phase shifts on qubit 2 cancel each other, we have $VV^{-1} = \mathbb{I}$. Therefore, the problem statement of implementing $U \otimes \mathbb{I}$ reduces to finding a matrix V such that $VR_z(\phi)V^{-1} = U$, where $\phi = \phi_1 - \phi_2$. Without loss of generality, U can be represented as a rotation of angle α about an arbitrary axis \hat{n} : $U = R_{\hat{n}}(\alpha) \equiv \exp(-i\alpha \hat{n} \cdot \vec{\sigma}/2) = \cos(\alpha/2)\mathbb{I} - i \sin(\alpha/2)\hat{n} \cdot \vec{\sigma}$, where $\vec{\sigma} = (\sigma_x, \sigma_y, \sigma_z)$ is the Pauli vector. Denoting the unit vector \hat{n} as $\hat{n} = (\sin \theta \cos \beta, \sin \theta \sin \beta, \cos \theta)$, we can write U in the matrix notation as,

$$U = \begin{bmatrix} \cos(\alpha/2) - i \sin(\alpha/2) \cos \theta & -ie^{-i\beta} \sin(\alpha/2) \sin \theta \\ -ie^{i\beta} \sin(\alpha/2) \sin \theta & \cos(\alpha/2) + i \sin(\alpha/2) \cos \theta \end{bmatrix} \quad (\text{C.9})$$

The matrix U can be diagonalized, revealing eigenvalues of $e^{\pm i\alpha/2}$. By using the corresponding eigenvectors (u_1, u_2) we can construct matrix V as,

$$V = [u_1, u_2] = \begin{bmatrix} \cos(\theta/2) & -e^{-i\beta} \sin(\theta/2) \\ e^{i\beta} \sin(\theta/2) & \cos(\theta/2) \end{bmatrix} \quad (\text{C.10})$$

so that $V^{-1}UV$ is diagonalized, leading to,

$$V^{-1}UV = \begin{bmatrix} e^{-i\alpha/2} & 0 \\ 0 & e^{i\alpha/2} \end{bmatrix} = R_z(\alpha) \quad (\text{C.11})$$

Therefore, the constructed matrix V satisfies the equation $VR_z(\phi)V^{-1} = U$ if $\phi = \alpha$, thereby implementing $U \otimes \mathbb{I}$. Moreover, the matrix V can also be expressed in terms of rotations about y and z axes, as $V = R_z(\beta)R_y(\theta)R_z(-\beta)$, which makes it easy to implement using MW pulses. $\mathbb{I} \otimes U'$ can also be implemented using the same sequence (C.8) but with $R_z(-\phi_1)$ instead.

As an example, for arbitrary x rotations ($\theta = 90^\circ$, $\beta = 0^\circ$), $V = R_y(\pi/2)$, which has been utilized to perform arbitrary x rotations in Figure 7.4a,b of Chapter 7. This protocol could be extended to $N > 2$ ions by considering $N - 1$ ion-selective optical z rotations together with global MW control.

C.5 Additional measurements on four ions

In this section, we provide additional details of measurements performed on the four ions labeled ion 3 through ion 6 (Figure 7.1b). The PC cavity is tuned to a spectral location such that spectral lines of all the four ions are situated within a cavity linewidth away from the cavity resonance.

Similar to ion 1 and ion 2 in Figure 7.2a, these ions also exhibit strong magnetic field orientation dependence of the spin-conserving transitions' cyclicity (Figure C.7). A magnetic field configuration of $(B, \theta, \varphi) = (112 \text{ G}, 90^\circ, 110^\circ)$ is chosen as an effective compromise that enables high cyclicities (780, 840, 750, and 850, respectively while using optical π -pulses) on the readout transitions, which are different for each

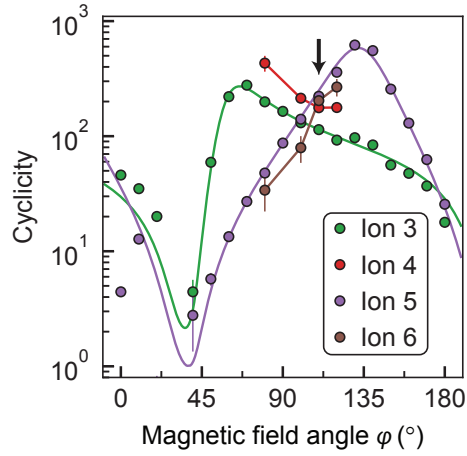


Figure C.7: **Four-ion cyclicity.** Magnetic field orientation dependence of cyclicity of the optical transitions measured for four ions ($B = 112 \text{ G}$, $\theta = 90^\circ$). Results for ion 3 and ion 5 are fitted to a theoretical model from Ref. [32]. Black arrow at $\varphi = 110^\circ$ denotes the orientation used in all subsequent experiments.

ion and chosen based on their relative spectral position with respect to the cavity resonance. Note that these cyclicities are slightly different from those in Figure C.7, which were obtained with long, saturating optical pulses instead of π -pulses.

We perform state-selective initialization experiments equivalent to the ones discussed in Section C.2, achieving near-unity initialization fidelity for all four ions with 50 repetitions of the initialization sequence. Following optimization on the number of readout pulses for each ion, we implement the pulse sequence shown in Figure 7.5a to perform simultaneous single-shot spin measurements. The average photon counts detected within the readout window for each ion is shown in Figure C.8 for varying combinations of four-ion initial states (note that the four-ion readout

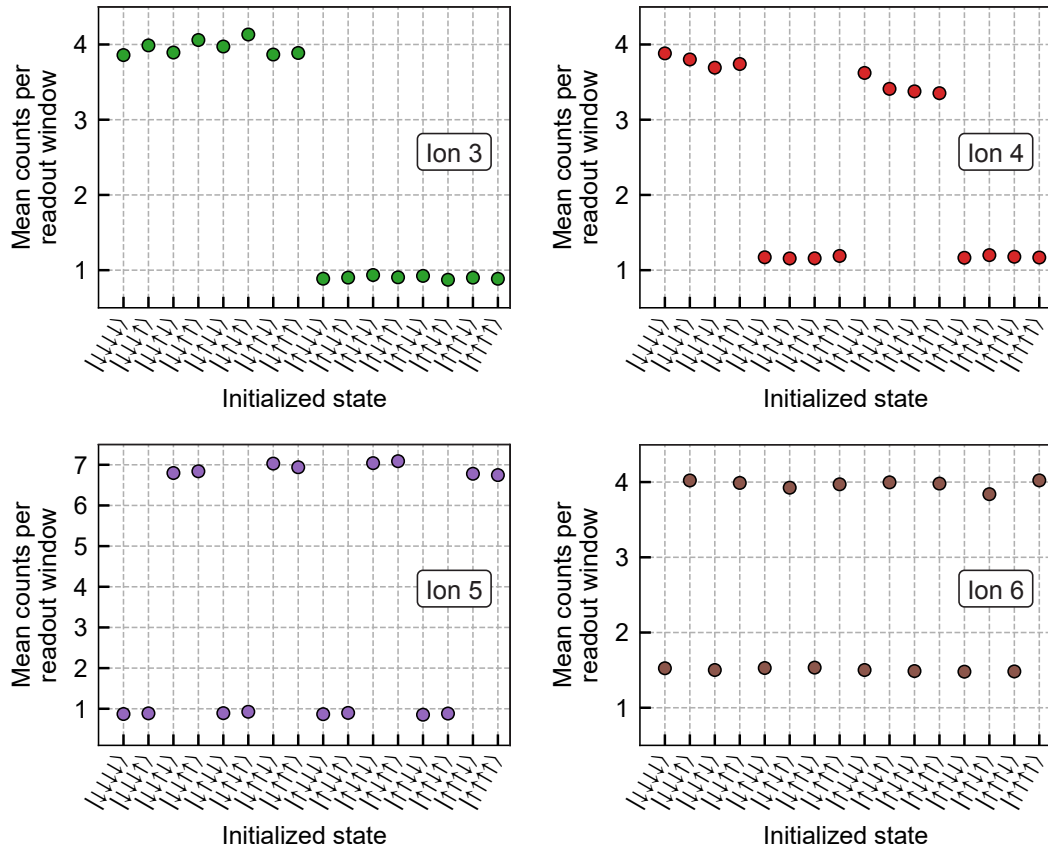


Figure C.8: **Measured photon counts per shot for four-ions.** Average photon counts detected within the readout sequence for each ion while implementing the pulse sequence in Figure 7.5a with varying initialized states but retaining the same readout sequence. $|\downarrow\uparrow\downarrow\uparrow\rangle$ corresponds to the product state $|\downarrow\rangle_{\text{ion } 3} \otimes |\uparrow\rangle_{\text{ion } 4} \otimes |\downarrow\rangle_{\text{ion } 5} \otimes |\uparrow\rangle_{\text{ion } 6}$.

configuration remains same throughout the experiment). For each ion, the detected photon counts are observed to be dependent only on its spin state and seemingly uncorrelated to operations performed on the other ions, indicating that measurement crosstalk in this multi-qubit initialization and readout scheme is small.

C.6 Generalization to N -ion control

Here, we address the generalization of the demonstrated local phase control to N ions (which was demonstrated for $N = 2$ ions in Figures 7.3 and 7.4 of Chapter 7).

The phase shifts can be expressed as a matrix equation $\mathbf{A} \cdot \mathbf{x} = \mathbf{b}$:

$$\begin{bmatrix} A_{1,1}, & A_{1,2}, & \cdots & A_{1,M} & \phi_0 \\ A_{2,1}, & A_{2,2}, & \cdots & A_{2,M} & \phi_0 \\ \vdots & \vdots & \ddots & \vdots & \vdots \\ A_{N,1}, & A_{N,2}, & \cdots & A_{N,M} & \phi_0 \end{bmatrix} \begin{bmatrix} x_1 \\ x_2 \\ \vdots \\ x_{M+1} \end{bmatrix} = \begin{bmatrix} b_1 \\ b_2 \\ \vdots \\ b_N \end{bmatrix} \quad (\text{C.12})$$

Here, $A_{i,j}$ represents the phase shift per unit time (see Equation C.4) generated on ion i ($i = 1, 2, \dots, N$) at the optical drive frequency f_j ($j = 1, 2, \dots, M$); x_j is the optical pulse width at f_j ; b_i is the target phase shift at ion i ; $\phi_{\text{MW}} \equiv \phi_0 x_{M+1}$ is the MW induced global z rotation ($\phi_0 \neq 0$). This equation has solutions \mathbf{x} for arbitrary \mathbf{b} as long as the columns of \mathbf{A} span \mathbb{R}^N , which will be true for most sets of frequencies $\{f_j\}$ with length $M \geq N - 1$. The negative pulse widths are accomplished by using phase shifts at corresponding optical drive frequencies with an opposite sign, as in Figures 7.3 and 7.4.

However, the question remains of what the *optimal* set of drive frequencies is that minimizes decoherence while allowing full phase control. Given a particular random instance of ion transition frequencies, we approach this as follows. First, we introduce a cost function $\mathbf{c}^T \cdot \mathbf{x}$, where c_j denotes the sum of errors (i.e. loss of visibility, see Eq. S5) per unit time for all ions due to the optical drive at f_j . Then, we construct a

very large frequency basis f_1, f_2, \dots, f_M ($M \gg N$) and exploit linear programming to find the optimal solution for a complete set of vectors \mathbf{b} (under the positivity constraint $\mathbf{x} \geq 0$, doubling the frequency list allows us to incorporate positive and negative phase shifts).

For each \mathbf{b} , the solutions have their weight concentrated on $N - 1$ (or fewer) drive frequencies as expected from the dimensionality of the problem. These frequencies differ between different \mathbf{b} , such that for a complete set \mathbf{b} , there are of order N^2 frequencies occurring in the optimal solutions. We can reduce this dramatically by re-running the linear programming with only these frequencies, and then removing them one at a time in order of impact on the cost function (averaged over \mathbf{b}). Empirically, we find that trimming the frequency list to length $2N$ has negligible impact on the error, while trimming to the minimum limit of $N - 1$ impacts the average error by less than a factor of 2 for $N = 20$ ions. Therefore, this approach is an efficient way to find a small set of optimal drive frequencies.

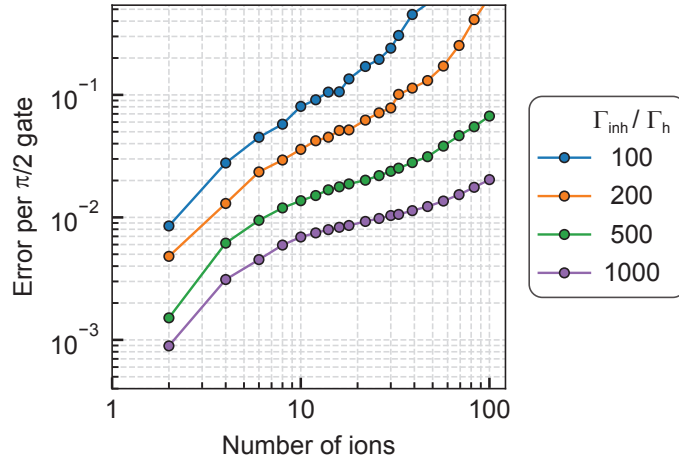


Figure C.9: Simulated optimal error for simultaneous control of multiple ions. Scaling of the optimized error with different numbers of ions for varying $\Gamma_{\text{inh}}/\Gamma_h$ ratios. $\Gamma_{\text{inh}} = 1$ GHz is used for all simulations, while the two spin-conserving optical transitions of each ion are Zeeman-split by 500 MHz.

In Figure C.9, we show the average optimized error for a $\pi/2$ rotation as a function of the number of ions N and the ratio of the inhomogeneous linewidth (Γ_{inh}) to the

homogeneous linewidth (Γ_h). The error presented is the *total* spontaneous emission probability $\mathbf{c}^T \cdot \mathbf{x}$ summed across all ions, averaged over all possible single-qubit $\pi/2$ rotations ($\mathbf{b} = [\pi/2, 0, \dots, 0]^T, [0, \pi/2, \dots, 0]^T, \dots, [0, 0, \dots, \pi/2]^T$). We compute this for 100 randomly selected sets of ion transition frequencies, and present the average of the best 90, removing the effect of pathologically bad distributions where two (or more) ions lie very close in frequency. As expected, the performance improves as the separation between ions (in units of Γ_h) increases. The error is shown before trimming the frequency list.

Furthermore, the inhomogeneous broadening of spin transitions can also be exploited to realize an ensemble of (MW) frequency-resolved spins. The frequency-multiplexing technique, when applied in both optical and MW domains, may enable more degrees of freedom for parallel control of larger spin ensembles with a higher fidelity.

Publications and Presentations

List of publications in chronological order (* Equally contributing authors):

1. A. M. Dibos*, M. Raha*, C. M. Phenicie*, and J. D. Thompson. Atomic source of single photons in the telecom band. *Physical Review Letters* **120**, 243601 (2018).
2. M. Raha, S. Chen, C. M. Phenicie, S. Ourari, A. M. Dibos, and J. D. Thompson. Optical quantum nondemolition measurement of a single rare earth ion qubit. *Nature Communications* **11**, 1605 (2020).
3. S. Chen*, M. Raha*, C. M. Phenicie, S. Ourari, and J. D. Thompson. Parallel single-shot measurement and coherent control of solid-state spins below the diffraction limit. *Science* **370**, 592–595 (2020).
4. S. Chen, S. Ourari, M. Raha, C. M. Phenicie, M. T. Uysal, and J. D. Thompson. Hybrid microwave-optical scanning probe for addressing solid-state spins in nanophotonic cavities. *Optics Express* **29**, 4902–4911 (2021).
5. D. Huang*, A. Abulnaga*, S. Welinski, M. Raha, J. D. Thompson, and N. P. de Leon. Hybrid III-V diamond photonic platform for quantum nodes based on neutral silicon vacancy centers in diamond. *Optics Express* **29**, 9174–9189 (2021).
6. M. Raha*, S. Chen*, M. T. Uysal*, C. M. Phenicie*, V. V. Dobrovitski, and J. D. Thompson. Coherent interactions between a single rare-earth ion and a nuclear spin in the solid-state. *Manuscript in preparation*.

List of presentations and posters in chronological order:

- M. Raha. Talk title: “Nanoscale Quantum-Optical Circuits with Rare Earth Ions”. Quantum Science and Engineering Group Meeting, Princeton University (Oct, 2017).
- M. Raha, A. M. Dibos, C. M. Phenicie, and J. D. Thompson. Poster title: “Atomic source of single photons in the telecom band”. PCCM/PRISM Poster Night, Princeton University (Feb, 2018).
- M. Raha, A. M. Dibos, C. M. Phenicie, and J. D. Thompson. Poster title: “Atomic source of single photons in the telecom band”. Gordon Research Conference Quantum Science, Stonehill College (July, 2018).
- M. Raha. Talk title: “Atomic source of single photons in the telecom band”. XIII Rare Earth Ions Workshop, University of Geneva (Oct, 2018).
- M. Raha. Talk title: “Spin dynamics of single erbium ions”. Princeton-GIA Diamond Symposium, Princeton University (Jan, 2019).
- M. Raha, C. M. Phenicie, A. M. Dibos, S. Chen, and J. D. Thompson. Poster title: “Spin dynamics of single erbium ions”. APS DAMOP meeting, Milwaukee (May, 2019).

Bibliography

- [1] H. J. Kimble. The quantum internet. *Nature* **453**, 1023–1030 (2008).
- [2] N. Gisin, G. Ribordy, W. Tittel, and H. Zbinden. Quantum cryptography. *Reviews of Modern Physics* **74**, 145 (2002).
- [3] C. Monroe, R. Raussendorf, A. Ruthven, K. Brown, P. Maunz, L.-M. Duan, and J. Kim. Large-scale modular quantum-computer architecture with atomic memory and photonic interconnects. *Physical Review A* **89**, 022317 (2014).
- [4] B. Hensen, H. Bernien, A. E. Dréau, A. Reiserer, N. Kalb, M. S. Blok, J. Ruitenberg, R. F. Vermeulen, R. N. Schouten, C. Abellán, *et al.* Loophole-free bell inequality violation using electron spins separated by 1.3 kilometres. *Nature* **526**, 682–686 (2015).
- [5] D. Gottesman, T. Jennewein, and S. Croke. Longer-baseline telescopes using quantum repeaters. *Physical Review Letters* **109**, 070503 (2012).
- [6] S. Wehner, D. Elkouss, and R. Hanson. Quantum internet: A vision for the road ahead. *Science* **362**, eaam9288 (2018).
- [7] W. K. Wootters and W. H. Zurek. A single quantum cannot be cloned. *Nature* **299**, 802–803 (1982).
- [8] H.-J. Briegel, W. Dür, J. I. Cirac, and P. Zoller. Quantum repeaters: the role of imperfect local operations in quantum communication. *Physical Review Letters* **81**, 5932 (1998).
- [9] B. B. Blinov, D. L. Moehrung, L.-M. Duan, and C. Monroe. Observation of entanglement between a single trapped atom and a single photon. *Nature* **428**, 153–157 (2004).
- [10] J. Volz, M. Weber, D. Schlenk, W. Rosenfeld, J. Vrana, K. Saucke, C. Kurtsiefer, and H. Weinfurter. Observation of entanglement of a single photon with a trapped atom. *Physical Review Letters* **96**, 030404 (2006).
- [11] E. Togan, Y. Chu, A. S. Trifonov, L. Jiang, J. Maze, L. Childress, M. G. Dutt, A. S. Sørensen, P. R. Hemmer, A. S. Zibrov, *et al.* Quantum entanglement between an optical photon and a solid-state spin qubit. *Nature* **466**, 730–734 (2010).

- [12] C. Nguyen, D. Sukachev, M. Bhaskar, B. Machielse, D. Levonian, E. Knall, P. Stroganov, C. Chia, M. Burek, R. Riedinger, *et al.* An integrated nanophotonic quantum register based on silicon-vacancy spins in diamond. *Physical Review B* **100**, 165428 (2019).
- [13] K. De Greve, L. Yu, P. L. McMahon, J. S. Pelc, C. M. Natarajan, N. Y. Kim, E. Abe, S. Maier, C. Schneider, M. Kamp, *et al.* Quantum-dot spin–photon entanglement via frequency downconversion to telecom wavelength. *Nature* **491**, 421–425 (2012).
- [14] D. L. Moehring, P. Maunz, S. Olmschenk, K. C. Younge, D. N. Matsukevich, L.-M. Duan, and C. Monroe. Entanglement of single-atom quantum bits at a distance. *Nature* **449**, 68–71 (2007).
- [15] C. Nölleke, A. Neuzner, A. Reiserer, C. Hahn, G. Rempe, and S. Ritter. Efficient teleportation between remote single-atom quantum memories. *Physical Review Letters* **110**, 140403 (2013).
- [16] H. Bernien, B. Hensen, W. Pfaff, G. Koolstra, M. S. Blok, L. Robledo, T. Taminiau, M. Markham, D. J. Twitchen, L. Childress, *et al.* Heralded entanglement between solid-state qubits separated by three metres. *Nature* **497**, 86–90 (2013).
- [17] W. Pfaff, B. J. Hensen, H. Bernien, S. B. van Dam, M. S. Blok, T. H. Taminiau, M. J. Tiggelman, R. N. Schouten, M. Markham, D. J. Twitchen, *et al.* Unconditional quantum teleportation between distant solid-state quantum bits. *Science* **345**, 532–535 (2014).
- [18] N. Kalb, A. A. Reiserer, P. C. Humphreys, J. J. Bakermans, S. J. Kamerling, N. H. Nickerson, S. C. Benjamin, D. J. Twitchen, M. Markham, and R. Hanson. Entanglement distillation between solid-state quantum network nodes. *Science* **356**, 928–932 (2017).
- [19] P. C. Humphreys, N. Kalb, J. P. Morits, R. N. Schouten, R. F. Vermeulen, D. J. Twitchen, M. Markham, and R. Hanson. Deterministic delivery of remote entanglement on a quantum network. *Nature* **558**, 268–273 (2018).
- [20] G. Zhang, Y. Cheng, J.-P. Chou, and A. Gali. Material platforms for defect qubits and single-photon emitters. *Applied Physics Reviews* **7**, 031308 (2020).
- [21] B. C. Rose, D. Huang, Z.-H. Zhang, P. Stevenson, A. M. Tyryshkin, S. Sangtawesin, S. Srinivasan, L. Loudin, M. L. Markham, A. M. Edmonds, *et al.* Observation of an environmentally insensitive solid-state spin defect in diamond. *Science* **361**, 60–63 (2018).
- [22] G. P. Agrawal. *Fiber-optic communication systems*. (John Wiley & Sons, Inc., New York, 2010).

- [23] Q. Li, M. Davanço, and K. Srinivasan. Efficient and low-noise single-photon-level frequency conversion interfaces using silicon nanophotonics. *Nature Photonics* **10**, 406–414 (2016).
- [24] A. Dréau, A. Tchebotareva, A. El Mahdaoui, C. Bonato, and R. Hanson. Quantum frequency conversion of single photons from a nitrogen-vacancy center in diamond to telecommunication wavelengths. *Physical Review Applied* **9**, 064031 (2018).
- [25] T. Walker, K. Miyanishi, R. Ikuta, H. Takahashi, S. V. Kashanian, Y. Tsujimoto, K. Hayasaka, T. Yamamoto, N. Imoto, and M. Keller. Long-distance single photon transmission from a trapped ion via quantum frequency conversion. *Physical Review Letters* **120**, 203601 (2018).
- [26] J. Yin, Y. Cao, Y.-H. Li, S.-K. Liao, L. Zhang, J.-G. Ren, W.-Q. Cai, W.-Y. Liu, B. Li, H. Dai, *et al.* Satellite-based entanglement distribution over 1200 kilometers. *Science* **356**, 1140–1144 (2017).
- [27] M. Lipson. Guiding, modulating, and emitting light on silicon-challenges and opportunities. *Journal of Lightwave Technology* **23**, 4222 (2005).
- [28] H. De Riedmatten, M. Afzelius, M. U. Staudt, C. Simon, and N. Gisin. A solid-state light-matter interface at the single-photon level. *Nature* **456**, 773–777 (2008).
- [29] E. Saglamyurek, N. Sinclair, J. Jin, J. A. Slater, D. Oblak, F. Bussieres, M. George, R. Ricken, W. Sohler, and W. Tittel. Broadband waveguide quantum memory for entangled photons. *Nature* **469**, 512–515 (2011).
- [30] C. Bradley, J. Randall, M. Abobeih, R. Berrevoets, M. Degen, M. Bakker, M. Markham, D. Twitchen, and T. Taminiau. A ten-qubit solid-state spin register with quantum memory up to one minute. *Physical Review X* **9**, 031045 (2019).
- [31] A. Dibos, M. Raha, C. Phenicie, and J. D. Thompson. Atomic source of single photons in the telecom band. *Physical Review Letters* **120**, 243601 (2018).
- [32] M. Raha, S. Chen, C. M. Phenicie, S. Ourari, A. M. Dibos, and J. D. Thompson. Optical quantum nondemolition measurement of a single rare earth ion qubit. *Nature Communications* **11**, 1605 (2020).
- [33] S. Chen, M. Raha, C. M. Phenicie, S. Ourari, and J. D. Thompson. Parallel single-shot measurement and coherent control of solid-state spins below the diffraction limit. *Science* **370**, 592–595 (2020).
- [34] M. Raha, S. Chen, M. T. Uysal, C. M. Phenicie, V. V. Dobrovitski, and J. D. Thompson. Coherent interactions between a single rare-earth ion and a nuclear spin in the solid-state. *Manuscript in preparation*.

- [35] A. I. Lvovsky, B. C. Sanders, and W. Tittel. Optical quantum memory. *Nature Photonics* **3**, 706–714 (2009).
- [36] N. Sangouard, C. Simon, H. De Riedmatten, and N. Gisin. Quantum repeaters based on atomic ensembles and linear optics. *Reviews of Modern Physics* **83**, 33 (2011).
- [37] R. M. Macfarlane. High-resolution laser spectroscopy of rare-earth doped insulators: a personal perspective. *Journal of Luminescence* **100**, 1–20 (2002).
- [38] T. Böttger, C. Thiel, R. Cone, and Y. Sun. Effects of magnetic field orientation on optical decoherence in $\text{Er}^{3+}:\text{Y}_2\text{SiO}_5$. *Physical Review B* **79**, 115104 (2009).
- [39] M. Zhong, M. P. Hedges, R. L. Ahlefeldt, J. G. Bartholomew, S. E. Beavan, S. M. Wittig, J. J. Longdell, and M. J. Sellars. Optically addressable nuclear spins in a solid with a six-hour coherence time. *Nature* **517**, 177–180 (2015).
- [40] A. J. Freeman and R. Watson. Theoretical investigation of some magnetic and spectroscopic properties of rare-earth ions. *Physical Review* **127**, 2058 (1962).
- [41] J. G. Bartholomew. *Investigation of the scalability of rare-earth-ion quantum hardware*. Ph.D. thesis, The Australian National University (2014).
- [42] R. Macfarlane and R. Shelby. Coherent transient and holeburning spectroscopy of rare earth ions in solids. In *Spectroscopy of Solids Containing Rare Earth Ions*, edited by A. A. Kaplyanskii and R. M. Macfarlane, *Modern Problems in Condensed Matter Sciences* **21**, 51–184 (Elsevier, 1987).
- [43] G. Liu and B. Jacquier. *Spectroscopic properties of rare earths in optical materials*. (Springer-Verlag Berlin Heidelberg, 2005).
- [44] R. Beach, M. D. Shinn, L. Davis, R. W. Solarz, and W. F. Krupke. Optical absorption and stimulated emission of neodymium in yttrium orthosilicate. *IEEE Journal of Quantum Electronics* **26**, 1405–1412 (1990).
- [45] C. Li, C. Wyon, and R. Moncorge. Spectroscopic properties and fluorescence dynamics of Er^{3+} and Yb^{3+} in Y_2SiO_5 . *IEEE Journal of Quantum Electronics* **28**, 1209–1221 (1992).
- [46] C. Li, R. Moncorge, J. Souriau, and C. Wyon. Efficient $2.05 \mu\text{m}$ room temperature $\text{Y}_2\text{SiO}_5:\text{Tm}^{3+}$ cw laser. *Optics Communications* **101**, 356–360 (1993).
- [47] C. Li, R. Moncorge, J. Souriau, C. Borel, and C. Wyon. Room temperature cw laser action of $\text{Y}_2\text{SiO}_5:\text{Yb}^{3+}$, Er^{3+} at $1.57 \mu\text{m}$. *Optics Communications* **107**, 61–64 (1994).

- [48] B. Lauritzen, J. Minář, H. De Riedmatten, M. Afzelius, N. Sangouard, C. Simon, and N. Gisin. Telecommunication-wavelength solid-state memory at the single photon level. *Physical Review Letters* **104**, 080502 (2010).
- [49] G. H. Fuller. Nuclear spins and moments. *Journal of Physical and Chemical Reference Data* **5**, 835–1092 (1976).
- [50] T. Böttger, Y. Sun, C. Thiel, and R. Cone. Spectroscopy and dynamics of Er³⁺:Y₂SiO₅ at 1.5 μm. *Physical Review B* **74**, 075107 (2006).
- [51] T. Böttger, C. Thiel, Y. Sun, and R. Cone. Optical decoherence and spectral diffusion at 1.5 μm in Er³⁺:Y₂SiO₅ versus magnetic field, temperature, and Er³⁺ concentration. *Physical Review B* **73**, 075101 (2006).
- [52] Y. Sun, T. Böttger, C. Thiel, and R. Cone. Magnetic g tensors for the ⁴I_{15/2} and ⁴I_{13/2} states of Er³⁺:Y₂SiO₅. *Physical Review B* **77**, 085124 (2008).
- [53] S. Probst, H. Rotzinger, S. Wünsch, P. Jung, M. Jerger, M. Siegel, A. Ustinov, and P. Bushev. Anisotropic rare-earth spin ensemble strongly coupled to a superconducting resonator. *Physical Review Letters* **110**, 157001 (2013).
- [54] S. Hastings-Simon, B. Lauritzen, M. U. Staudt, J. L. M. van Mechelen, C. Simon, H. de Riedmatten, M. Afzelius, and N. Gisin. Zeeman-level lifetimes in Er³⁺:Y₂SiO₅. *Physical Review B* **78**, 085410 (2008).
- [55] S. Probst, H. Rotzinger, A. Ustinov, and P. Bushev. Microwave multimode memory with an erbium spin ensemble. *Physical Review B* **92**, 014421 (2015).
- [56] C. M. Dodson and R. Zia. Magnetic dipole and electric quadrupole transitions in the trivalent lanthanide series: Calculated emission rates and oscillator strengths. *Physical Review B* **86**, 125102 (2012).
- [57] R. Kolesov, K. Xia, R. Reuter, R. Stöhr, A. Zappe, J. Meijer, P. Hemmer, and J. Wrachtrup. Optical detection of a single rare-earth ion in a crystal. *Nature Communications* **3**, 1029 (2012).
- [58] T. Utikal, E. Eichhammer, L. Petersen, A. Renn, S. Götzinger, and V. Sandoghdar. Spectroscopic detection and state preparation of a single praseodymium ion in a crystal. *Nature Communications* **5**, 3627 (2014).
- [59] I. Nakamura, T. Yoshihiro, H. Inagawa, S. Fujiyoshi, and M. Matsushita. Spectroscopy of single Pr³⁺ ion in LaF₃ crystal at 1.5 K. *Scientific Reports* **4**, 7364 (2014).
- [60] P. Siyushev, K. Xia, R. Reuter, M. Jamali, N. Zhao, N. Yang, C. Duan, N. Kukharchyk, A. Wieck, R. Kolesov, *et al.* Coherent properties of single rare-earth spin qubits. *Nature Communications* **5**, 3895 (2014).

- [61] E. M. Purcell. Spontaneous emission probabilities at radio frequencies. *Physical Review* **69**, 674 (1946).
- [62] L. Allen and J. H. Eberly. *Optical Resonance and Two-level Atoms*. (Dover Publications, New York, 1987).
- [63] H. J. Carmichael. *Statistical Methods in Quantum Optics 1: Master Equations and Fokker-Planck Equations*. (Springer-Verlag Berlin Heidelberg, 1999).
- [64] P. Rice and H. Carmichael. Single-atom cavity-enhanced absorption. I. Photon statistics in the bad-cavity limit. *IEEE Journal of Quantum Electronics* **24**, 1351–1366 (1988).
- [65] M. O. Scully and M. S. Zubairy. *Quantum Optics*. (Cambridge University Press, Cambridge, 1997).
- [66] T. Tiecke, J. D. Thompson, N. P. de Leon, L. Liu, V. Vuletić, and M. D. Lukin. Nanophotonic quantum phase switch with a single atom. *Nature* **508**, 241–244 (2014).
- [67] L. Robledo, L. Childress, H. Bernien, B. Hensen, P. F. Alkemade, and R. Hanson. High-fidelity projective read-out of a solid-state spin quantum register. *Nature* **477**, 574–578 (2011).
- [68] D. D. Sukachev, A. Sipahigil, C. T. Nguyen, M. K. Bhaskar, R. E. Evans, F. Jelezko, and M. D. Lukin. Silicon-vacancy spin qubit in diamond: a quantum memory exceeding 10 ms with single-shot state readout. *Physical review letters* **119**, 223602 (2017).
- [69] J. G. Bartholomew, R. L. Ahlefeldt, and M. J. Sellars. Engineering closed optical transitions in rare-earth ion crystals. *Physical Review B* **93**, 014401 (2016).
- [70] D. Huang, A. Abulnaga, S. Welinski, M. Raha, J. D. Thompson, and N. P. de Leon. Hybrid III-V diamond photonic platform for quantum nodes based on neutral silicon vacancy centers in diamond. *Optics Express* **29**, 9174–9189 (2021).
- [71] T. Asano, Y. Ochi, Y. Takahashi, K. Kishimoto, and S. Noda. Photonic crystal nanocavity with a Q factor exceeding eleven million. *Optics Express* **25**, 1769–1777 (2017).
- [72] S. Hu and S. M. Weiss. Design of photonic crystal cavities for extreme light concentration. *ACS Photonics* **3**, 1647–1653 (2016).
- [73] H. Choi, M. Heuck, and D. Englund. Self-similar nanocavity design with ultrasmall mode volume for single-photon nonlinearities. *Physical Review Letters* **118**, 223605 (2017).

- [74] P. Seidler, K. Lister, U. Drechsler, J. Hofrichter, and T. Stöferle. Slotted photonic crystal nanobeam cavity with an ultrahigh quality factor-to-mode volume ratio. *Optics Express* **21**, 32468–32483 (2013).
- [75] C. Yin, M. Rancic, G. G. de Boo, N. Stavrias, J. C. McCallum, M. J. Sellars, and S. Rogge. Optical addressing of an individual erbium ion in silicon. *Nature* **497**, 91–94 (2013).
- [76] N. Q. Vinh, N. N. Ha, and T. Gregorkiewicz. Photonic properties of Er-doped crystalline silicon. *Proceedings of the IEEE* **97**, 1269–1283 (2009).
- [77] L. Weiss, A. Gritsch, B. Merkel, and A. Reiserer. Erbium dopants in nanophotonic silicon waveguides. *Optica* **8**, 40–41 (2021).
- [78] T. Zhong, J. Rochman, J. M. Kindem, E. Miyazono, and A. Faraon. High quality factor nanophotonic resonators in bulk rare-earth doped crystals. *Optics Express* **24**, 536–544 (2016).
- [79] S. G. Johnson and J. D. Joannopoulos. Block-iterative frequency-domain methods for Maxwell’s equations in a planewave basis. *Optics Express* **8**, 173–190 (2001).
- [80] A. F. Oskooi, D. Roundy, M. Ibanescu, P. Bermel, J. D. Joannopoulos, and S. G. Johnson. Meep: A flexible free-software package for electromagnetic simulations by the FDTD method. *Computer Physics Communications* **181**, 687–702 (2010).
- [81] J. Chan, M. Eichenfield, R. Camacho, and O. Painter. Optical and mechanical design of a “zipper” photonic crystal optomechanical cavity. *Optics Express* **17**, 3802–3817 (2009).
- [82] Q. Quan and M. Loncar. Deterministic design of wavelength scale, ultra-high Q photonic crystal nanobeam cavities. *Optics Express* **19**, 18529–18542 (2011).
- [83] D. McAuslan, J. J. Longdell, and M. Sellars. Strong-coupling cavity QED using rare-earth-metal-ion dopants in monolithic resonators: What you can do with a weak oscillator. *Physical Review A* **80**, 062307 (2009).
- [84] H. T. Dung, S. Y. Buhmann, and D.-G. Welsch. Local-field correction to the spontaneous decay rate of atoms embedded in bodies of finite size. *Physical Review A* **74**, 023803 (2006).
- [85] S. Chen, S. Ourari, M. Raha, C. M. Phenicie, M. T. Uysal, and J. D. Thompson. Hybrid microwave-optical scanning probe for addressing solid-state spins in nanophotonic cavities. *Optics Express* **29**, 4902–4911 (2021).
- [86] G.-H. Lee, C.-H. Lee, A. M. Van Der Zande, M. Han, X. Cui, G. Arefe, C. Nuckolls, T. F. Heinz, J. Hone, and P. Kim. Heterostructures based on inorganic and organic van der Waals systems. *APL Materials* **2**, 092511 (2014).

- [87] S. Gröblacher, J. T. Hill, A. H. Safavi-Naeini, J. Chan, and O. Painter. Highly efficient coupling from an optical fiber to a nanoscale silicon optomechanical cavity. *Applied Physics Letters* **103**, 181104 (2013).
- [88] E. D. Black. An introduction to Pound–Drever–Hall laser frequency stabilization. *American Journal of Physics* **69**, 79–87 (2001).
- [89] E. R. Abraham and E. A. Cornell. Teflon feedthrough for coupling optical fibers into ultrahigh vacuum systems. *Applied Optics* **37**, 1762–1763 (1998).
- [90] T. Tiecke, K. Nayak, J. D. Thompson, T. Peyronel, N. P. de Leon, V. Vuletić, and M. Lukin. Efficient fiber-optical interface for nanophotonic devices. *Optica* **2**, 70–75 (2015).
- [91] S. M. Meenehan. *Cavity Optomechanics at Millikelvin Temperatures*. Ph.D. thesis, California Institute of Technology (2015).
- [92] S. Mosor, J. Hendrickson, B. Richards, J. Sweet, G. Khitrova, H. Gibbs, T. Yoshie, A. Scherer, O. Shchekin, and D. Deppe. Scanning a photonic crystal slab nanocavity by condensation of xenon. *Applied Physics Letters* **87**, 141105 (2005).
- [93] S. Strauf, M. T. Rakher, I. Carmeli, K. Hennessy, C. Meier, A. Badolato, M. J. DeDood, P. M. Petroff, E. L. Hu, E. Gwinn, and D. Bouwmeester. Frequency control of photonic crystal membrane resonators by monolayer deposition. *Applied Physics Letters* **88**, 043116 (2006).
- [94] E. Miyazono, I. Craiciu, A. Arbabi, T. Zhong, and A. Faraon. Coupling erbium dopants in yttrium orthosilicate to silicon photonic resonators and waveguides. *Optics Express* **25**, 2863–2871 (2017).
- [95] T. Zhong, J. M. Kindem, J. G. Bartholomew, J. Rochman, I. Craiciu, E. Miyazono, M. Bettinelli, E. Cavalli, V. Verma, S. W. Nam, *et al.* Nanophotonic rare-earth quantum memory with optically controlled retrieval. *Science* **357**, 1392–1395 (2017).
- [96] S. Welinski, P. J. Woodburn, N. Lauk, R. L. Cone, C. Simon, P. Goldner, and C. W. Thiel. Electron spin coherence in optically excited states of rare-earth ions for microwave to optical quantum transducers. *Physical Review Letters* **122**, 247401 (2019).
- [97] I. Kurkin and K. Chernov. EPR and spin-lattice relaxation of rare-earth activated centres in Y_2SiO_5 single crystals. *Physica B+C* **101**, 233–238 (1980).
- [98] M. Afzelius, I. Usmani, A. Amari, B. Lauritzen, A. Walther, C. Simon, N. Sangouard, J. Minář, H. De Riedmatten, N. Gisin, *et al.* Demonstration of atomic frequency comb memory for light with spin-wave storage. *Physical Review Letters* **104**, 040503 (2010).

- [99] J. Longdell, M. Sellars, and N. Manson. Demonstration of conditional quantum phase shift between ions in a solid. *Physical Review Letters* **93**, 130503 (2004).
- [100] D. D. Awschalom, R. Hanson, J. Wrachtrup, and B. B. Zhou. Quantum technologies with optically interfaced solid-state spins. *Nature Photonics* **12**, 516–527 (2018).
- [101] G. Kucsko, P. C. Maurer, N. Y. Yao, M. Kubo, H. J. Noh, P. K. Lo, H. Park, and M. D. Lukin. Nanometre-scale thermometry in a living cell. *Nature* **500**, 54–58 (2013).
- [102] P. Maletinsky, S. Hong, M. S. Grinolds, B. Hausmann, M. D. Lukin, R. L. Walsworth, M. Loncar, and A. Yacoby. A robust scanning diamond sensor for nanoscale imaging with single nitrogen-vacancy centres. *Nature Nanotechnology* **7**, 320–324 (2012).
- [103] F. Dolde, H. Fedder, M. W. Doherty, T. Nöbauer, F. Rempp, G. Balasubramanian, T. Wolf, F. Reinhard, L. C. Hollenberg, F. Jelezko, *et al.* Electric-field sensing using single diamond spins. *Nature Physics* **7**, 459–463 (2011).
- [104] W. Gao, P. Fallahi, E. Togan, J. Miguel-Sánchez, and A. Imamoglu. Observation of entanglement between a quantum dot spin and a single photon. *Nature* **491**, 426–430 (2012).
- [105] T. H. Taminiau, J. Cramer, T. van der Sar, V. V. Dobrovitski, and R. Hanson. Universal control and error correction in multi-qubit spin registers in diamond. *Nature Nanotechnology* **9**, 171–176 (2014).
- [106] A. Sipahigil, R. E. Evans, D. D. Sukachev, M. J. Burek, J. Borregaard, M. K. Bhaskar, C. T. Nguyen, J. L. Pacheco, H. A. Atikian, C. Meuwly, *et al.* An integrated diamond nanophotonics platform for quantum-optical networks. *Science* **354**, 847–850 (2016).
- [107] D. J. Christle, A. L. Falk, P. Andrich, P. V. Klimov, J. U. Hassan, N. T. Son, E. Janzén, T. Ohshima, and D. D. Awschalom. Isolated electron spins in silicon carbide with millisecond coherence times. *Nature Materials* **14**, 160–163 (2015).
- [108] T. Zhong, J. M. Kindem, J. G. Bartholomew, J. Rochman, I. Craiciu, V. Verma, S. W. Nam, F. Marsili, M. D. Shaw, A. D. Beyer, *et al.* Optically addressing single rare-earth ions in a nanophotonic cavity. *Physical Review Letters* **121**, 183603 (2018).
- [109] A. Delteil, W.-b. Gao, P. Fallahi, J. Miguel-Sánchez, and A. Imamoglu. Observation of quantum jumps of a single quantum dot spin using submicrosecond single-shot optical readout. *Physical Review Letters* **112**, 116802 (2014).

- [110] P. Tamarat, N. Manson, J. Harrison, R. McMurtrie, A. Nizovtsev, C. Santori, R. Beausoleil, P. Neumann, T. Gaebel, F. Jelezko, *et al.* Spin-flip and spin-conserving optical transitions of the nitrogen-vacancy centre in diamond. *New Journal of Physics* **10**, 045004 (2008).
- [111] S. Sun, H. Kim, G. S. Solomon, and E. Waks. Cavity-enhanced optical readout of a single solid-state spin. *Physical Review Applied* **9**, 054013 (2018).
- [112] A. Abragam and B. Bleaney. *Electron paramagnetic resonance of transition ions*. (Dover, 1986).
- [113] S. Gammelmark, K. Mølmer, W. Alt, T. Kampschulte, and D. Meschede. Hidden Markov model of atomic quantum jump dynamics in an optically probed cavity. *Physical Review A* **89**, 043839 (2014).
- [114] D. Hume, T. Rosenband, and D. J. Wineland. High-fidelity adaptive qubit detection through repetitive quantum nondemolition measurements. *Physical Review Letters* **99**, 120502 (2007).
- [115] B. Car, L. Veissier, A. Louchet-Chauvet, J.-L. Le Gouët, and T. Chanelière. Optical study of the anisotropic erbium spin flip-flop dynamics. *Physical Review B* **100**, 165107 (2019).
- [116] J. R. Petta, A. C. Johnson, J. M. Taylor, E. A. Laird, A. Yacoby, M. D. Lukin, C. M. Marcus, M. P. Hanson, and A. C. Gossard. Coherent manipulation of coupled electron spins in semiconductor quantum dots. *Science* **309**, 2180–2184 (2005).
- [117] C. M. Phenicie, P. Stevenson, S. Welinski, B. C. Rose, A. T. Asfaw, R. J. Cava, S. A. Lyon, N. P. De Leon, and J. D. Thompson. Narrow optical line widths in erbium implanted in tio_2 . *Nano Letters* **19**, 8928–8933 (2019).
- [118] D. D. Awschalom, L. C. Bassett, A. S. Dzurak, E. L. Hu, and J. R. Petta. Quantum spintronics: engineering and manipulating atom-like spins in semiconductors. *Science* **339**, 1174–1179 (2013).
- [119] G. Waldherr, Y. Wang, S. Zaiser, M. Jamali, T. Schulte-Herbrüggen, H. Abe, T. Ohshima, J. Isoya, J. Du, P. Neumann, and J. Wrachtrup. Quantum error correction in a solid-state hybrid spin register. *Nature* **506**, 204–207 (2014).
- [120] S. Choi, J. Choi, R. Landig, G. Kucsko, H. Zhou, J. Isoya, F. Jelezko, S. Onoda, H. Sumiya, V. Khemani, *et al.* Observation of discrete time-crystalline order in a disordered dipolar many-body system. *Nature* **543**, 221–225 (2017).
- [121] P. Maurer, J. Maze, P. Stanwix, L. Jiang, A. V. Gorshkov, A. A. Zibrov, B. Harke, J. Hodges, A. S. Zibrov, A. Yacoby, *et al.* Far-field optical imaging and manipulation of individual spins with nanoscale resolution. *Nature Physics* **6**, 912–918 (2010).

- [122] P. Neumann, R. Kolesov, B. Naydenov, J. Beck, F. Rempp, M. Steiner, V. Jacques, G. Balasubramanian, M. Markham, D. Twitchen, S. Pezzagna, J. Meijer, J. Twamley, F. Jelezko, and J. Wrachtrup. Quantum register based on coupled electron spins in a room-temperature solid. *Nature Physics* **6**, 249–253 (2010).
- [123] F. Dolde, I. Jakobi, B. Naydenov, N. Zhao, S. Pezzagna, C. Trautmann, J. Meijer, P. Neumann, F. Jelezko, and J. Wrachtrup. Room-temperature entanglement between single defect spins in diamond. *Nature Physics* **9**, 139–143 (2013).
- [124] M. Grinolds, P. Maletinsky, S. Hong, M. Lukin, R. Walsworth, and A. Yacoby. Quantum control of proximal spins using nanoscale magnetic resonance imaging. *Nature Physics* **7**, 687–692 (2011).
- [125] S. Kolkowitz, Q. P. Unterreithmeier, S. D. Bennett, and M. D. Lukin. Sensing distant nuclear spins with a single electron spin. *Physical Review Letters* **109**, 137601 (2012).
- [126] T. Taminiau, J. Wagenaar, T. Van der Sar, F. Jelezko, V. V. Dobrovitski, and R. Hanson. Detection and control of individual nuclear spins using a weakly coupled electron spin. *Physical Review Letters* **109**, 137602 (2012).
- [127] N. Zhao, J. Honert, B. Schmid, M. Klas, J. Isoya, M. Markham, D. Twitchen, F. Jelezko, R.-B. Liu, H. Fedder, *et al.* Sensing single remote nuclear spins. *Nature Nanotechnology* **7**, 657–662 (2012).
- [128] K. Ichimura. A simple frequency-domain quantum computer with ions in a crystal coupled to a cavity mode. *Optics Communications* **196**, 119–125 (2001).
- [129] N. Ohlsson, R. K. Mohan, and S. Kröll. Quantum computer hardware based on rare-earth-ion-doped inorganic crystals. *Optics Communications* **201**, 71–77 (2002).
- [130] J. H. Wesenberg, K. Mølmer, L. Rippe, and S. Kröll. Scalable designs for quantum computing with rare-earth-ion-doped crystals. *Physical Review A* **75**, 012304 (2007).
- [131] R. Ahlefeldt, M. Pearce, M. Hush, and M. Sellars. Quantum processing with ensembles of rare-earth ions in a stoichiometric crystal. *Physical Review A* **101**, 012309 (2020).
- [132] G. Pryde, M. Sellars, and N. Manson. Solid state coherent transient measurements using hard optical pulses. *Physical Review Letters* **84**, 1152 (2000).

- [133] J. Longdell and M. Sellars. Experimental demonstration of quantum-state tomography and qubit-qubit interactions for rare-earth-metal-ion-based solid-state qubits. *Physical Review A* **69**, 032307 (2004).
- [134] J. M. Kindem, A. Ruskuc, J. G. Bartholomew, J. Rochman, Y. Q. Huan, and A. Faraon. Control and single-shot readout of an ion embedded in a nanophotonic cavity. *Nature* **580**, 201–204 (2020).
- [135] M. Afzelius, M. U. Staudt, H. De Riedmatten, N. Gisin, O. Guillot-Noël, P. Goldner, R. Marino, P. Porcher, E. Cavalli, and M. Bettinelli. Efficient optical pumping of zeeman spin levels in Nd³⁺:YVO₄. *Journal of Luminescence* **130**, 1566–1571 (2010).
- [136] B. Buckley, G. Fuchs, L. Bassett, and D. Awschalom. Spin-light coherence for single-spin measurement and control in diamond. *Science* **330**, 1212–1215 (2010).
- [137] B. E. Kane. A silicon-based nuclear spin quantum computer. *Nature* **393**, 133–137 (1998).
- [138] L. Childress, M. G. Dutt, J. Taylor, A. Zibrov, F. Jelezko, J. Wrachtrup, P. Hemmer, and M. Lukin. Coherent dynamics of coupled electron and nuclear spin qubits in diamond. *Science* **314**, 281–285 (2006).
- [139] M. G. Dutt, L. Childress, L. Jiang, E. Togan, J. Maze, F. Jelezko, A. Zibrov, P. Hemmer, and M. Lukin. Quantum register based on individual electronic and nuclear spin qubits in diamond. *Science* **316**, 1312–1316 (2007).
- [140] J. Cramer, N. Kalb, M. A. Rol, B. Hensen, M. S. Blok, M. Markham, D. J. Twitchen, R. Hanson, and T. H. Taminiau. Repeated quantum error correction on a continuously encoded qubit by real-time feedback. *Nature Communications* **7**, 11526 (2016).
- [141] T. Kornher, D.-W. Xiao, K. Xia, F. Sardi, N. Zhao, R. Kolesov, and J. Wrachtrup. Sensing individual nuclear spins with a single rare-earth electron spin. *Physical Review Letters* **124**, 170402 (2020).
- [142] C.-K. Hong, Z.-Y. Ou, and L. Mandel. Measurement of subpicosecond time intervals between two photons by interference. *Physical Review Letters* **59**, 2044 (1987).
- [143] J. Bylander, I. Robert-Philip, and I. Abram. Interference and correlation of two independent photons. *The European Physical Journal D - Atomic, Molecular, Optical and Plasma Physics* **22**, 295–301 (2003).
- [144] K. Groot-Berning, T. Kornher, G. Jacob, F. Stopp, S. T. Dawkins, R. Kolesov, J. Wrachtrup, K. Singer, and F. Schmidt-Kaler. Deterministic single-ion implantation of rare-earth ions for nanometer-resolution color-center generation. *Physical Review Letters* **123**, 106802 (2019).

- [145] S. D. Barrett and P. Kok. Efficient high-fidelity quantum computation using matter qubits and linear optics. *Physical Review A* **71**, 060310 (2005).
- [146] T.-M. Zhao, H. Zhang, J. Yang, Z.-R. Sang, X. Jiang, X.-H. Bao, and J.-W. Pan. Entangling different-color photons via time-resolved measurement and active feed forward. *Physical Review Letters* **112**, 103602 (2014).
- [147] D. M. Toyli, C. D. Weis, G. D. Fuchs, T. Schenkel, and D. D. Awschalom. Chip-scale nanofabrication of single spins and spin arrays in diamond. *Nano Letters* **10**, 3168–3172 (2010).
- [148] Y. Chu, N. P. de Leon, B. J. Shields, B. Hausmann, R. Evans, E. Togan, M. J. Burek, M. Markham, A. Stacey, A. S. Zibrov, *et al.* Coherent optical transitions in implanted nitrogen vacancy centers. *Nano Letters* **14**, 1982–1986 (2014).
- [149] K. Xia, R. Kolesov, Y. Wang, P. Siyushev, R. Reuter, T. Kornher, N. Kukharchyk, A. D. Wieck, B. Villa, S. Yang, *et al.* All-optical preparation of coherent dark states of a single rare earth ion spin in a crystal. *Physical Review Letters* **115**, 093602 (2015).
- [150] T. Kornher, K. Xia, R. Kolesov, N. Kukharchyk, R. Reuter, P. Siyushev, R. Stöhr, M. Schreck, H.-W. Becker, B. Villa, *et al.* Production yield of rare-earth ions implanted into an optical crystal. *Applied Physics Letters* **108**, 053108 (2016).
- [151] M. Berthel, O. Mollet, G. Dantelle, T. Gacoin, S. Huant, and A. Drezet. Photophysics of single nitrogen-vacancy centers in diamond nanocrystals. *Physical Review B* **91**, 035308 (2015).
- [152] M. Weber, J. Volz, K. Saucke, C. Kurtsiefer, and H. Weinfurter. Analysis of a single-atom dipole trap. *Physical Review A* **73**, 043406 (2006).
- [153] G. Sallen, A. Tribu, T. Aichele, R. André, L. Besombes, C. Bougerol, M. Richard, S. Tatarenko, K. Kheng, and J.-P. Poizat. Subnanosecond spectral diffusion measurement using photon correlation. *Nature Photonics* **4**, 696–699 (2010).
- [154] T. Böttger, Y. Sun, C. W. Thiel, and R. L. Cone. Material optimization of Er³⁺:Y₂SiO₅ at 1.5 μm for optical processing, memory, and laser frequency stabilization applications. *Proc. SPIE* **4988**, (2003).
- [155] L. D. Barron. *Molecular light scattering and optical activity*. (Cambridge University Press, Cambridge, 2004).
- [156] E. Sabisky and C. Anderson. Spin-lattice relaxation of Tm²⁺ in CaF₂, SrF₂, and BaF₂. *Physical Review B* **1**, 2028 (1970).